Through-thickness microstructure and mechanical properties of electron beam similar welded AISI 316L stainless steel and dissimilar welded AISI 316L / Ti6Al4V

By

Muhaed Alali

A thesis submitted for the degree of Doctor of Philosophy

The University of Sheffield

Department of Material Science and Engineering

August 2017

Summary

Through thickness microstructure and mechanical properties of defect-free electron beam welded 20 mm thick AISI 316L austenitic stainless steel has been investigated as a function of beam power. The weld microstructure is characterised by a columnar and equiaxed dendritic ferrite in an austenite matrix. The dendritic structure was finer at the bottom of the weld zone. A microstructural boundary called "Parting" was seen along the weld centreline. Tensile tests, using a digital image correlation technique, demonstrated that the highest strain was concentrated in the fusion zone. The bottom section of the weld metal exhibited a yield strength of about 14 – 52 MPa higher than the top section. The ultimate tensile strength in the bottom of the weld was also about 4% higher than the top. The final fracture was detected in the parting region. It was observed from the EBSD scan that the grains in the weld zone contained a weak orientation and showed a high Schmid factor intensity with interception between some strong grains and soft grains at the weld centreline boundary. This explains the high weld ductility and the failure to happen in the parting region.

Dissimilar welding of 20 mm thick AISI 316L stainless steel to TiAl6V4 using electron beam welding process was carried out. A successful joint was possible through using of copper sheet with 1.5 mm thick as a transition layer between the two metals. Preheating the weld samples was performed to lower the heat input and reduce the residual stresses. A double pass welding technique was applied to achieve full weld penetration. The weld microstructure was studied by SEM, EDS and XRD. The sensitivity of the microstructure to cracking was evaluated by a microhardness test of the weld cross-section. The weld region near the stainless steel contained Fe and Cu in solid solution. While the weld area near the titanium alloy characterised by the copper solid solution with Cu-Ti and Cu-Fe-Ti intermetallic phases. Ti-Fe intermetallic compounds was suppressed and replaced by relatively soft Cu-Ti intermetallics, which significantly improved the joint toughness. However, the formation of Ti-Cu at the Ti/Cu interface makes this region still susceptible to cracking.

Contents

Acknowledgements

This research project would not have been possible without the support of many people. Firstly, I would like to express my gratitude to my supervisor, Prof. Brad Wynne for his support and guidance throughout the project and for the knowledge that I received from him and his great amount of time and effort he spent to help me to finish my project. I would also thank my second supervisor Prof. Iain Todd for the valuable information that he gave me and his support during my study.

I also want to thank all the technical staff in the Department of Materials Science and Engineering for helping me to carry out my experimental work and providing laboratory facilities, in particular James Hunt, Ben Palmer, Mike Bell and Dean Haylock. I also thank my all friends and colleagues in D1, the place where I spent my time, especially Jamie Pennington, Oliver Hatt and Faris Karouni for their cooperation.

I would like to acknowledge my country, Iraq, represented by the Iraqi ministry of high education and scientific research and the Iraqi cultural attaché for the generous financial support and the great chance of study they gave me. I would also like to thank all the staff at the Faculty of Engineering-University of Kufa, the place from which I came, for facilitating all the documentations required to start this scholarship.

I was also fortunate to know some great Iraqi students in Sheffield who also study in this great university.

I would like to express my love and gratitude to my beloved family; for their understanding & endless love, who have always given me their support through the duration of my studies. My wife and my children Shams and Laith, I love you all.

Finally, I would like to thank from all my heart, my mother for her unlimited encouragement, support and non-stopping prayer for me.

Table of figures

List of tables

Nomenclature

A	Austenite solidification mode
AF	Austenite Ferrite solidification mode
AISI	American Iron and Steel Institute
ASTM	American Society for Testing and Materials
BCC	Body Centered Cubic
BM	Base Metal
BS	British Standard
D/W	Depth to Width Ratio
DIC	Digital Image Correlation
EBW	Electron Beam Welding
EBSD	Electron Back Scatter Detection
EDM	Electrical Discharged Machining
EDS	Energy Dispersive Spectroscopy
eq	Equivalent
Eut	Eutectic
F	Ferrite
FA	Ferrite Austenite
FCC	Face centered Cubic
FN	Ferrite Number
FZ	Fusion Zone
G	Temperature gradient in the liquid
HAZ	Heat Affected Zone
HCP	Hexagonal Closed Pack
L	Low carbon stainless steel grade
LBW	Laser Beam Welding
MIG	Metal Inert Gas
PH	Precipitation Hardened
Q/V	Heat input per unit length
R	Solidification rate
R_{C1}	Critical growth rate
R_{C2}	Higher growth rate
SEM	Scanning Electron Microscopy
SDAS	Secondary Dendrite Arm Spacing
TIG	Tungsten Inert Gas
UTS	Ultimate Tensile Strength
VH	Vickers Hardness
WRC	Welding Research Council
Wt%	Weight Percentage
XRD	X-Ray Diffraction
YS	Yield Strength

Chapter 1 Introduction

1.1 Introduction

The importance of welding in manufacturing can be realized through the ability of the welding technique to join a variety of materials and components with different shapes and sizes. This can provide significant design flexibility and component complexity that other manufacturing techniques cannot match, e.g., Figure 1.1 shows an example of a complex multi-material application only made possible through welding [1, 2].
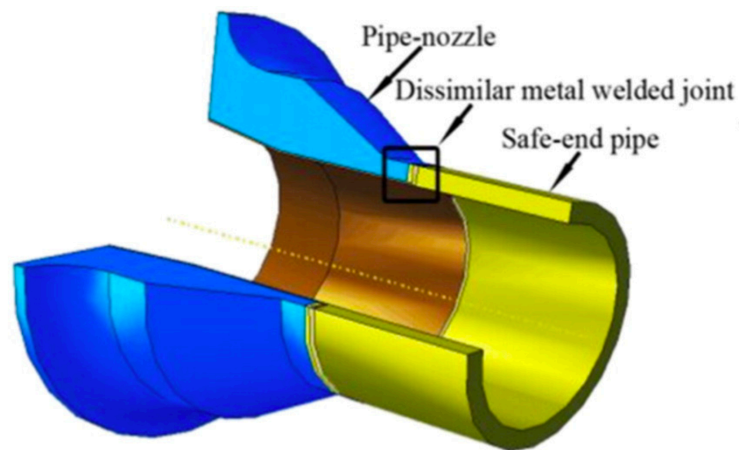
Figure 1.1 Ferritic steel pipe nozzle joined with austenitic stainless steel end in a pressure vessel part [3].

Fabrication of thick section structures by high temperature, low pressure fusion welding, i.e. melting at the joint, is a commonly used method in many industry sectors, such as the nuclear, petrochemical and oil industries. Currently, the most prevalent thick section welding processes are those based on arc welding, e.g. submerged arc welding and tungsten inert gas (TIG). These methods are relatively slow and require many passes, which generate a very high heat input and produce significant distortion and/or residual stresses, leading to significant difficulties especially with welding dissimilar materials, e.g. formation of brittle phases and segregation of alloying elements attributed to the high and uncontrollable heat input of these methods [4-6].

Solid-state welding techniques, i.e. low temperature, high pressure processes, such as friction welding and other joining methods such as brazing and soldering and adhesive

bonding have been used successfully in welding materials with enhanced joint strength. These welding processes can be performed while the material remains in the solid state, which can eliminate the difficulties associated with a fusion welding process. However, these techniques have limited applications, e.g. soldering and adhesive bonding cannot be used for joining components that are working in high temperature applications. In addition, some techniques, such as friction welding, require specific component shape and geometry in order to be applied [1, 7].

All the limitations above have led to the emergence of high power density techniques of laser beam welding (LBW) and electron beam welding (EBW). These processes provide high speed, deep weld penetration, low distortion, together with precise, controllable heating position and size. All these advantages make them applicable for a wide range of industrial application areas, Figure 1.2, and ideally suited for joining thick sections parts particularly when a high depth to width ratio (D/W), narrow heat affected zone (HAZ) and controllable heat distribution are required. [4, 5, 8]. Figures 1.3 and 1.4 show a comparison of weld distortion between the EBW and TIG processes.
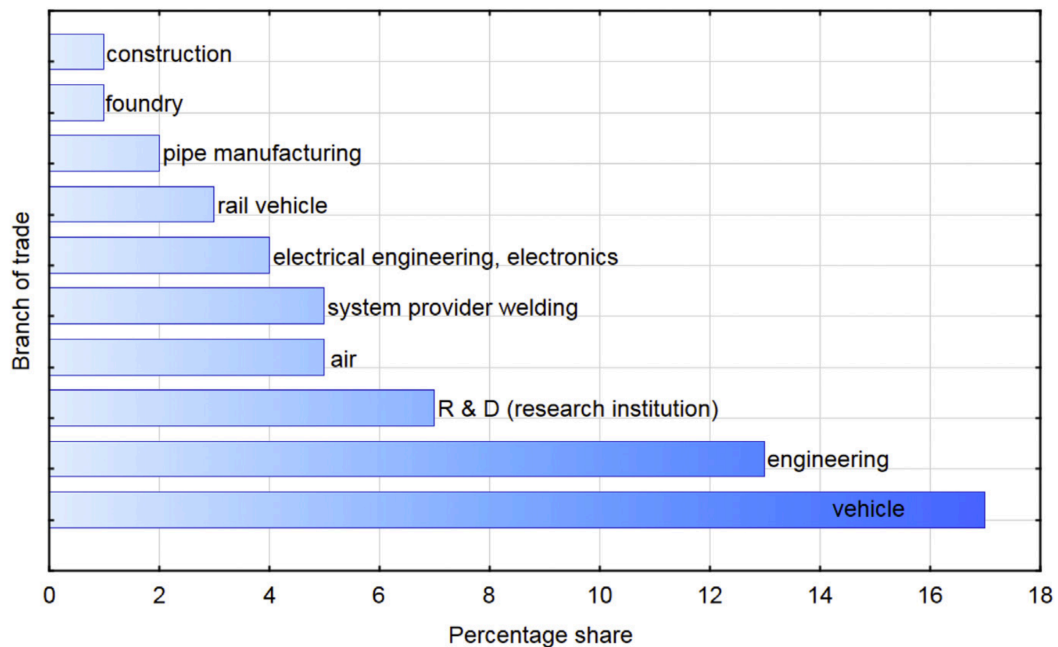
Figure 1.2 Application sectors of EBW [9].
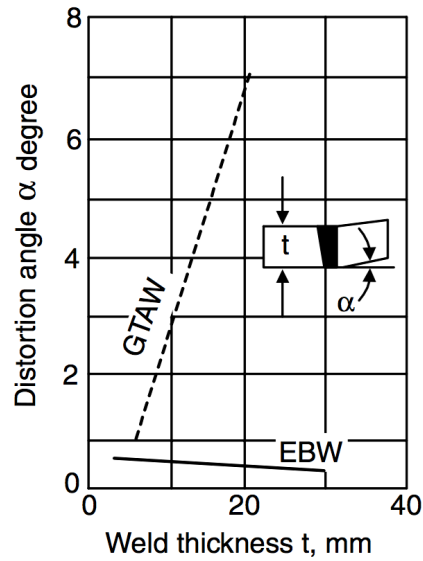
Figure 1.3 Comparison of angular distortion originated by EBW and TIG [10].
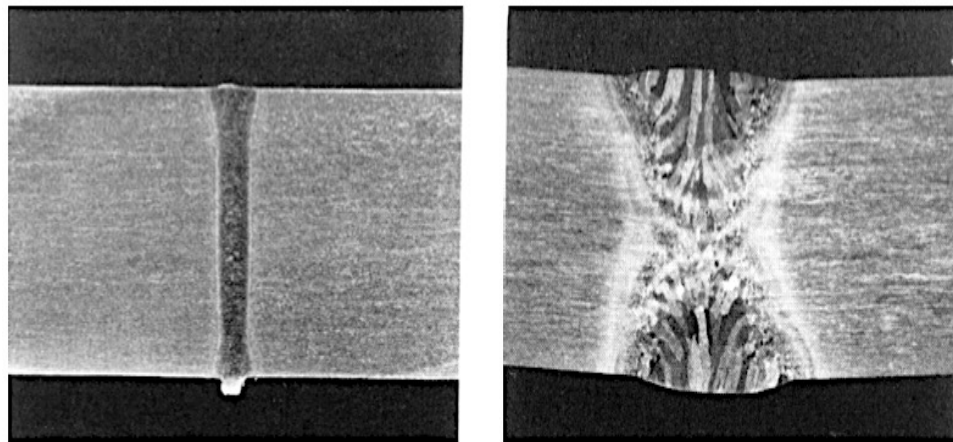
Figure 1.4 Cross sections of 12 mm Al welds performed with (a) EBW and (b) TIG [11].

Joining of titanium alloy to stainless steel is widely used in various industrial applications, taking advantage of the specific features of each metal, such as the high specific strength and the excellent corrosion resistance of titanium alloys and the relatively low cost of the stainless steel. However, the joining of these metals has considerable problems due to their differences in metallurgical and physical properties, thereby requiring special conditions and parameters in order to be welded together, Figure 1.5. The properties of the EBW process have made it possible to overcome most of these

difficulties by minimizing the effect of welding heat and suppressing the mixing of each metal [2, 7].

The use of intermediate materials can improve the joining possibility between titanium and steel. This is because they can have a good metallurgical compatibility with titanium and steel, i.e. not forming intermetallic phases and adding some ductility that enhances the joint's toughness. Materials such as Zr, Mo, Ta and Ag can be used as a potential interlayer. However, their limited availability combined with high cost and poor weldability with steel have led to the use of more available and lower cost materials such as Cu [6, 12]. There is, however, limited knowledge of how the microstructure may vary through the thickness following EBW. Furthermore, the suitable procedure and parameters that are required to successfully join stainless steel to itself and to titanium of such thickness, is a significant knowledge gap that must be determined before the maximum potential of the technology is fulfilled.

1.2 Aims and objectives

The aim of this thesis is to investigate the through thickness microstructure and mechanical properties of defect-free electron beam welded 20mm thick AISI 316L austenitic stainless steel as a function of beam power. The possibility of electron beam welding of 20mm thick AISI 316L austenitic stainless steel to a Ti6Al4V alloy has also been investigated. These have been undertaken with the aim of identifying key aspects of the as-welded microstructure or its variation through the weld that will define its design requirements and limitations.
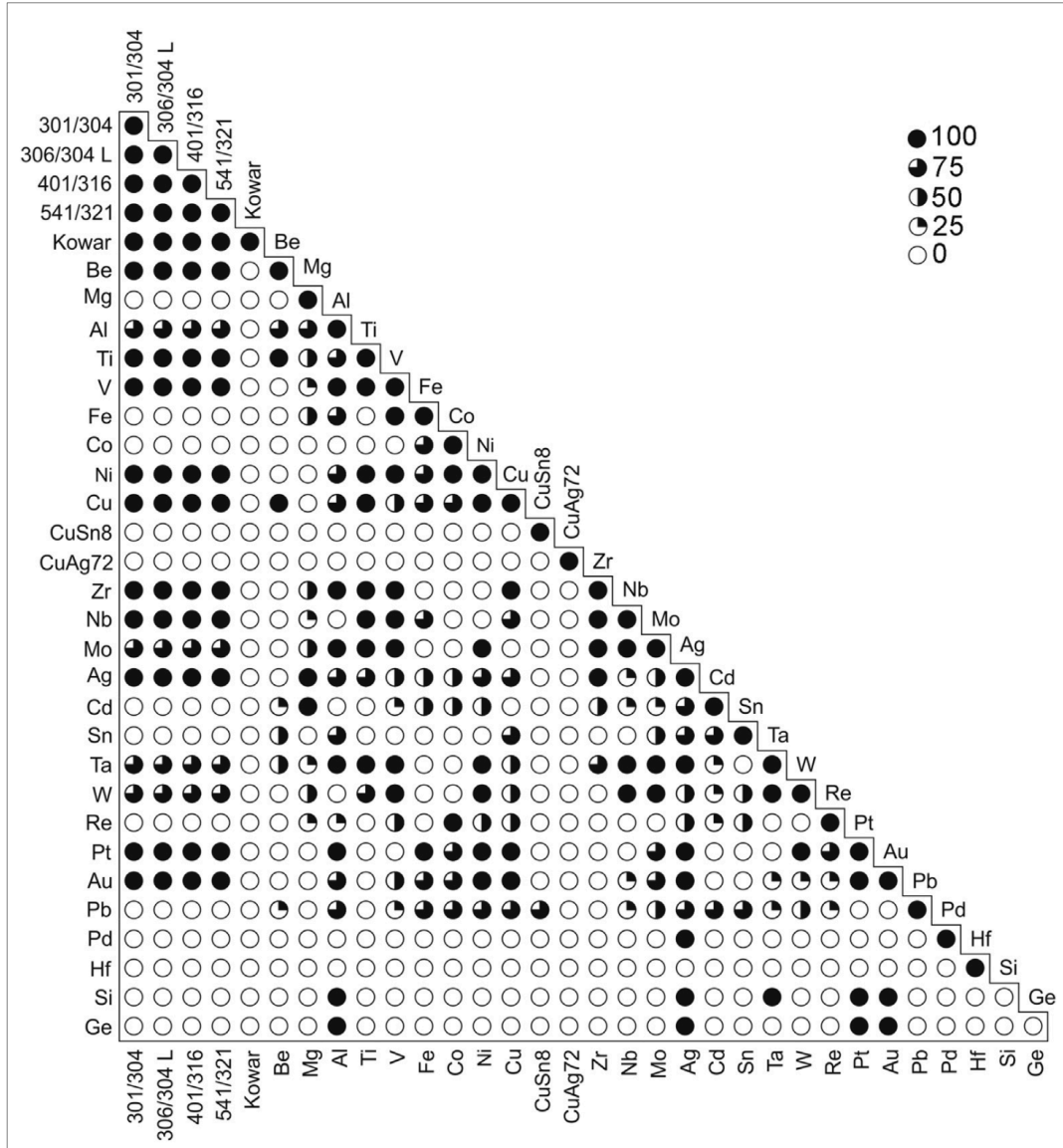
Figure 1.5 The ability of joining various materials by EBW process. 100-Very desirable (solid solubility in all combinations) or already validated, 75-Probably acceptable (complex structures may exist), 50-Use with caution (not enough data for appropriate evaluation), 25-Use with extreme caution (no data available), and 0- Undesirable combinations (intermetallic compounds formed) [13].

1.3 Thesis Outline

Chapter 2 introduces principles and features of the EBW technique. This includes the advantages, weaknesses and process variables. Then some of previous studies that have used different process parameters are also explored. The chapter then illustrates the materials that are used in this work, starting with a stainless steel background, welding metallurgy and weldability of stainless steel, including phase transformation and solidification during welding and welding defects. A general background to titanium is also covered. The chapter later focuses on the dissimilar welding between stainless steel and titanium.

Chapter 3 illustrates the experimental and analytical methods used with a detailed description of the EBW welding procedure, sample preparation, etching, and analytical techniques used during this study.

Chapter 4 presents and analyses the results of AISI 316L similar welding and discusses the microstructure and the mechanical properties of the welds.

Chapter 5 covers and discusses the results of dissimilar Ti6Al4V-AISI 316L autogenous welds and welds using a Cu interlayer.

Chapter 6 concludes this work including experimental welding and testing procedures, weld microstructure features and mechanical properties.

Chapter 7 presents the final further work subsection detailing the author's suggested areas of further research.

Chapter 2 Literature Review

2.1 Introduction

This chapter presents an overview of the related literature starting with the principles and fundamentals of the EBW process including its main advantages and drawbacks. The important variables that control the EBW process are also covered. This is then followed by an overview of stainless steels and titanium alloys with an emphasis on austenitic stainless steel and Ti6Al4V alloy in respect of their welding metallurgy and weldability. The chapter ends with an analysis of dissimilar welding of AISI 316L austenitic stainless steel to Ti6Al4V alloy using the EBW process.

2.2 Electron beam welding

The first use of an electron beam as a heat source for welding was in 1958 by Steigerwald, who used it to weld 5mm plates of Zircaloy. It was found that by regulating parameters such as increasing the beam current, it becomes possible to produce a high full penetration weld with a relatively small width [14, 15]. Currently, the electron beam process is firmly established in many industrial fields such as the aerospace and automobile industries. It is used with different manufacturing techniques including welding and cutting technologies because of its high reliability, efficiency and accuracy.

The EBW process is categorized as a high-energy beam fusion welding that has the following main features in comparison with other welding methods [14-16]:

1. An outstanding power density of around more than 10^6 W/cm^2.
2. High welding speed resulting in narrow weld and heat affected zone (HAZ) with little distortion of the workpiece.
3. Inertia free oscillation of the electron beam making it possible, in many cases, to join materials otherwise considered unsuitable for welding.
3. Good protection of the weld pool from contamination by oxidation because the welding process is commonly carried out under vacuum.

2.2.1 EBW process system and beam formation

In an electron beam welding system, the electrons are generated as a current is passed through a tungsten filament in a high vacuum chamber. An electrostatic field between the negative cathode and positively charged electrode (anode) then accelerates the electrons to about two-thirds the speed of light to achieve sufficient kinetic energy for welding. The divergent high speed electrons then can be shaped and focused through several magnetic and electrostatic lenses to a spot diameter of between 0.1 and 1.0 mm to reach the required power density of 10^6 to 10^7 W/cm^2. The electron beam is then guided into the workpiece by deflection coils. [15]. Oscillating of the electron beam can also be employed by applying an alternating current in the deflection coils system. An Illustration of an EBW machine is shown in Figure 2.1 [17].
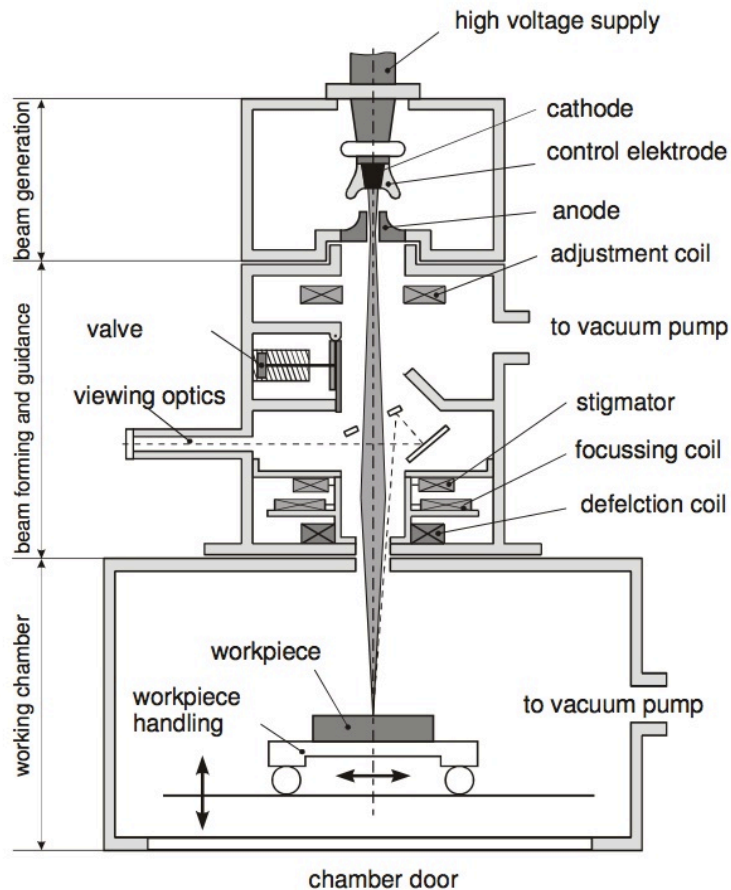
Figure 2.1 Schematic illustration of an EBW machine [18].

2.2.2 Penetration mechanism in EBW

When a focused electron beam hits the surface of the workpiece, the kinetic energy of the electrons transforms into thermal energy and starts to penetrate the component. However, the depth of penetration is very shallow due to the low mass of the electrons. Thus, an additional process is required to achieve large weld depth, this process called deep penetration effect [19].The extremely high power per unit area (power density) of the electron beam can raise the temperature of the metal at the impact area to a temperature that could exceed the boiling point of all known materials [20]. This high power density evaporates the metal and allows for the new electrons to reach the fresh new metal and causes a deeper penetration and generates a vapour with very high pressure, which pushes away the molten metal to the sides and upwards. This consequently creates a cavity inside the metal surrounded by a shell of fluid metal known as a keyhole, as shown in Figure 2.2 [19, 21]. When the beam moves during welding, the molten metal moves towards the depth of the weld pool through the side wall of the keyhole. The driving forces for the molten metal movement are the surface tension that resulted from differences in the surface temperatures of the keyhole walls, the reactive pressure of evaporating atoms and the hydrostatic forces. Vapour pressure keeps the keyhole open by countering the hydrostatic pressure and the surface tension and pressing the molten metal around the vapour column against the cavity walls, Figure 2.3 [20].
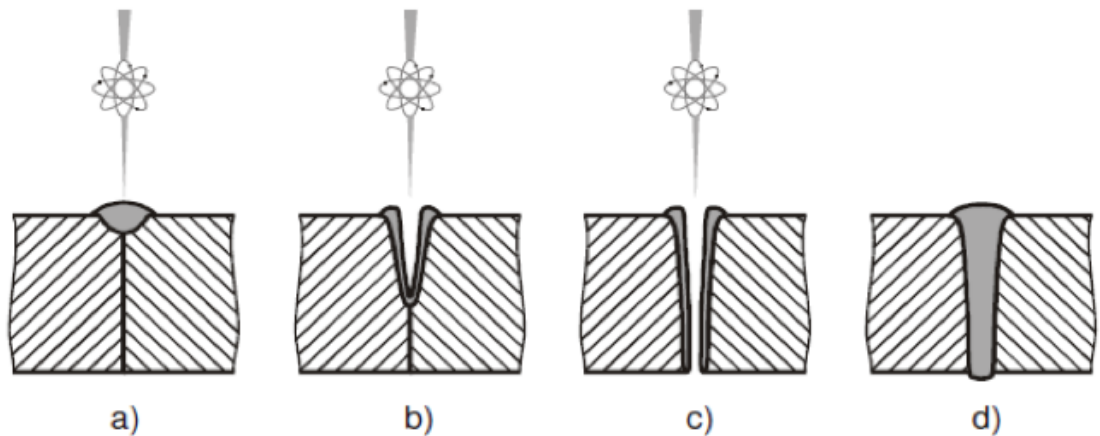
Figure 2.2 The stages of deep penetration in EBW[15].
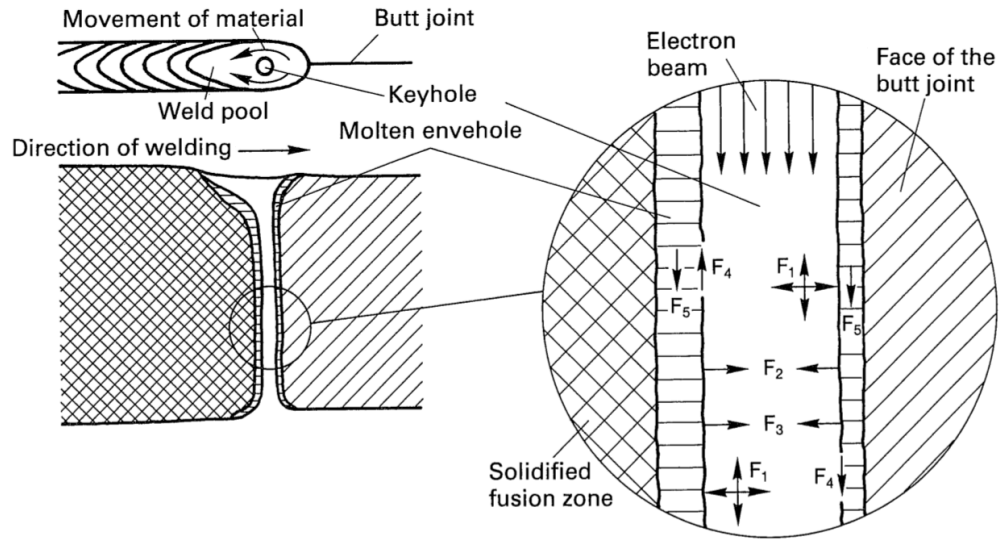
F_1 = Vapour pressure; F_2 = Force resulting from surface tension; F_3 = Hydrostatic pressure; F_4 = Frictional force from the escaping metal vapour; F_5 = Weight of the molten mantle.

Figure 2.3 The major forces in the keyhole and the molten envelop in EBW [15].

2.2.3 The effect of power density

The power density can be defined as the power transferred to the work per unit surface area, W/mm^2, so that in EBW the power density is expressed as

$$PD = \frac{f_1 EI}{A} \ \text{......} \qquad\qquad\qquad .....$$

(2.1)

Where PD = power density, W/mm^2; f_1 = heat transfer factor; E = accelerating voltage, V; I = beam current, A; and A = the work surface area on which the electron beam is focused, mm^2 [22].

It has been found that the minimum power density required to melt most metals in welding is about 10^7 W/m^2. Above around 10^{12} W/m^2, the localized temperature vaporises the metal in the affected region. As such, there is a practical range of values for power density within which welding can be performed, as shown in Figure 2.4 [23]. The capability of the EBW method to make a deep and narrow weld, as shown in Figure 2.5, makes using this method very applicable in welding thick sections with a single pass, instead of using the multi-pass welding technique, which is required in other conventional welding techniques, as illustrated schematically in Figure 2.6 [11].

10
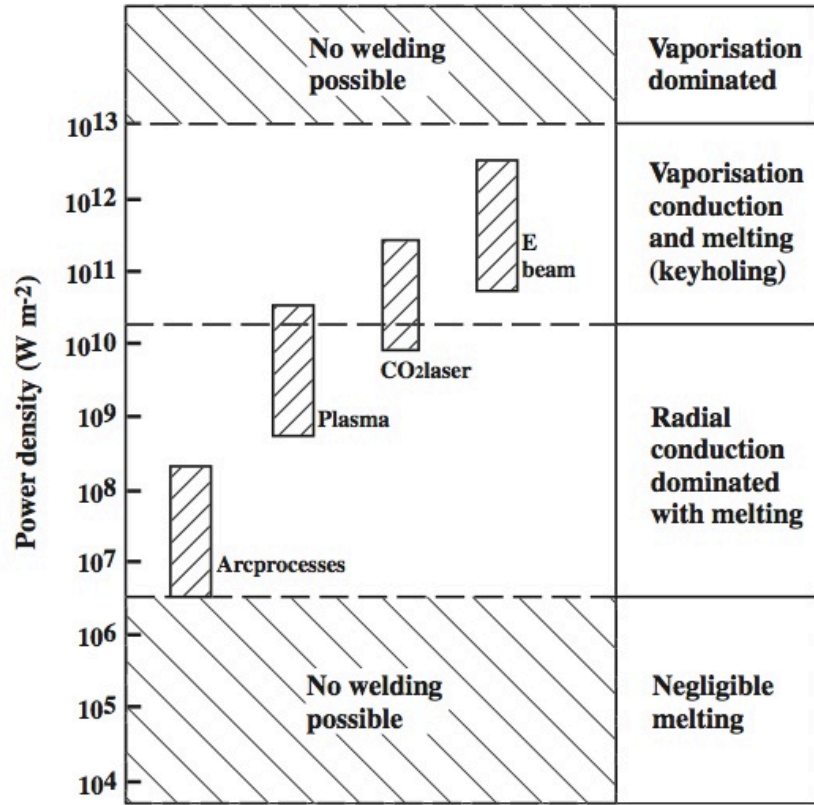
Figure 2.4 Spectrum of practical heat intensities of several fusion welding processes[23].
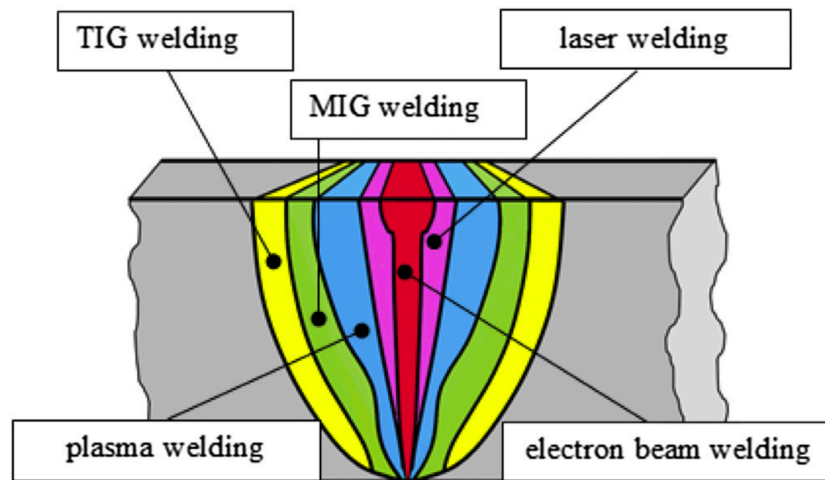
Figure 2.5 A comparison of weld size between different welding technique. TIG and metal inert gas (MIG) welding processes [13].
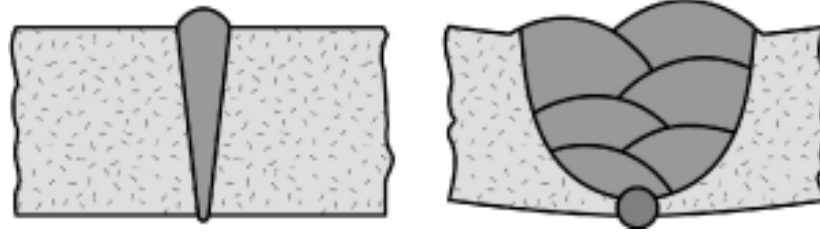
Figure 2.6 Cross sections of welds performed with (a) EBW and (b) TIG [11].

Under the same heat input and welding speed, weld penetration decreases with decreasing power density of the heat source, as indicated in Figure 2.7. As an approximation, the power density distribution at the workpiece surface is often considered Gaussian, as shown by the following equation:

$$q = \frac{3Q}{\pi a^2} \exp\left[-\frac{r^2}{\frac{a^2}{3}}\right] \dots \qquad \dots$$

(2.2)

Where q is the power density, Q the rate of heat transfer from the heat source to the workpiece and a the effective radius of the heat source and r the weld penetration [10].

High-power density increases the efficiency of the welding process and allows for higher welding speeds. This makes the process require less heat input for the same joint, resulting in a stronger weld with minimum distortion, as show in Figure 2.8 [10, 18].However, high-power density processes, such as laser beam and EBW, cannot be humanly controlled and must therefore be automated, which requires a highly skilled fully trained operator. This leads to increased capital costs, as shown in Figure 2.9 [11]. In EBW, the power input per unit distance along the workpiece during welding can be calculated using the following formula:

$$E_{input} = 60\ VI_b\ /\ s \ \dots\dots \qquad \dots\dots$$

(2.3)

Where V, I_b and s are the beam accelerating potential in volts, the beam current in amps and welding speed in m/min, respectively [24].
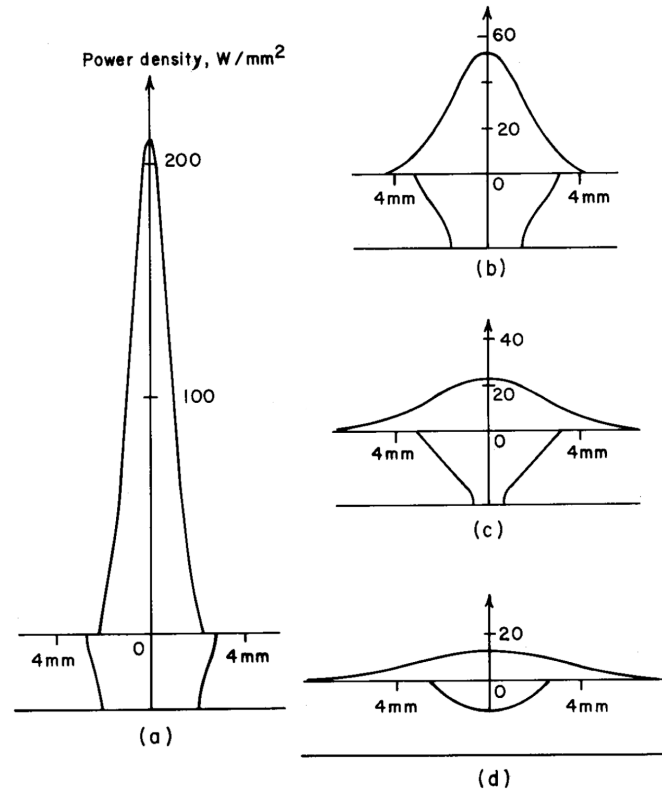
Figure 2.7 Effect of power density distribution on weld shape in TIG of 3.2-mm 6061 aluminium with 880 W and 4.23 mm/s. The power density decreases from 200 to 20 W/mmm^2 from (a) through (d) [10].

2.2.4 Controlling of EBW

In EBW, controlling of beam variables is very important to achieve the desired fusion zone (FZ) shape, acceptable penetration depth, to avoid defects and consequently ensure good mechanical properties [25]. The following variables can be used to control the EBW process:

a.   Accelerating voltage

This determines the kinetic energy of the accelerated electrons. For most EBW operations, the accelerating voltage is kept constant at maximum value, which, depending upon the type of high voltage generator and accelerating beam gun is set at 60 or 150kV. The required beam power can be achieved by controlling the beam current [15].

13

b. Beam current

The beam current and accelerating voltage determine the beam power and consequently have biggest gredi effect on the resultant weld. The beam current that impinges the surface of the work piece is divided into (i) the work piece current, which has the greatest proportion and is conducted to the earth through the workpiece, and (ii) the transmitted current that keeps the keyhole open at the underside of the workpiece and significantly affects the shape of the weld [15].

c. Welding speed

Welding speed significantly affects the amount of heat input during welding. At high welding speed the heat input decreases due to the low loss of heat by conduction, and that consequently affects the shape of the weld bead. Both the speed of welding and the beam power determine the depth of weld [20, 25]. It was found that the higher beam power allows for a higher welding speed to be used and for the required penetration to be achieved [26].
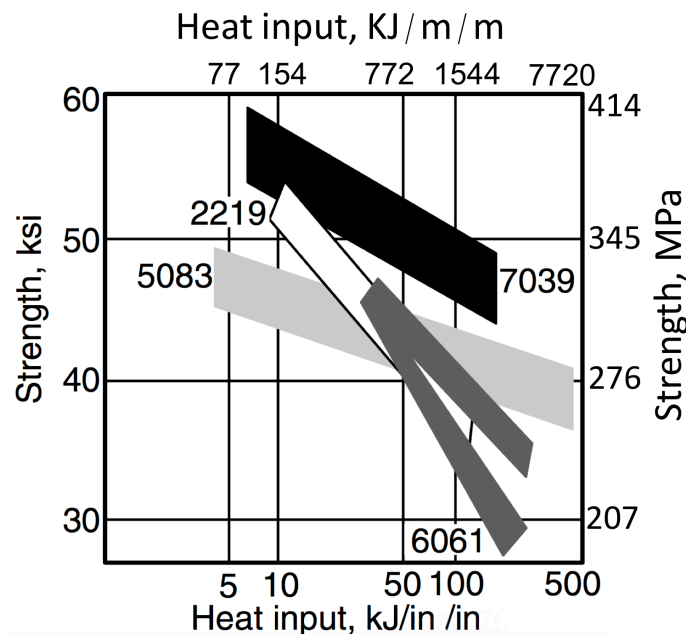
Figure 2.8 Weld strength as a function of heat input in a number of aluminium alloys welds [11].

14
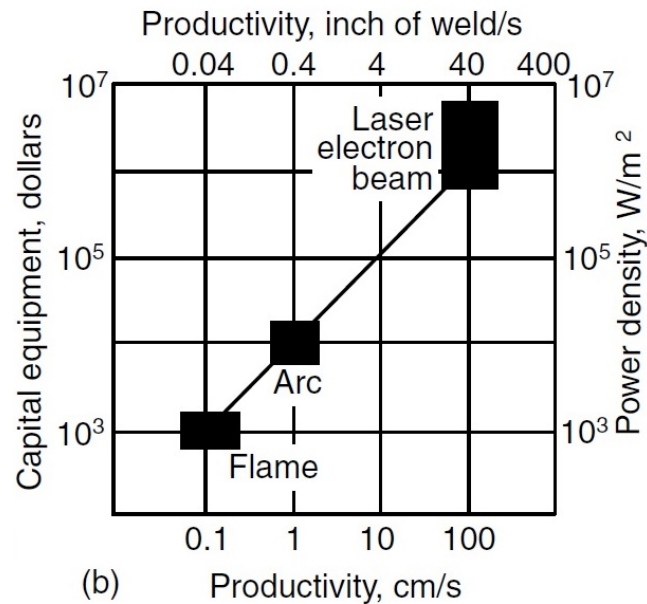
Figure 2.9 Capital equipment costs, speed of production and the power density as a function of different welding processes [27].

d. Beam deflection

The electron beam can be deflected from its normal axis into different shapes, directions and frequencies by using electric and magnetic fields. This is done through varying the currents periodically as shown in Figure 2.10. The beam oscillation sometimes has a very beneficial effect on the weld quality. It can be used to increase the fusion zone size and prevent the formation of the voids at the weld by allowing the gas porosity to escape from the weld pool [15, 17].

e. Lens current and focal position

The required power density can be achieved through controlling the beam diameter. This can be done by focusing the beam divergence using an electromagnetic lens. The position of the beam focusing on the component surface, i.e. above and below the surface, Figure 2.11, is also important to obtain the required weld integrity, full penetration and suitable weld bead shape.

15
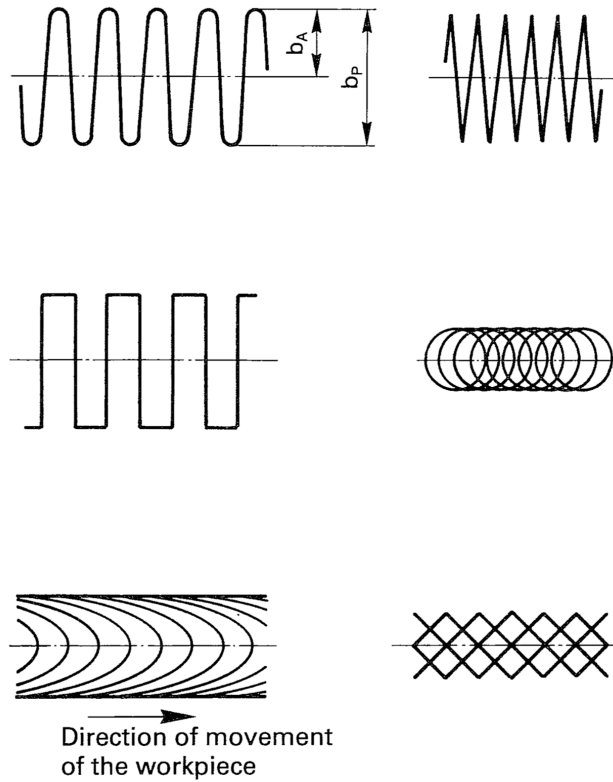
Figure 2.10 Various ways of oscillating the electron beam. b_A = the amplitude of oscillating, b_P = width of oscillation [15].

There are two types of focusing often used in EBW, normal focus and optimal focus. In the former, the beam focuses on the surface of the material and the smallest possible focal spot diameter is achieved, Figure 2.11 (a). While in optimal focusing, the beam impinges on the surface of the workpiece with a spot diameter greater than the actual focal diameter as shown in Figure 2.11 (b and c) [15].
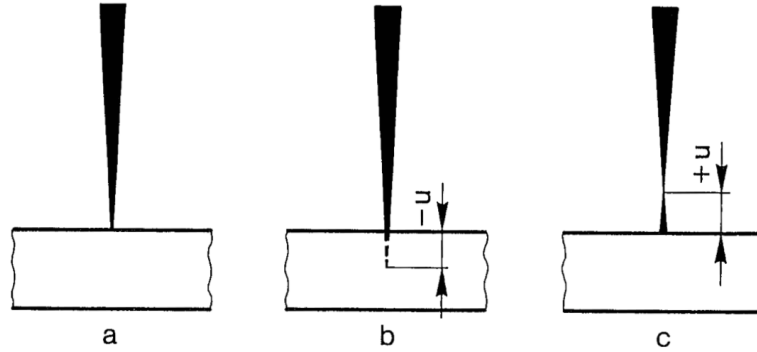
Figure 2.11 Different focus positions of electron beam: (a) Normally focused, (b) Underfocused, (c) Over focused. Taken from [15].

It was found that a small focal spot size and beam-convergence angle can produce a narrow FZ. The highest penetration can be achieved when the focal spot is located at the position between the workpiece surface and the bottom of the FZ [28]. It was also observed that higher energy absorption and deeper weld penetration can be achieved by adjusting the beam focus position below the base metal surface through increasing the cavity [29].

The depth (h) and width (b) of welding penetration, Figure 2.12, the specific power of the electron beam (P_{sf}) and the HAZ of the material depend on the diameter of the electron beam applied on the material's surface. The electron beam's diameter is a function of focusing distance. By considering the electron beam current, the accelerating voltage and electron beam speed as constants, the relationship between the specific power, depth, width and the beam diameter are [30]:

$$P_{sf} = \frac{I_f \, U_{acc}}{\pi \, d_f^2/4} \ldots \ldots \ldots \ldots$$

(2.4)

Where I_f is the beam current, U_{acc} is the accelerating voltage, d_f is the beam diameter.
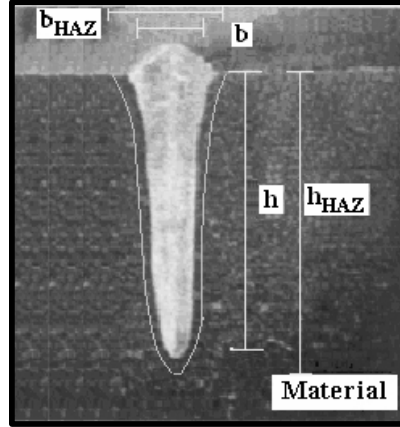
Figure 2.12 The depth (h) and width (b) of welding penetration [30].

$$h = \frac{2\,U_{acc}\,I_f}{v\,d_f\,H\,[1+1.2\,\lambda\,\left\{\frac{1}{d_f\,v}+\frac{1}{2\,a_t}\right\}]} \quad \ldots\ldots \qquad \ldots\ldots (2.5)$$

$$b = 2\,\sqrt{\frac{I_f\,U_{acc}\,\eta_i\,\eta_t\,d_f}{\pi\,v\,h\,H}}\ldots\ldots \qquad \ldots\ldots$$

(2.6)

Where v is the welding speed, a_t is the thermal diffusion coefficient, λ is the thermal conductivity, η_i is the electrical efficiency, η_t is the thermal efficiency, $H=c.\,\rho.\,(T_t\text{-}273)$ $+H_t$, c is the heat absorption capacity, ρ is the density, T_t is the melting temperature and H_t is the melting latent heat.

The EBW parameters have an impact on the mechanical properties and the metallurgical characteristics of the weld e.g. solidification mode and ferrite number in stainless steels, which consequently affects the resulting microstructure and mechanical properties of the weld [31, 32].

18

2.3 Stainless steels

2.3.1 Introduction

Stainless steels are iron based alloys containing a minimum of 11% Cr that forms a thin, protective surface layer of chromium oxide (Cr_2O_3) when the steel is exposed to oxygen. The oxide layer means the steels do not rust in sea water and are resistant to most acids [33, 34]. Other desired properties include excellent formability, high cryogenic and ambient temperature impact properties, good resistance to oxidation and creep. Many other elements such as Ni and C may be added to stabilize particular phases such as austenite and ferrite, or both, to provide extra corrosion resistance and enhance the mechanical properties [35]. Most stainless steel types are weldable. However, at specific temperatures during heating, they may suffer from some metallurgical issues such as grain growth, formation of intermetallic constituents or the presence of impurity elements, which can negatively affect properties [36].

2.3.2 Types of stainless steels

The predominating metallurgical phase, e.g. austenite, ferrite and martensite that present in the microstructure at room temperature is generally used to categorize the stainless steel alloys. Stainless steels with microstructure contains more than one phase, e.g. approximately 50% ferrite and 50% austenite are designated as duplex stainless steels. Other designation includes precipitation hardenable (PH) grades that contain Al, Nb or Ta. These alloying elements make the stainless steel hardenable by an age hardening heat treatment [33, 37].

2.4 Austenitic stainless steels

Austenitic stainless steels are the most common type of stainless steels. Their corrosion resistance is very good in most environments and they have excellent formability, good weldability, extremely good low temperature impact properties and are nonmagnetic [38]. They have a minimum yield strength of about 210 MPa, which is equal to those of mild steels and can only be strengthened by work hardening [33]. The significant element that is added to stabilize the austenite phase is nickel, generally over 8 wt%. The other austenite-stabilizing elements are C, N, and Cu. Carbon and nitrogen are added to improve strength at high and low temperatures respectively. Table 2.1 shows the compositions range of standard austenitic stainless steels. [18]. The effect of alloying elements on the properties of austenitic stainless steel standards is shown in Figure 2.13 [39].

Table 2.1 Compositions range of standard austenitic stainless steels. Adapted from [40].

Element	Compositions range (wt%)
Chromium	16-25
Nickel	8-20
Manganese	1-2
Silicon	0.5-3
Carbon	0.02-0.08 (>0.03 wt% designated L grades)
Molybdenum	0-2
Nitrogen	0-0.15 (usually designated with N)
Titanium and Niobium	0-0.2

2.4.1 Designations of austenitic stainless steels

The American Iron and Steel Institute (AISI) provides a system with three numbers, sometimes followed by letters, to designate stainless steels. Austenitic stainless steels include both the 200 series and 300 series alloys. The 200 series alloys contain high levels of carbon, manganese, and nitrogen with lower nickel content than the 300 series alloys to balance the high carbon and nitrogen levels [41, 42].

The 300 series alloys are the most widely used austenitic grades with alloys 304, 316, 321 and 347 of the "18-8" type with nominal values of 18 Cr and 8-10 Ni are the most commonly used alloys. The L grades represent low carbon content of 0.03wt%, which have improved resistance to intergranular attack in corrosive environments [43, 44]. H grades have carbon levels of approximately 0.1wt% making these alloys suitable for use at elevated temperatures since they have higher elevated temperature strength than the

standard or the L grades [40]. The N grades contain as much as 0.2wt% nitrogen in the 300 series alloys (304N, 316N) and to even higher levels in alloys that contain high manganese content as manganese increases the solubility of nitrogen in the austenite phase. The higher nitrogen improves the strength, galling resistance, and pitting corrosion resistance of austenitic stainless steels[44]. Alloys 321 and 347 contain titanium and niobium, which stabilize the alloy against the formation of $M_{23}C_6$, chromium carbides; these are called stabilized grades [45]. These elements form stable MC carbide at elevated temperatures and restrict the formation of chromium carbides and reduce the possibility of sensitization, i.e. reduction in chromium in the regions adjacent to the grain boundaries due to precipitation of Cr-rich carbide at this region, which leads to create a microstructure sensitive to intergranular corrosion [46].

2.4.2 Mechanical properties of austenitic stainless steels

One of the common disadvantages of austenitic stainless steels is their relatively low yield strength, which limits these steels' use in a number of engineering applications. Generally, they may only be significantly strengthened by cold working. Phase transformation and precipitation heat treatment are not applicable for strengthening purposes since recrystallization occurs at high temperatures. Therefore, it does not reduce the grain size and the transformation from austenite to ferrite [47-49]. However, under particular conditions, martensite can be produced in some austenitic stainless steel grades. This has been seen in alloys that are specially heat treated and/or toughly cold-worked [50, 51]. The mechanical properties of some of the most common austenitic stainless steels are listed in Table 2.2.

2.4.3 Structure of austenitic stainless steels

The primary microstructure of austenitic stainless steel is austenite. However, the alloying elements that stabilize ferrite or austenite phases play a major role in determining whether the final microstructure is either fully austenitic or a mixture of austenite and ferrite [52]. Two examples of wrought austenitic stainless steel microstructures are shown in Figure 2.14. The fully austenitic steel consists of equiaxed austenite grains, Figure 2.14a and Figure 2.14b shows a microstructure contains some high-temperature ferrite called delta ferrite, which is aligned along the rolling direction. This ferrite type results from solidification during thermo-mechanical processing due to the segregation of ferrite promoting elements (primarily chromium) [40]. Delta ferrite is usually present in relatively low volume fractions (less than 2 to 3%), and sometimes causes a lack of

ductility and toughness. It can also be a preferred site for the precipitation of $M_{23}C_6$ carbides and sigma phase, which is considered an embrittlling agent in stainless steels [35].

302 General purpose 18-8	**202** N and Mn partly replace Ni

302B Si added to increase scaling resistanc escaling

205 N and Mn partly replace Ni

201 N and Mn partly replace Ni

317 More Mo and Cr added better corrosion resistance

316 Mo added to increase corrosion resistance

309 **309S** Cr and Ni increased for heat resistance

308 Higher Cr and Ni used primarily for welding

304 Lower C for better corrosion resistance in welding structure

305 Ni increased foe lower work hardening

303S added to improve machinabili ty

301 Cr and Ni lowered to increase work hardening

317L C reduced for better weld characterist ic

316L C reduced for better corrosion resistance

310 **310S** More Cr and Ni for even better heat resistance

347 Nb and Ta added to oppose chromium carbide precipitatio n

321 Ti added to oppose chromium carbide precipitate

304L C reduced even further

384 More Ni to lower work hardening

303Se Se added to better machined surface

316LN C reduced N added to increased strength

314 Si increased for higher eat resistance

348 Ta and Co restricted for nuclear application

304N N added to increased strength

304LN N added to increase strength

316F S and P added to improve machinabili ty

316N N added to increase strength

330 Ni added to resist carburizatio n and thermal shock

Figure 2.13 Alloying elements in austenitic stainless steel standards and some of their impact on the properties. Adapted from [53].

Table 2.2 Mechanical properties of Austenitic Stainless Steels. Adapted from [40].

Alloy	Tensile strength		Yield strength		Elongation	Reduction in area
	MPa	Ksi	MPa	Ksi	(%)	(%)
302	515	75	205	30	40	50
304	515	75	170	30	40	50
304L	480	70	205	25	40	50
308	515	75	205	30	40	50
309	515	75	205	30	40	50
310	515	75	205	30	40	50
316	480	75	205	30	40	50
316L	515	70	170	25	40	50
317	515	75	205	30	40	50
321	515	75	205	30	40	50
330	480	70	205	30	30	-
347	515	75	205	30	40	50

The Fe-Cr-Ni phase diagram at 70% constant iron, Figure 2.15, can be used to describe the transformation behaviour of austenitic stainless steels. As the chromium is the ferrite promoting element, the primary solidification occurs as delta ferrite at a high percentage of chromium/nickel ratios and as austenite at lower ratios. However, when alloys solidify as ferrite, they may be either fully ferritic or consist of a mixture of ferrite and austenite at the end of solidification [54].
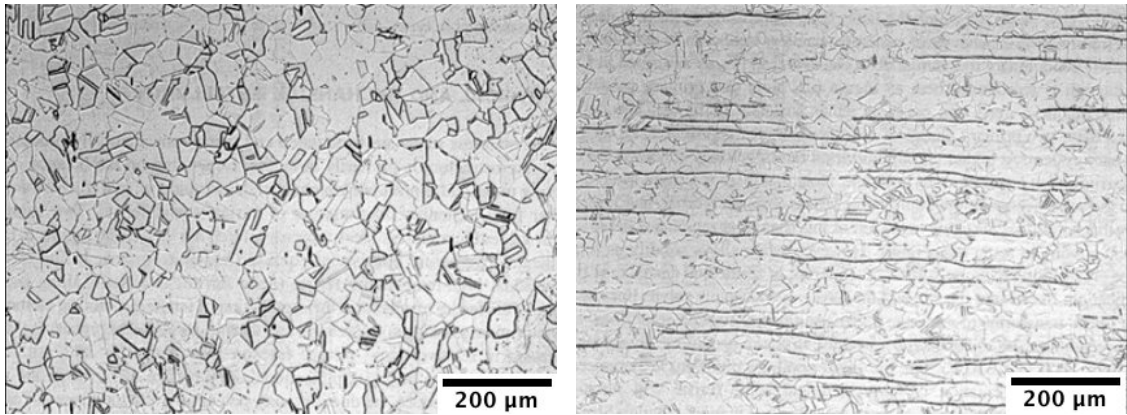
Figure 2.14 Microstructure of Type 304 stainless steel plate (a) fully austenitic and (b) austenite with δ-ferrite stringers. Adapted from [40].
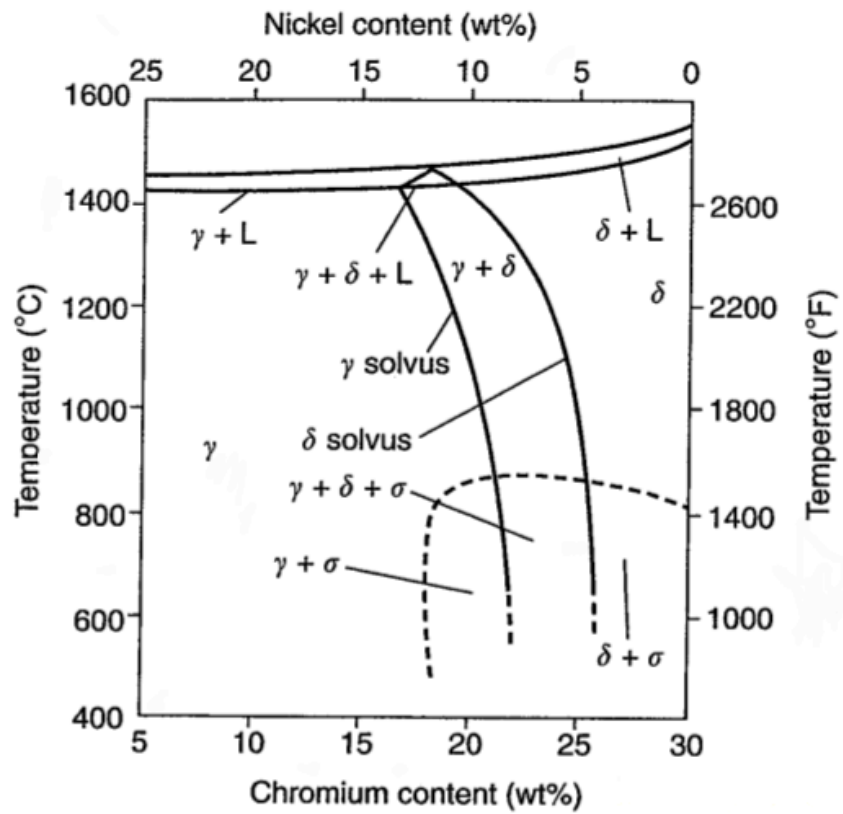
Figure 2.15 Relationship between the solidification type and pseudobinary phase diagram[55].

2.4.4 Formation of precipitates in austenitic stainless steels

Different types of precipitation may form in austenitic stainless steels, Table 2.3. The chemical composition and heat treatment control the type and structure of precipitates, with carbides being the most common. The high percentage of Cr and presence of other carbides promoting alloying elements such as Mo, Nb and Ti increase the possibility of carbides' precipitation. Carbides' formation is very important in austenitic stainless steel, especially $M_{23}C_6$ since it can be lead to intergranular corrosion by precipitating along the grain boundaries in temperatures between 700 to 900°C [56].

Table 2.3 Precipitates in Austenitic Stainless Steels. Adapted from [40].

Precipitate	Crystal Structure	Stoichiometry
MC	FCC	NbC
MC	NaCl	TiC
M_6C	Diamond cubic	$(FeCr)_3Mo_3C$, Fe_3Nb_3C, Mo_5SiC
$M_{23}C_6$	FCC	$(Cr,Fe)_{23}C_6$, $(Cr,Fe,Mo)_{23}C_6$
NbN	FCC	NbN
Z phase	Tetragonal	CrNbN
Sigma phase	Tetragonal	Fe-Ni-Cr-Mo
Laves phase *(η)*	Hexagonal	Fe_2Mo, Fe_2Nb
Chi phase *(χ)*	BCC	$Fe_{36}Cr_{12}zMo_{10}$
G phase	FCC	$Ni_{16}Nb_6Si_7$, $Ni_{16}Ti_6Si_7$
R	Hexagonal	Mo-Co-C
	Rhombohedral	Mo-Co- C
ε Nitride (Cr2N)	Hexagonal	Cr_2N
Ni_3Ti	Hexagonal	Ni_3Ti
$Ni_3(Al, Ti)$	FCC	Ni_3AI

2.4.5 Microstructural characteristics of the FZ in austenitic stainless steel

As with any fusion weld, the grains in the FZ of austenitic stainless steel can exist in columnar and equiaxed structures similar to castings, Figure 2.16. However, the solidification behaviour and the final grains structure in welding is governed by the weld pool shape, welding process parameters, epitaxial growth and the alteration of the thermal gradient and solidification rate in the weld pool [57].

The grains in the weld metal tend to grow in a direction perpendicular to the fusion boundary due to the highest thermal gradient in this direction. In an autogenous weld, the grains grow epitaxially from the base metal grains at the fusion boundary with preferred crystallographic growth direction, which is <100> direction, as shown schematically in Figure 2.17. However, away from the pool boundary, the grains continue their growth in the same preferred crystallographic direction and start to crowd out the grains with less favourably oriented grains and competitive growth begins, Figure 2.18 [58, 59]. The grains continue to grow straight towards the weld centreline until they meet with the grains that grew from the opposite weld interface side, which forms the weld centreline boundary, Figure 2.19. The weld centreline is a probable defect in any weld as it is susceptible to solidification cracking [60, 61] and is a location of segregation of the alloying elements and impurities, producing potential brittle phases reducing toughness. It is worth mentioning that when a filler metal is used in welding stainless steel or when joining the stainless steel to a different metal, the weld metal composition and crystal structure becomes different from the base metal. In this case, epitaxial growth can no longer occur and the new grains will nucleate at the fusion boundary [62].

The grains in the FZ can also exhibit a variety of microstructural morphologies, such as cellular and dendritic grains. The type of these morphologies is governed by the level of constitutional super cooling, i.e. the liquid cools below its liquidus temperature and stays in the liquid state due to the compositional change in the liquid. Generally, depending on the solidification condition and the material system involved, the constitutional super cooling can enhance the change in solidification mode from planar to cellular and from cellular to dendritic, as shown in Figure 2.20 [63, 64]. The solidification mode can vary within a single weld from the fusion line to the centerline, as can be seen in Figure 2.21. This variation across the weld depends on temperature gradient G and the cooling rate R. When the G/R ratio decreases, the solidification mode changes from cellular to dendritic. This ratio decreases towards the centerline and enhances the dendritic structure in this region, Figure 2.22 [65, 66].
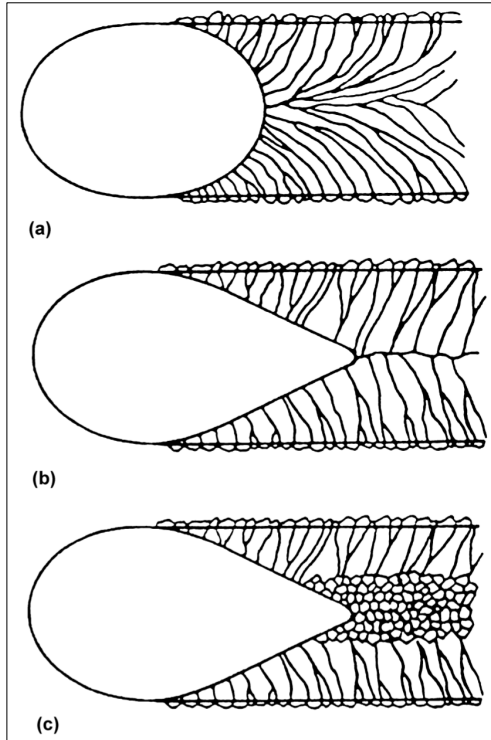
Figure 2.16 Schematic figure of Different types of grains structure and weld pool shape in fusion weld. (a) elliptical weld pool shape with axial structure at low welding speed (b) tear-drop shaped weld pool with centreline structure at high welding speed (c) tear-drop shaped weld pool with equiaxed structure at higher welding speed [10].
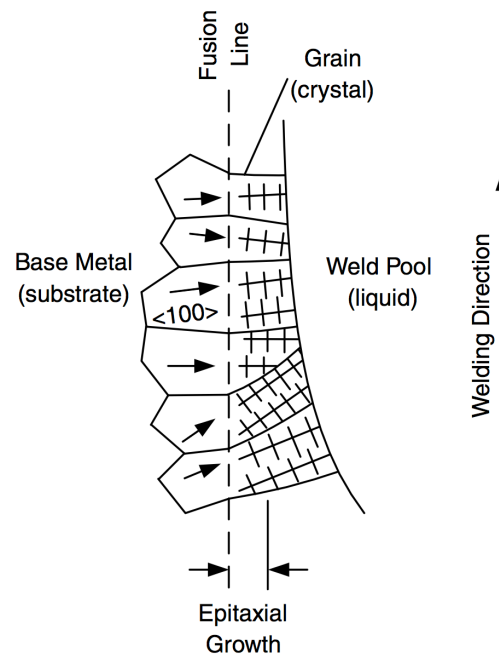
Figure 2.17 Epitaxial growth fusion weld [57]
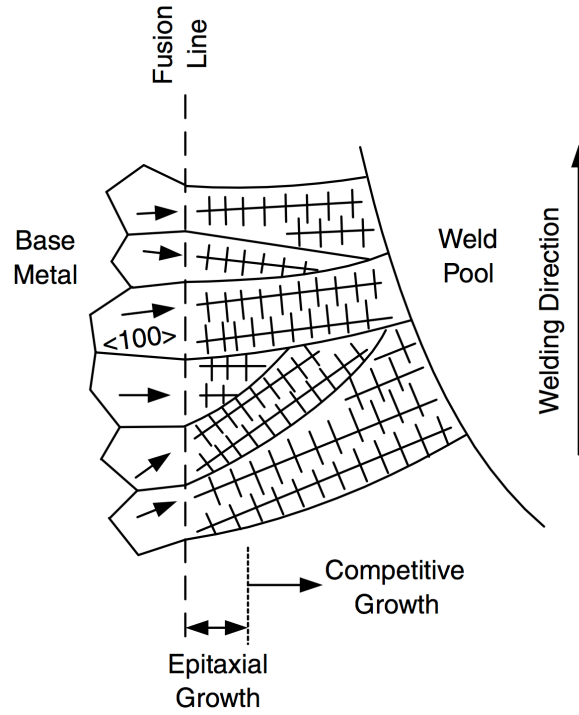
Figure 2.18 Schematic graph of competitive growth in fusion weld [10].
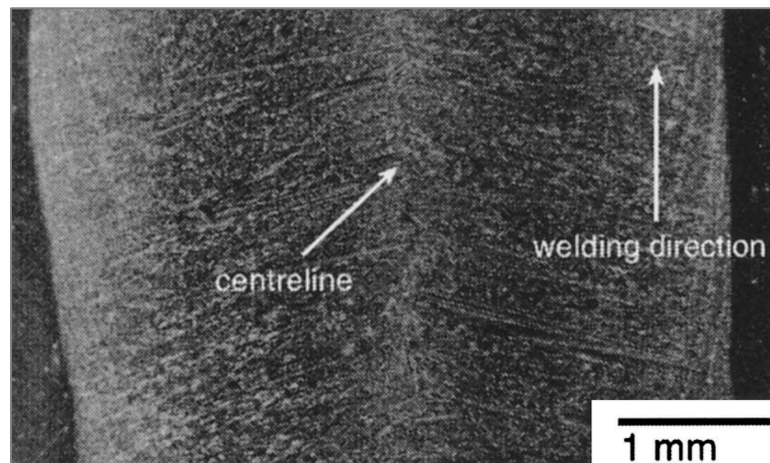
Figure 2.19 Weld solidification centreline [61].
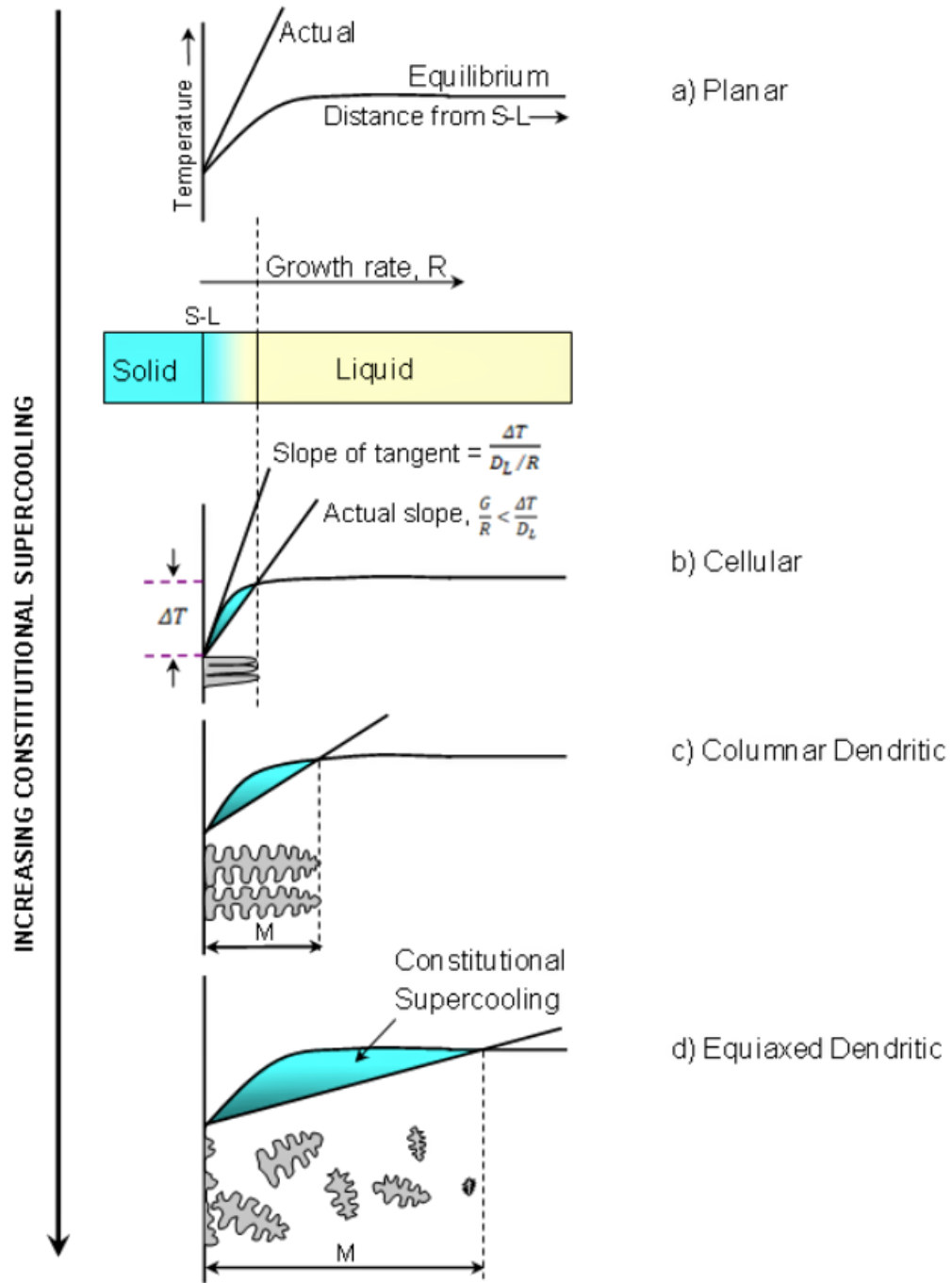
Figure 2.20 Influence of constitutional supercooling on solidification mode during welding: (a) planar; (b) cellular; (c) columnar dendritic; (d) equiaxed dendritic. Constitutional supercooling increases from (a) through (d). S-L is the solid-liquid interface, ΔT is the temperature difference at the fusion boundary layer and $\Delta T = T_L - T_S$, where T_L is the liquidus temperature and T_S is the solidus temperature. D_L=Liquid's diffusion coefficient [67].
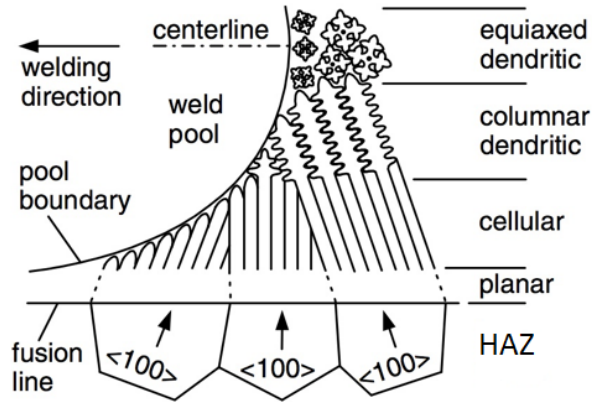
Figure 2.21 Variation in solidification mode across the FZ [10].
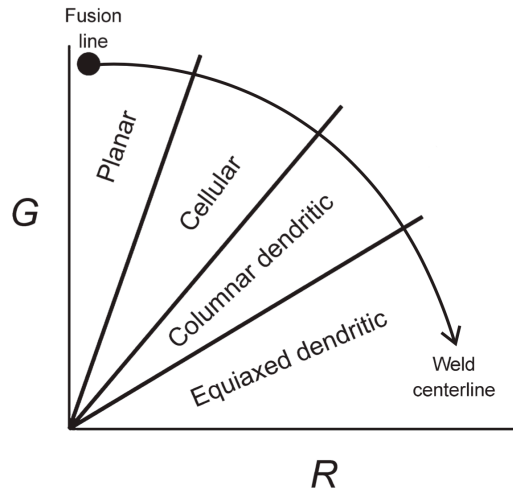
Figure 2.22 Effect of G/R on the grains microstructural morphologies in the FZ [10].

2.4.6 Effect of welding parameters on the grain structure

2.4.6.1 Grains morphology

The grain morphology of the weld metal is significantly affected by the welding parameters used such as heat input and welding speed. According to Equation (2.7), at higher heat input (Q) under the same welding speed, the solidification mode changes from cellular to dendritic due to the lower thermal gradient, hence the lower G/R ratio that enhances the dendritic mode [68, 69].

$$\left(\frac{\partial T}{\partial x}\right)_t = \frac{Q}{2\pi x}\frac{-1}{x^2} = -2\pi k\frac{(T-T_0)^2}{Q} \text{.....} (2.7) [10]$$

therefore *G=1/Q*

Where,

T = temperature

T_0 = workpiece temperature before welding, *k* = workpiece thermal conductivity,

∂ = workpiece thermal diffusivity, namely, *k/pC*, where *p* and *C* are density and specific heat of the workpiece, respectively.

2.4.6.2 Dendrite spacing

The secondary dendrite arm spacing (SDAS) is defined as the distance between the protruding adjacent secondary arms of a dendrite. Across the weld, due to the different cooling rates from the fusion line to centerline, the dendrite arm spacing also changes. The distance between the arms decreases towards the weld centerline because of the high solidification rate in this region.

Welding parameters can influence the distance between the dendrite arms too. According to Equation (2.8), for a particular welding process under the same heat input, the cooling rate increases with increasing welding speed, thus, decreasing the dendrite arm spacing [10, 70, 71].

$$\left(\frac{\partial T}{\partial t}\right)_x = \left(\frac{\partial T}{\partial x}\right)_t\left(\frac{\partial x}{\partial t}\right)_T = -2\pi kV\frac{(T-T_0)^2}{Q} \text{......... } (2.8) [10]$$

Therefore, as the amount of heat per unit length (Q/V) is increased, the dendrite arm spacing increases. This relationship was proven by Davis [72] and Xue [73] as shown in Figures 2.23 (a) and (b), respectively.
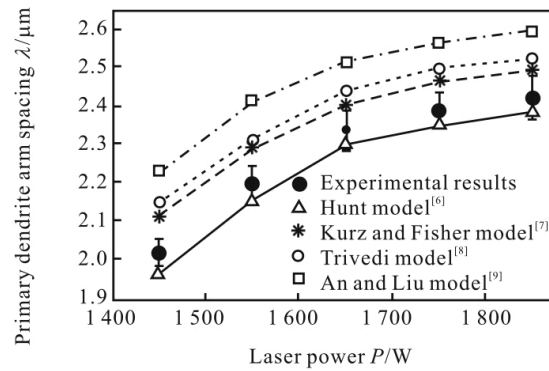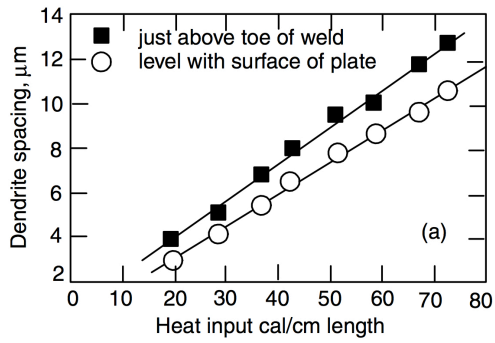
Figure 2.23 Dendrite arm spacing as a function of heat input (a) LBW of For Al–Mg–Mn alloy [10, 72] (b) Laser beam dissimilar welding of Cu-Al [73].

Another example can be seen in Figure 2.24, showing three welds with dendritic structures produced by three different welding processes. The finest DAS can be clearly seen in Figure 2.24 (b), which resulted from LBW with lower heat input and faster welding speed than the TIG and Hybrid TIG-LBW processes.
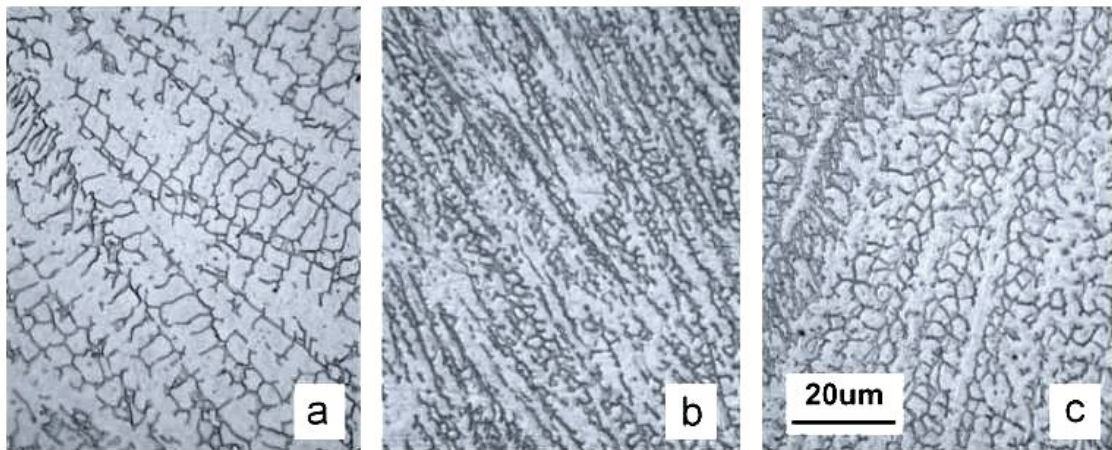
Figure 2.24 Weld metal microstructure of 404 stainless steel welded by (a) TIG (b) LBW (c) LBW-TIG hybrid welding. Adapted from [74].

2.4.6.3 Weld pool shape

Weld pool shape is mainly affected by the surrounding thermal conditions in the FZ and HAZ and the molten metal flow during welding. Generally, the volume of the weld pool increases with increasing heat input and decreases with increasing welding speed [75]. In welding process with low power density such as TIG, the weld pool takes the elliptical shape at low welding speed and tear drop at higher welding speed. With high power density welding techniques such as EBW and LBW, weld pool shape changes from circular to elliptical or teardrop shape as welding speed increases, as can be seen in Figure 2.16 [75]. The higher the welding speed, the more elongated the welding pool due to the high thermal gradient produced by the fast moving heat source [67].

2.4.7 FZ microstructure evolution in austenitic stainless steels

The FZ in an austenitic stainless steel can undergo four possible solidification types and phase transformations, listed in Table 2.4. The A (austenite) and AF (austenite+ferrite) are primary austenite solidification modes, since the austenite forms first during solidification. The FA (ferrite+austenite) and F (ferrite) solidification modes are primary ferrite as the delta ferrite is first phase to solidify. All these reactions are related to the Fe-Cr-Ni phase diagram, Figure 2.15 [52].

2.4.7.1 Austenite mode

In the austenite solidification mode, the primary austenite formed on initial solidification remains upon cooling to room temperature, without formation of any other phases. Figure 2.25 shows a metallographic example of this solidification type. The cells and dendrites in the microstructure can be clearly seen due to the effect of some alloying elements such as Cr and Mo in the type 304 and 316 that segregate during solidification and their relatively low diffusivity at high temperature [40].

2.4.7.2 Austenite-ferrite mode

This ferrite solidification mode consists of the primary austenite plus some ferrite, which forms at the end of the primary austenite solidification process via a eutectic reaction. The partition of ferrite-promoting elements to the solidification sub-grain boundaries during solidification promotes the formation of ferrite. This ferrite is relatively stable and does not transform to austenite during weld cooling as it is enriched in ferrite-stabilising

33

elements. Figure 2.26 shows an example of a microstructure that exhibits ferrite along solidification sub-grain boundaries [54].

Table 2.4 Solidification Types, Reactions, and Resultant Microstructure. Adapted from [39].

Solidification Type	Reaction	Microstructure
A	L→L+A→A	Fully austenitic
AF	L→L+A→L+A+(A+F)$_{eut}$→ A+F$_{eut}$	Ferrite at cell and dendrite boundaries
FA	L→L+F→L+F+(F+A)$_{per/eut}$ →F+A	Skeletal and/or lathy ferrite resulting from ferrite to austenite transformation
F	L→L+F→F→F+A	Acicular ferrite or ferrite matrix with grain boundary austenite and Windmastätten side plates
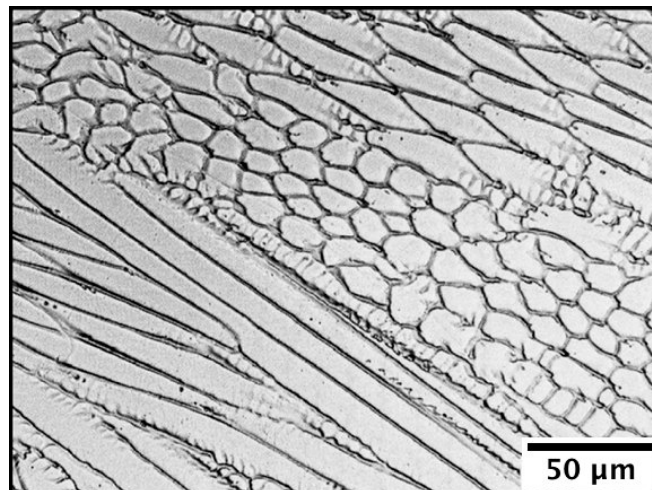
Figure 2.25 FZ microstructure resulting from fully austenitic (Type A) solidification. Adapted from [40].
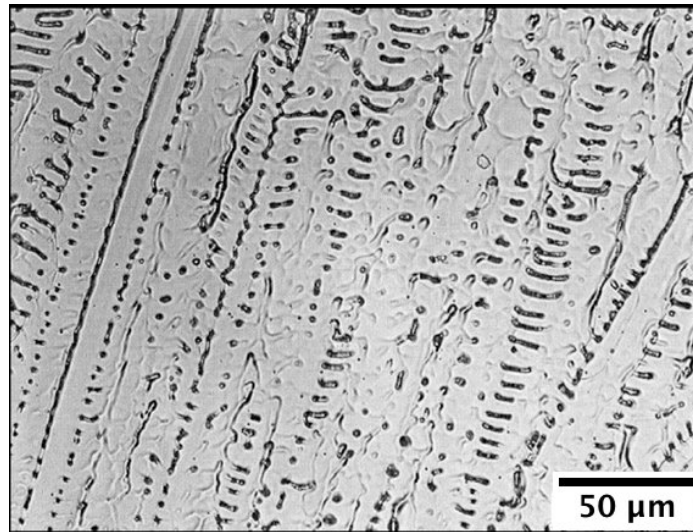
Figure 2.26 FZ microstructure resulting from Type AF. Adapted from [40].

2.4.7.3 Ferrite-Austenite mode

The microstructure in the ferrite-austenite mode is governed by the chemical composition and cooling rate. The chemical composition is represented by the chromium equivalent (Cr_{eq}) to nickel equivalent (Ni_{eq}) ratio (Cr_{eq}/Ni_{eq}). Cr_{eq} of a given alloy can be determined from the ferrite promoting elements and Ni_{eq} can be determined from the austenite formers [10]. When the Cr_{eq}/Ni_{eq} value increases, the amount of primary austenite decreases until the primary solidification mode is entirely ferritic. The microstructure in this mode consists of primary ferrite and some austenite that forms at the end of solidification, resulting from the peritectic-eutectic reaction in the Fe-Cr-Ni system (Figure 2.15). The resulting ferrite morphology is governed by cooling rate. Vermicular ferrite morphology, Figure 2.27, is resulted from moderate cooling rate and lathy ferrite, Figure 2.28, is resulted from high cooling rate. The high cooling rate restricts diffusion during the ferrite-austenite transformation and the structure has more tightly spaced laths [40, 76].

2.4.7.4 Ferrite mode

When the Cr_{eq}/Ni_{eq} value is > 1.95, the alloy can solidify completely as a ferrite. However, part of the ferrite can transform into austenite; the degree of transformation depending on the Cr_{eq}/Ni_{eq} value and cooling rate [77]. Once the molten metal cools below the ferrite solvus, austenite starts to form at the ferrite grain boundaries. The fully ferritic structure in the solid state between the solidus and ferrite solvus allows diffusion to eliminate all

composition gradients that have resulted from solidification. Thus, the microstructure consists of large and homogeneous ferrite grains.
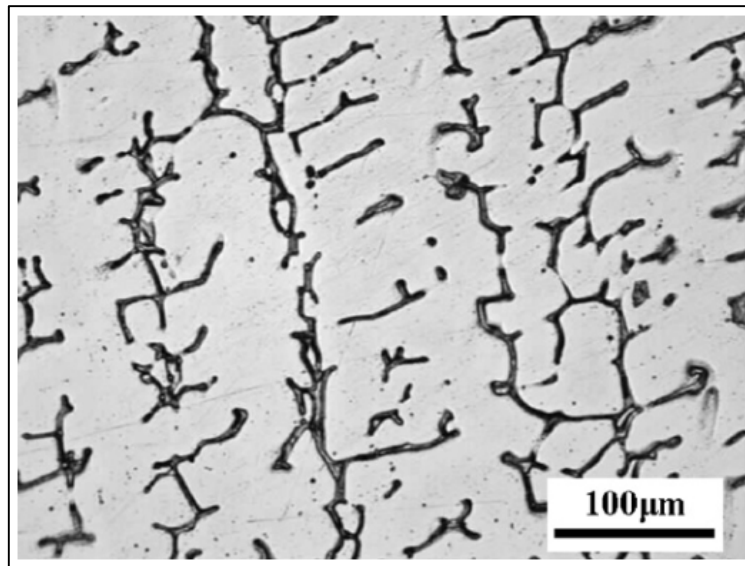
Figure 2.27 Vermicular or skeletal ferrite. Adapted from [40].

Figure 2.28 Lathy ferrite Adapted from [40].

In the range of F solidification mode, the low Cr_{eq}/Ni_{eq} raises the transformation temperature. At low to moderate cooling rate, the ferrite is notably consumed. At high cooling rates, diffusion is suppressed and transformation from ferrite to austenite is

limited. In contrast, high Cr_{eq}/Ni_{eq} value lowers the transformation temperature. However, in both cases, high ferrite contents will result in the FZ.

The microstructure in the F mode, at low Cr_{eq}/Ni_{eq} values, is an acicular ferrite structure within the ferrite grains as shown schematically in Figure 2.29 (a). The long range diffusion at a low transformation temperature pushes the transformation to occur rapidly resulting in the acicular ferrite structure. At high Cr_{eq}/Ni_{eq} values and the same cooling rate, the microstructure consists of a ferrite matrix with austenite grain boundaries and a Widmanstatten austenite structure, which nucleates at the ferrite grain boundaries due to the low diffusion rate, as presented schematically in Figure 2.29 (b) and in a micrograph, Figure 2.30 [77]. The high Cr_{eq}/Ni_{eq} ratio reduces the ferrite solvus and driving force for the ferrite to austenite transformation.
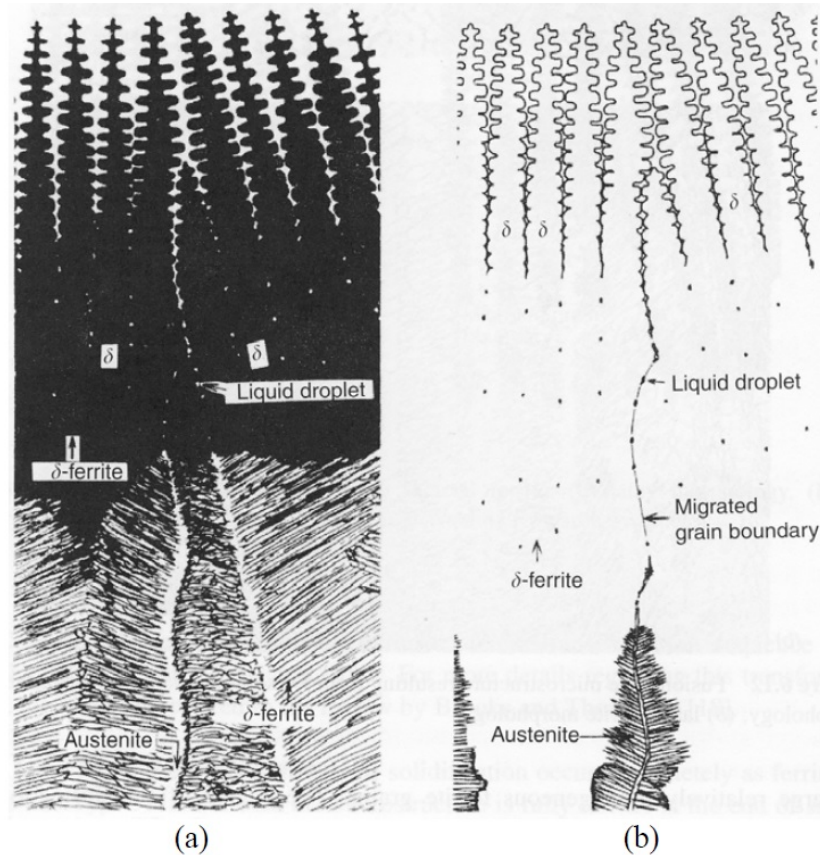
Figure 2.29 Schematic of ferrite solidification mode: a) acicular ferrite b) ferrite and Windmanstätten austenite [78].
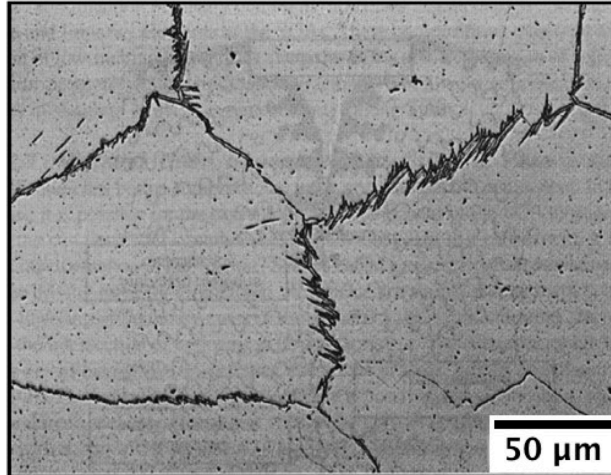
Figure 2.30 Initial growth of Widmanstätten austenite which nucleates from austenite along the ferrite grain boundaries in a FZ microstructure resulting from F solidification. Adapted from [40].

2.4.8 Heat affected zone in austenitic stainless steel welds

The composition and microstructure of the base metal (BM) are the main factors that affect the characteristics of the HAZ in austenitic stainless steels. This region may experience the following metallurgical reactions [40].

2.4.8.1 Grain growth

Significant grain growth may take place in the HAZ region if the BM is strengthened by cold working. Recrystallization and grain growth can result in significant HAZ softening, Figure 2.31 [10].

2.4.8.2 Ferrite formation

It is known from the literature [40, 79] that ferrite formation increases with increasing Cr_{eq}/Ni_{eq} ratio, Figure 2.15. Ferrite formation is usually along the grain boundaries and this will restrict the grain growth in this region and reduce the susceptibility to the HAZ liquation cracking. However, the fast thermal cycle in the HAZ lowers the possibility of austenite to ferrite transformation.

2.4.8.3 Precipitation

During welding, the HAZ is heated to temperatures close to the solidus temperature of the alloy. This can lead to the possibility of most of the precipitates that exist in the base metal dissolving. On cooling, a super saturation of austenite matrix occurs and different

precipitates form, e.g. carbides and nitrides precipitates. These precipitates usually form along grain boundaries or at the ferrite-austenite interface (if ferrite is present). Their size, distribution, and morphology are a function of the alloy composition and the HAZ thermal cycle. A high amount of precipitates can lower the corrosion resistance of the steel [80, 81].
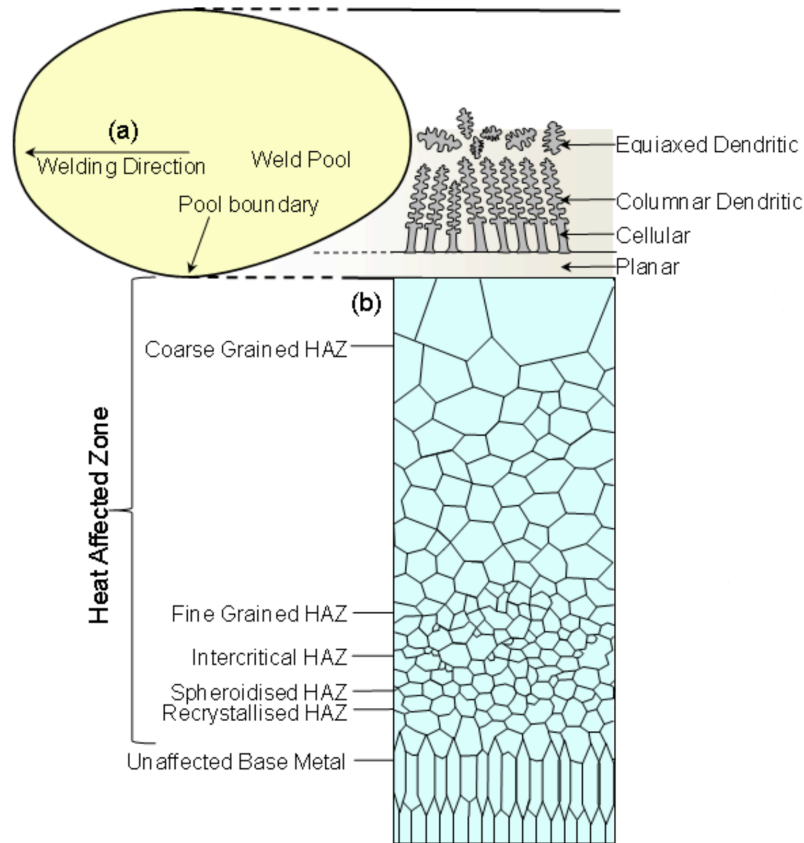
Figure 2.31(a) Weld pool and grain structure in solidified weld metal (b)HAZ grain structure. Adapted from [67].

2.4.8.4 Grain boundary liquation

Segregation of impurity elements along the austenite grain boundaries reduces the melting temperature in that region and causes local melting along the grain boundaries. Stainless steel alloys that contain MC carbide forming elements such as titanium and niobium may undergo constitutional liquation that lead to HAZ liquation cracking. Segregation of impurities, such as sulphur and phosphorus, along the grain boundary can also increase the possibility of liquation [40].

2.4.9 Weldability of austenitic stainless steels

Generally, austenitic stainless steels are considered to be very weldable by most welding processes. However, proper precautions should be taken to avoid or minimize any weldability problems such as weld solidification cracking, liquation cracking and lack of corrosion resistance. Thus, successful welding requires the appropriate selection of alloy (base and filler metal) and correct welding procedure.

2.4.9.1 Weld solidification cracking

Generally, the weld microstructure that consists of fully austenitic phase or primary austenite solidification with low Cr_{eq}/Ni_{eq} ratio is more sensitive to cracking, as shown in Figure 2.32. The presence of the delta ferrite phase in the weld microstructure increases the resistance to solidification cracking [82, 83]. Thus, it can be concluded that the weld microstructure, which is controlled by solidification conditions, i.e. chemical composition and cooling rate, has a high impact on the crack susceptibility [77].

It is important to note that impurities, such as sulfur and phosphorus, have a big influence in increasing the cracking sensitivity of the FZ [84]. An example of weld solidification cracks in a fully austenitic weld can be seen in Figure 2.33.
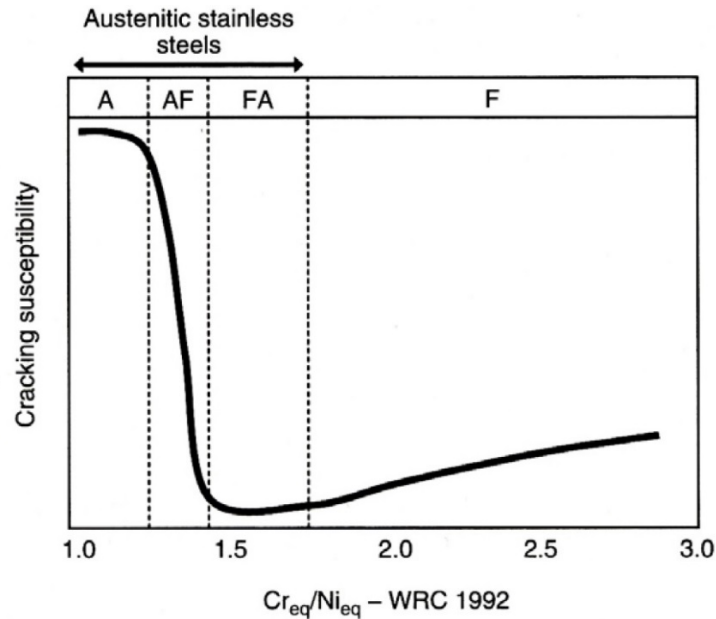
Figure 2.32 The effect of composition and microstructure on the weld solidification cracking susceptibility [85].
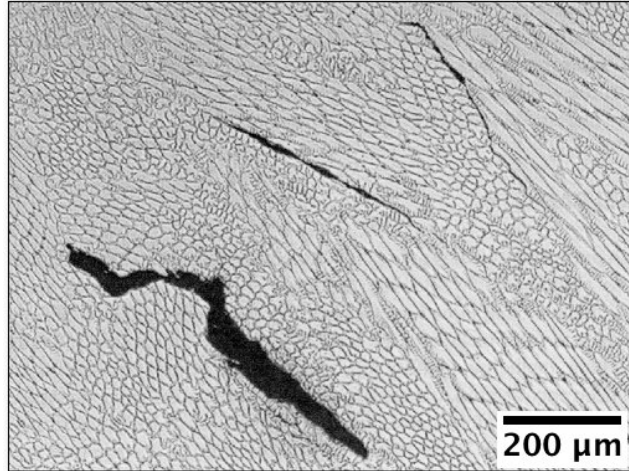
Figure 2.33 Weld solidification cracks in fully austenitic weld metal [86].

Fully austenitic stainless steel weld metal is highly sensitive to cracking due to the existence of low melting point films near the grain and sub-grain boundaries. These low melting films contain high amounts of alloying elements such as sulfur, phosphorus, silicon, and manganese that increase the solidification cracking possibility. The weld metal microstructure with two phases withstands wetting by the continuous films and forms a tortuous (not straight and smooth) boundary along which cracks must grow [39, 87]. In addition, delta ferrite has a greater solubility for harmful elements such as sulfur and phosphorus than austenite that reduces the volume of low-melting constituents formed during solidification [86]. The residual amount of delta ferrite after solidification can be used to predict the solidification behaviour of the BM. Therefore, many constitutional diagrams have been developed to predict the residual delta ferrite content after solidification based on the chemical composition of the alloy, such as the Schaeffler, DeLong and Suutala diagrams.

(1)   Schaeffler diagram

This constitution diagram was developed by Anton Schaeffler in 1949 and is used as a tool to predict ferrite content in stainless steel weld metal. The prediction can be done by calculating Ni and Cr equivalents, which are both based on the chemical composition of the alloy. Ferrite-promoting elements are included in the chromium-equivalent equation and austenite-promoting elements in the nickel-equivalent equation, Figure 2.34. This diagram is considered accurate for Types 308, 309, 309Cb, 310, 312, 316, 317, 318 and 347 with ±4 % ferrite [88-90].

(2)   Delong diagram

Major developments and expansions to the Schaeffler diagram were made by Delong in 1956. The modifications included adding nitrogen to the nickel equivalent, which affected the location of the lines in the diagram. The distance between the ferrite lines is approximately equal and the slope of the isoferrite was increased giving greater accuracy for calculated and measured ferrite content in highly alloyed stainless steels such as 316 and 309, Figure 2.35. These modifications give an overall better calculation accuracy for a range of stainless steels. In 1973, further changes were made by Long and DeLong, as shown in Figure 2.36. The key modification was the adding of a Ferrite Number (FN) scale to the diagram to the ability of calculating of the delta ferrite. FN values are based on magnetic measurements, since the BCC delta ferrite is ferromagnetic, whilst the FCC austenite is not [40, 88].
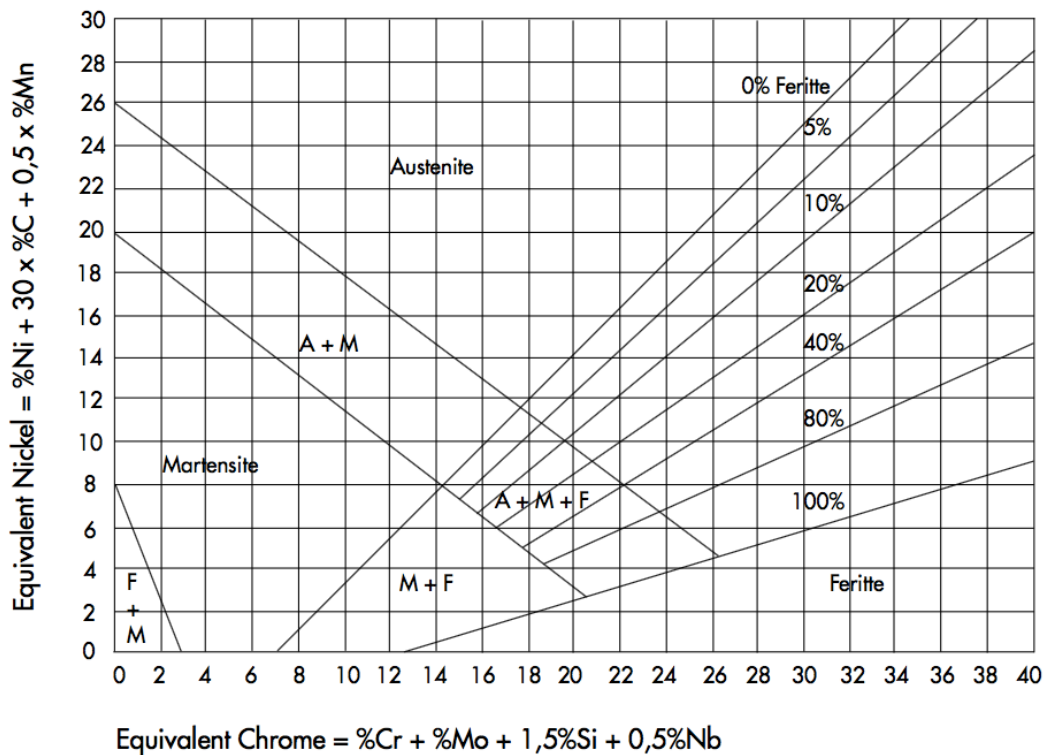
Figure 2.34 Schaeffler diagram of 1949 for ferrous metals [91].
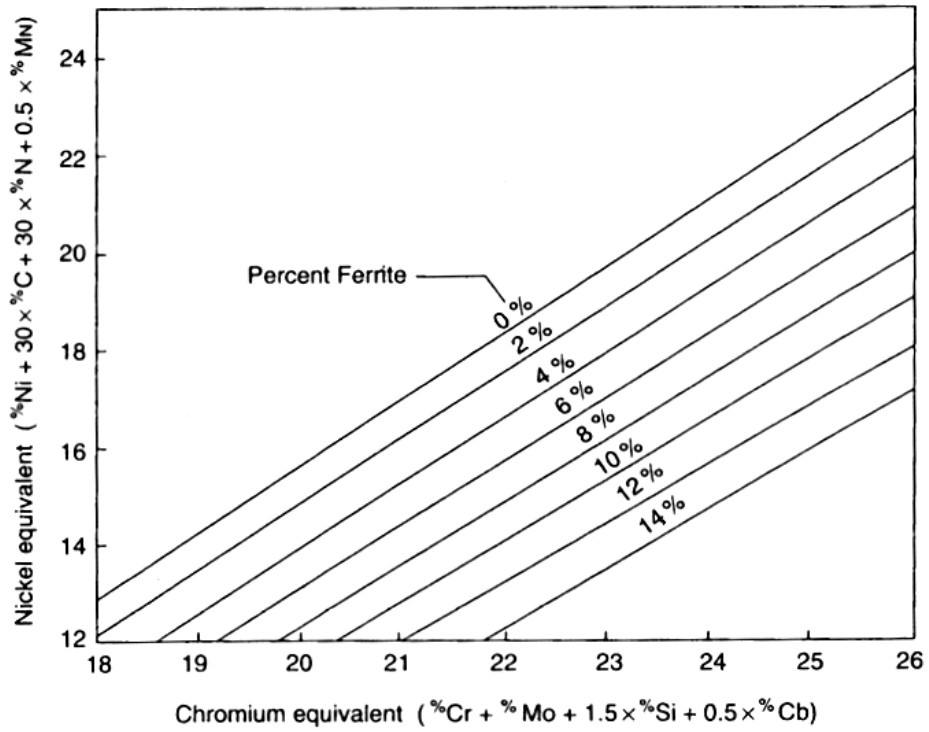
Figure 2.35 DeLong 1st diagram (1956) for austenitic stainless steels [40].
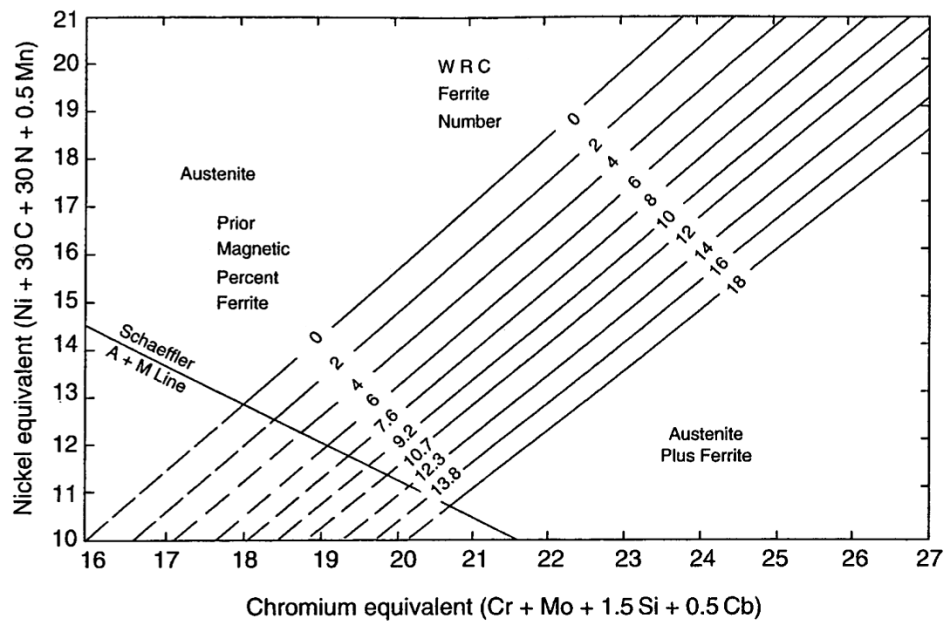
Figure 2.36 DeLong 2nd diagram (1973) for austenitic stainless steels [88].

(3)   Suutala Diagram

Suutala diagram, Figure 2.37, was developed by Kujanpää and Suutala in the 1980s through evaluating a series of published studies regarding austenitic stainless steel weld cracking. The Cr_{eq} and Ni_{eq} used were developed by Hammar and Svenson [92]. This diagram shows that the increase of the Cr_{eq}/Ni_{eq} ratio raises the crack resistance. Extremely low sulfur and phosphor contents can also improve the resistance to cracking. The segregation of these elements at the austenitic grain boundaries during solidification increases hot cracking susceptibility. It can be seen in the Suutala diagram that an alloy with high amounts of S+P wt% is still susceptible to cracking even with high Cr_{eq}/Ni_{eq} ratio because P and S have a tendency to combine with iron and form low-melting point compounds such as FeS and Fe_3P. They also create other low-melting eutectics, such as FeS-Fe and Fe_3P-Fe in addition to Ni₃S2-Ni and Ni_3P-Ni [93]. It is worth noting that P has a more significant role than S content in preventing solidification cracking. The minimum suggested P content is 0.005% and S content should not exceed 0.005% [94].
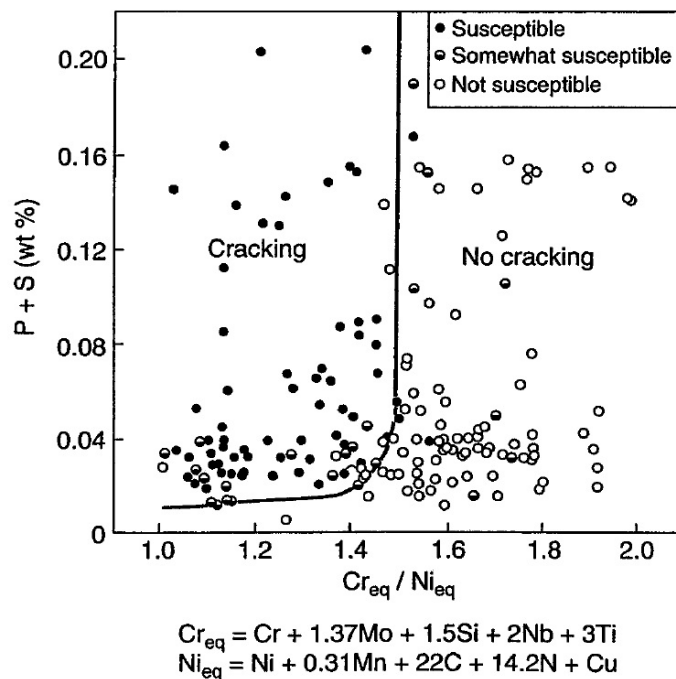
Figure 2.37 Suutala diagram for predicting weld solidification
cracking from weld metal composition [95].

(4) WRC-1988 and WRC-1992 Diagrams

The Schaeffler and DeLong diagrams were expanded in a study funded by the Welding Research Council (WRC) in 1988 to improve the accuracy of ferrite prediction in stainless steel weld metal. The new predicative diagram, known as WRC-1988, has the ability to cover a wider range of compositions, from 0 to 100 FN instead of 1 to 18 and includes boundaries that define the solidification mode. A modification to WRC-1988 diagram was made in 1992 by Kotecki and Siewert, Figure 2.38, which includes a Cu coefficient of 0.25 in the nickel-equivalent formula [96]. To date, the WRC-1992 diagram is the most recommended and accurate tool for predicting the FN in the austenitic and austenitic-ferritic stainless steel welds [97]. Its only weakness may be the lack of a factor for titanium, which is a strong carbide former and can impact the phase balance by taking carbon from the matrix. Titanium is also a ferrite stabilizing element in the absence of carbon [40].
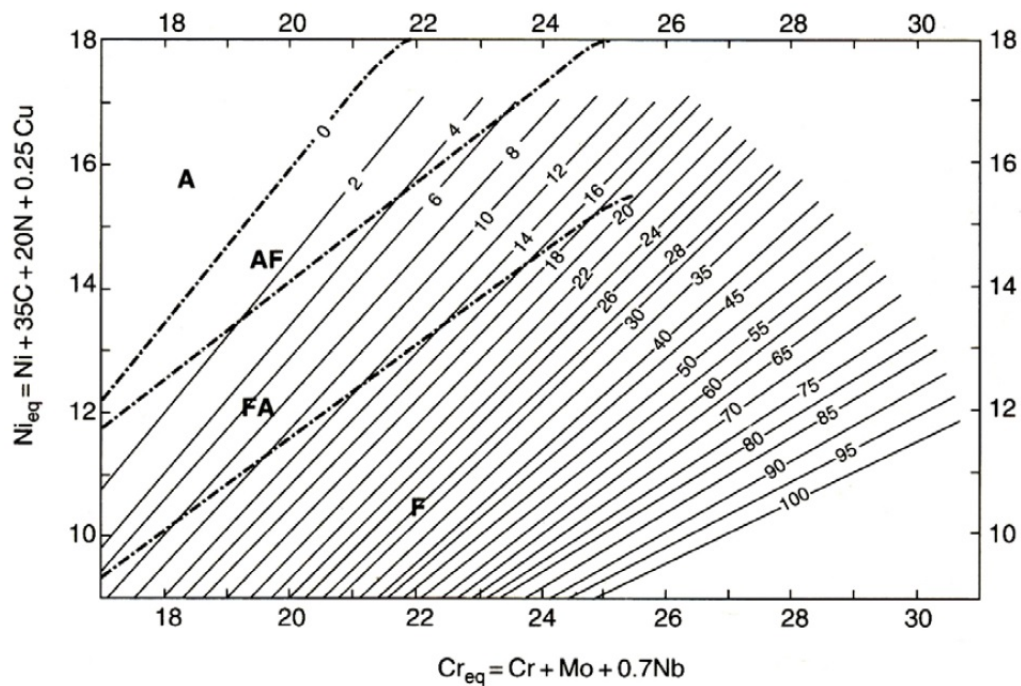
Figure 2.38 The WRC-1992 diagram. Adapted from [98].

45

(5) Other ferrite content measurement methods

Ferrite content of the weld in stainless steels can be measured by methods that do not depend on the chemical composition of the alloy such as metallographic and magnetic techniques. Both processes can give better accuracy since depending only on composition may not be adequate because slight differences in composition may lead to high differences in predicted measurement [99].

Cracking susceptibility can also be affected by other factors, such as weld pool shape and weld restraint conditions especially when the weld metal solidifies in primary austenite mode. The high levels of restraint and tear drop weld pool shape, resulting from excessive welding speed, both increase the cracking susceptibility [79].

2.4.9.2 *Rapid solidification effect*

In high speed welding processes, such as electron beam and laser beam welding, the solidification rate is very rapid and causes a shifting in the solidification behaviour of the alloy so that the constitutional diagrams may not accurately predict either solidification behaviour or ferrite content.

Kurz and Fisher [100] found that the shift in solidification mode from primary ferrite to primary austenite is associated with dendrite tip undercooling. This effect in austenitic stainless steel welds has been described in some detail by Lippold [39] and Brooks and Baskes [101]. It can be seen in Figure 2.39 that under rapid solidification conditions, the stability of austenite, relative to the ferrite, increases with increasing dendrite tip undercooling. As the growth rate increases, austenite becomes favoured over ferrite. Alloys with low Cr_{eq}/Ni_{eq} values, require a lower solidification rate than the alloys with higher Cr_{eq}/Ni_{eq} values for ferrite solidification, as can be seen in Figure 2.39. R_{C1} and R_{C2} represent the critical growth rate to produce austenite over ferrite for the low and high Cr_{eq}/Ni_{eq} ratio, respectively [95]. Figure 2.40 combines the effects of composition and solidification rate on the microstructure of stainless steel, based on EBW travel speed. The increase in welding speed results in a transition in the solidification behaviour of the alloy from AF and FA solidification to type A. A microstructure example for the phase transition is given in Figure 2.41.
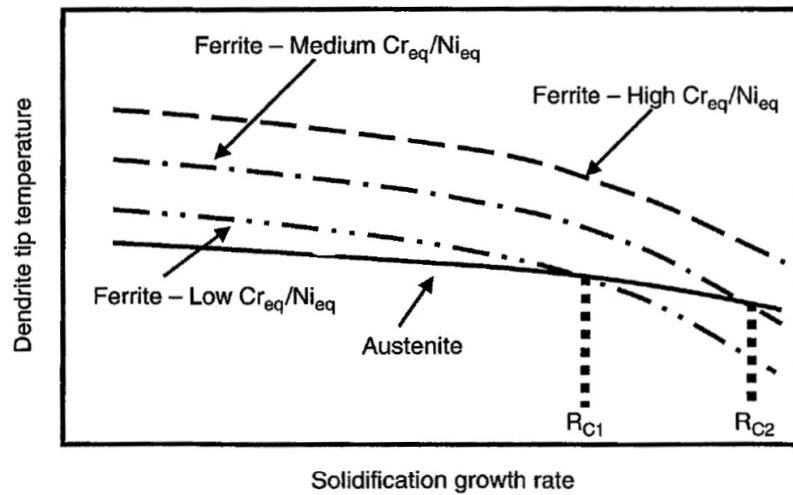
Figure 2.39 Schematic representation of the effect of rapid solidification on the dendrite tip undercooling [40].
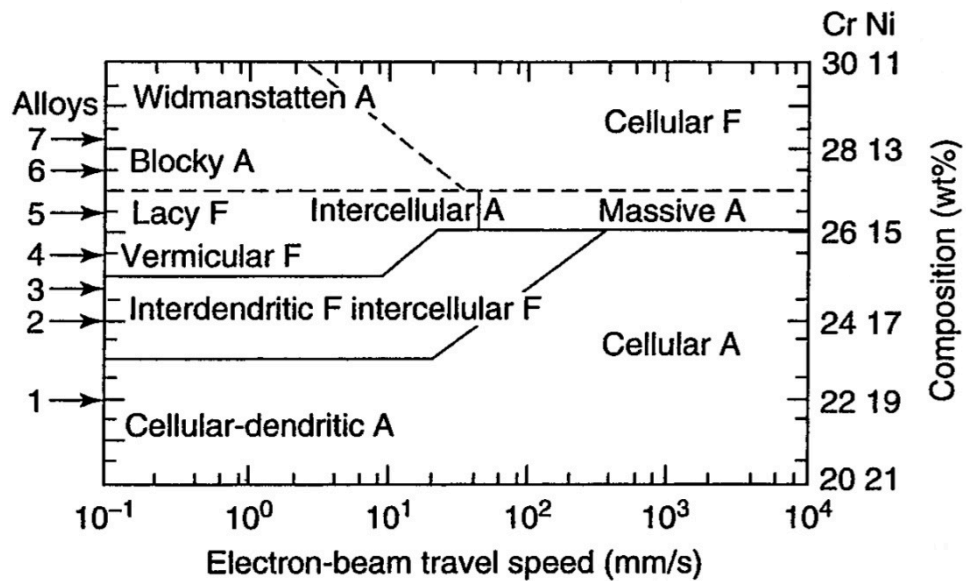
Figure 2.40 Effect of EBW speed on the microstructure of austenitic stainless steel [40].
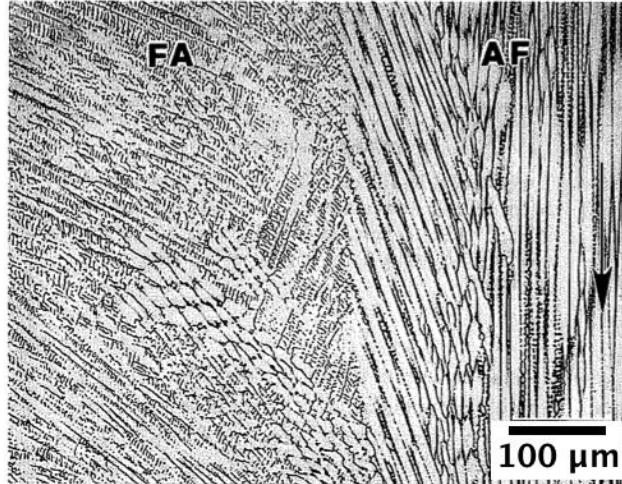
Figure 2.41 A transition in solidification mode from AF to FA due to the increase in
solidification velocity [102].

To predict and control solidification cracking during high-speed solidification, the
Suutala diagram has been modified based on rapid solidification in pulsed LBW, Figure
2.42 [40]. This diagram is also applicable when using other processes that produce very
high solidification rates, such as EBW or TIG. For pulsed laser welds the curve has shifted
to a higher value (from 1.48 to 1.68). Consequently, alloys that are crack resistant under
normal weld solidification conditions may be crack susceptible if the solidification rate is
extremely rapid.

In 1989, the effect of solidification time and cooling rate on the variation of ferrite
number was investigated by Eagar [103]. It was shown that the solidification time and
cooling rate significantly altered the ferrite number of different samples. The
microstructures of the weld and FZ were affected by the composition of the BM and
welding parameters. In 1995, Tjong [68] investigated the characteristics of the 316L weld
following electron and laser beam welding. Microstructure, hardness properties and creep
rupture of the welds were studied. The weld metal microstructure of the two welding
processes was a fully austenitic with solidification structure consisted of cellular and
equiaxed dendrites. The welds showed better mechanical properties than the BM.

48
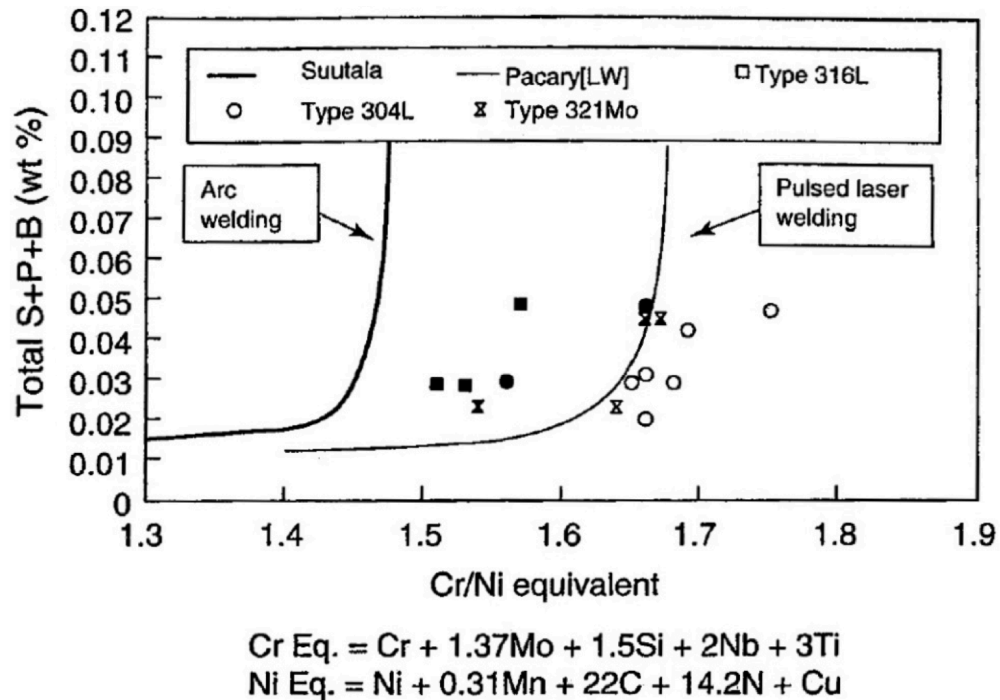
Figure 2.42 Modified Suutala diagram. Solid symbols, cracking, open symbols, no cracking [40].

2.4.9.3 Weld centreline cracking

The formation of centreline boundary in the weld zone creates an area with high potential to cracking during solidification. It is the last area to solidify in the weld, which encourages impurities and alloying elements to segregate in it. This consequently lowers the melting point of the weld in this zone limiting the service conditions of the component. Mechanical and corrosion properties may also decrease due to the probability of formation of brittle phase and eutectics [60]. In high power density welding processes such LBW, the centreline boundary acts as a weak interface that arrests stresses and helps cracks propagation to generate. This attributed to the sudden transition in the grain orientation due the high welding speed [104]. However, the high cooling rates and low contamination associated with welding process that are combined with vacuum technique, such as EBW, reduces the precipitation of brittle phases at the weld centreline [105].

The grain orientations can also play an important role in determining the mechanical behaviour of the weld. BCC and FCC grains with slip direction <111> and <110> respectively, and slip plane normal are oriented 45° to the direction of the applied stresses, requiring lowest possible stress to yield. To identify the grains orientation and relate the tensile stresses with grain orientation (texture), Electron backscattered diffraction (EBSD) and Schmid factor maps can be utilized [106]. Schmid factor can be represented by

49

equation 2.9,

$$\text{Schmid factor} = \cos \phi \cos \lambda \ \ldots \quad\quad \ldots(2.9) \ [33].$$

Where, ϕ is the angle between slip plane normal and direction of the applied stress, λ is the angle between slip direction and direction of the applied stress. Grains with a low Schmid factor are strong grains and harder to yield [107]. Schmid factor intensity values is between 0 and 0.5. Grains with ϕ and λ equal to 45° give the highest Schmid factor producing lower yield and tensile strength [108, 109].

2.4.9.4 HAZ liquation cracking

This type of cracking occurs in the HAZ region adjacent to the fusion boundary. It is particularly prevalent in fully austenitic stainless steels. The metallurgical reason for cracking includes the formation of liquid films along grain boundaries in the partially melted zone adjacent to the fusion line where temperatures are close to the weld metal solidus. These films are unable to accommodate the thermally and/or mechanically induced strain experienced during weld cooling [95]. The liquation is associated with the segregation of impurities such as sulfur and phosphorus to the grain boundaries at elevated temperatures or the formation of low melting eutectic phases caused by segregation of elements such as niobium and titanium along with these impurities [82]. HAZ liquation cracking can be minimized by adjusting the composition and the microstructure of the BM [110]. Base metals that have a ferrite number (on the WRC-1992 diagram) of 1 or higher will form some ferrite along the HAZ boundary, as illustrated in Figure 2.26 and effectively prevent the formation of liquation cracking. In fully austenitic HAZ microstructure, there is no grain boundary ferrite, meaning restricting impurity levels and grain size can minimize the liquation cracking. The higher grain boundary area raises the amount of total stress required to start cracking by decreasing the segregation and local stresses on individual grain. Examples of HAZ liquation cracking are presented in Figure 2.43 [40]. The existence of ferrite along the austenite grain boundaries decreases the crack growth, as shown in Figure 2.43 (a).
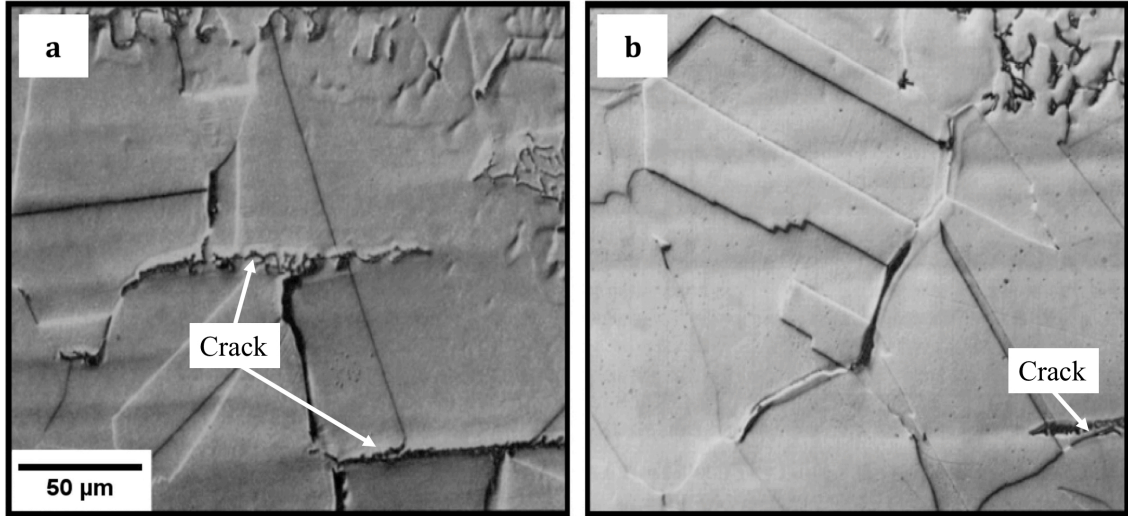
Figure 2.43 HAZ liquation cracking in the HAZ of a) Type 304 with ferrite potentials 1 and b) Type 304L with ferrite potentials 0. Adapted from [111].

2.5 Titanium and titanium alloys

The Kroll process is the most popular method for producing Ti. In this process, the TiO_2 is converted into $TiCl_4$, then sodium or magnesium are used to make the Ti metal. Recently, other processes have been reported to produce titanium by thermomechanical processing of TiO_2 [112].

Titanium has excellent corrosion resistance, high strength to weight ratio and good mechanical properties even at high temperatures. It is used in many applications such as chemical and petrochemical industries, aerospace and biomaterials applications [33]. Titanium exhibits an allotropic behaviour showing a phase transition at about 882ºC, altering from BCC β phase to HCP α phase on cooling. The addition of alloying elements can change the transformation temperature, affect the stability of the β and α phase and provide solid solution strengthening for Ti alloys. Alloying elements in titanium can be classified into 4 groups, Figure 2.44 [113].
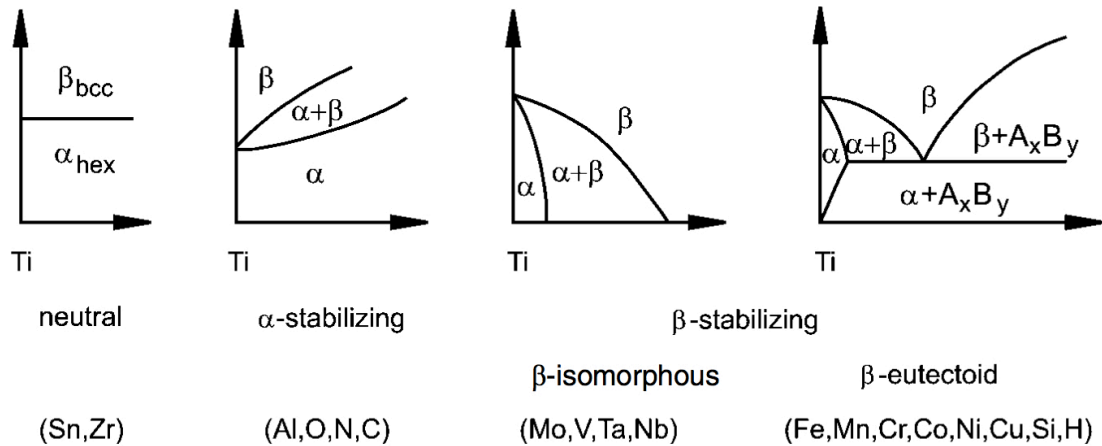
Figure 2.44 Effect of adding alloying elements on Ti phase stability and final microstructure [114].

Alloying elements such as Sn and Zr produce solid solution strengthening with no influence on phase stability and transformation temperature. Al, N, C and O stabilize the alpha phase and increase the β transus temperature. Mo, Nb, V are β stabilizing elements and lower the temperature at which alpha transforms to beta even to room temperature. Finally, the addition of Mn, Co, Cu, Fe, Si and Ni form a combination of the alpha and beta phases at room temperature through a eutectoid reaction. The addition of alloying elements produces five different titanium alloys, α, near α, β, near β and α + β alloy. This classification is based on the dominate phase structure at room temperature, as illustrated in the pseudo-phase diagram in Figure 2.45 [115].
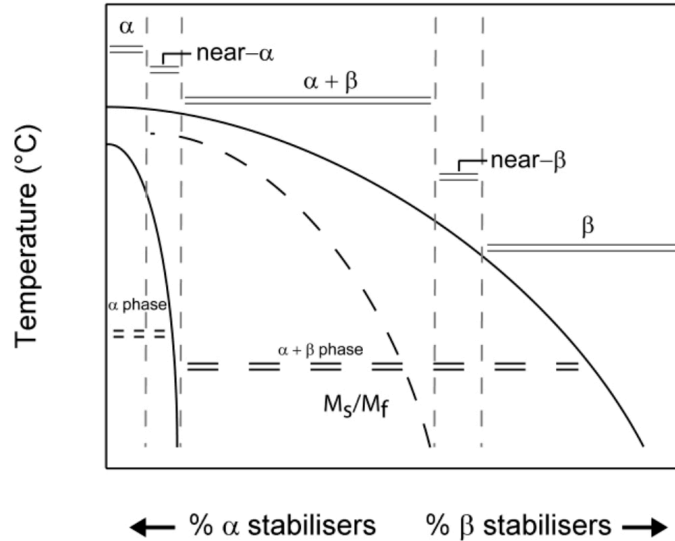
Figure 2.45 The pseudo-phase diagram for titanium alloys [112].

2.5.1 The α and near α alloys

α alloys are completely HCP α phase structure alloys. The most common examples of α alloys are commercially pure titanium (CP-Ti), Ti-5Al-2.5Sn and Ti-2.5Cu [116]. These alloys are not heat treatable and can only be strengthened by either adding solid solution strengthening elements such as Al and Sn, or by cold working [33, 112]. Improvement of fatigue life can be achieved through rapidly cooling the solution treated alloy to produce acicular or Widmanstätten α grain structure that provides better fatigue resistance. The α alloys have excellent corrosion resistance, high deformability and show no transus temperature at cryonic temperatures. Therefore, they are used in chemical processing equipment such as pressure vessels and hydrogen storage tanks [113].

The near α alloys contain small amounts of β phase that is retained in the microstructure after cooling to room temperature. The presence of β phase enhances the workability during forging, significantly improves resistance to creep and increases strength at high temperatures. Near α alloys can be obtained by adding a certain amount of β phase stabilizing elements (≤2%) such as silicon and molybdenum. Examples of these alloys are Ti829 and Ti834 [117, 118]. The α and near α alloys have good weldability because they have good ductility. For alloys in an annealed condition, the welding thermal cycle has a minimal influence on the strength of the HAZ. However, for the alloys in a cold work condition, the strength of the HAZ drops due to the heating effect during welding. Therefore, it is preferable to weld these alloys in annealed conditions.

2.5.2 α + β and near β alloys

With certain amounts of α and β stabilizers (4-6 wt%) a broad combination of the two phases can be obtained at room temperature after solution treatment. Ti6Al4V and Ti6Al2Sn4Zr2Mo0.5Si are examples of this class. Due to the combination of excellent mechanical properties, good corrosion resistance and high temperature capability, these alloys are mainly used in the aircraft and aerospace industries. The strength and fatigue life of α + β alloys can be controlled through thermomechanical heat treatments since the alloys contain two phases [119, 120].

The mechanical properties of α+β titanium alloys can be significantly affected by the welding thermal cycle. However, the degree of effect depends on the amount and type of the alloying elements. Phase transformations that occur during welding decrease the ductility of the weld metal and HAZ. Therefore, filler metals of titanium or alpha-titanium alloy can be used for welding alpha-beta alloys to improve the ductility of the weld metal by producing weld with lower beta phase [21].

2.5.3 β alloys

A high percentage of β stabilizing elements such vanadium or molybdenum produces a structure close to single-phase β structure, which is under rapid cooling, a complete but metastable β structure. Strengthening of these alloys can be achieved by solid-solution strengthening alloying elements and by age hardening through reheating the metastable structure to produce α phase precipitates. Aerospace parts such as high-strength fasteners and beams are the main applications of these alloys due to their high strength and thermal stability.

β titanium alloys have poor creep behaviour and exhibit a ductile to brittle transition [33, 116, 118]. Most of the β alloys are considered weldable such as Ti-13V-llCr-3AI and Ti-llSMo-6Zr-4.5Sn alloys. However, the β alloys in annealed condition show better weldability than the alloys in heat treated condition. For higher joint efficiency, the alloy should be welded in annealed condition. The weld then is cold worked and then solution treated followed by aging. This will produce a weldment with good strength and ductility [121]. Figure 2.46 summarizes the influences of alloying elements on titanium structure, together with properties and classification of titanium alloys.

54

2.5.4 Ti6Al4V

Ti6Al4V is the most common titanium alloy. It covers about 50% usage in the alloys' market having been referred by Timet, in 1954, as the "workhorse" alloy of the industry. It is widely used in the aerospace industry and automotive components due to its good combination of mechanical properties and high corrosion resistance in addition to its high strength-to-weight ratio [122].

This alloy is a dual phase alloy containing 6wt% aluminium and 4wt% vanadium as the main alloying elements to stabilize the $\alpha + \beta$ phases. Aluminium stabilizes the α phase and increases the alloy strength through solution strengthening effect. Vanadium is added as a β phase stabilizer and to improve the workability at high temperature [120]. As a dual phase alloy the microstructure can be controlled by heat treatment. Different microstructures can be developed under different solution treatments and cooling rates, Figure 2.47 [123]. The common structures that can be obtained in Ti6Al4V and any $\alpha+\beta$ titanium alloy through different thermomechanical treatments are: lamellar, equiaxed and bi-modal structures.

2.5.4.1 Full lamellar structure

This microstructure can be achieved through annealing of the alloy in the β phase, hence the name "β annealed". The cooling rate is the critical parameter in determining the final shape and characteristics of the lamellar structure, such as the size of α grains and colonies, and the α lamellar thickness. The faster the cooling rate, the finer the structure that can be obtained, as shown in Figure 2.48.

Generally, the lamellar structure is produced when high fracture toughness, superior creep and fatigue resistance are required. The coarse lamellar structure enhances impact properties and creep resistance. The fine structure has low fatigue crack growth rate, adequate strength and ductility properties [119, 124].

Alpha-stabilizing elements

For example:
aluminum
oxygen
nitrogen

Beta-stabilizing elements

For example:
molybdenum
iron
vanadium
chromium
manganese

Increasing quantities of alpha stabilizers promote alpha phase.

Increasing quantities of beta stabilizers promote beta phase.

Alpha structure	Near-alpha (some beta)		Mixed alpha-beta structure		Near-beta (some alpha)		Beta structure	
Unalloyed Ti	Ti-5Al-6Sn-2Zr-1Mo-0.2Si	Ti-6Al-2Sn-4Zr-2Mo	Ti-6Al-4V	Ti-6Al-6V-2Sn	Ti-6Al-2Sn-4Zr-6Mo-	Ti-8Mn	Ti-8Mo-8V-2Fe-3Al	Ti-11.5Mo-6Zr-4.5Sn
Ti-5Al-2.5Sn								Ti-13V-11Cr-3Al
	Ti-8Al-1Mo-1V							

Higher density →
Increasing heat-treatment response →
Higher short-time strength →
← Higher creep strength
Increasing strain rate sensitivity →
← Improved weldability
Improved fabricability →

Figure 2.46 The effect of alloying elements on titanium structure and properties [125].
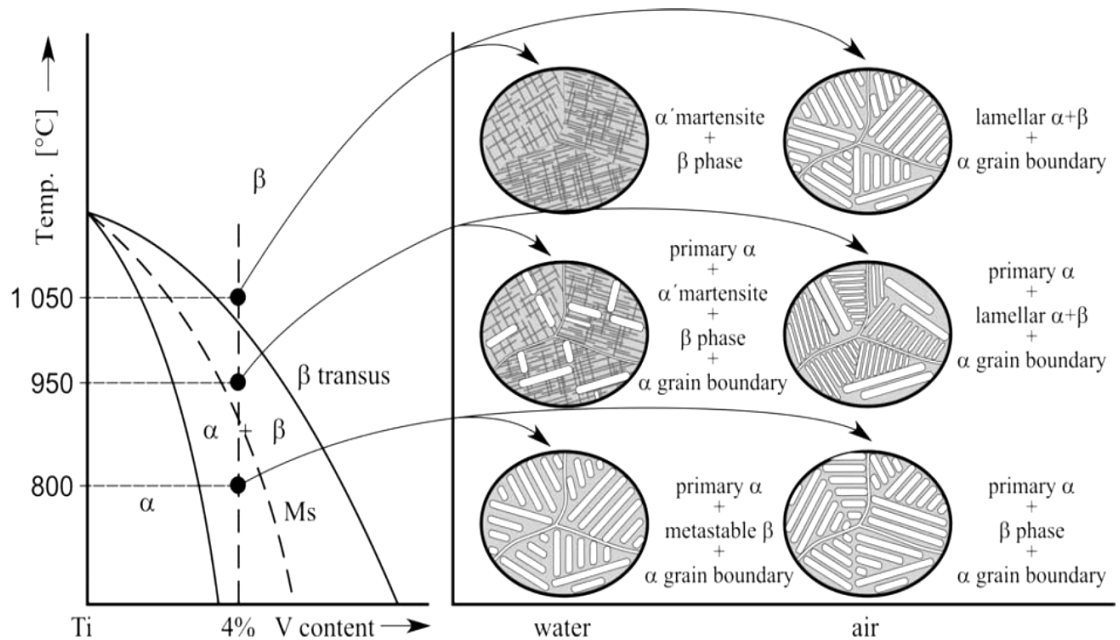
Figure 2.47 Schematic examples of microstructures for casted Ti6Al4V alloy
produced by different heat treatments [123].
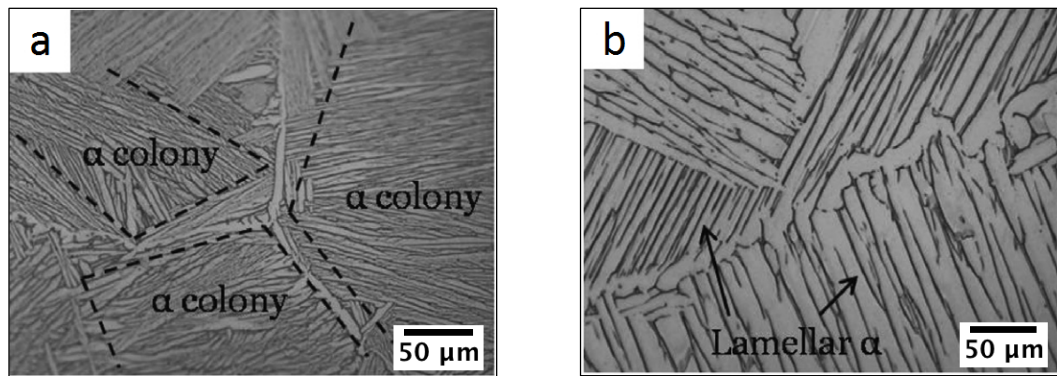
Figure 2.48 Ti6Al4V lamellar microstructure produced under different heat treatment. (a)
fast cooling rate. (b) slow cooling rate. Adapted from [123].

2.5.4.2 Bi-Modal Microstructures

This microstructure is characterised by the duplex microstructure. It consists of primary
alpha (α_p) phase and transformed beta regions, Figure 2.49 [126]. The thermomechanical
process to produce this microstructure includes four steps and is summarized
schematically in Figure 2.50. One of the most critical steps in determining the final

microstructure is the cooling rate, particularly after the homogenization process, step I. The faster cooling rate results in a thinner α lamellar width and smaller equiaxed primary α size. The annealing temperature in step III can also influence the bimodal microstructure by controlling the volume fraction of the recrystallized equiaxed primary α. Both the size and volume fraction of primary α can both determine the grain size of β phase, which has a significant effect on the mechanical properties [127, 128]. The duplex structure combines the properties of equiaxed and lamellar structures in one properties profile. It shows high strength, good fatigue resistance and better ductility than the other α+β structure types [119].
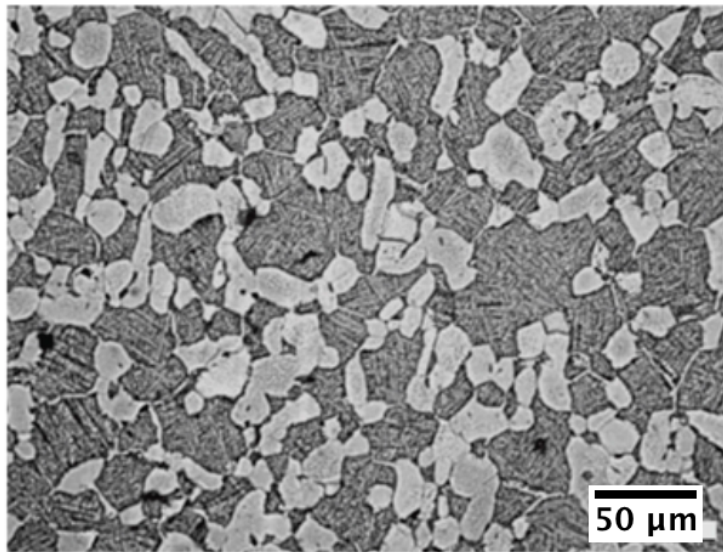
Figure 2.49 Bimodal structure of Ti6Al4V. Adapted from [129].

2.5.4.3 Fully equiaxed microstructures

If sufficiently slow cooling rates after the recrystallization step are achieved, Figure 2.50, there is sufficient time for primary α grains to grow, resulting in a fully equiaxed structure without α lamella existing within the β grains, Figure 2.51. The equiaxed structure enhances strength and ductility with a decline in fatigue life and crack initiation resistance. Ti6Al4V shows the best weldability among the alpha-beta alloys. This can be attributed to the lower beta stabilisers content compared to other alpha-beta alloys. This results in more ductile and lower brittleness microstructure. In addition, the alloy shows a relatively low hardenability. This leads to the formation of the desired Widmanstätten alpha with a

retained beta microstructure even at high cooling rates [21, 121].
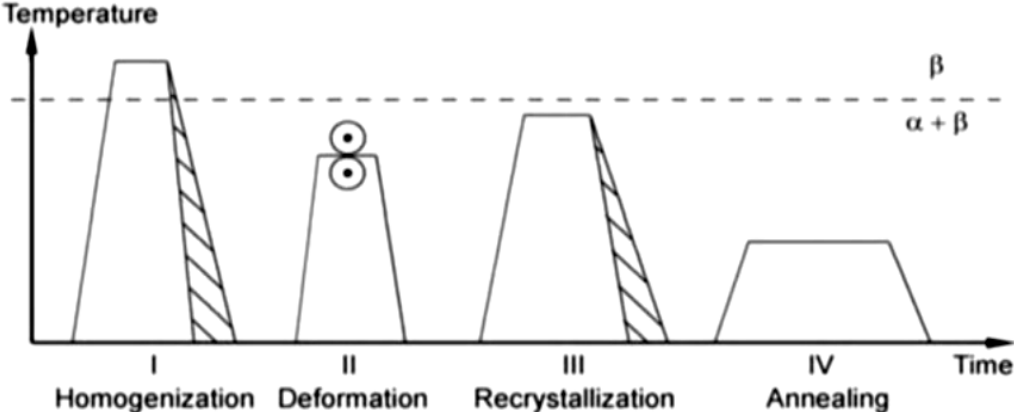
Figure 2.50 Schematic examples of microstructures for casted Ti6Al4V alloy produced by different heat treatments [124].
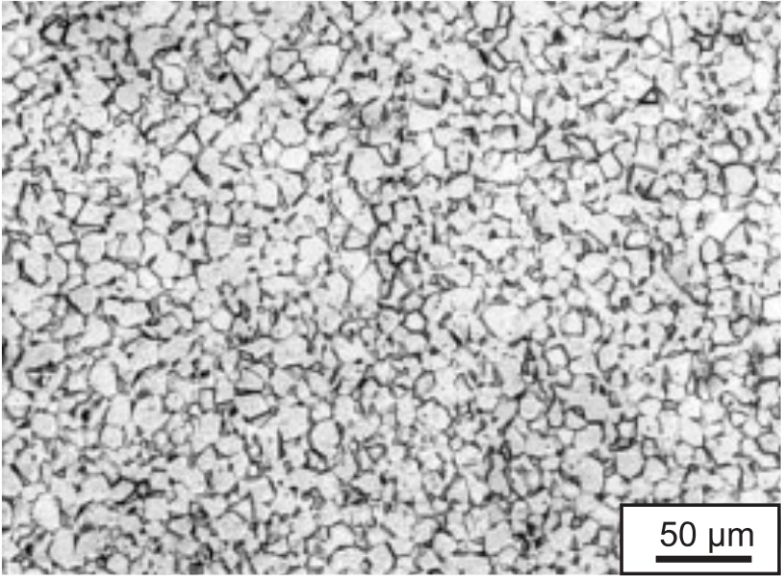
Figure 2.51 Ti6Al4V equiaxed microstructure [113].

2.6 Dissimilar welding of austenitic stainless steel

Austenitic stainless steels are frequently joined to other metals, being widely used in many industrial fields that require a transition in properties and performance [40, 130]; for example, the combination between ferritic steel and austenitic steel in tubes and pipes used in power stations. The service conditions in this application require materials with different properties, i.e. the austenitic stainless steels have superior creep strength and oxidation resistance at higher temperature in areas such as super-heaters and re-heaters. While the ferritic stainless steels are a commercially attractive choice for resisting creep for low temperature service components such as boiler and heat exchanger parts [131, 132]. An effective joint between two different materials affords great advantage and flexibility to the designer in selecting the correct material for a specific application [133]. However, significant challenges and problems will sometimes arise during the joining of dissimilar materials due to the differences in the metallurgical, physical and mechanical properties of the materials being joined [130].

Joining of austenitic stainless steels to other metals can present a range of problems depending on the degree of dissimilarity [2, 40, 130]. The joining of stainless steels to nonferrous alloys such as aluminium, copper and titanium are usually associated with a series of difficulties, e.g. formation of intermetallic compounds and high residual stresses. Such difficulties almost exclusively arise from fusion welding processes [1]. However, high power density welding techniques such as EBW and LBW have the capability to reduce some of these problems, e.g. the size and shape of the molten metal can be precisely controlled, which can significantly minimize the formation of brittle phases. Additionally, the relatively low heat input per unit length of the process can dramatically decrease the residual stresses [32, 134, 135].

2.6.1 Joining of AISI 316 austenitic stainless steel to Ti6Al4V using EBW process

The dissimilar junction between AISI 316 austenitic stainless steel and Ti6Al4V has a key advantage in many industrial fields since it reduces the requirement of using titanium alloys for many components in regions where the key mechanical properties of Ti6Al4V are not need. This will consequently lead to lower costs while still maintaining superior corrosion resistance performance [136].

Joining titanium alloys to steels through fusion welding techniques is usually accompanied by many metallurgical issues, i.e. formation of brittle intermetallic compounds. This is due to the very low solubility of Fe in titanium as can be seen in the Fe-Ti phase diagram, Figure 2.52 [137]. The brittle phases cause the joint to break

instantly after welding due to the thermal stresses produced from the mismatch in physical properties between the two metals. Thus, restricting the formation of intermetallic compounds (IMCs) is crucial to attain reliable joint strength [138]. It was found that controlling the size of the intermetallics and keeping them under 10μm will limit their effect in increasing the brittleness of the weld [2].
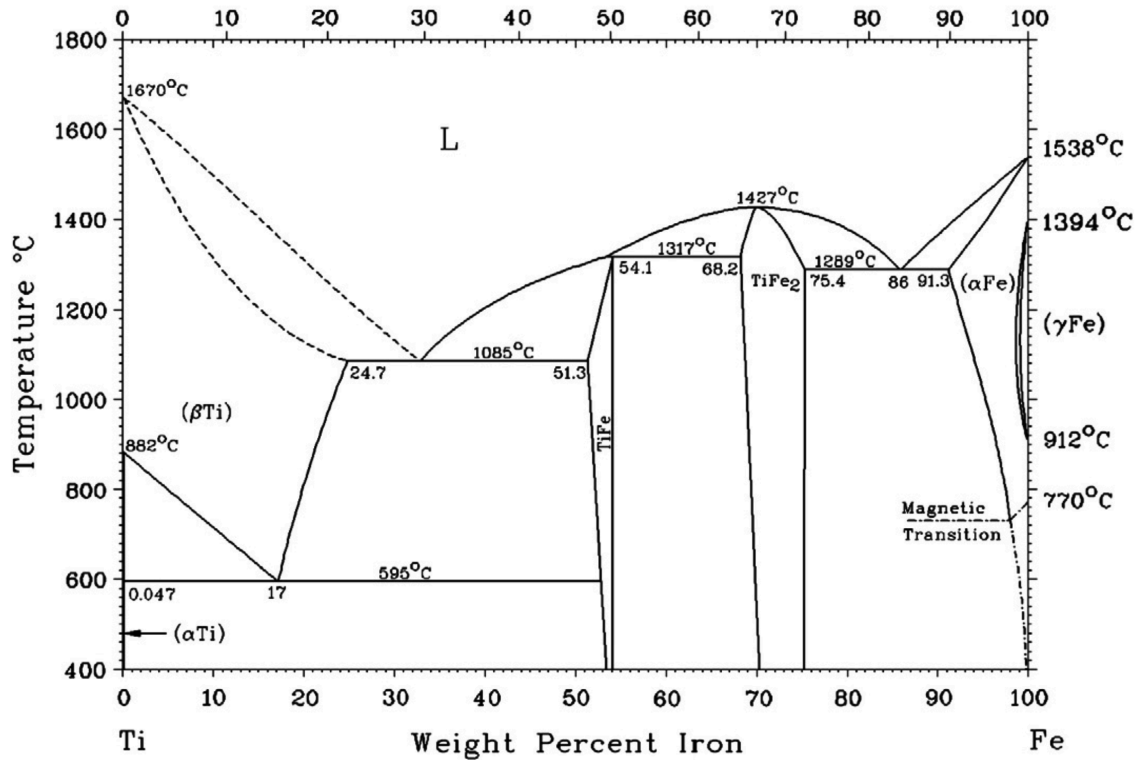
Figure 2.52 Fe-Ti binary phase diagram [139].

To control the formation of the brittle phase the following options can be used: solid state joining techniques that keep the parent metals non-melted such as friction stir welding [140, 141], diffusion bonding [142-144] and explosive welding [145-147] or high power density welding techniques such as LBW and EBW that precisely controlling the amount of the heat input, welding speed and position of the heat source [137, 148] or using a third material as an intermediate layer such as silver and copper . The intermediate layer approach has been used with solid state welding [149, 150] and fusion welding techniques with high power density [151, 152]. In the fusion welding process, adding an intermediate material will help in isolating the incompatible base materials from mixing and reduce the melting volume of titanium, which has a tendency to form intermetallic compounds with most metallic elements [152].

Using the EBW process to join titanium to stainless steel has been a subject for many studies in recent years. The unique features of the process are that it is very effective in precisely controlling the mixing of each metal in the weld pool, which consequently enhances the opportunity to achieve a successful joint between them [7]. Through inserting a copper transition sheet, it was found that it is possible to obtain a crack free joint by avoiding the metallurgical issues and improving the joint toughness. The solid solution of copper can distribute uniformly in the FZ and form Ti-Cu intermetallic compounds in the titanium-copper interface, which are less brittle than Ti-Fe and therefore improve the weld plasticity [148]. A copper solid solution separates the Ti-Fe intermetallic and substitutes the $TiFe/TiFe_2$ interface with $TiFe_2/Cu$. Whilst in the Ti/weld interface, the relatively soft Ti-Cu intermetallic layer replaces the brittle Ti-Fe intermetallic layer [6]. An example of electron beam dissimilar welding between Ti-15-3 and AISI304 with and without using a copper interlayer is given in Figure 2.53.

The location of the electron beam across the weld has an important influence on the weld pool microstructure and mechanical properties. Shifting the beam towards the stainless steel side reduces the melting of titanium alloy and consequently decreases the formation of intermetallic compounds at the titanium interface. The electron beam shifting towards the titanium side produces a large volume of the brittle Ti/Fe phases at the stainless steel interface [148]. The electron beam welding parameters, such as the heat input and the travel speed, can also influence the morphology of the FZ. The molten amount of each metal and the thickness of the intermetallic layer at the titanium interface are directly influenced by the welding speed and consequently the weld metal microstructure as shown in Figure 2.54 [12].

In this study, the possibility of joining 20 mm thick AISI 316L to Ti6AL4V by EBW was investigated through applying a range of welding parameters such as welding power, travel speed and beam offset. Other factors that can enhance the joint feasibility, e.g. using copper interlayer with different thickness, preheat and double pass weld technique were also studied.
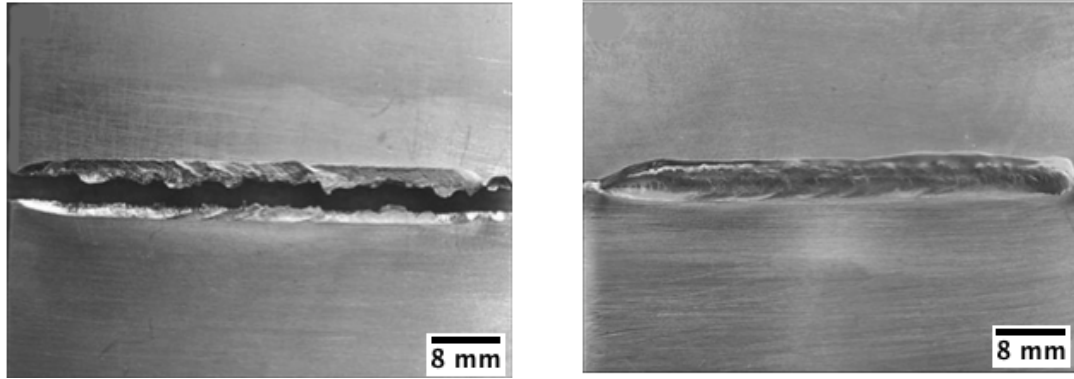
Figure 2.53 Ti-15-3/304 electron beam welded joints a) without (b) with inserting copper sheet. Adapted from [148].
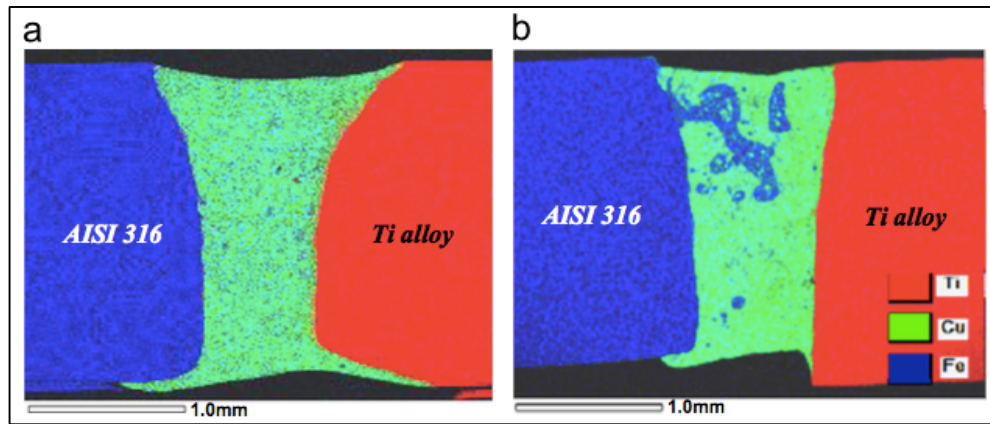
Figure 2.54 X-ray element map of Ti6Al4V-AISI316L joint with (a) 1 m/min (b) 2.5 m/min travel speed at beam offset 0.25 from the weld centreline toward stainless steel interface [12].

Chapter 3 Experimental methods

This chapter outlines all the experimental works undertaken in the present study. The chapter provides details of the materials used, samples' preparation and welding procedures. It then explains the testing and analysis techniques used in the project. The following flow chart, Figure 3.1, demonstrates the welding experiments and characterization methods that are applied in this research.
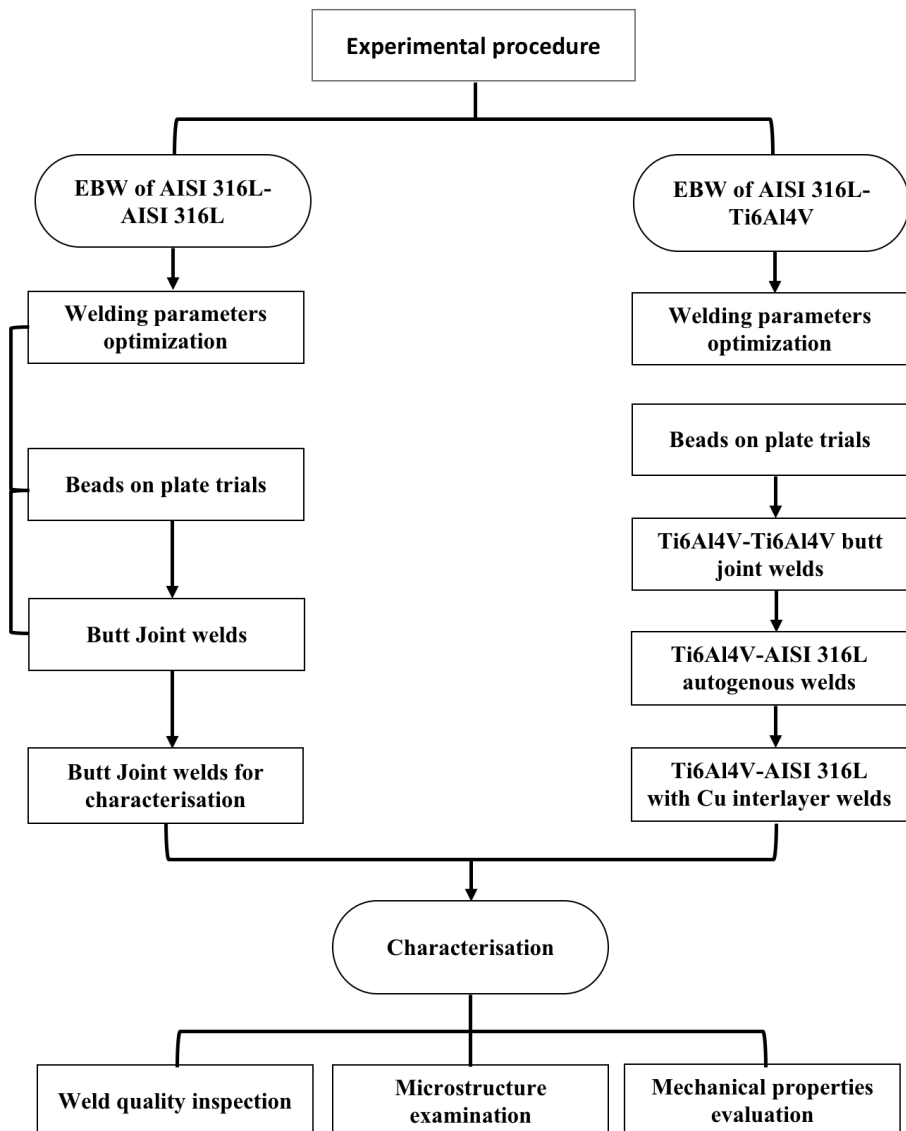
Figure 3.1 Research morphology structure

3.1 Materials

The electron beam welding was carried out on 20 mm thickness AISI 316L austenitic stainless steel and 20 mm thickness Ti6Al4V plates; both materials were used as a base metal. A sheet of 1.5 mm thickness commercial pure copper was used as a transition layer and was fixed at the interface between the titanium and steel during the dissimilar welding.

All the materials were received in the as-rolled and mill annealed condition. The chemical compositions, physical properties and mechanical properties of the metals are given in Tables 3.1, 3.2 and table 3.3 respectively. The chemical composition of the materials was analyzed in the AMG Superalloys UK Limited company.

Table 3.1 Chemical composition (wt%) of the used materials.

Element	Cr	Ni	C	Si	Mn	Mo	N	P	Cu	Co	Ti	Al	V	Fe	Total
316L	16.63	10.14	0.03	0.46	1.32	1.87	0.08	0.027	0.67	0.11	-	-	0.07	Bal.	100
316L (Standar)	16-18	10-14	0.03	0.75	2	2-3	0.1	0.045	-	-	-	-	-	Bal.	100
Ti6Al4V	-	-	-	-	-	-	-	-	-	-	Bal.	6	4	-	100

Table 3.2 Physical properties of AISI 316L, Ti6Al4V and Cu.

Material	Melting point/^{o}C	Specific heat capacity (J.Kg^{-1}.K^{-1})	Thermal conductivity (W.m^{-1}.K^{-1})	Thermal expansion (μm.m^{-1}.K^{-1})
AISI 316L	1375	490	15	16
Ti6Al4V	1649	560	7.2	8.6
Cu	1083.4	384.4	401	16.6

Table 3.3 Mechanical properties of AISI 316L, Ti6Al4V and commercial pure Cu in annealed condition at room temperature [153-155].

Material	Tensile strength, min, MPa	Yield strength, min, MPa	Elongation in 50mm, min, %	Hardness VH
AISI 316L	485	170	40	220
Ti6Al4V	895	828	10	396
Commercial pure Cu	221	69	55	40

3.2 Welding equipment

A universal chamber electron beam machine, type K40 (Probeam, Germany), shown in Figure 3.2, was used for welding. The machine is located in the Mercury Centre, University of Sheffield. The working pressure of the electron beam machine chamber was approximately 10^{-5} mbar and the accelerating voltage was 60 KV (constant). The welding was carried out at room temperature. A series of welding parameters, such as beam current and travelling speed, were applied in this work.

Figure 3.2 EBW (Probeam) machine.

3.3 Stainless steel-stainless steel welding procedure

3.3.1 Bead on plate experiments for welding parameter optimization

Firstly, beads on plate experiments were undertaken on AISI 316L austenitic stainless steel plates of dimensions of 150×75×20mm, as shown in Figure 3.3 (a, b and c). Abrasive blast cleaning and solvent degreasing were used to clean the plates. The beads were applied perpendicular to the rolling direction (RD) using a series of different welding parameters, such as welding current and speed as shown in Tables 3.3, 3.4 and 3.5 to define the weld parameters for the following butt joint. The initial welding parameters

were chosen based on the guide diagram shown in Figure 3.4. The diagram was designed for steel and shows the possible weld thickness as a function of electron beam power and welding speed.

(a)

(b)

(c)

Figure 3.3 First weld bead trials (a) plate 1 (b) plate 2 (c) plate 3.

Table 3.4 EBW parameters used for initial trials of plate 1

Line	Beam current (mA)	Speed (mm/s)	Focus offset (mA)	Weld figure	Weld length (mm)	Frequency (Hz)
1	90	9	-25	Line	50	-
2	100	7	-25	Line	50	-
3	100	9	-50	Line	50	-
4	100	9	-30	Line	50	-
5	100	9	-25	Line	50	-
6	100	9	-15	Line	50	-
7	100	9	0	Line	50	-
8	100	9	+30	Line	50	-
9	100	9	-25	Circle	50	300
10	100	9	-25	Circle	50	600
11	100	9	-25	Triangle	50	300
12	100	9	-25	Circle	50	300
13	110	9	-25	Line	50	-
14	100	11	-25	Line	50	-

(-): The beam focus position under the surface, (+): The beam focus position over the surface

Weld figure = beam oscillation pattern.

Table 3.5 EBW parameters used for initial trials of plate 2

Line	Beam current (mA)	Speed (mm/s)	Focus offset (mA)	Weld figure	Weld length (mm)
1	100	9	-20	Line	50
2	100	9	-15	Line	50
3	100	9	-10	Line	50
4	142	13	-15	Line	50
5	142	13	-10	Line	50
6	142	13	+10	Line	50
7	142	10	-15	Circle	50
8	142	11	-15	Triangle	50

(-): The beam focus position under the surface, (+): The beam focus position over the surface

Weld figure = beam oscillation pattern.

Table 3.6 EBW parameters used for initial trials of plate 3

Line	Beam current (mA)	Speed (mm/s)	Focus offset (mA)	Weld figure	Weld length (mm)
1	100	8	-10	Line	50
2	100	8	-5	Line	50
3	100	9	-15	Line	50
4	100	9	-8	Line	50
5	100	9	-5	Line	50
6	100	9	-3	Line	50
7	100	9	0	Line	50
8	100	9	+5	Line	50
9	100	9	+10	Line	50

(-): The beam focus position under the surface, (+): The beam focus position over the surface

Weld figure = beam oscillation pattern.
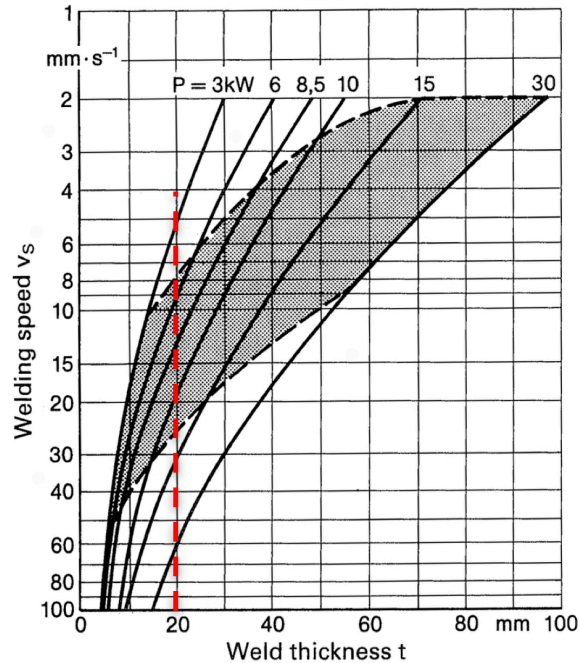
Figure 3.4 Guide values showing the relationship between thickness of the weld, beam power and welding speed. P= the maximum power of the EBW machine. Shaded gray area is the economically applicable area of working. Adapted from [15].

3.3.2 Butt joint welds for welding parameter optimization

Nine butt welds were made using nine sets of welding parameters, Table 3.6. The welds were done perpendicular to the rolling direction (RD) on plates of dimensions of 50×75×20mm. J-Clamps were used to fix the plates together prior to welding, Figure 3.5. The edges of the plates were carefully machined by milling before performing the welds in order to obtain a perfect square butt joint and to ensure the gap between the two plates was as narrow as possible. For the electron beam weld with no filler metal, the interfaces should be well mated and fully touched. The maximum weld gap permission is given in the guided Figure 3.6. It should be noted in the guided figure that the gap allowance increased with the workpiece thickness. However, in an ideal situation, the contact surfaces should touch without leaving a gap.

The electron beam was applied at the plates interface, Figures 3.7, 3.8 and 3.9. The welding parameters and conditions were chosen based on the bead on plate trials to attain the optimum welding parameters in terms of full penetration and weld profile, with the aid of radiographic testing to ensure the weld was defect free.

70

Table 3.7 EBW parameters used for 1st butt joint welds

Joint	Beam current (mA)	Speed (mm/s)	Focus offset (mA)	Weld figure	Weld length (mm)
1	100	9	-15	Line	50
2	100	9	-10	Line	50
3	100	9	-10	Line	50
4	100	9	-6	Line	50
5	100	9	-5	Line	50
6	110	9	-15	Line	50
7	110	9	-6	Line	50
8	110	9	-6	Line	50
9	120	9	-15	Line	50

(-): The beam focus position under the surface, (+): The beam focus position over the surface

Weld figure = beam oscillation pattern.

Figure 3.5 Fixture of the first butt welds.
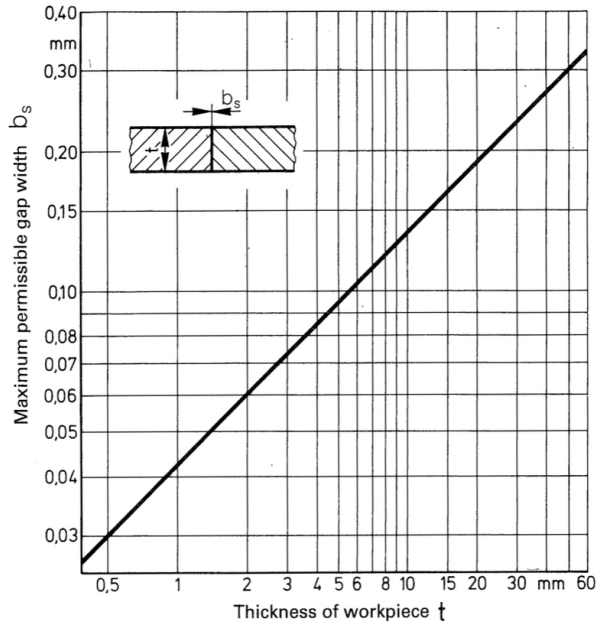
Figure 3.6 Relationship between the gap value and thickness of the plate.
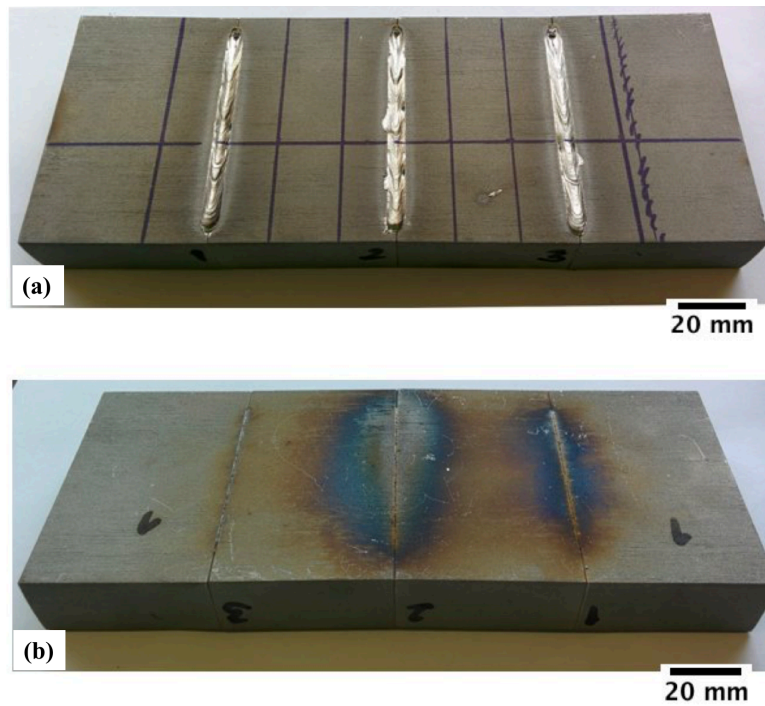
Figure 3.7 First butt joint weld. Joints 1 to 3, (a) top surface (b) bottom surface.
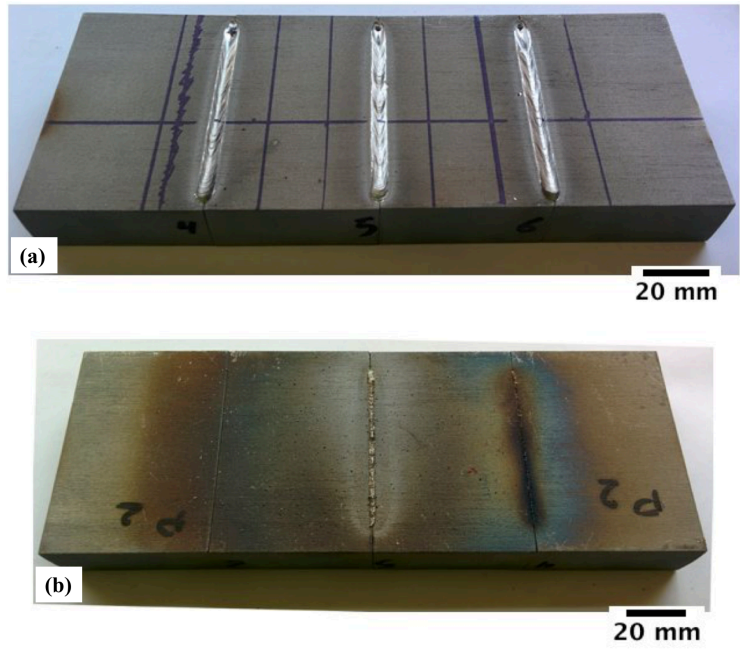
Figure 3.8 First butt joint welds. Joints 4to6, (a) top surface (b) bottom surface.
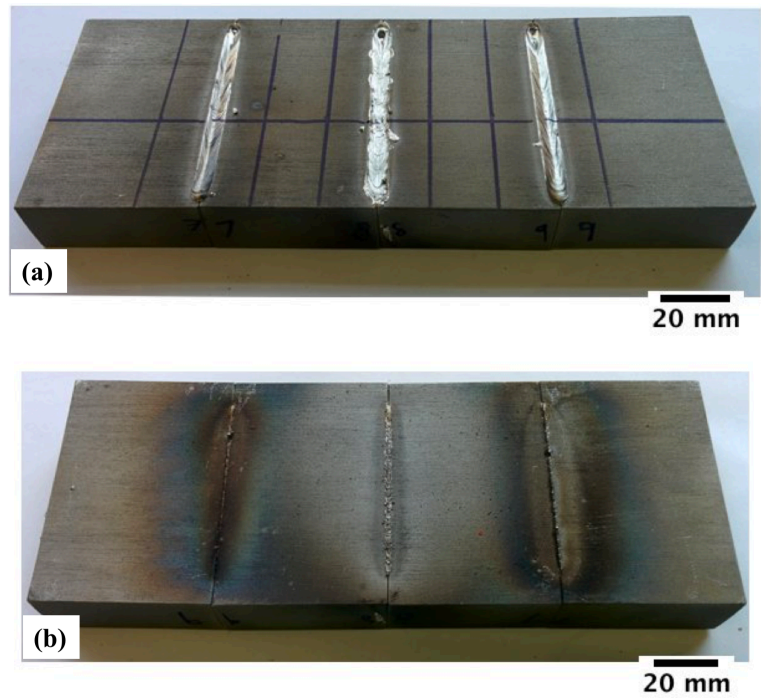
Figure 3.9 First butt joint welds. Joints 7to9, (a) top surface (b) bottom surface.

3.3.3 Butt joint welds for characterisation purposes

Three sets of welding parameters, Table 3.7, were taken for microstructure and mechanical properties investigation. To obtain the maximum amount of weld material for each welding condition, two welds were undertaken on 3 plates with dimensions of 60×150 cm, shown in Figure 3.10 (a, b and c).

Table 3.8 EBW parameters of butt welds used for characterisation.

Weld (W)	Beam Current (mA)	Lens current (mA)	Speed (mm/s)	Focus Offset (mA)	Weld figure	Weld Length (mm)
1	100	60	9	-5	Line	150
2	110	60	9	-5	Line	150
3	120	60	9	-5	Line	150

(-): The beam focus position under the surface, (+): The beam focus position over the surface

Weld figure = beam oscillation pattern.

3.4 Stainless steel-titanium welding procedure

3.4.1 Beads on plate trials

Beads on plate welding trials were carried out on 20 mm thick Ti6Al4V, Figure 3.11, to determine EBW parameters using the depth of penetration and weld bead shape as an indication of a successful weld. The beads were applied perpendicular to the rolling direction using a range of welding parameters as listed in Table 3.8. Solvent degreasing and blast cleaning were used to remove any dirt and to prepare the plate for welding.

(a)
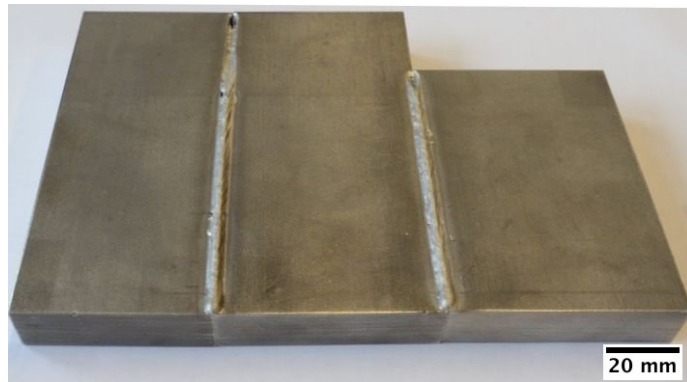
(b)
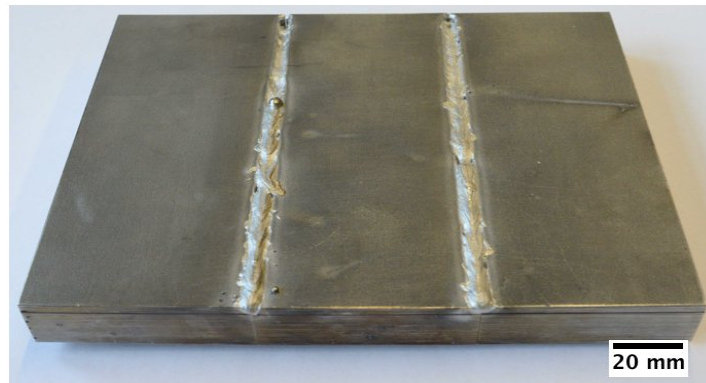
(c)

Figure 3.10 Butt joint welds for characterisation (a) W1 (b) W2 (c) W3.

Figure 3.11 Beads on plate experiments of Ti6Al4V.

Table 3.9 EBW parameters used in Ti6Al4V beads on plate experiments

Weld	Beam current (mA)	Speed (mm/s)	Focus offset (mA)	Weld length (mm)	Weld figure
1	110	13	-5	50	Line
2	110	14	-5	50	Line
3	110	17	-5	50	Line
4	120	15	-5	50	Line
5	120	16	-5	50	Line
6	120	18	-5	50	Line

(-): The beam focus position under the surface, (+): The beam focus position over the surface

Weld figure= beam oscillation pattern.

3.4.2 Ti6Al4V – Ti6Al4V butt joints

The EBW were performed on 30×75×20 mm Ti6Al4V plates using a butt joint, Figure 3.12. This was undertaken as a second step in identifying the suitable welding parameters for the Ti6Al4V and as a prior step to the titanium-stainless steel dissimilar welding. Based on beads on plate experiments, three sets of welding parameters were applied as listed in Table 3.9. The optimum parameters were chosen depending on visual welding inspection including the weld profile and penetration.
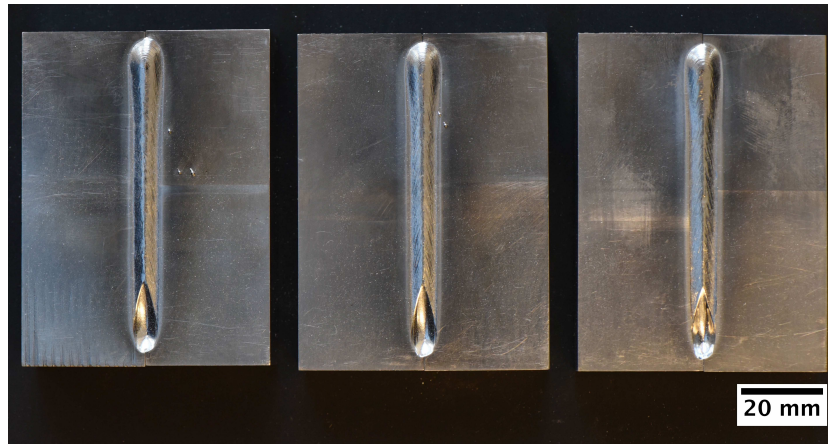
Figure 3.12 Welds 1, 2 and 3 from left to right respectively of Ti6Al4V to Ti6Al4V.

Table 3.10 EBW parameters used in Ti6Al4V to Ti6Al4V weld.

Weld	Beam current (mA)	Speed (mm/s)	Focus offset (mA)	Weld length (mm)	Weld figure
1	110	14	-5	50	Line
2	110	15	-5	50	Line
3	110	16	-5	50	Line

(-): The beam focus position under the surface, (+): The beam focus position over the surface

Weld figure = beam oscillation pattern.

3.4.3 Ti6Al4V – AISI 316L autogenous welds

The first attempts of dissimilar metal welding of AISI 316L to Ti6Al4V were undertaken on plates of dimensions of 30×75×20 mm, the weld configuration is shown in Figure 3.13. The beam current and welding speed were chosen based on the optimum parameters of similar welded samples. The welding was carried out with an electron beam offset, e.g. the electron beam offsets towards titanium side to induce more titanium into the joint interface. The beam position varied relatively to zero point at the contact surfaces from 1.4 mm towards AISI 316L to 0.7 mm towards Ti6Al4V. The beam offset towards the stainless steel was considered positive and towards titanium was considered negative. A list of all the parameters used in the autogenous welding are shown in Table 3.10.
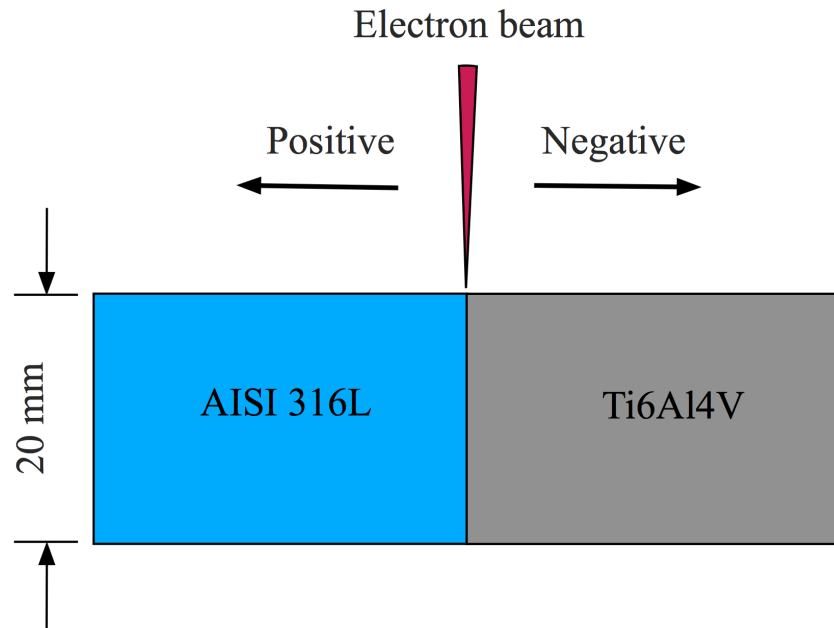
Figure 3.13 A schematic representation of the Ti6Al4V to AISI 316L autogenous weld.

Table 3.11 EBW parameters used in Ti6Al4V-AISI 316L autogenous weld

Autogenous Dissimilar Weld	Beam current (mA)	Speed (mm/s)	Focus offset (mA)	Beam offset (mA)	Cu layer thickness (mm)
1	110	9	-5	0.7 (+)	-
2	110	9	-5	1.4 (+)	-
3	110	9	-5	0.7 (-)	-
4	110	11	-5	1 (+)	-
5	110	11	-5	0.7 (-)	-
6	110	12	-5	1 (+)	-
7	110	12	-5	0.7 (-)	-

(-): The beam focus position under the surface, (+): The beam focus position over the surface

The beam oscillation pattern is line weld figure.

3.4.4 Ti6Al4V – AISI 316L butt joints with Cu interlayer

A second set of dissimilar joining attempts were performed using Cu sheets as an interlayer with different thicknesses, 0.5, 1 and 1.5 mm, as shown in Figure 3.14. The copper sheets of 0.5 and 1 mm thick were manufactured through cold rolling of 1.5 mm thick copper sheet. The electron beam offset was applied and varied with a range between 0.7 mm towards AISI 316L and 0.7mm towards Ti6Al4V relative to zero point at the centre of the Cu interlayer.

   Preheating was applied on some of the weld samples to reduce the effect of the residual stresses and make it possible to use a lower heat input. The preheat was performed using an electron beam with low power that does not melt the BM. A thermocouple was used to ensure approaching the required preheat temperature.

   Furthermore, a number of the preheated weld samples were made with a low heat input and were welded with a double pass welding technique to insure full weld penetration. This technique was carried out by performing the weld on the top and bottom surfaces as illustrated in Figure 3.15. It should be noted that the preheated weld samples were left to cool down to room temperature and taken out of the vacuum chamber then flipped them manually to prepare them for the second weld pass with repeating the preheat. Table 3.11 shows full details of the dissimilar welding experiment parameters.
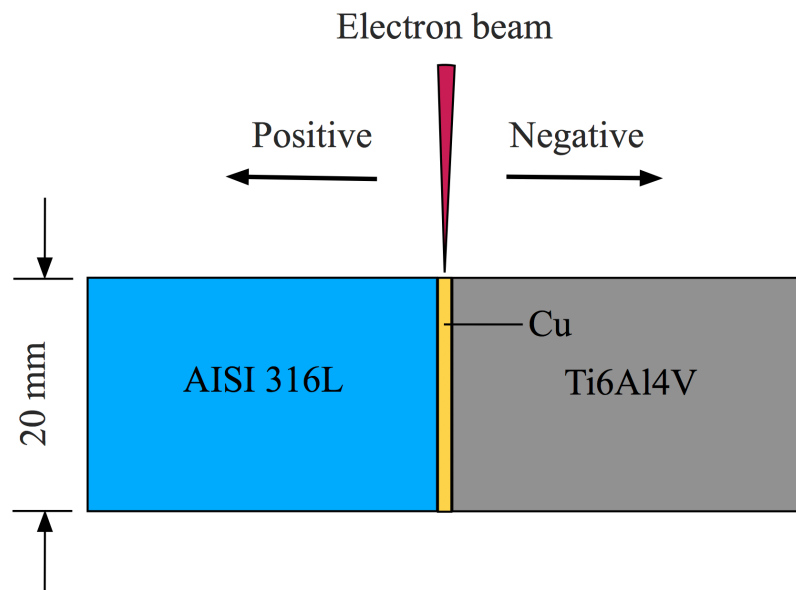
Figure 3.14 A schematic representation of the Ti6Al4V – Cu – AISI 316L weld.
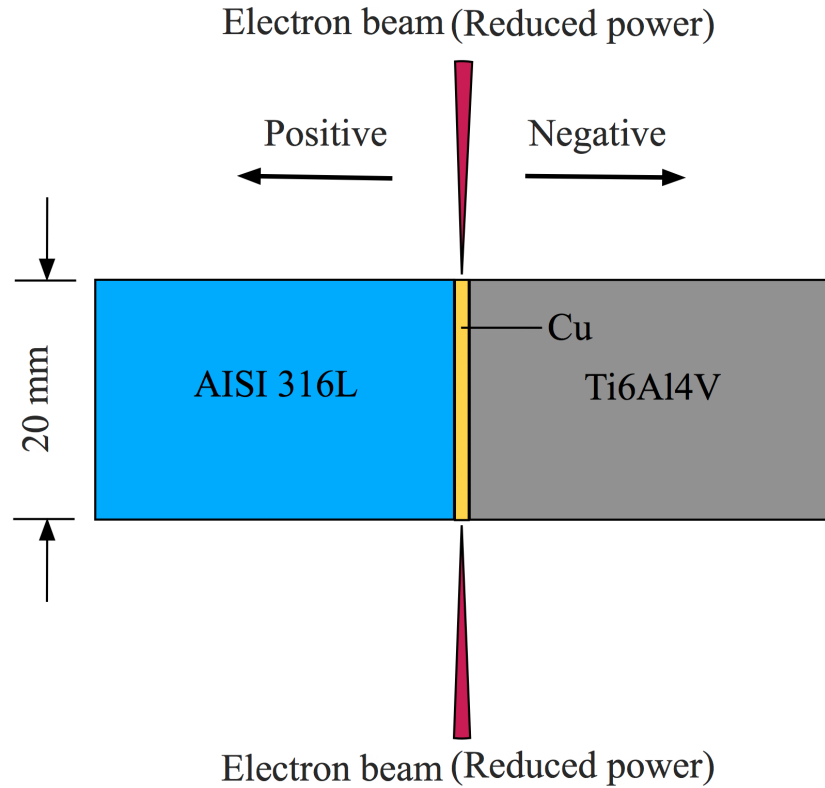
Figure 3.15 A schematic representation of the Ti6Al4V – Cu – AISI 316L weld.

3.5 Characterisation methods

3.5.1 Weld quality inspection

The evaluation of the joint quality was based on British Standards such as BS EN 970:1997 and BS EN ISO 13919-1:1997. Welding imperfections such as incomplete penetration, undercut and excessive penetration were inspected visually. Cavities and cracks were identified with the aid of radiographic testing and microscopic examination. The radiographic test was done in NDT Ltd Materials Testing and Training Consultancy in Sheffield, UK.

Table 3.12 EBW parameters used in Ti6Al4V to AISI 316L with Cu interlayer weld

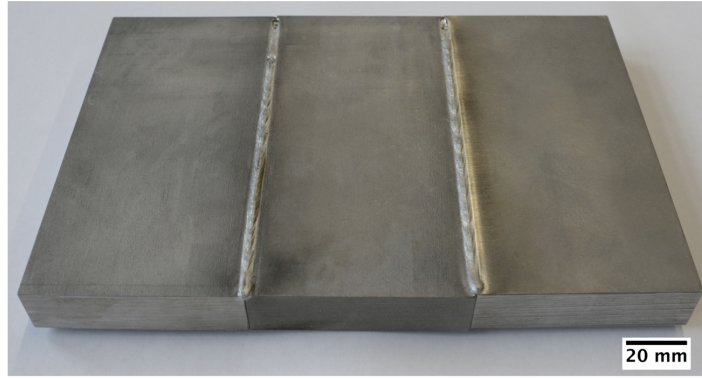| Dissimilar Weld	Beam current (mA)	Speed (mm/s)	Focus offset (mA)	Beam offset (mA)	Cu layer thickness (mm)	Preheat (°C)	Number of passes
1	130	15	-5	0	0.5	-	1
2	140	15	-5	0.3 (+)	0.5	-	1
3	140	16	-5	0.5 (+)	0.5	-	1
4	110	9	0	0	1	-	1
5	110	10	0	0	1	-	1
6	110	11	0	0	1	-	1
7	110	11	-5	0	1	-	1
8	110	14	-5	0	1	-	1
9	140	11	0	0.3 (+)	1	-	1
10	140	12	0	0.3 (+)	1	-	1
11	140	13	0	0.3 (+)	1	-	1
12	70	25	0	0.3 (+)	0.5	450	1
13	100	25	0	0.3 (+)	0.5	450	1
14	100	25	0	0.5 (+)	1	450	1
15	100	16	0	0.5 (+)	1.5	450	1
16	100	18	0	0.5 (+)	1.5	450	1
17	100	20	0	0.5 (+)	1.5	450	1
18	100	20	0	0.75 (+)	1.5	450	1
19	100	22	0	0.5 (+)	1.5	450	1
20	100	25	0	0.5 (+)	1.5	450	1
21	70	20	0	0.75 (+)	1.5	450	2
22	70	25	0	0 (+)	1.5	450	2
23	70	25	0	0.75 (+)	1.5	450	2

(-): The beam focus position under the surface, (+): The beam focus position over the surface

The beam oscillation pattern is line weld figure.

3.5.2 Microstructure examination

3.5.2.1 Sample preparation

Material for microstructure analysis was prepared using standard grinding and polishing methods for both optical and scanning electron microscopy. Prior to grinding, the samples were cut using Abrasivement Blue cutting machine fitted with BUEHLER A80KB & 95-B-2201 cut-off wheel for cutting the stainless steel samples and MetPrep Type T 109920 cut-off wheel for cutting titanium alloy samples. For precision cutting, such as preparation of samples for electron backscatter detection test, a Sturer Secetom-50 with Sturer 10S20 cutting wheel was used. To reveal the microstructure of the stainless steel weld samples following polishing, the samples were etched in a mixture of equal amounts of HCL, Acetic and HNO_3 acids for 20-25 s at room temperature.

3.5.2.2 Optical microscopy observation

Optical light microscopy was performed using a Nikon Eclipse LV150 microscope in order to examine the weld and BM microstructure of the etched samples. The device was equipped with Buehler OmniMet software for the image analysis.

The line intercept method [70, 156, 157] was used to measure the secondary dendrite arm spacing (SDAS) in the FZ in regions near the top, middle and bottom of the weld. The measurement of each sample's SDAS was applied to many micrographs, an example of which is shown in Figure 3.16.

The average austenite grain size in the BM and HAZ was determined according to ASTM standard E112 standard. The volume fraction of delta ferrite was measured using the point counting method as described in ASTM standard E562 [158].
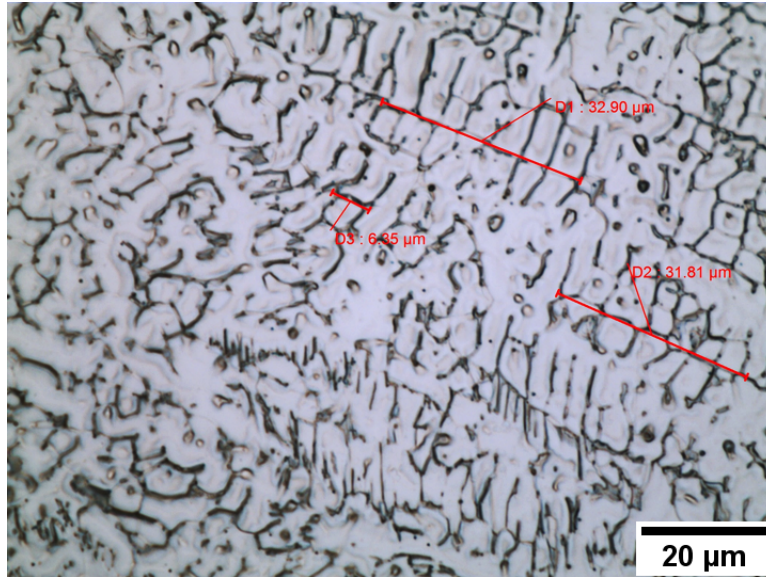
Figure 3.16 Measurements of SDAS.

3.5.2.3 Scanning electron microscopy (SEM)

Scanning electron microscopy was carried out using a field emission gun Inspect F, at an accelerating voltage of 20 kV and spot size of 5 μm, in secondary imagining mode and back scattered mode to observe the microstructural features and fracture surfaces at higher magnification.

3.5.2.4 X-ray energy dispersive spectroscopy (EDS)

To study the chemical composition of the morphological reactions and elements distribution through the weld and HAZ, quantitative EDS analysis was performed using a XL30 electron microscope at accelerating voltage of 20 KV and spot size 5 μm, in secondary imagining mode and back scattered mode to observe the microstructural features. The software used for the analysis was JEOL 6400-INCA. Cobalt standard was used and loaded with each sample to calibrate the software prior to the test.

3.5.2.5 Electron Back Scattered Diffraction (EBSD)

Electron backscatter detection (EBSD) mapping was carried out on the AISI316L-AISI 316L weld to investigate the grains orientation and their impact on the mechanical properties of the weld. The scan was performed using FEI Sirion electron microscope, at 20 KV and 5 μm spot size. The step size was 2 μm to cover a large area in the FZ. The

software used for acquisition was Oxford Instrument HKL Channel 5 Flamenco, and Tango for generating Schmid factor map.

3.5.2.6 X-Ray Diffraction analysis

X-ray diffraction (XRD) analysis was performed to confirm the elements and phases existing in the dissimilar weld region using a Bruker D2 Phaser XRD. The equipment is located at the X-Ray Research Facility (XRF) centre at the University of Sheffield. The scan was carried out on the fractured region of the weld at the Ti-Cu side and on the cross section of the weld at the Cu-stainless steel side. The operating parameters were 30KV voltage and 10mA current. The equipment uses copper tube target with an average λ = 1.54184 Å. The scanning angle (2Theta) was used between 30-80° at 2sec scanning time. Diffrac.EVA V 3.1 software was used to analyse the data.

3.5.3 Mechanical properties examination

3.5.3.1 Micro-hardness test

Vickers hardness maps were taken in a two dimensional grid. For stainless steel to stainless steel weld, a grid with a 0.4 mm spacing covering the FZ, HAZ and part of the BM, was applied, as indicated in Figure 3.17. For stainless steel to titanium weld, a grid with 0.1 mm spacing covering part of the weld with area of 0.5 ×5 mm across the cross section was applied, as shown in Figure 3.18. A 100 gm load and 3-second dwell time were used in the tests.
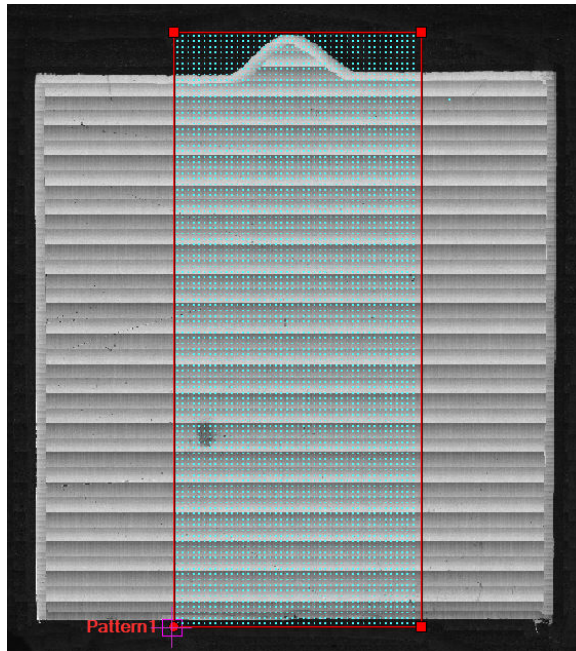
Figure 3.17 Position of the microhardness measurements across a weld cross section in the similar welding.
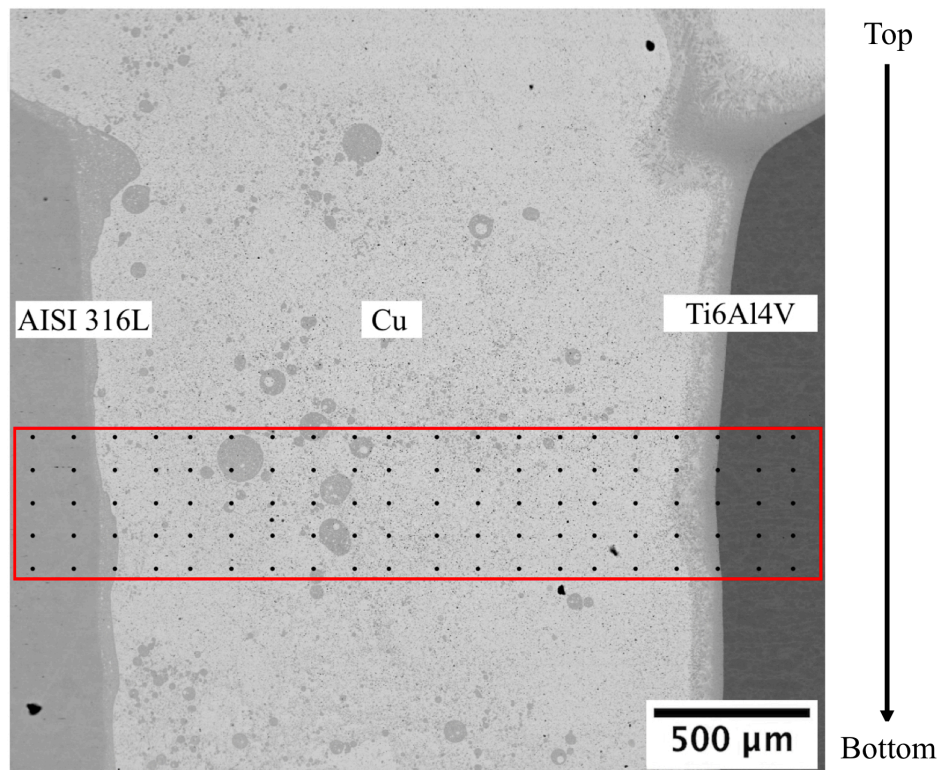
Figure 3.18 Location of the microhardness measurements across a weld cross section in the dissimilar welding.

3.5.3.2 Tensile test

For tensile strength test, the tensile test samples were cut from three locations through the weld thickness (top, middle and bottom), Figure 3.19. The samples were machined according to ASTM E8M-04 guidelines [159], as shown in Figure 3.20. The cutting and machining processes were done by electrical discharge machining (EDM) The tensile tests were performed at room temperature using a Zwick/Roll Z050 machine with a 50 KN load cell and a crosshead speed of 0.1 mm/s.
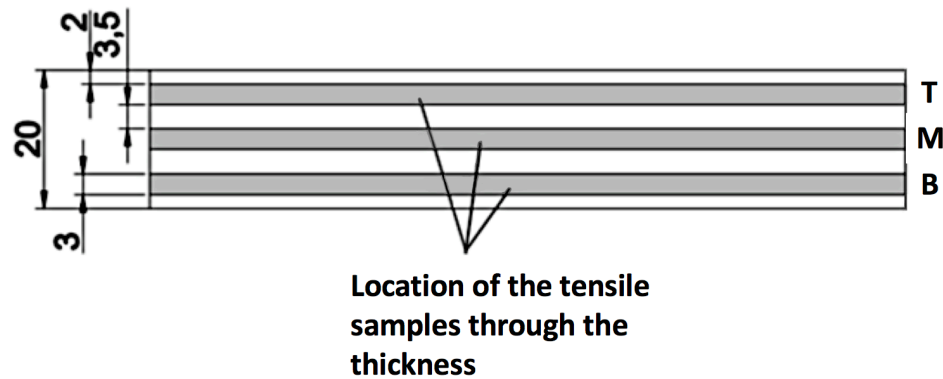
Figure 3.19 The tensile samples position through the thickness (dark area). T= Top, M= Middle, B= Bottom.
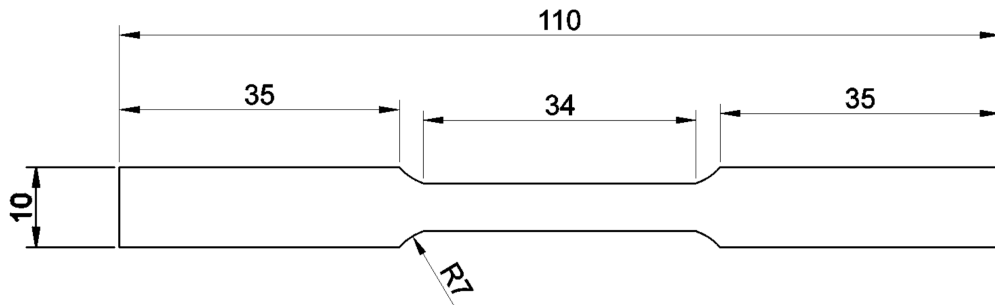
Figure 3.20 Dimensions of the tensile sample used with all the dimensions in mm.

3.5.3.3 Digital image correlation technique

The digital image correlation (DIC) is a measurement technique that can be used to measure the deformation in a test specimen such as strains, rotations and shear, based on analysing the series of images taken during a tensile or compression test [160].

To map the strain variation across the weld and characterise the mechanical behaviour of different weld zones during deformation, the DIC technique was used during tensile testing in this project.

Before the test, the tensile specimens were painted white, then with a random black speckle pattern, as shown in Figure 3.21, to enable data capture by DIC. To attain effective correlation, the pattern must not be repetitive, isotropic or high contrast.

A high-resolution Nikon camera was used and set up with a 105 mm macro lens to take three pictures per second. The pictures were then analysed using the vic-2D software to provide two dimensional strain maps [160-162]. Prior to the test, the camera was placed at the same height position as the sample, using a tripod, and the optical axis was aligned to be normal to the centre of the gauge length with a sharp focus.

10 mm

Figure 3.21 Macrograph of tensile test sample with speckle pattern prior to DIC test.

3.5.3.4 Deformation measurement inside the necking area

To map the deformation development inside the necking region with higher resolution and accuracy and to determine the weakest area in the microstructure, three tensile samples were fully prepared for microscopic examination then loaded to three different forces namely 10 KN, 10.5 KN and 11 KN. The first chosen load (10 KN) represents the minimum force that is required to start the necking in the sample during the tensile test. The samples were then examined with optical microscopy and SEM to investigate the deformed microstructure. 3D optical microscopy, Figure 3.22, was used to measure the height differences inside the necking area to precisely detect the beginning and localization of the necking. A series of images along the FZ were taken and stitched together to obtain precise and statistically meaningful deformation measurement.
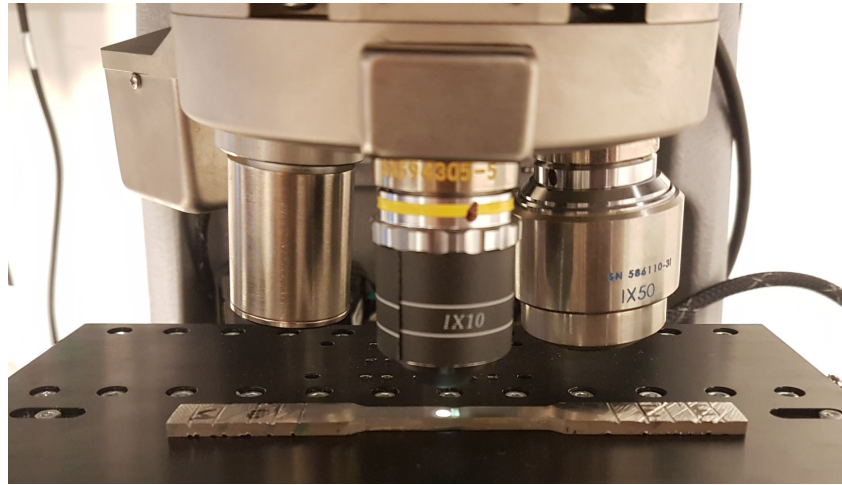
Figure 3.22 3D optical microscopy.

Chapter 4 Similar Welding / Results and Discussion

4.1 Introduction

This chapter presents the results of the optimization and characterisation of the similar stainless steel welds produced with EBW butt joint. The study aims to evaluate the influence of a range of welding parameters i.e. welding current, welding speed and beam focus offset on the microstructure and mechanical properties of the welds. The main goal of this research was understanding the development of the microstructure and the resulting mechanical properties of the weld through 20mm thickness joint.

4.2 Weld visual inspection

The visual test was utilized firstly on the bead on plate trials of plates 1, 2 and 3 to investigate the effect of welding parameters on the weld profile and penetration depth. Each weld bead was evaluated in order to optimize the welding parameters. It was found that the increasing the beam current, decreases the depth to width ratio and causes a lack of penetration in the weld. The excessive heat input that resulted from the high beam current melts high amount of the metal at the top of the workpiece and causes unbalance in the forces inside the keyhole that keep the keyhole open, e.g. molten metal weight higher than vapour pressure and friction forces, and this consequently decreases the depth of the keyhole and the penetration of the weld. An example is given in Figure 4.1where excessive weld bead width and poor penetration can be seen visually and through the cross section of the macrostructure of weld beads, as shown Figure 4.1 (b and c). The beam current and welding speed conditions that produced the best weld penetration and profile are highlighted in Figure 4.2. Cavities and porosities can also be seen in some weld beads in Figure 4.2. These resulted from the unbalance of the forces inside the keyhole that causes some regions in the keyhole to stay not filled with the molten metal after solidification. It was also observed that the electron beam focus offset has an important role in determining the weld profile. Generally, it is always preferred to weld with slight under focus to achieve maximum depth of the FZ with good weld shape [15]. In this study, it was found that using -5 mA focus offset provided the best weld profile, Figure 4.2. The relationship between depth of the FZ (s) and beam spot diameter (d_{FI}) and beam focus offset is shown in Figure 4.3. After determining the optimum welding parameters; beam

power, welding speed and focus offset, the selected parameters were used for butt joints trials. It should be noted that the beam current was increased from 100 (optimum for bead on plate) to 110 mA to achieve full penetration and best weld profile, suggesting a gap in the butt joint.

In Figure 4.4, joints 5 and 7 have the best weld profile since they have more asymmetrical weld shape and best weld penetration according to British Standard BS EN ISO 13919-1:1997.

(a)

(b)   (c)
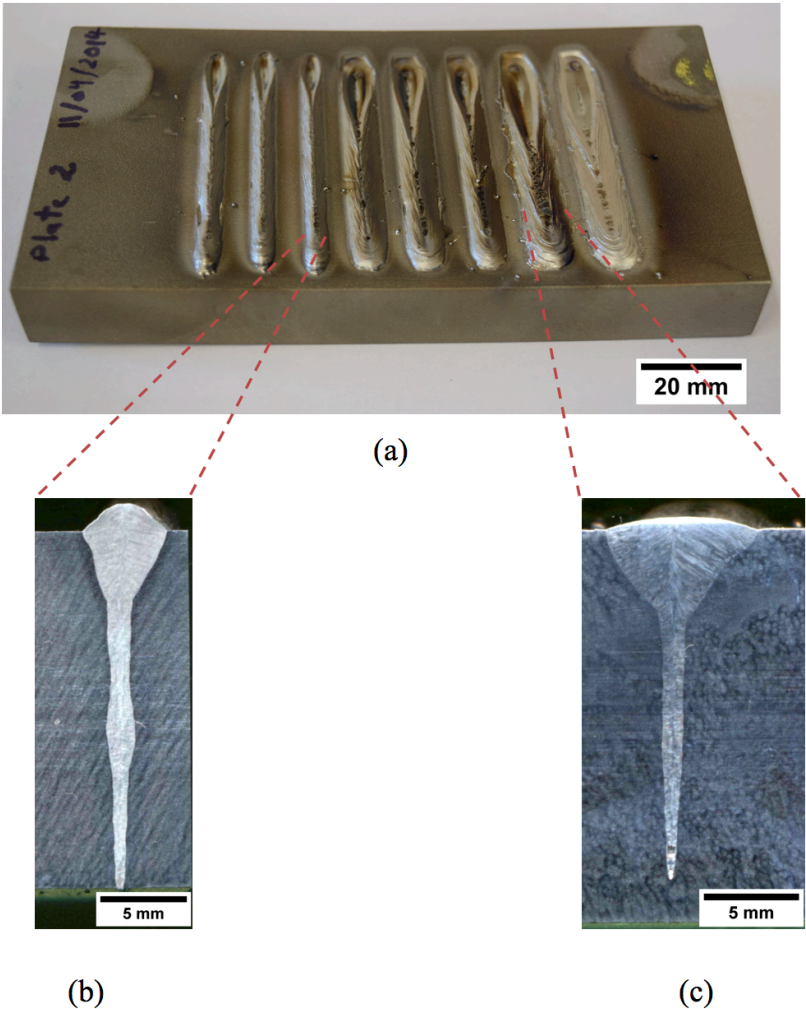
Figure 4.1 The effect of the beam current and welding speed on the weld penetration and profile. (a) Weld beads in plate 2 (b) Cross section of weld Bead 3 with 100mA, 9 mm/s (c) Cross section of weld Bead 7 with 142 mA, 13mm/s.

Line 1: 8 mm/s welding speed, -10 mA focus offset	Line 2: 8 mm/s welding speed, -5 mA focus offset	Line 3: 9 mm/s welding speed, -15 mA focus offset	Line 4: 9 mm/s welding speed, -8 mA focus offset	Line 5: 9 mm/s welding speed, -5 mA focus offset ✔
Line 6: 9 mm/s welding speed, -3 mA focus offset	Line 7: 9 mm/s welding speed, 0 mA focus offset	Line 8: 9 mm/s welding speed, +5 mA focus offset	Line 9: 9 mm/s welding speed, +10 mA focus offset	

Figure 4.2 Plate 3 weld beads cross as a function of focus offset. Beam current = 100 mA, line 5 gives the optimum weld profile and penetration according to the BS EN ISO 13919-1:1997.
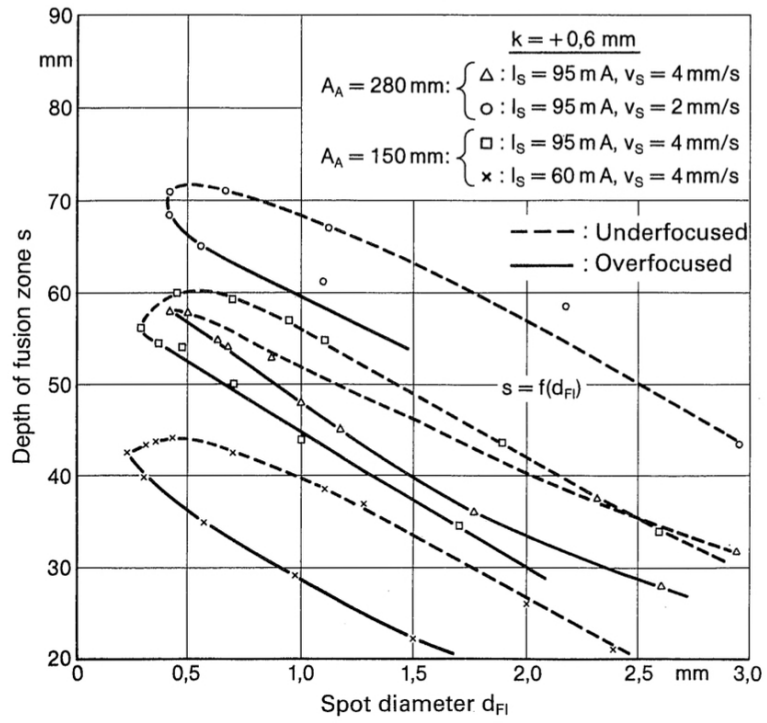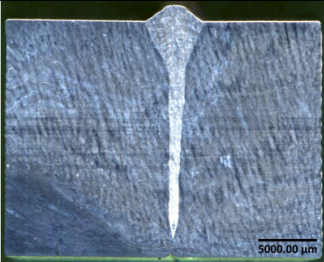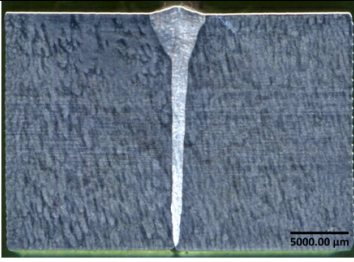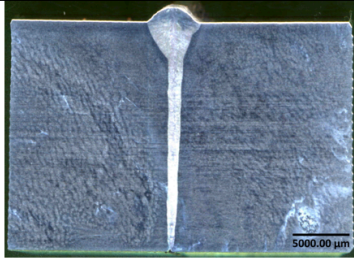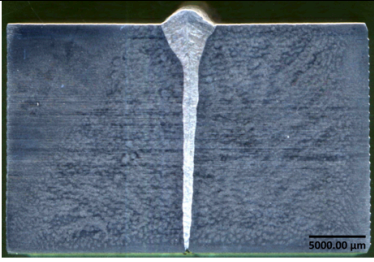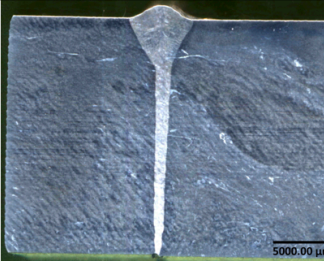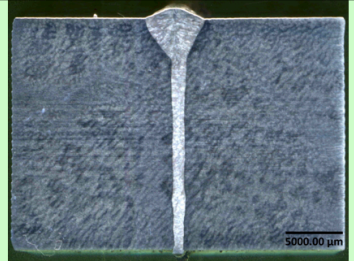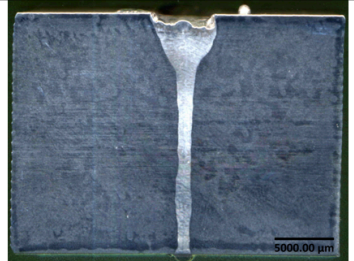
Figure 4.3 Relationship between depth of the FZ and beam spot diameter d_F, K= the vertical distance between the cathode and the control electrode, I_S=beam current, V_S=welding speed [15].

Joint 1: 100 mA beam current, -15 mA focus offset	Joint 2: 100 mA beam current, -10 mA focus offset	Joint 4: 100 mA beam current, -6 mA focus offset	Joint 5: 100 mA beam current, -5 mA focus offset
Joint 6: 110 mA beam current, -15 mA focus offset	Joint 7: 110 mA beam current, -6 mA focus offset ✔	Joint 9: 120 mA beam current, -15 mA focus offset	

The joints welded with repeated welding parameters have been ignored.

Figure 4.4 Macrograph of butt joint trials. 9 mm/s welding speed was used for all the joints.

4.3 Weld radiographic examination

The results of the radiographic test, for the butt joint trials revealed some welding defects in each joint. For the joints 1 and 7, undercut defect was detected. However, the weld defect was in a limited area especially in the joint 7. Lack of penetration was detected in the joints 2, 3 and 4, Figure 4.6. This could be due to using low heat input in these joints. In joint 8, there were some porosity and voids, Figure 4.7, these could be resulted from the high beam current with relatively low welding speed, which caused unstable movement and solidification of the molten metal inside the keyhole.

Figure 4.5 Undercut (red bounded areas) in joints 1 on the left and 7 on the right.
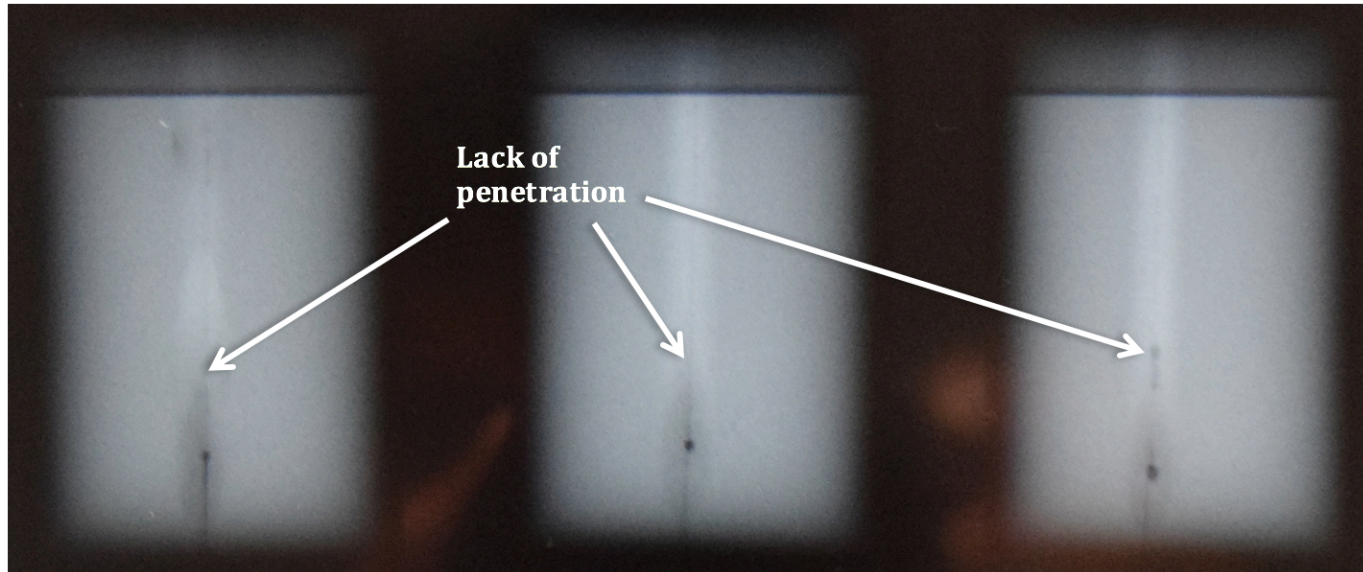
Figure 4.6 Lack of penetration in the joints 2, 3 and 4 from right to left respectively.
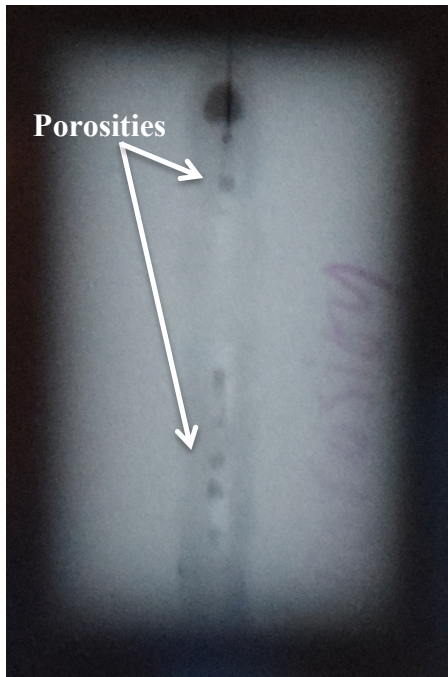
Figure 4.7 Porosities and cavities in joint 8.

4.4 The application of the constitutional diagrams and ferrite content measurements

Measuring the ferrite content of the weld metal is very important since it gives an indication of weld solidification behaviour and crack susceptibility [163]. As discussed previously, constitutional diagrams such as the Suutala and WRC-1992 diagrams are not sufficient for use with a high speed welding process, such as electron beam welding, since rapid solidification and shifting in solidification behaviour may occur. Under such conditions, these diagrams may lack the accuracy to predict the ferrite content and solidification mode [164]. In this study, more than one method and diagram was applied to predict ferrite number and solidification behaviour of the alloy.

A diagram based on WRC-1992, Figure 4.8, showing the transition from primary austenite to primary ferrite solidification under rapid solidification conditions, was used [95]. According to this diagram, since this steel has a $(Cr_{eq}/Ni_{eq})_{WRC} = 1.44$ and $(S+P) = 0.0272$, the weld for this chemical composition could be susceptible to cracking if it solidified as primary austenite.

A microstructural map, Figure 4.9, proposed by Lippold was also used [40]. This diagram combines the influence of composition and solidification rate. According to this

diagram, and if the solidification rate is equal to the welding speed, the solidification mode for this stainless steel could be FA, AF or A mode, depending on the solidification rate. This behaviour was seen in the root of W1, which underwent lack of penetration due to the very high cooling rate resulted from low heat input in this weld.

In respect of metallographic measurement techniques, the point counting method was also performed to calculate the volume percent of ferrite phase, which was less than 1.8%.
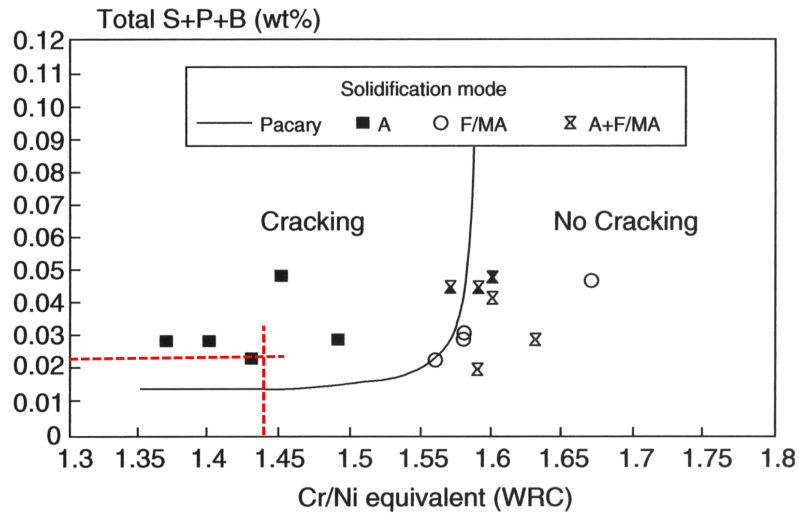
Figure 4.8 Modified-Suutala diagram. Solid symbols, cracking, open symbols, no cracking. Adapted from [40].
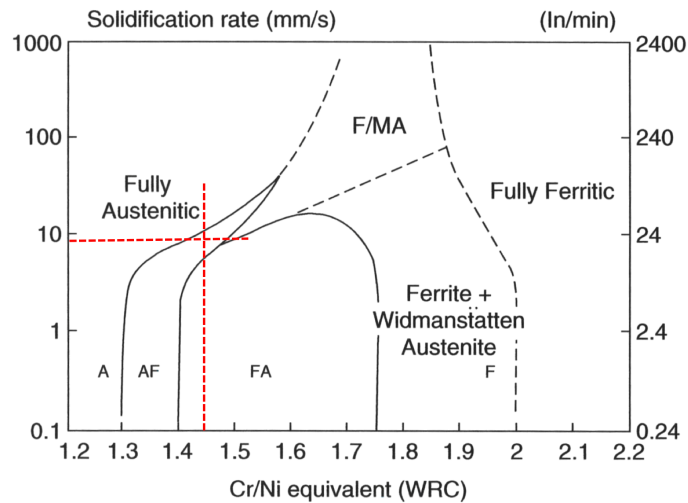
Figure 4.9 Effect of solidification rate on the microstructure of Fe-Cr-Ni alloy. Adapted from [40]

97

4.5 Macro and microstructure of the AISI 316L stainless steel weld

Like all high temperature low pressure welding processes, the macrostructure of the welds contained regions of BM, HAZ and FZ. Figure 4.10 (a) through (c) are macrographs of transverse section from the welds. The typical nail shape of the FZ can be observed for the three welds. A clear difference in weld penetration can be noticed between the welds. W1 in Figure 4.10 (a) does not exhibit full penetration and has an asymmetrical weld bead shape at the top of the FZ. Full penetration with symmetrical FZ shape was obtained in W2, Figure 4.10 (b) and excessive penetration was detected with more molten metal in the root cap and an asymmetrical weld bead in the top part of the FZ in W3, Figure 4.10 (c). All of the visual inspections were done according to the British Standard [165]. A suggestion for the irregular FZ shape is that the use of insufficient weld current in W1 and excessive beam current in weld W3 affected the heat flow and fluid flow i.e. producing an unsteady fluid flow in the weld pool. This is due to the unbalanced opposing forces generated inside the weld pool e.g. the surface tension and hydrostatic pressure that influence the heat transfer, which has been shown to affect the FZ shape and properties of the weld [15, 166]. This effect can be seen in the hardness distribution maps, Figure 4.11. This figure shows asymmetrical hardness distribution in the HAZ in the W1 and W3. Additionally, it shows that the FZ has the lowest hardness compared to the HAZ and BM and how the low hardness areas emulate the FZ shape in the whole weld.

(a) **(b)** **(c)**
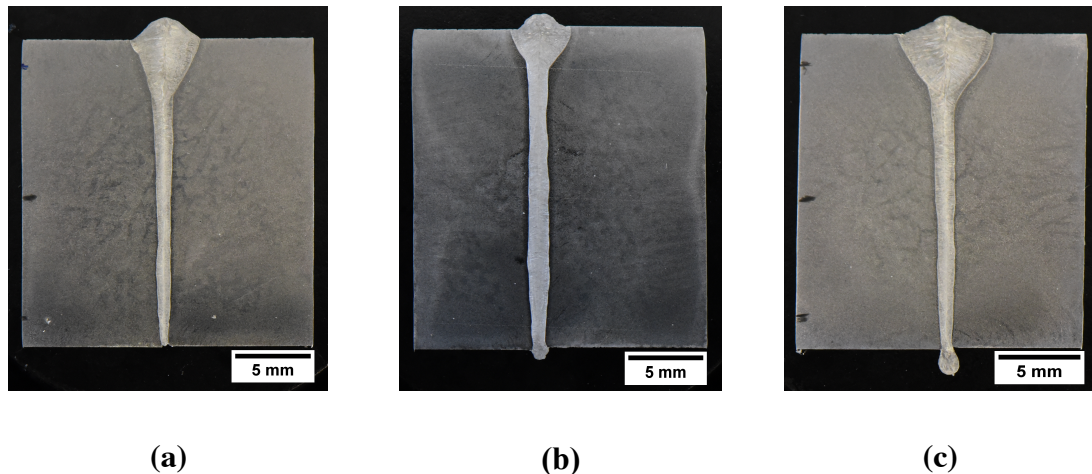
Figure 4.10 Macrstructure of the welds (a) W1, 100 mA beam current (b) W2, 110 mA beam current (c) W3, 120 mA beam current. 9 mm/s welding speed and -5 mA focus offset were used for the three welds.
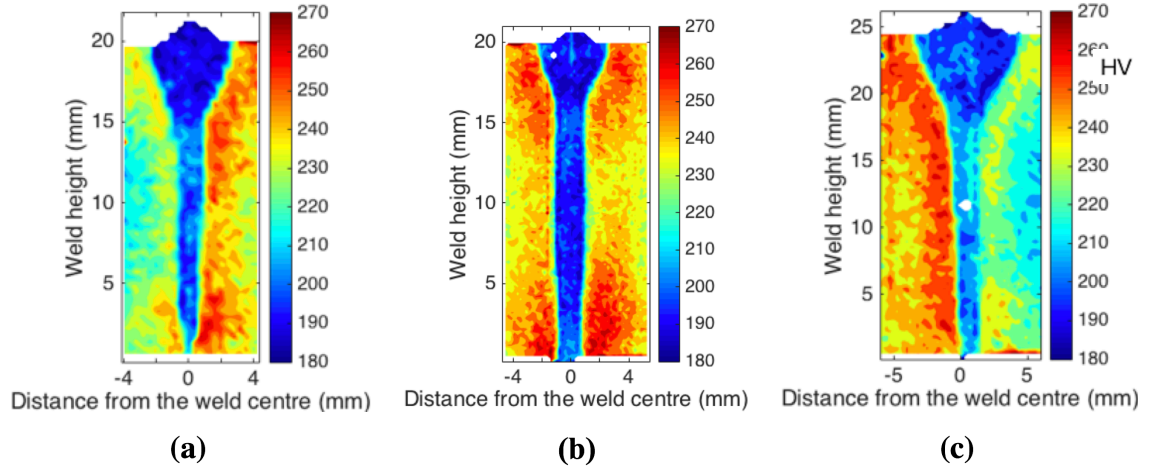
Figure 4.11 Microhardness measurements across the weld for (a) W1, 100 mA beam current (b) W2, 110 mA beam current (c) W3, 120 mA beam current. 9mm/s welding speed and -5 mA focus offset were used for the three welds.

Figures 4.12, 4.13 and 4.14 show optical macro and micrographs of W1, W2 and W3 respectively. The higher magnification optical micrographs are presented in Figures 4.12, 4.13 and 4.14 (b) through (g). Figures 4.12, 4.13 and 4.14 (b) show the microstructure of the top part of the FZ, which consists of columnar and axial dendritic δ-ferrite structure in an austenite matrix. The columnar grains grew in a direction perpendicular to the weld boundary and the axial grains grew in the welding direction, following the maximum temperature gradient and heat extraction path [10]. The columnar grains microstructure is revealed with higher magnification in Figures 4.12, 4.13 and 4.14 (d).

Figures 4.12, 4.13 and 4.14 (c) illustrate the microstructure at the middle of the FZ. The structure in this area contains both columnar and equiaxed δ-ferrite morphologies as in W1 or columnar δ-ferrite grains only in W2 and W3. Higher magnification for these microstructures are shown in Figures 4.12, 4.13 and 4.14 (d) and (e). The equiaxed structure is located at the weld centre and governed by G:R ratio, where G is the thermal gradient and R is the solidification rate. The high solidification rate at the centre of the electron beam weld facilitates the formation of the equiaxed grains along the weld centreline [36, 68, 167-169]. It was found that the columnar dendrite in the FZ microstructure exists in a vermicular or lathy shape depending on the cooling rate, as can be seen in Figure 4.15; the high velocity produces a tightly spaced lathy ferrite due to the restricted diffusion during the phase transformation[170-172].

Figures 4.12, 4.13 and 4.14 (f) and (g) show the microstructure at the bottom of the welds. A microstructure consists of a combination of dendritic and cellular austenite was

observed in the root of W1 weld, where lack of penetration occurred. A cellular austenite structure was detected in the weld interface and the dendritic existed in the weld centre due to the high G:R ratio at the fusion boundary. The presence of the primary and fully austenite structure is due to the very high cooling rate at this region, which may change the solidification behaviour from FA to AF or A mode via massive transformation [39, 77]. In W2 and W3, a combination of columnar dendrite and equiaxed structure has occurred in the bottom part. The high solidification rate in this area is the reason for the existence of the equiaxed structure.

Comparing the through-thickness microstructure of the three welds, the top part of the FZ
consisted of axial and columnar grains structure due to the relatively slow cooling rate at this area. With higher cooling rate at the middle and the bottom parts of the FZ, the grain structure became either columnar or columnar equiaxed grains, the faster the cooling rate, the more likely to the equiaxed structure to form.

It is worth mentioning that a boundary can be seen at the centre of the FZ, this boundary is the weld solidification centreline called "Parting" and resulted from an intersection of groups of sub-grains that have different growth orientation e.g. columnar grains with opposite grain growth and columnar-axial grains or from an intersection between two different grains structure i.e. columnar and equiaxed grains [68, 173-175]. The parting is a favorite location to form the continuous liquid film of low melting temperature impurities and brittle phases that cause poor mechanical properties and reduction in corrosion resistance. Thus, it is considered the weakest part of the weld, especially when the weld is exposed to sufficient transverse stresses [10, 60]. The parting appears in two lines and separates three different oriented columnar grains at the upper parts of the FZ, Figures 4.12, 4.13 and 4.14 (b). In the lower parts of the FZ, where the molten metal is far from the heat source and the solidification rate is higher, the parting appears as either one line that separates two different oriented columnar grains, as shown in the middle part of W2 and W3, Figures 4.13 and 4.14 (c) and (e) or as two lines between columnar and equiaxed grains, Figure 4.12 (c) and Figures 4.13 and 4.14 (f) and (g). Schematic figures showing parting types are shown in Figure 4.16. The presence of two types of weld centreline boundary occurred due to high thickness FZ, since there is a difference in thermal gradient and growth rate along the weld thickness.

Generally, the formation of the ferrite-austenite microstructure could have resulted from the non-equilibrium solidification due to the very high cooling rate during EBW that can lead to incomplete ferrite to austenite transformation [176].

100
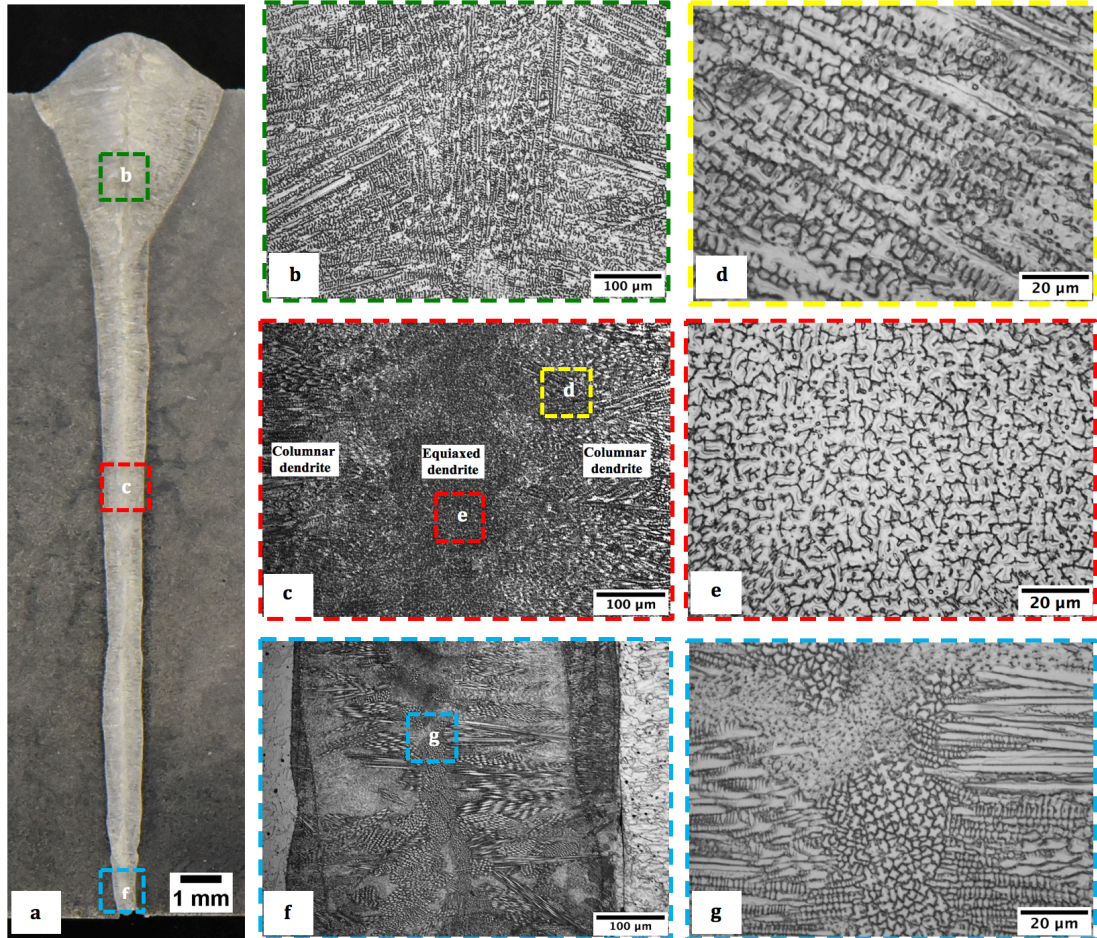
Figure 4.12 Macro and microstructure of W1 (a) Macrostructure of the FZ (b) columnar dendritic structure at the top part of the FZ (c) columnar and equiaxed microstructure at the middle part of the FZ (d) columnar dendritic structure at higher magnification (e) equiaxed dendritic structure at higher magnification (f) primary austenite microstructure at the bottom edge of the FZ (g) primary austenite microstructure at higher magnification.
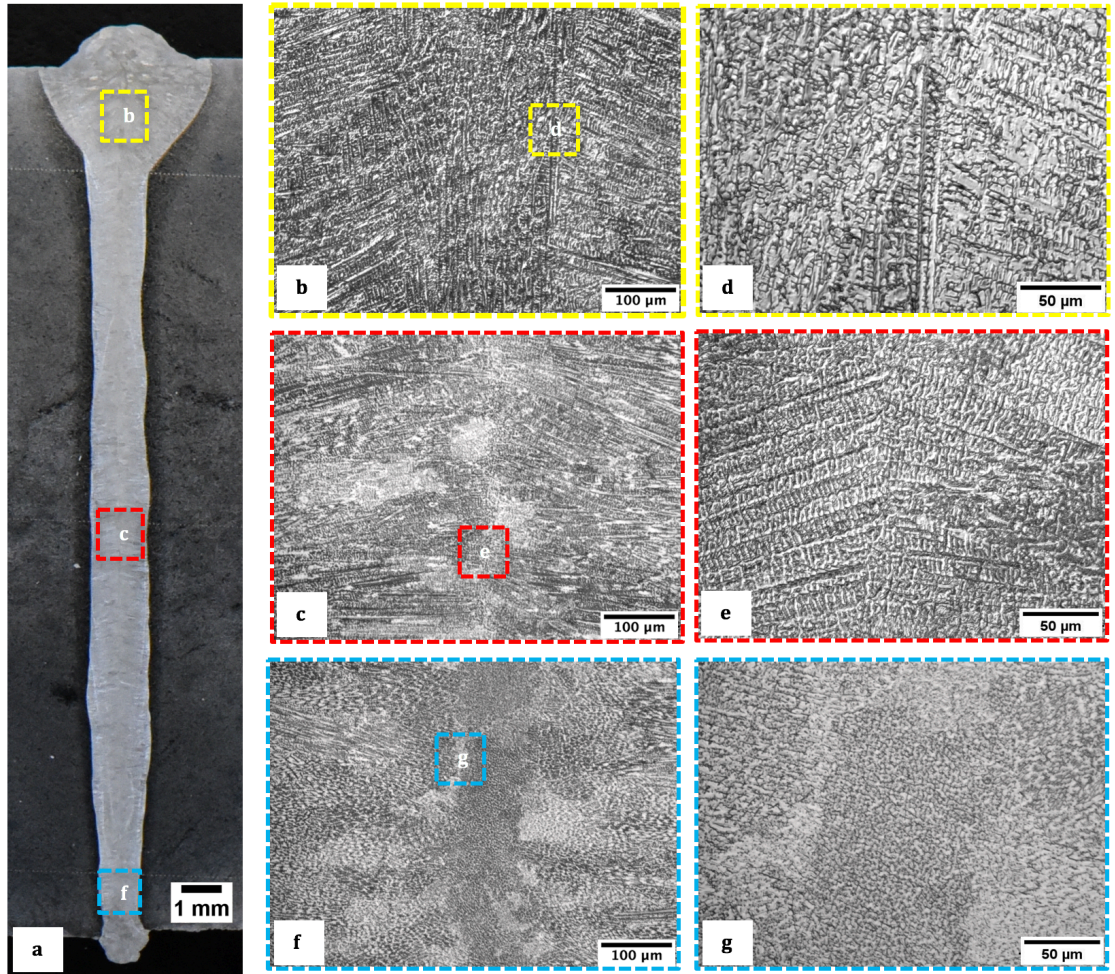
Figure 4.13 Macro and microstructure of the W2 (a) Macrostructure of the FZ (b) columnar dendritic structure at the top part of the FZ (c) columnar dendritic structure at the middle part of the FZ (d) weld solidification centreline at the top part of the FZ (e) weld solidification centreline at the middle of the FZ (f) weld microstructure at the bottom edge of the FZ (g) fine equiaxed structure at the bottom edge of the FZ.
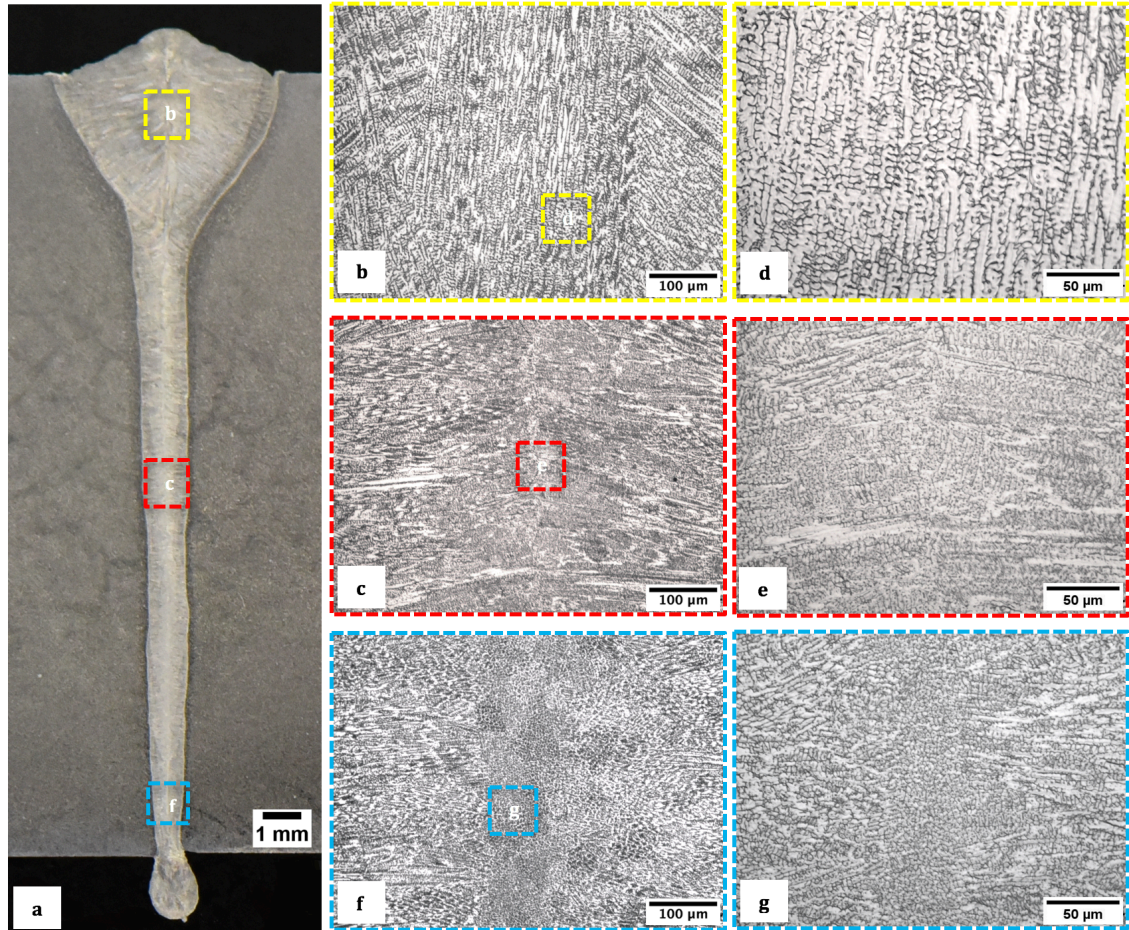
Figure 4.14 Macro and microstructure of the W3 (a) Macrostructure of the FZ (b) columnar dendritic structure at the top part of the FZ (c) columnar dendritic structure at the middle part of the FZ (d) columnar dendritic structure at the top part of the FZ at higher magnification (e) weld solidification centreline at the middle of the FZ (f) weld microstructure at the bottom edge of the FZ (g) fine equiaxed and columnar structure at the bottom edge of the FZ.
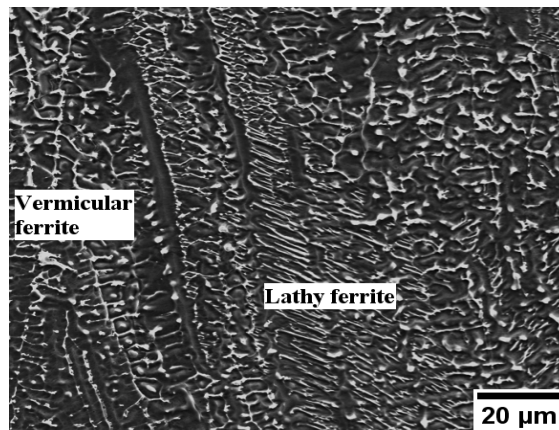
Figure 4.15 SEM micrograph of lathy and vermicular ferrite morphologies.

103
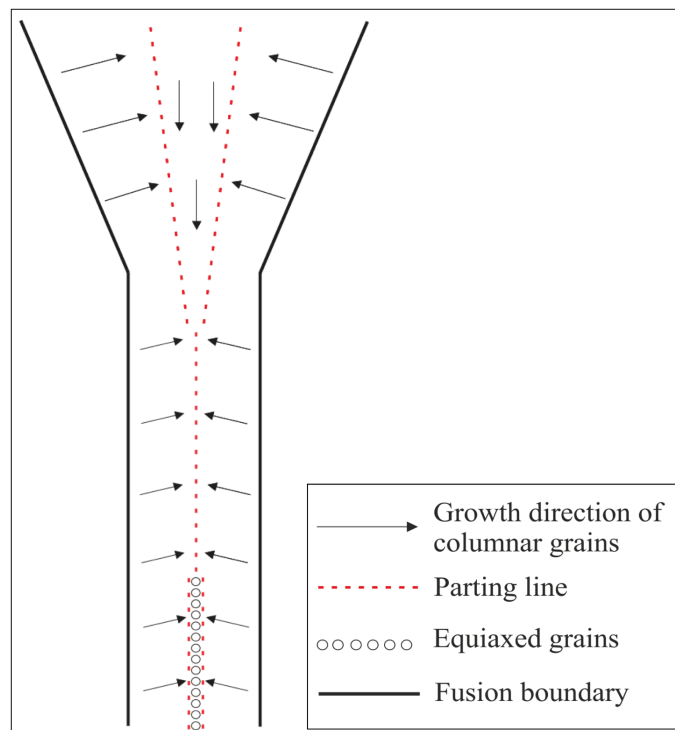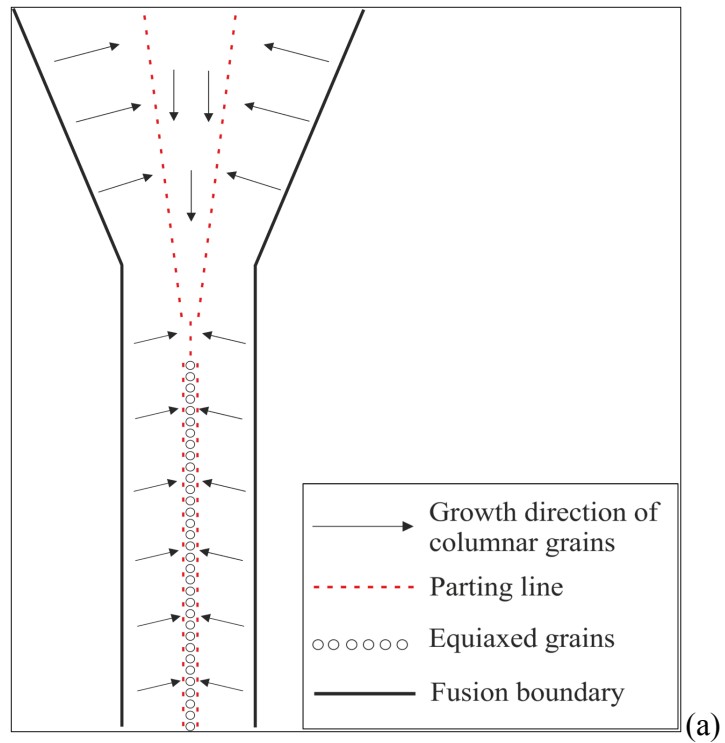
Figure 4.16 Types of parting feature (a) in FZ of W1 (b) in FZ of W2 and W3.

The BM microstructure, Figure 4.17, of the 316L stainless steel consisted of equiaxed austenite grains with small amounts of residual δ-ferrite, aligned along the rolling direction, and some equiaxed MnS inclusions according to the EDS analysis. The average grain size of austenite for the three welds is illustrated in Table 4.1. The microstructure of the HAZ for the all welds was similar to the BM microstructure with some grain growth in the area near the fusion boundary, as shown in Figure 4.18. The average grain size of the austenite grains that underwent grain growth is presented in Table 4.1.
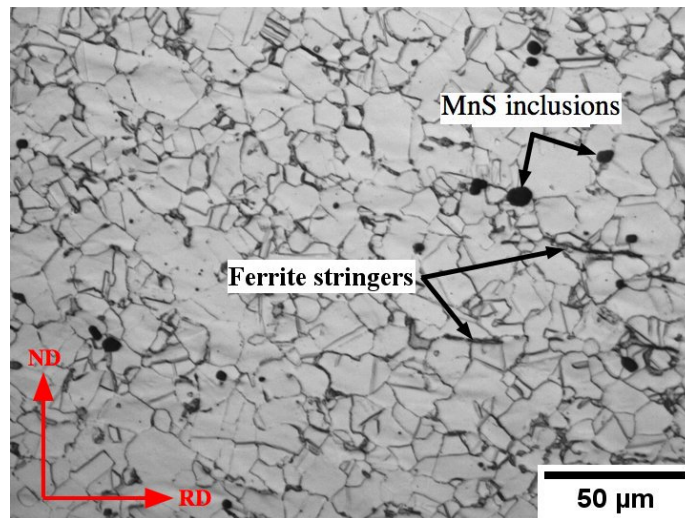
Figure 4.17 Optical micrograph of 316Lstainless steel BM. (ND) is the normal direction.
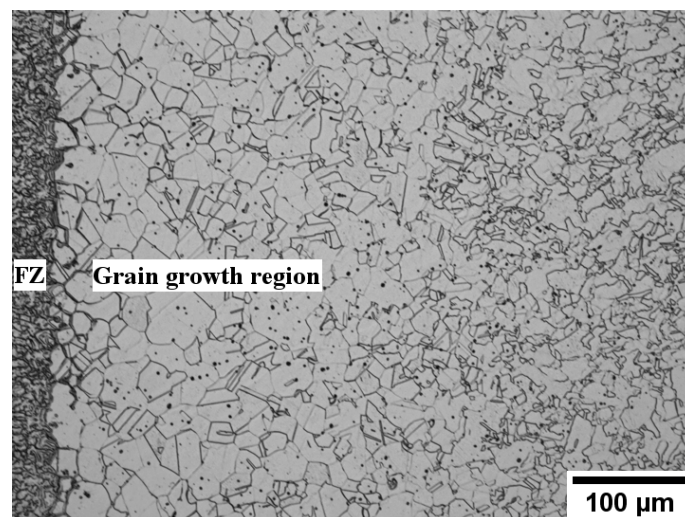
Figure 4.18 The HAZ microstructure.

105

Table 4.1 Grain size of the BM and the HAZ through the weld thickness

Weld Number	Position	Grain size (µm)	
		BM	HAZ
1	T	7.2	21.5
1	M	8.9	14.2
1	B	9.3	9.5
2	T	7.5	21
2	M	7.3	17
2	B	7.6	17.6
3	T	7.8	25.4
3	M	10	21.8
3	B	8.9	17.2

- T=Top, M=-Middle, B=Bottom

4.6 EDS analysis

The EDS analysis was performed on W1 and W2 for the following zones:

- BM and HAZ: To analyse the black inclusion in the BM and HAZ inclusions.
- FZ: 1. To identify any change in the metal chemistry in the weld centreline.
  2. To identify the dendrite and matrix phases structure chemistry.

In the BM and HAZ, globular and randomly distributed inclusions were found throughout the structure, the EDS analysis shows these inclusions are MnS, by showing higher amounts of sulfur and manganese in the inclusions area, Figure 4.19. Manganese is usually added to the steel during the production process to prevent the formation of FeS, which is less thermodynamically stable and has lower melting point than MnS and cause poor mechanical properties and corrosion resistance [177, 178].

In the FZ, many EDS analyses were applied across the weld zone, an example is shown in Figure 4.20, to identify any segregation of alloying elements in the weld centreline, since the centreline is the weakest area in the weld. The results show no segregation in the parting region at the weld centreline.

The dendritic structure was analysed with EDS, the dendrite showed higher amounts of Cr and Mo and Si, which are ferrite stabilizer elements. This confirms that the dendritic structure in the FZ is ferrite phase, Figure 4.21.

Spectrum	C	Si	S	Cr	Mn	Fe	Ni	Mo	Total
Spectrum 1	2.69	0	1.12	19.7	4.68	64.21	6.81	0.8	100
Spectrum 2	3.2	0.64	0	17.29	1.47	65.07	9.93	2.41	100
Spectrum 3	3.35	0	0	17.34	1.57	65.44	9.91	2.49	100
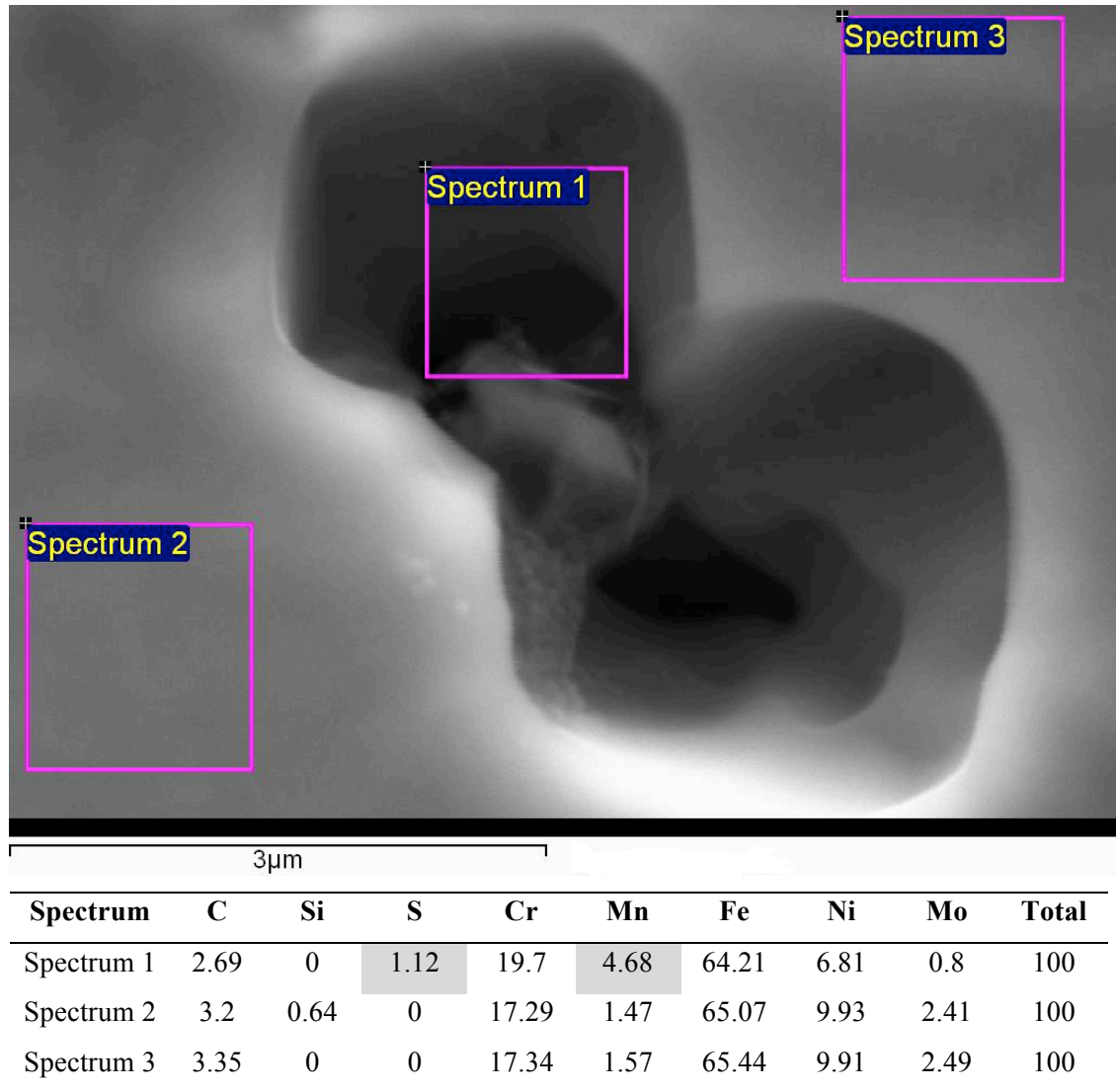
Figure 4.19 EDS analysis of the MnS inclusions.
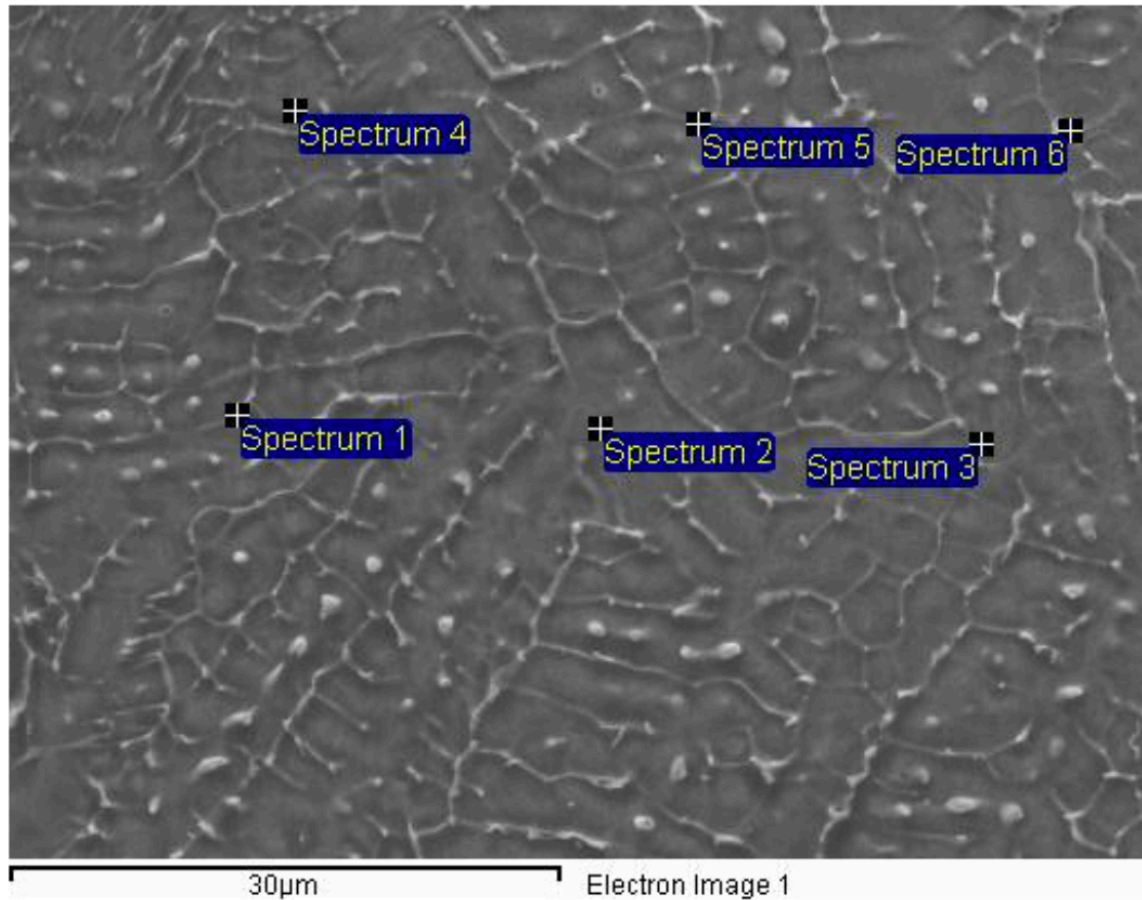
Spectrum	Si	Cr	Mn	Fe	Co	Ni	Cu	Mo	Total
Spectrum 1	0.56	19.31	1.35	67.24	0.36	7.47	0.51	3.21	100.00
Spectrum 2	0.57	17.46	1.44	67.01	0.64	9.94	0.46	2.48	100
Spectrum 3	0.64	17.30	1.47	67.34	0.60	9.93	0.48	2.24	100
Spectrum 4	0.52	17.40	1.41	67.47	0.39	10.16	0.47	2.18	100
Spectrum 5	0.63	17.35	1.44	67.08	0.56	10.06	0.38	2.49	100
Spectrum 6	0.54	17.66	1.17	68.41	0.47	9.23	0.33	2.19	100

Figure 4.20 EDS analysis of the weld centreline.

Figure 4.21 EDS analysis of the dendritic structure in the FZ.
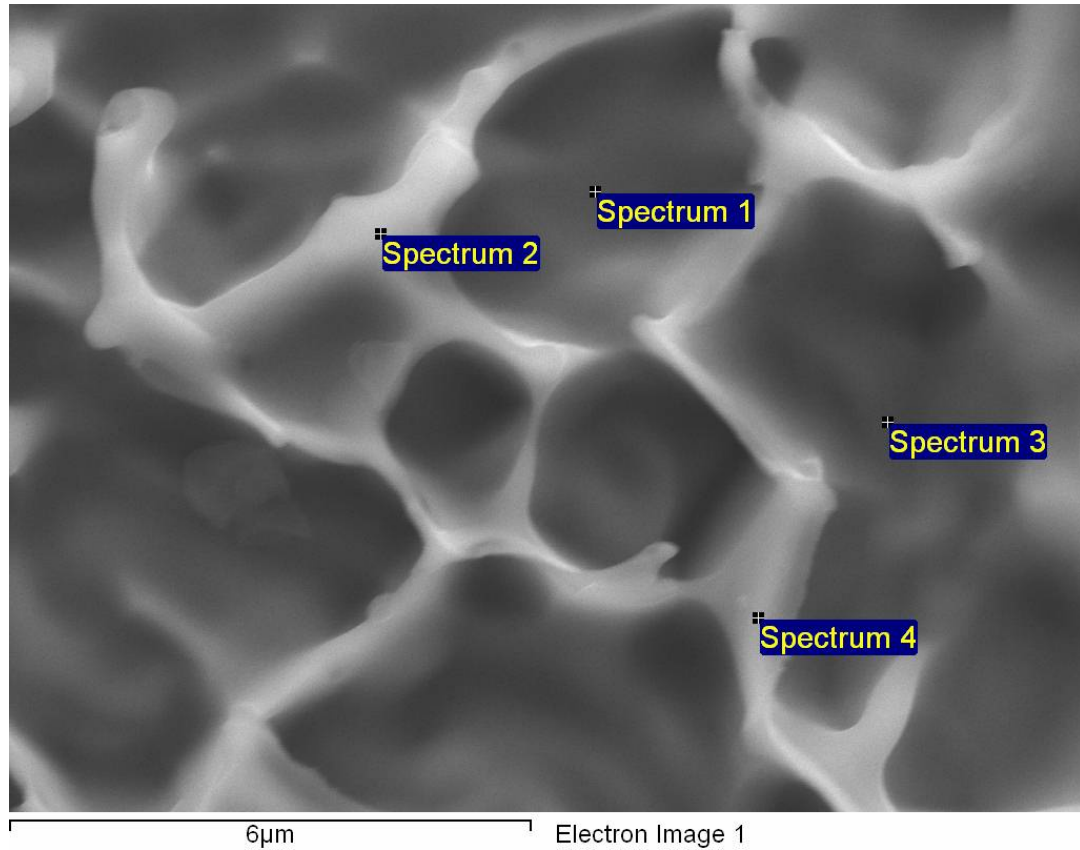
Spectrum	Si	P	Cr	Mn	Fe	Ni	Cu	Mo	Total
Spectrum 1	0.41	0	17.89	1.43	68.5	9.41	0.38	1.97	100
Spectrum 2	0.66	0.11	19.56	1.43	66.76	7.93	0.52	3.04	100
Spectrum 3	0.49	0	17.83	1.65	67.47	9.99	0.62	1.98	100
Spectrum 4	0.9	0.06	18.8	1.52	66.15	8.76	0.41	3.4	100

4.7 SDAS calculations and cooling rate calculation

SDAS was measured across and through the FZ thickness. Figure 4.22 (a, b and c) show that the SDAS decreased towards the centre of the FZ and decreased towards the weld bottom. This change in SDAS could be attributed to the effect of heat input and cooling rate across the weld. The high solidification rate at the weld bead centre and the bottom regions of the weld, produces fine dendrites since there is insufficient time for the

dendrites to remelt, consequently the spacing between the dendrite arms decreases.

Depending on SDAS, the cooling rate across the austenitic stainless steel weld can be predicted using the following formula [179-182].

$$\lambda_2 = 25(\varepsilon)^{-0.28} \qquad\qquad (4.1)$$

Where λ is SDAS and ε is the cooling rate. 25 is a coefficient and -0.28 is an exponent, both values depend on the alloy system. This formula was used by Elmer and Eager [39] to calculate the cooling rates in electron beam melts for austenitic stainless steel alloys. The formula confirms the relationship between cooling rate and the SDAS, Figure 4.23.

4.8 Mechanical properties

4.8.1 Hardness properties

Figure 4.11 (a, b and c) show the Vickers microhardness distribution 2D maps of the W1, W2 and W3, respectively. These figures reveal that the microhardness increases from 180-210 VHN in the FZ to 220-260VHN in the HAZ and BM. The highest hardness appeared at the HAZ in all the welds. The increment in the microhardness can be attributed to the high residual stresses formed after welding in the HAZ, due to the high temperature gradient [183]. The fine grain structure in the part of HAZ next to the BM can also enhance the hardness property [184]. Along the HAZ parallel to the fusion boundary, the hardness slightly decreased at the centre, as shown in the hardness maps. This could have resulted from the low cooling rate in this area compared to the top and the bottom, i.e. the heat sink only through the metal body in this area [184]. The maps also reveal that the FZ of W2 was slightly softer than W1 and W3 at the top and middle parts.

Through the FZ thickness, the microhardness increased towards the root of the weld. This can be mainly linked to SDAS, which decreases towards the bottom of the FZ, Figure 4.24, which means high volumetric fraction of δ-ferrite at the middle and bottom parts of the weld, the small spacing between the secondary dendrites enhances the hardness of the weld [86, 170, 185]. It can be seen that the hardness map of the optimum sample (W2) is more symmetrical than W1 and W3. The reason could be the use of relatively poor welding parameters in W1 and W3, i.e. insufficient or excessive welding power, which affected the fluid flow and heat flow and consequently the properties of the weld, as previously discussed.
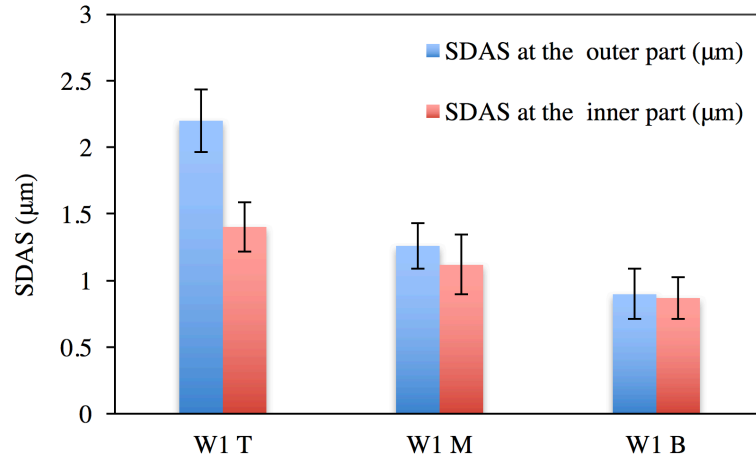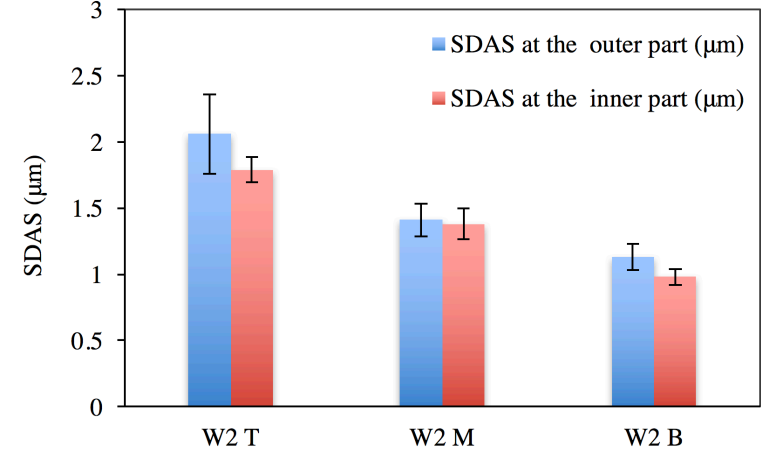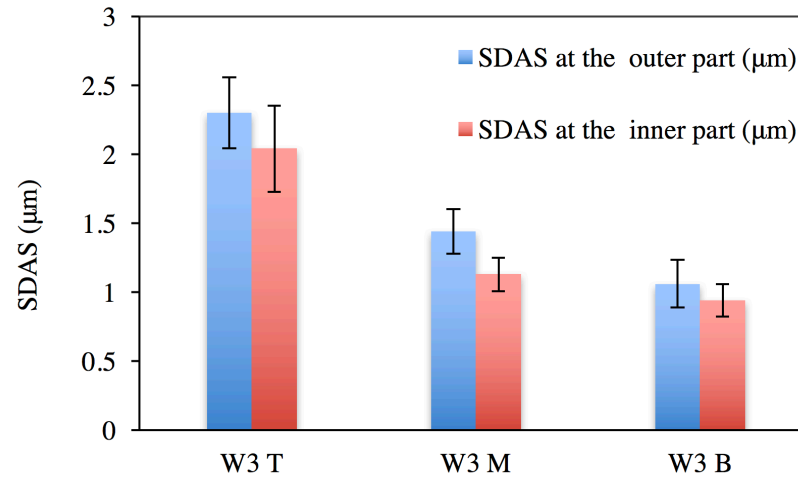
Figure 4.22 SDAS measurement (a) W1 (b) W2 (c) W3.T=Top, M= Middle and B=Bottom.
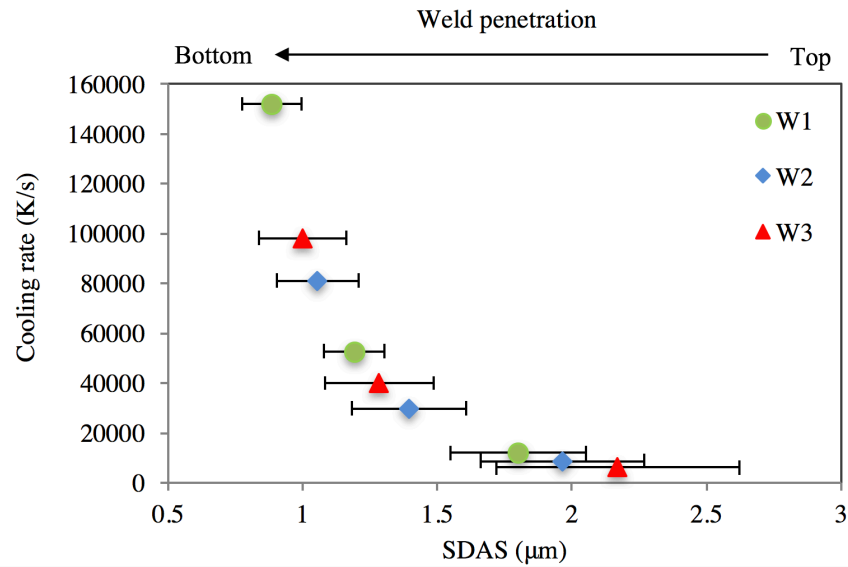
Figure 4.23 SDAS through the weld thickness as a function of cooling rate.

4.8.2 Tensile properties

The weld and BM tensile samples were loaded until fracture to determine and evaluate the joint strength and performance at room temperature. The weld tested samples fractured in the FZ, and the BM tested samples broke at the middle of the gauge length. The stress-strain curves, Figure 4.25, demonstrate a large plastic deformation and high ductility in the test samples. However, the weld samples were weaker than both the HAZ and BM, which is in line with hardness data. By accident, some samples were prepared in the way that the FZ located out of the area of maximum strain at the centre of the gauge length. Yet, the failure still occurred at centre of the FZ at the parting region leading to the conclusion that this area is the weakest part of the weld.

The yield strength YS and ultimate tensile strength UTS were calculated, Figures 26 and 27 respectively. The maximum YS was 511 MPa and the UTS was 652 MPa for the weld samples. In the BM samples, the maximum YS and UTS were slightly higher with 560 MPa and 700 MPa respectively.

The total true strain to failure was measured for each sample and the strain distribution maps were obtained using the DIC technique, Figure 4.28 to 39 (a, b and c). The strain maps verified that the maximum strain and the final fracture took place in the FZ. The reason for the fracture occurring in this region is that the relatively soft FZ, surrounded by hard HAZ and BM, led to a larger deformation in the FZ than in the HAZ and the BM. This effect was compounded by the location of the weld centreline boundary, which is considered the weakest part of the weld [173, 174, 183].

112
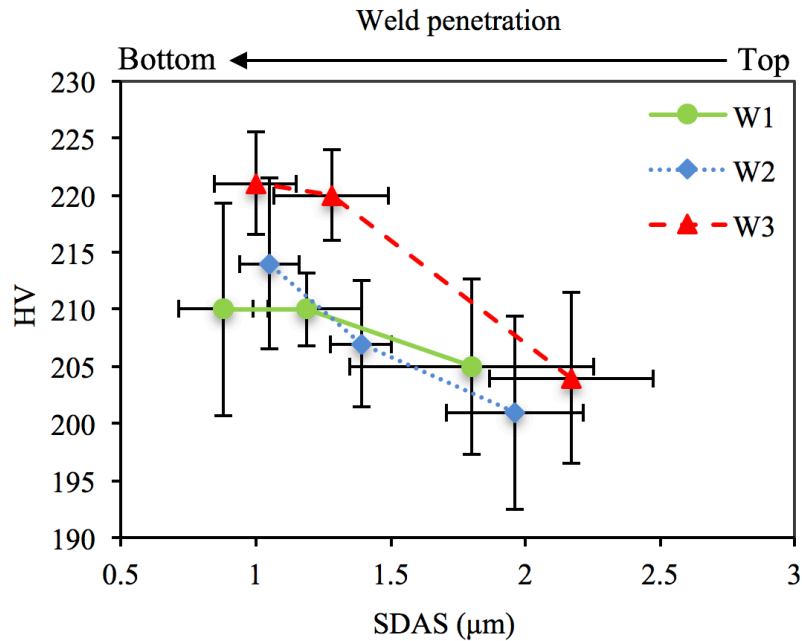
Figure 4.24 The average microhardness of the weld as a function of SDAS and weld penetration.

The strain behavior of BM tensile sample is different from the weld sample as can be seen in example shown in Figure 4.40. In the weld samples, the stain concentrates at the weld zone and the necking takes place at the early stages of the plastic deformation during the tensile test. While for the BM, the necking occurred at the final stages after the maximum load is reached in the test.

A detailed height difference map using 3D optical microscopy, was taken inside the necking area in the FZ, Figure 4.41 (a, b and c), to detect the largest deformed part of the microstructure and to determine precisely the localization of the necking. This was undertaken by measuring the height differences along the necking region. The area with the red colour in the map represents the undeformed or slightly deformed parts and consequently, the highest part of the test sample. While the blue coloured area represents the part that underwent the largest deformation and thus the lowest part of test sample. It was observed that the larger amount of plastic deformation is localized in the parting area. The results of the 3D optical microscopy confirmed that the parting was the softest part in the FZ since the deformation begins and localizes at the interfaces between groups of sub-grains that have different growth orientation as illustrated in Figure 4.41 (a, b and c
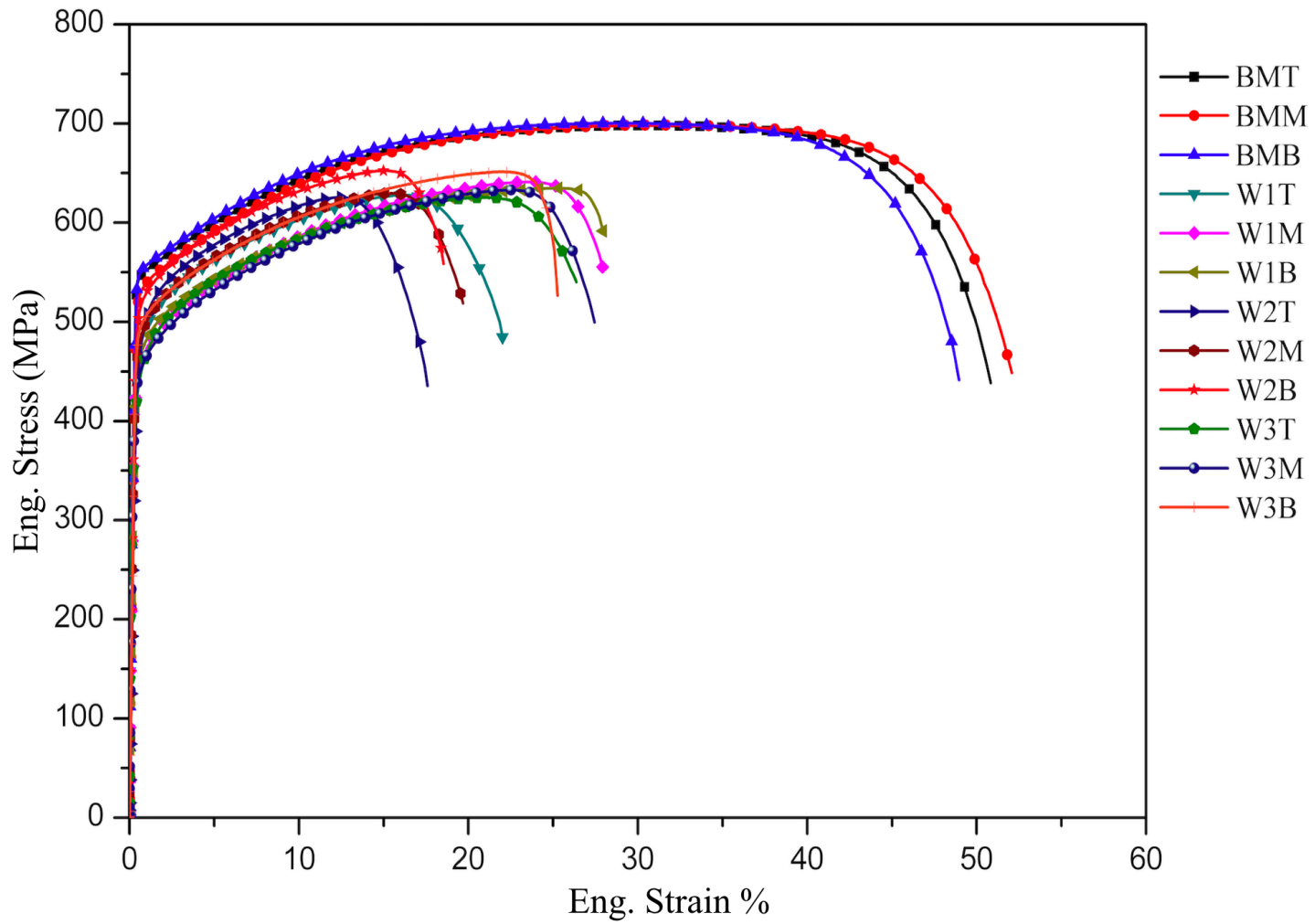
Figure 4.25 Tensile stress-strain curves of the transverse weld and BM samples.
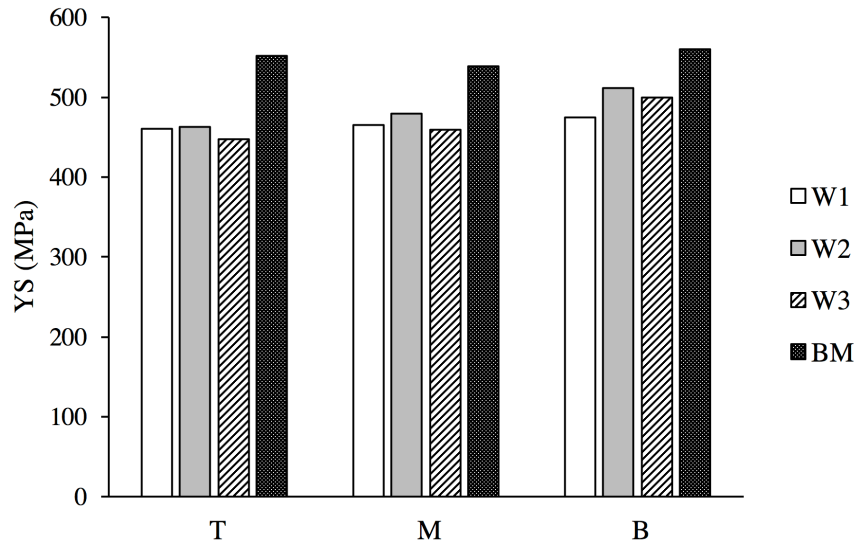
Figure 4.26 YS for the BM and transverse tensile samples.
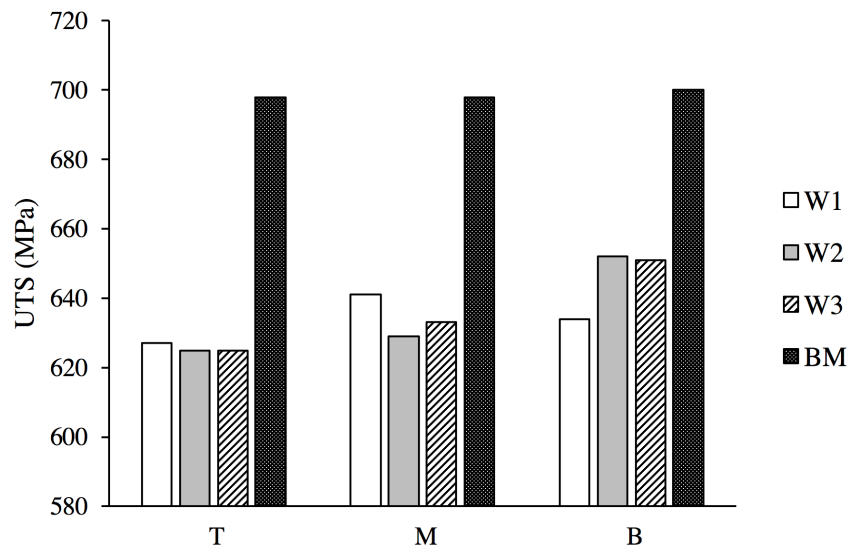
Figure 4.27 UTS for the BM and transverse tensile samples.
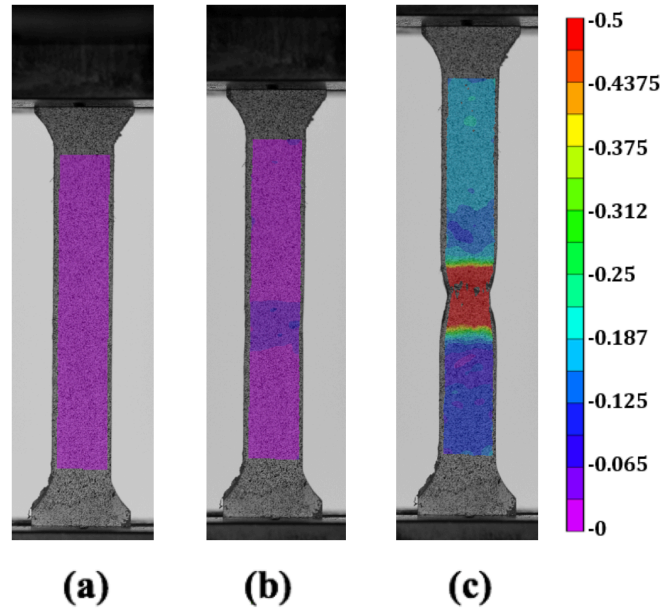
Figure 4.28 Strain distribution map for the W1 T tensile sample

(a) before the test (b) at the necking (c) prior to fracture.
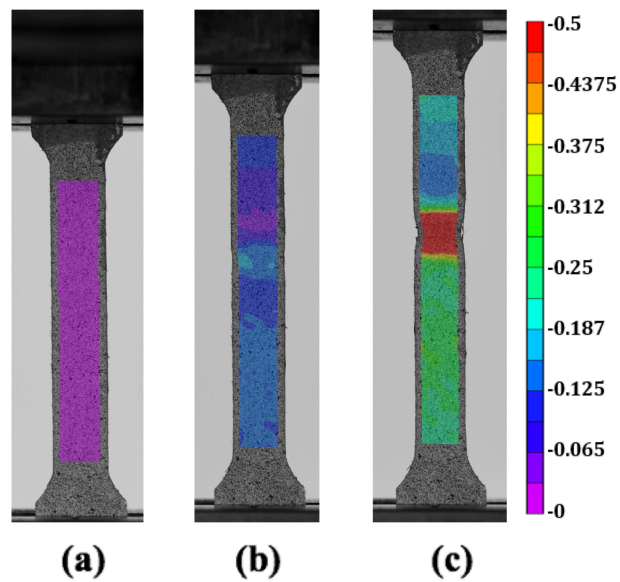
Figure 4.29 Strain distribution map for the W1 M tensile sample

(a) before the test (b) at the necking (c) prior to fracture.
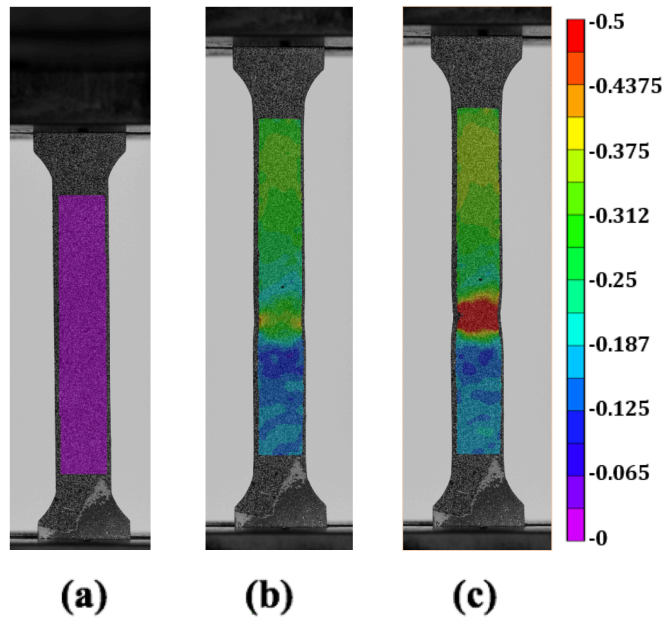
Figure 4.30 Strain distribution map for the W1 B tensile sample

(a) before the test (b) at the necking (c) prior to fracture.
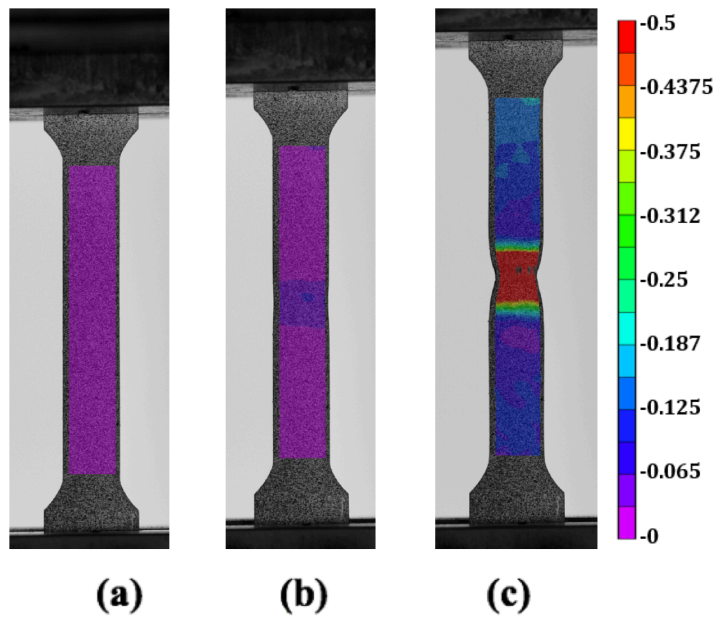
Figure 4.31 Strain distribution map for the W2 T tensile sample

(a) before the test (b) at the necking (c) prior to fracture.
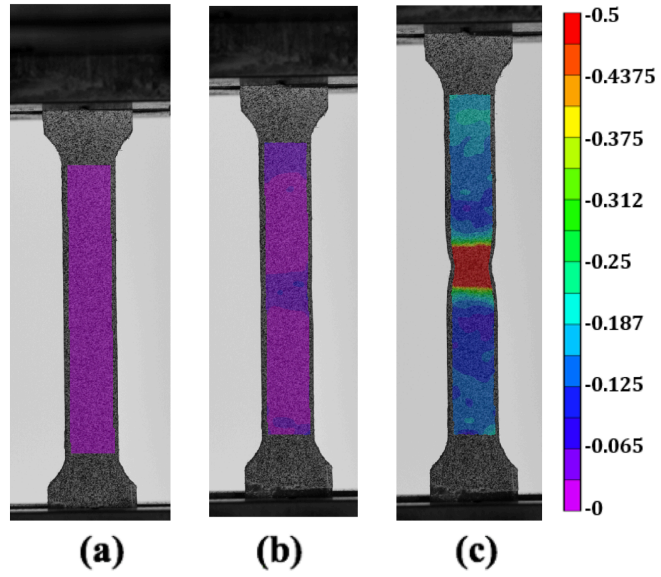
Figure 4.32 Strain distribution map for the W2 M tensile sample

(a) before the test (b) at the necking (c) prior to fracture.
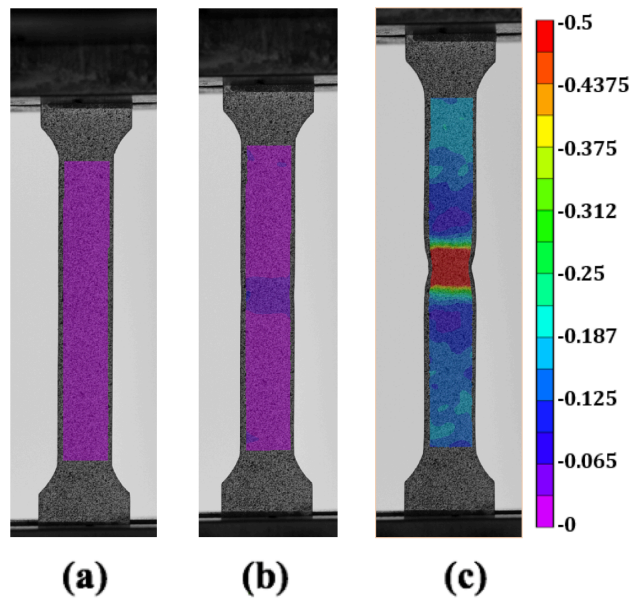
Figure 4.33 Strain distribution map for the W2 B tensile sample

(a) before the test (b) at the necking (c) prior to fracture.
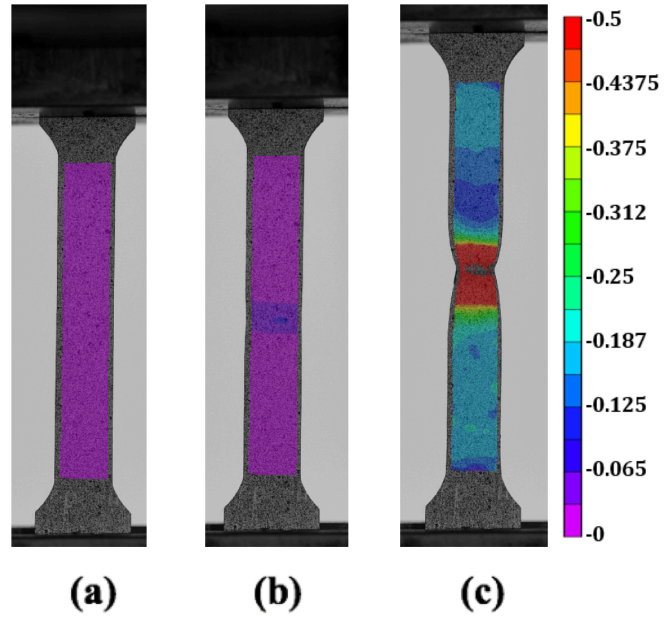
Figure 4.34 Strain distribution map for the W3 T tensile sample (a) before the test (b) at the necking (c) prior to fracture.
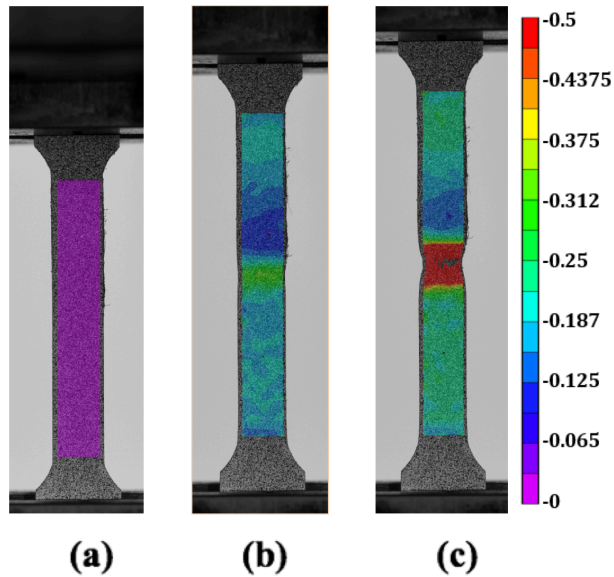
Figure 4.35 Strain distribution map for the W3 M tensile sample

(a) before the test (b) at the necking (c) prior to fracture.
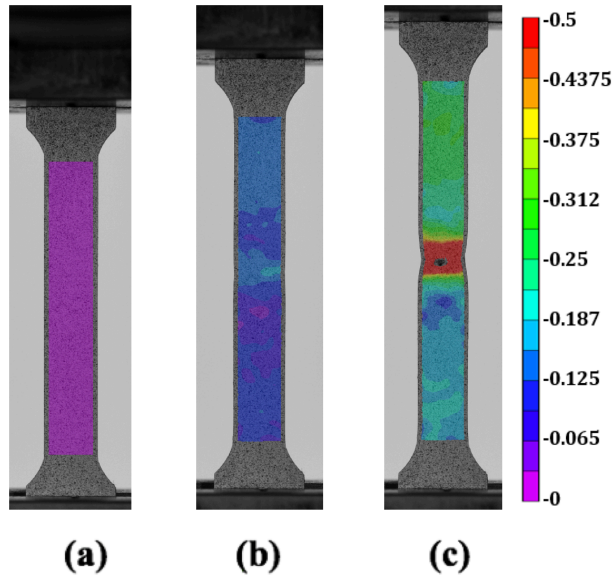
Figure 4.36 Strain distribution map for the W3 B tensile sample

(a) before the test (b) at the necking (c) prior to fracture.
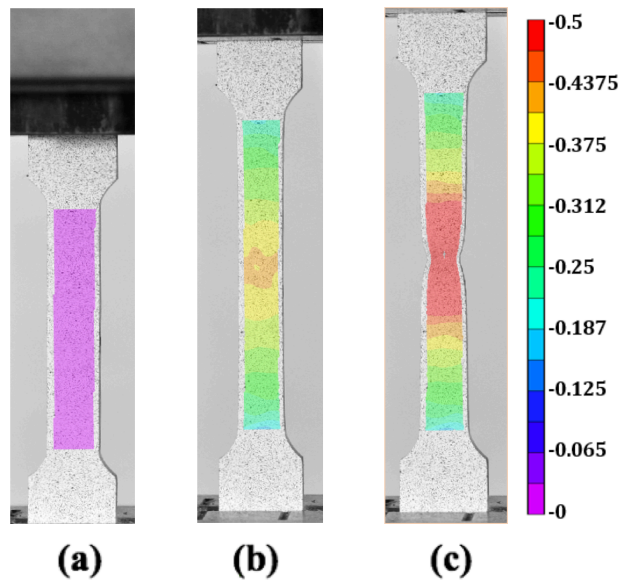
Figure 4.37 Strain distribution map for the BM T tensile sample

(a) before the test (b) at the necking (c) prior to fracture.
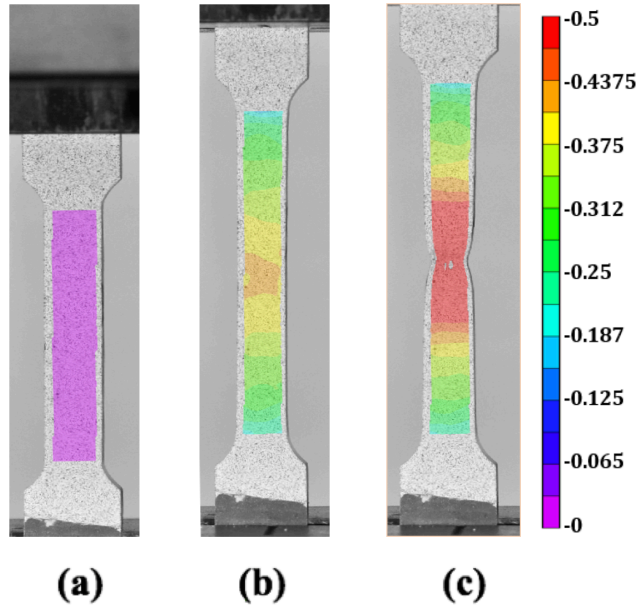
Figure 4.38 Strain distribution map for the BM M tensile sample

(a) before the test (b) at the necking (c) prior to fracture.
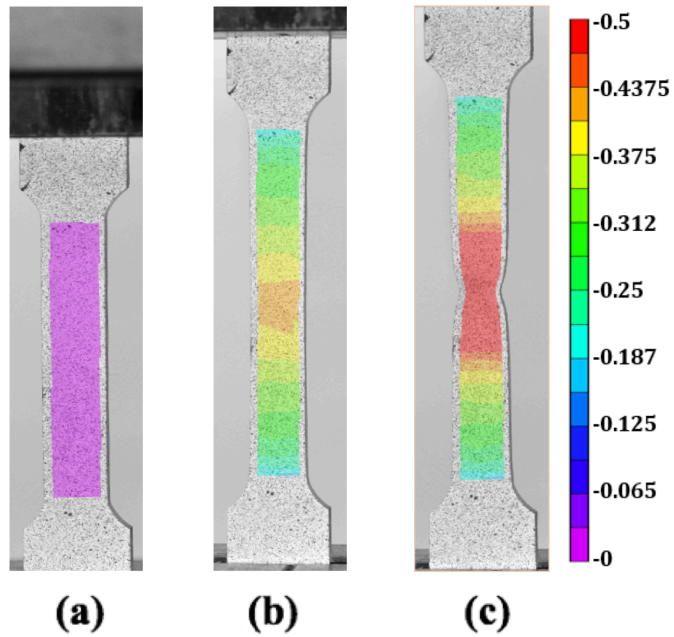
Figure 4.39 Strain distribution map for the BM B tensile sample

(a) before the test (b) at the necking (c) prior to fracture.

EBSD orientation map, was used to study the mechanical behaviour in the weld zone. In metals with any type of crystal structure, at least one slip system is required to be oriented 45° to the direction of the applied stress to make the grains yield at lowest possible tensile stress. In FCC metals with grains oriented in a way that (111) slip plane and <110> slip directions are oriented 45° to the applied stress, the slip will occur at lowest tensile stress [33, 104].

Figure 4.42 shows a Schmid factor intensity map for a transverse section of a part of FZ and HAZ at the top of the weld. The Schmid factor was calculated and used to correlate the grains slip plane and slip direction to the direction of the applied stresses. The higher the Schmid factor, the lower stress required for plastic deformation, since the Schmid factor indicates that the slip plane and slip direction are oriented near 45° to the direction of the applied stresses. It can be seen in the map that the grains in the weld zone show high Schmid factor which explains the high ductility behaviour of the weld. Interestingly, at the columnar-axial interface, a soft grains region intercepts with strong grains region in which consequently led to the localisation of stresses in the interception area and so the failure happened in the parting.

Along the weld thickness, the YS and the UTS are slightly higher at the bottom part of the FZ except W1, which showed lower UTS at the weld root, Figures 4.26 and 4.27. The YS ranged between 467 and 511 MPa in the weld tensile samples extracted from the bottom, and 447 to 461 MPa for the samples obtained from the top. The relatively high strength in the bottom parts of the FZ could be explained in terms of the effect of the microstructure on the mechanical properties of the weld.

The columnar and equiaxed ferrite morphology with a small SDAS structure at the middle and bottom parts of the weld, Figures 4.43 and 4.44, can act as a barrier to dislocation movement during slip processes, and thus increasing the weld strength [186-188]. In W1, the bottom region showed lower UTS because of the microstructure in this area contains predominately a primary and fully austenite structure as shown in Figure 4.12, which consequently reduces the weld strength.

All the tensile weld samples that were taken from the middle showed a slightly higher elongation to failure than the top and bottom, Figure 4.45. This could be attributed to the contribution of the relatively soft HAZ in the middle of the weld thickness, Figure 4.11, due to the low cooling rate in this area. The tensile test samples of W2 showed lower elongation and work hardening than W1 and W3, as illustrated in Figures 4.45 and 4.46.
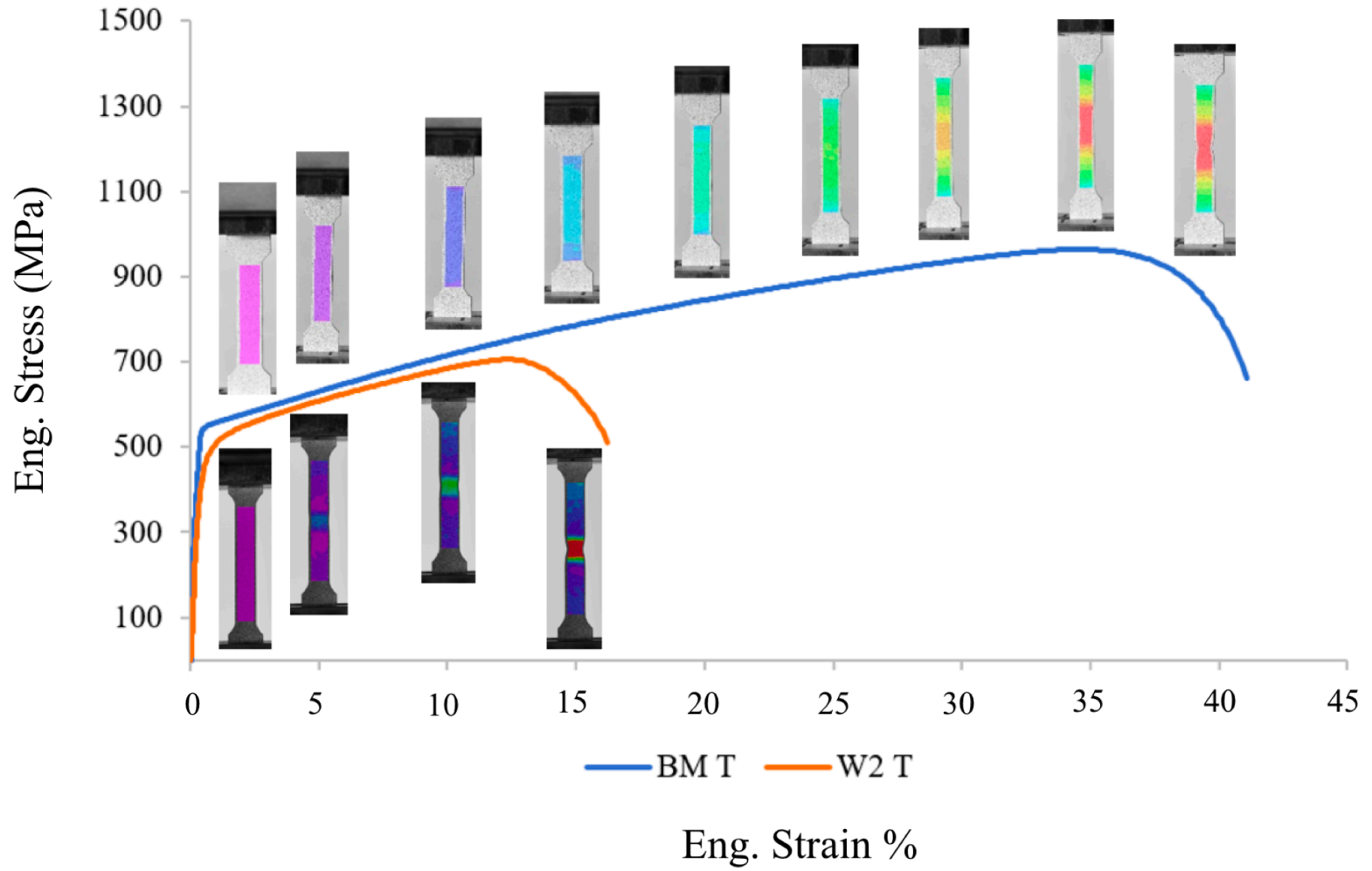
Figure 4.40 Stress-Strain curves for top section of the BM and weld tensile sample with strain distribution maps.

The weld with high strain hardening exponent is more responsive to work hardening and consequently shows higher resistance to fracture and higher plastic deformation [33, 189]. The low elongation of W2 is because the FZ is softer than W1 and W3 and surrounded by harder HAZ, as can be seen in Figure 4.11. This could reduce the plasticity of the FZ in the W2, since the contribution of the HAZ to W2 strength is lower than W1 and W3.

With the aid of the DIC technique, the local strain inside the weld zone was also measured and compared to the strain localised in the middle of the gauge length of the BM samples to ensure the weld metal ductility. The local stress strain curves, shown in Figure 4.47, confirm the high weld ductility. However, the weld was weaker than the BM due to the crystallographic effects in the weld zone as detailed in this work.

4.9 Fracture analysis

The fractured surfaces of all the weld tensile test samples were investigated by SEM to analyse the fracture surfaces' micro-characteristics. As predicted from the high ductility of all samples, a typical transgranular failure with ductile dimples was detected in the all samples, examples shown in Figures 4.48 (a and b). It is believed that the fracture is always related to the parting in the middle of the FZ.
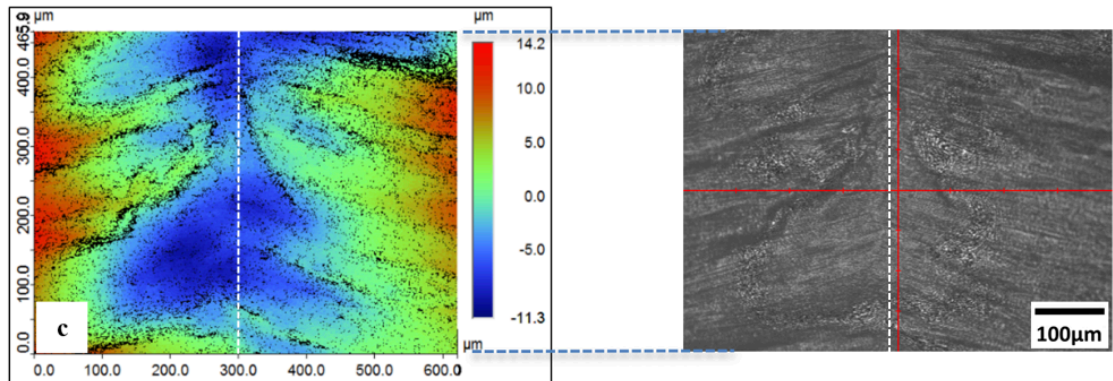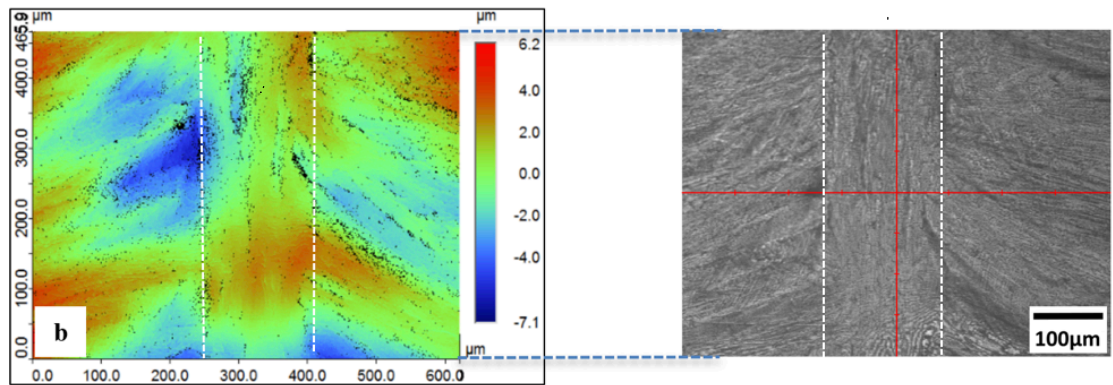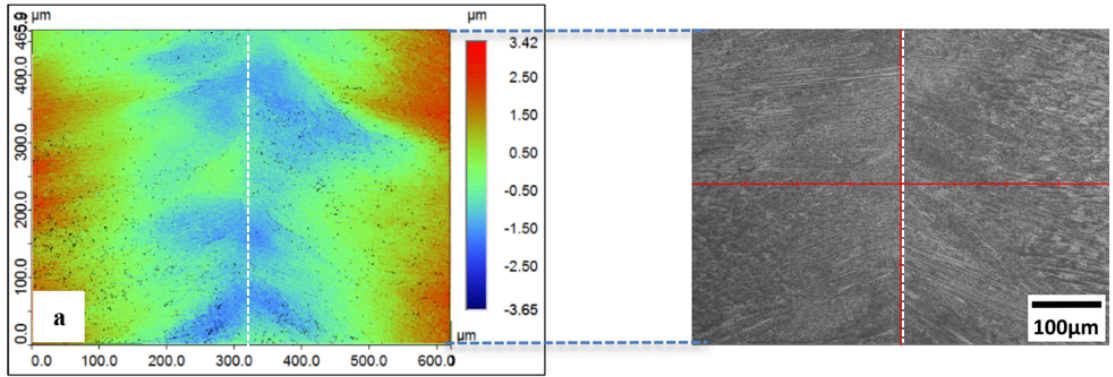
Figure 4.41 Surface deformation map of FZ for plastically deformed tensile test samples (a) Sample 1 with 10KN (b) Sample 2 with 10.5KN at the top part of FZ (c) Sample 3 with 11KN. The micrographs on the right showing the examined part of FZ. The dashed white lines represent the location of parting.
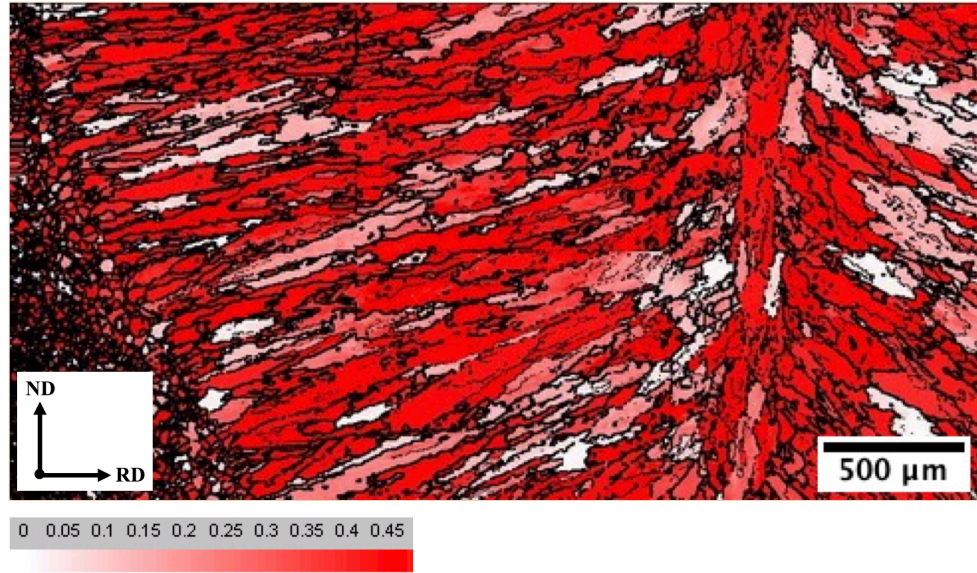
Figure 4.42 Schmid factor intensity map. Tensile stress applied in RD.
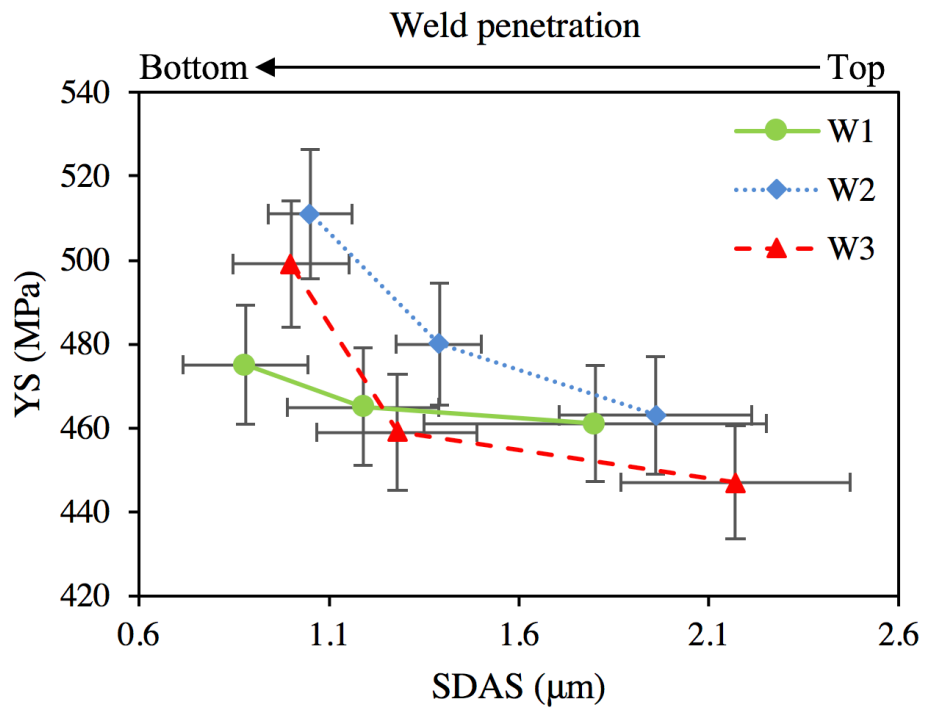
Figure 4.43 Variation of YS through the weld.
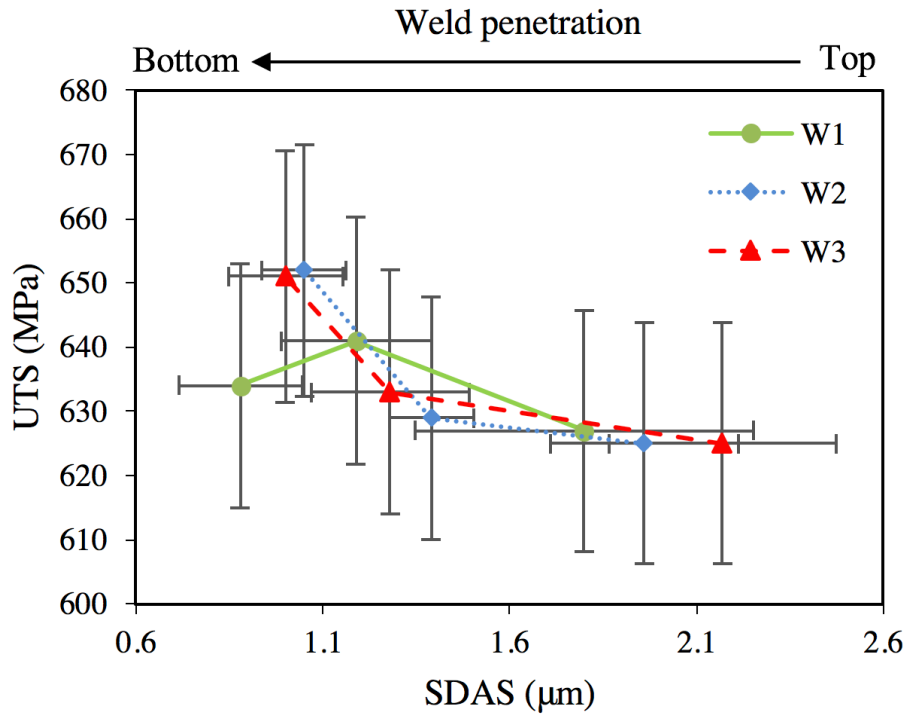
Figure 4.44 UTS values through the weld.
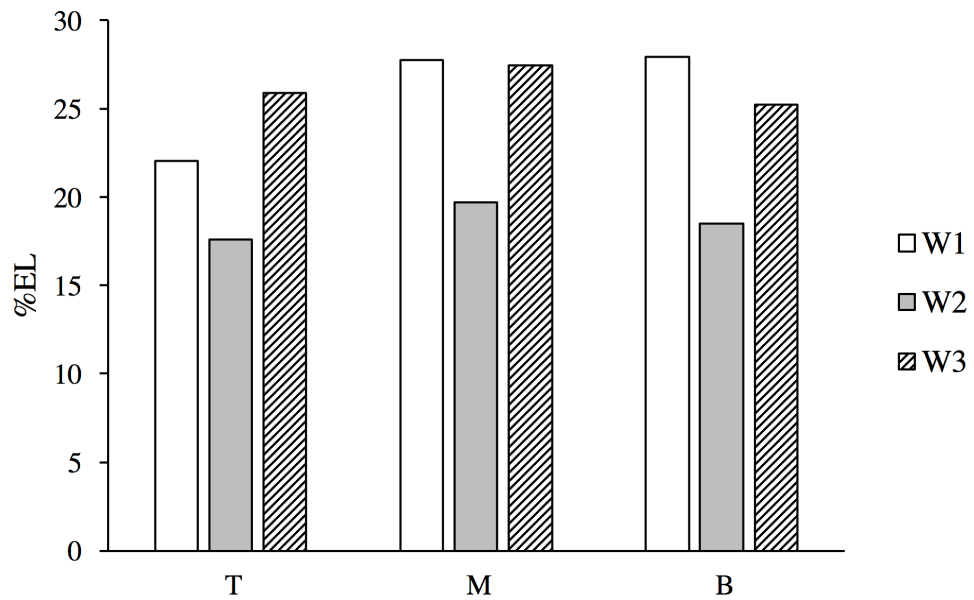
Figure 4.45 Total %EL to failure through the weld thickness.
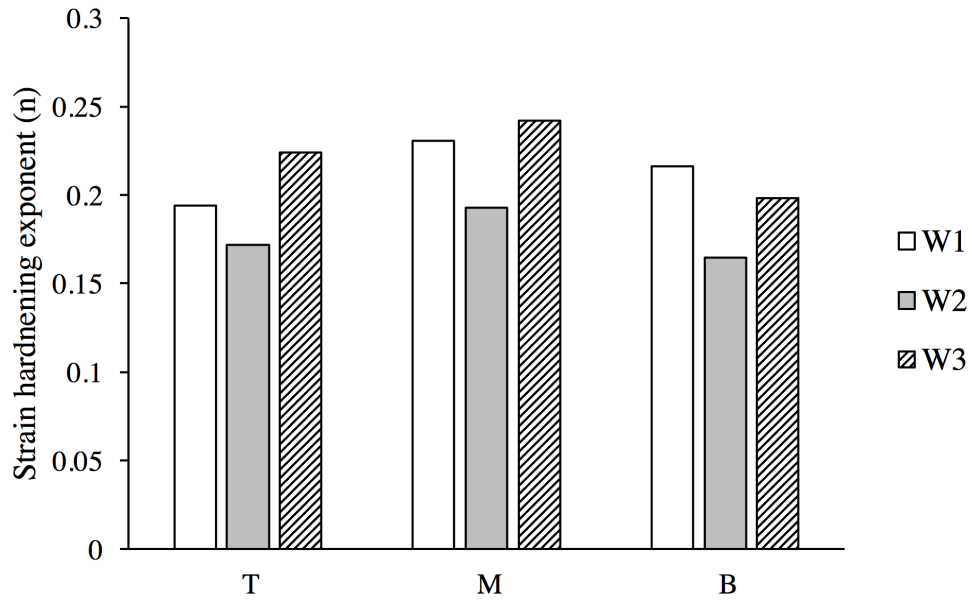
Figure 4.46 Strain hardening exponent through the weld thickness.
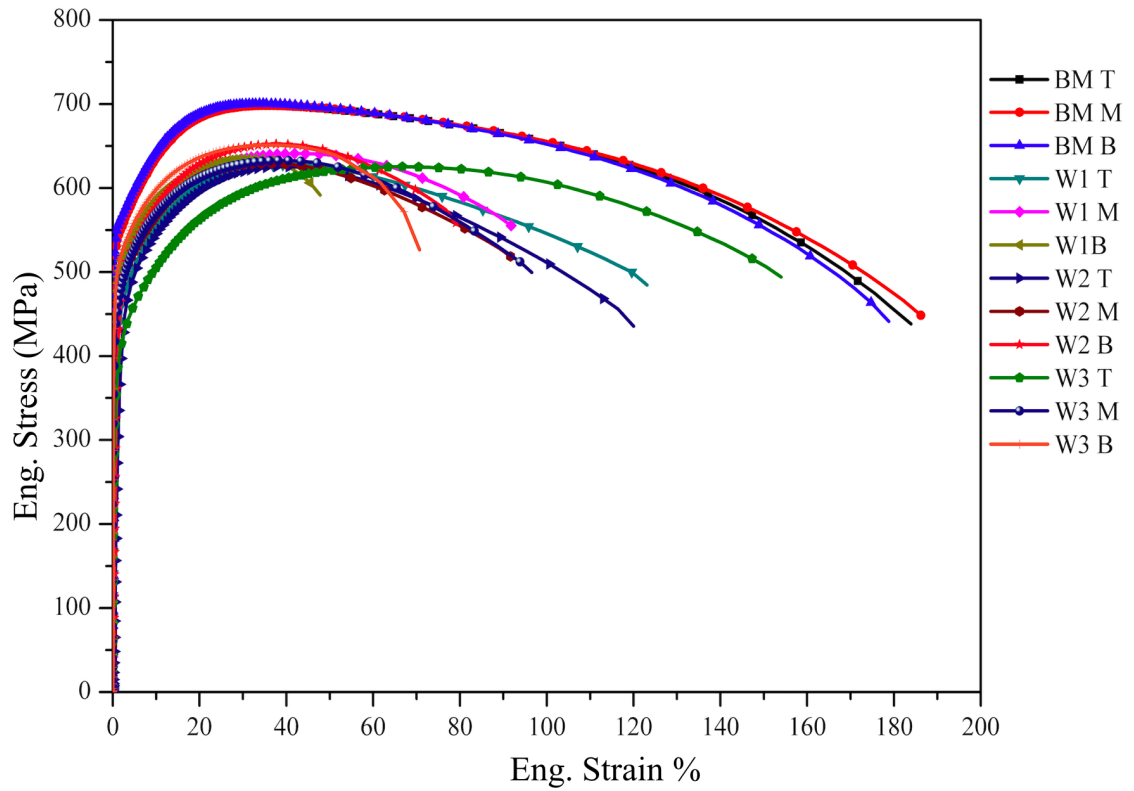
Figure 4.47 Tensile stress-strain curves for the transverse weld and BM samples.
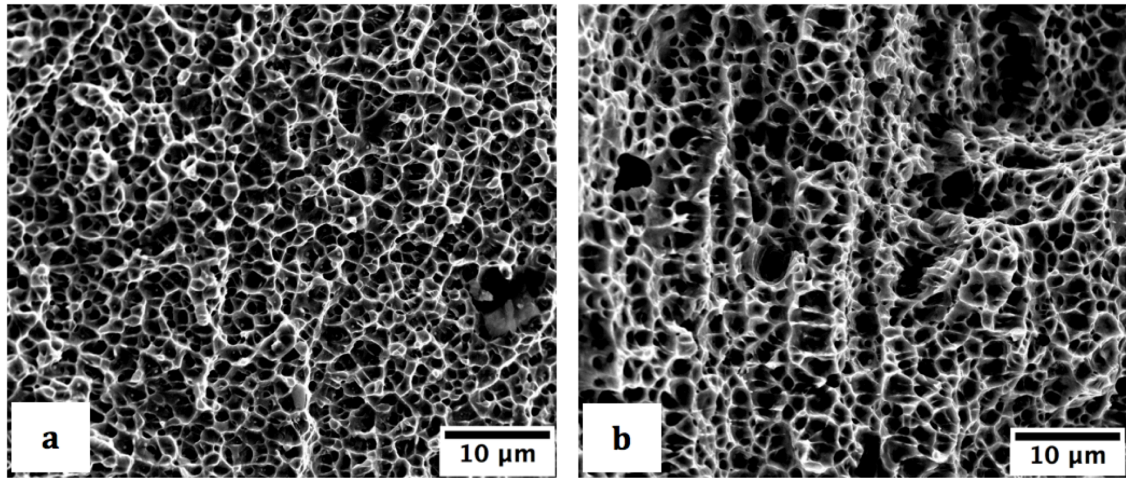
Figure 4.48 SEM micrographs of fracture surface for different samples. (a) W1 M (b) W3 B.

Chapter 5 Dissimilar Welding / Results and Discussion

5.1 Introduction

This chapter presents and discusses the results of the dissimilar welding trials between 20mm thickness Ti6Al4V and AISI316L stainless steel, using EBW process. This includes optimization of the welding parameters and characterisation of the weld microstructure and mechanical properties. The study was aimed to investigate the possibility of welding Ti6Al4V to AISI 316L stainless steel through analyzing many variables, such as using of a range of welding parameters, intermediate layer and preheating.

5.2 Beads on plate and butt joint experiments of Ti6Al4V

Realizing the optimum parameters of welding 20mm thickness Ti6Al4V and AISI 316L stainless steel separately, is an important step for the dissimilar welding between the two metals. For this reason, beads on plate trials were carried out on 20mm thick Ti6Al4V plate, Figure 5.1. Depending on visual test, i.e. depth of penetration and weld bead shape, welding parameters were chosen for the butt joint weld trials. The results of Ti6Al4V-Ti6Al4V weld showed that the parameters that were used for weld 1, listed in Table 3.9, produced optimum weld penetration, as shown in Figure 5.2. All the welds exhibited good weld bead shape.

5.3 Ti6Al4V - AISI 316L autogenous butt joint

The autogenous weld of Ti6Al4V-AISI316L was performed using the welding parameters listed in Table 3.10. The welding current was kept 110mA and the welding speed was varied to manipulate the heat input. A beam offset was applied to control the size of the intermetallic compounds and consequently, improve the weld mechanical properties, e.g. offsetting the beam towards the steel side, which has higher thermal conductivity, produces intermetallic phases with more uniform thickness along the joint interface [137]. However, all the trials failed and fractured instantly after welding. This can be attributed to the formation of the Ti-Fe intermetallic in the FZ, as can be seen in XRD pattern from the fractured surface, Figure 5.3, resulting in very brittle weld and for a crack to generate

easily from the residual stresses [6, 12, 152, 190]. Examples of broken joints with clear crack at the weld bead are shown in Figure 5.4.

(a)
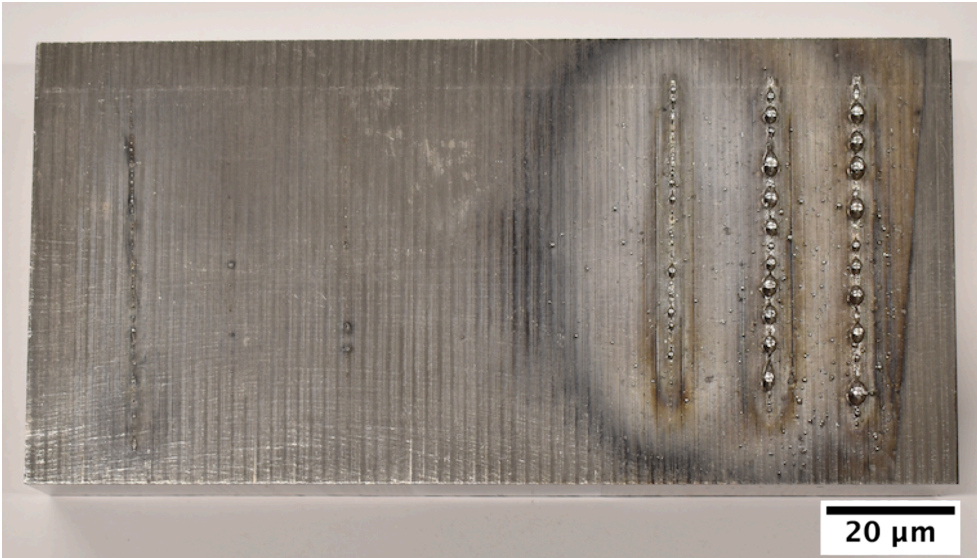
(b)

Figure 5.1 Bead on plate experiments of Ti6Al4V. (a) weld beads face (b) weld beads root. For welding parameters see Table 3.8.
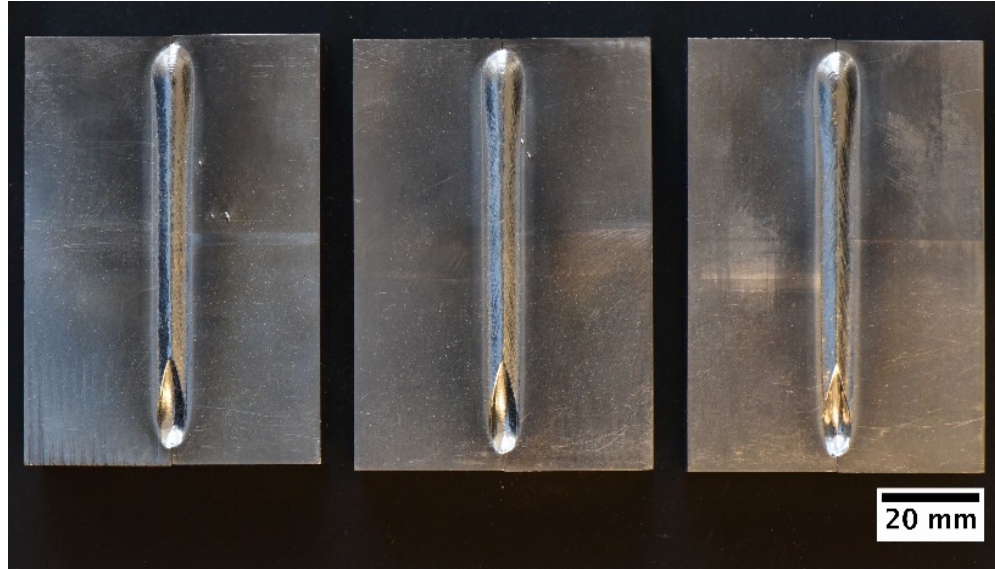
(a)

(b)

Figure 5.2 Weld 1, 2 and 3 from left to right respectively of

Ti6Al4V-Ti6Al4V butt joint (a) weld face (b) weld root.
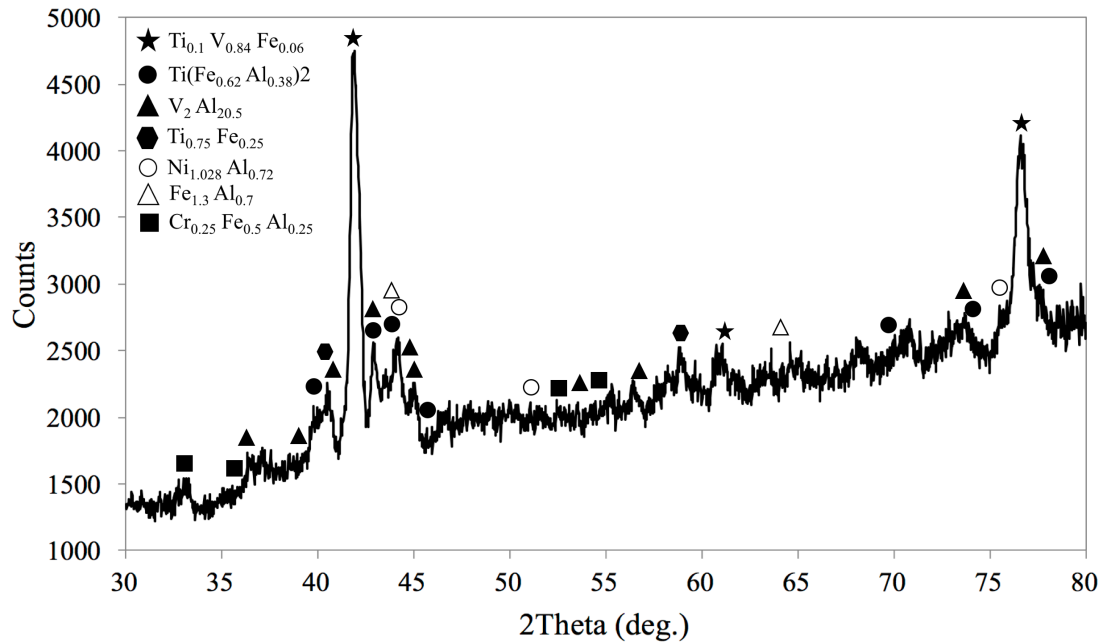
Figure 5.3 XRD pattern for the weld fracture surface at the titanium/Fe without using copper interlayer.

5.4 Ti6Al4V - AISI 316L butt joint with interlayer

Copper sheets with 0.5 and 1mm thickness were used as an interlayer and fixed at the contact face between the two materials. In both cases the welds showed poor toughness and broke after removing the fixtures, as shown Figures 5.5 to 5.8.

Since the thickness of the BM is quite high (20mm), a relatively high heat input was required to achieve full weld penetration. It was found that using copper interlayers with 0.5 and 1mm thickness are not sufficient to avoid or restrict the mixing between Ti and Fe and reduce the size of the intermetallics since the relatively low melting temperature Cu layer either mostly melted at the upper part of the weld but there was a lack of penetration occurring at the lower part, as can be seen in Figures 5.5 and 5.8 or fully melted when using high heat input as can be seen in Figure 5.7. This combined with the effect of the residual stresses that resulted from the difference in thermal expansion coefficient between titanium and stainless steel, which exposes the joint to fracture spontaneously after welding. For this reason, it was realized that it is important to reduce the amount of heat input during welding, use a higher thickness copper interlayer and applying the preheat technique to achieve crack-free weld.

133
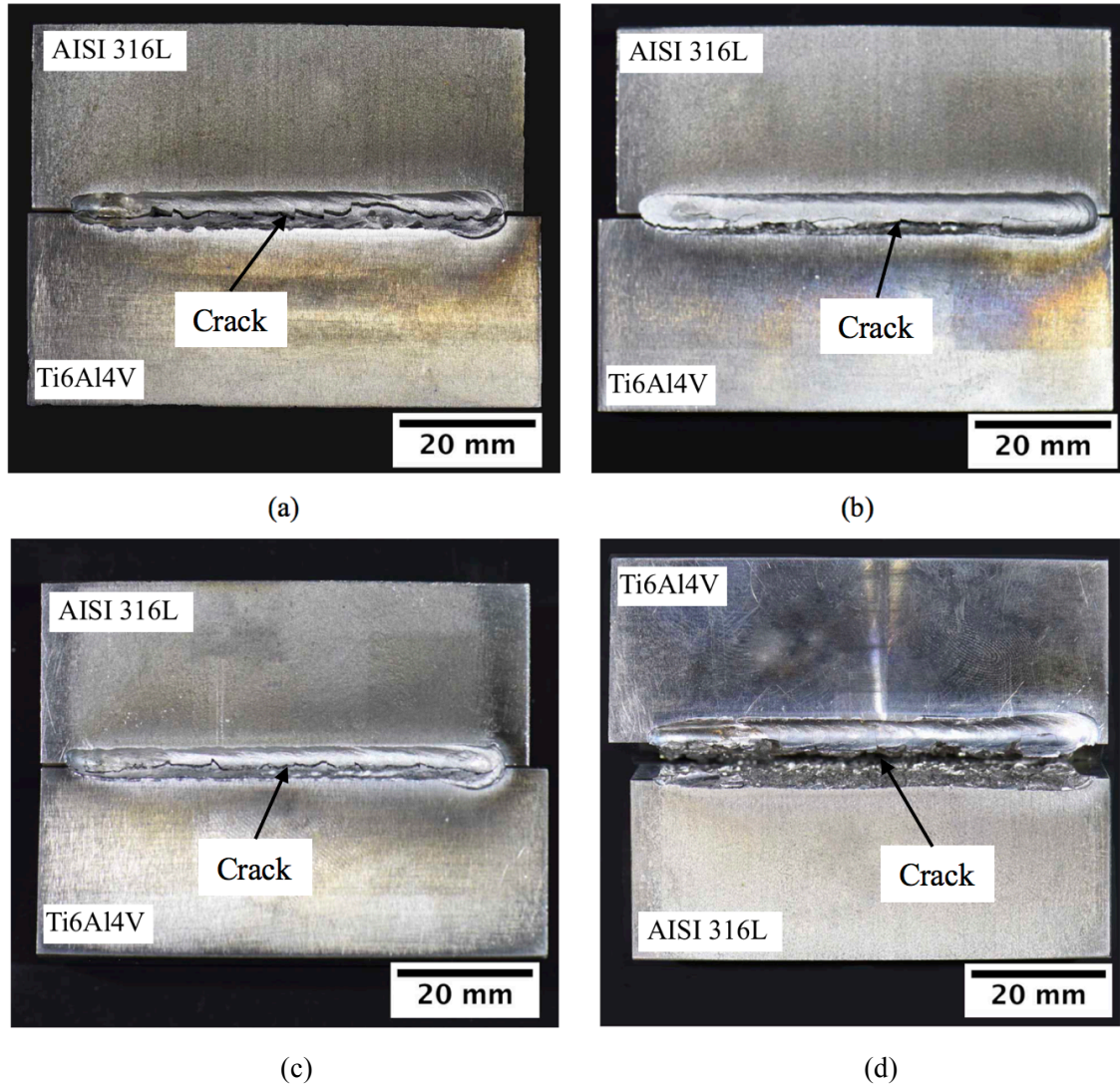
Figure 5.4 Ti6Al4V-AISI 316L autogenous weld surface (a) weld 1 (b) weld 3 (c) weld 4 (d) weld 5. The all welds showed crack at the weld bead. All welding parameters are listed in table 3.10.
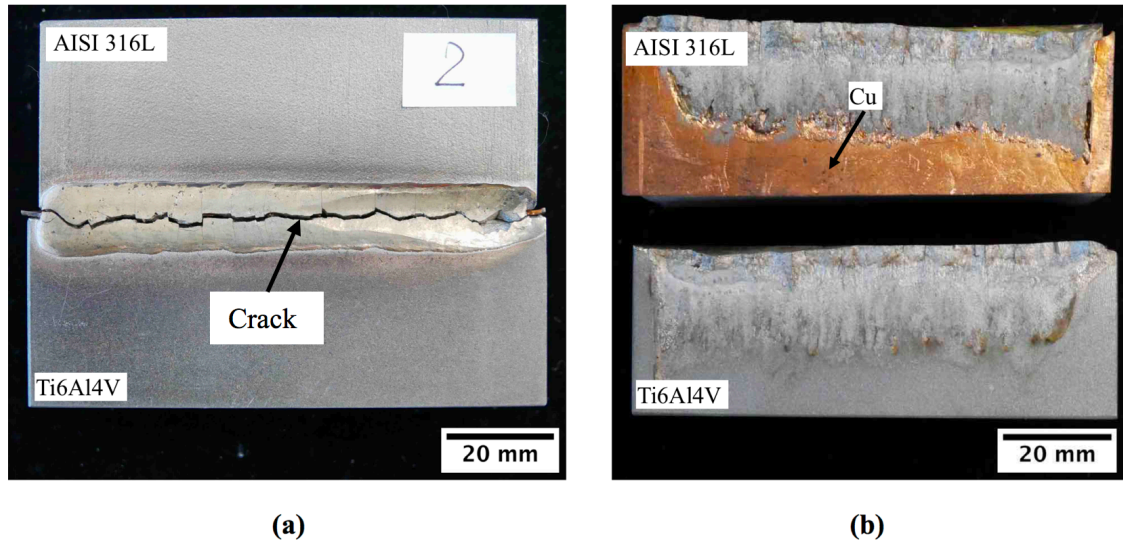
Figure 5.5 Dissimilar weld 2 (a) weld top surface (b) joint contact surface with the copper sheet welded to stainless steel side.
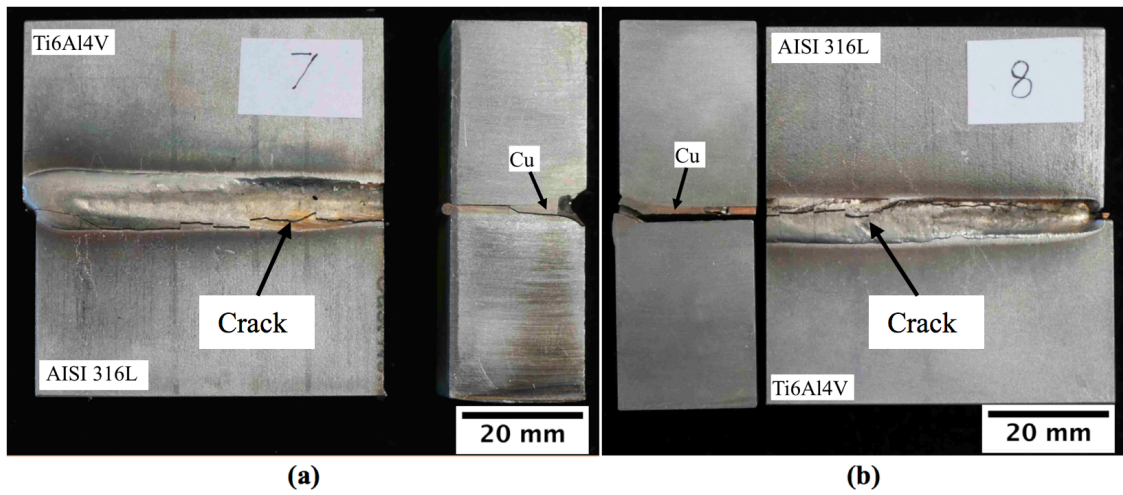
Figure 5.6 Dissimilar weld surface and cross section (a) weld 7 (b) weld 8.
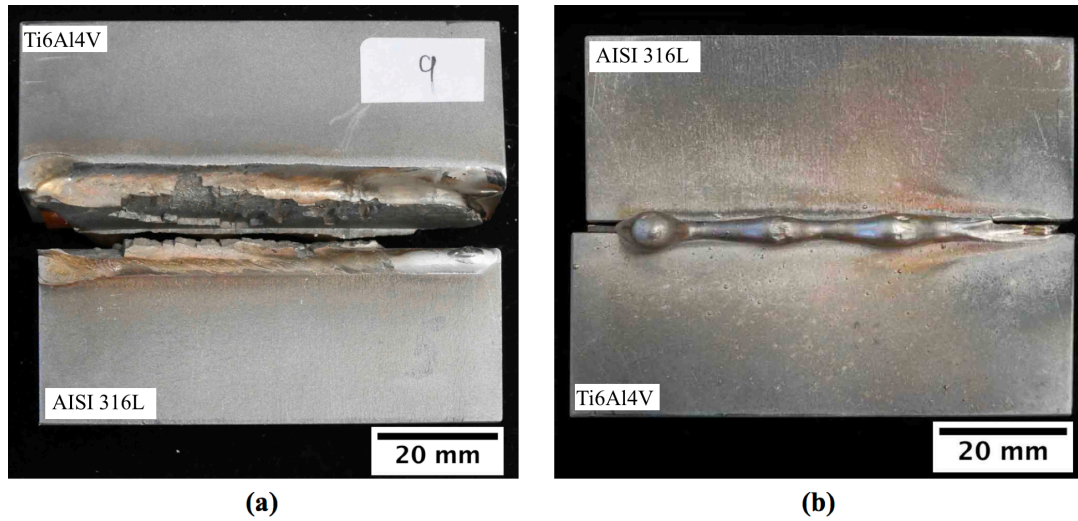
Figure 5.7 Dissimilar weld 9 (a) weld surface (b) weld root.
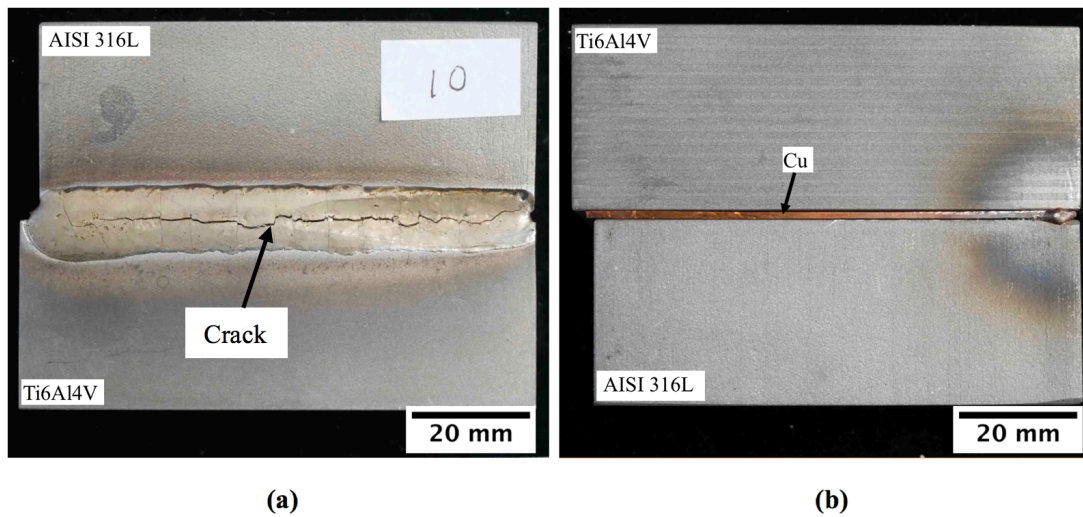
Figure 5.8 Dissimilar weld 10 (a) weld surface (b) weld root.

5.5 Butt weld with interlayer and preheat

Heating the weld sample before performing the welding process was an option to reduce the welding process heat input and minimize the effect of the residual stresses. The weld samples were preheated to 450°C prior to welding and the welding current was reduced to 70 and 100 mA whilst increasing the welding speed to 25 mm/s as shown in weld 12 to weld 20 in Table 3.11. It was found that the weld strength is slightly improved yet full weld penetration was not achieved. In addition, the copper interlayer stilled melt quickly at the top part of the weld as can be seen in Figure 5.9.
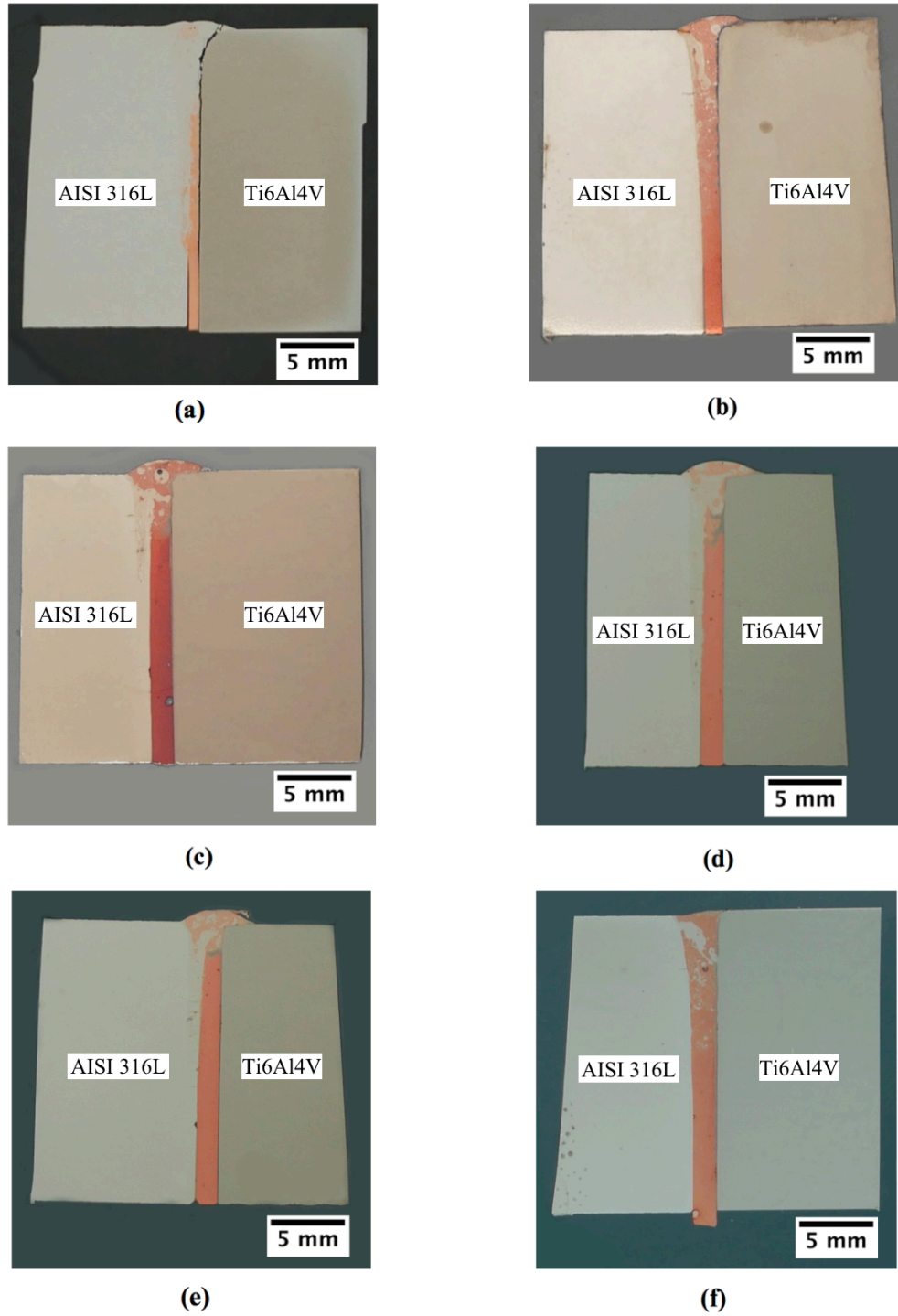
Figure 5.9 Cross section of Ti6Al4V-AISI 316L one pass weld preheated samples (a) weld 13 (b) weld 14 (c) weld 16 (d) weld 18 (e) weld 19 (f) weld 20. All welding parameters are listed in table 3.11.

5.6 Double pass butt weld with interlayer and preheat

To insure full weld penetration while reducing the welding heat input, the welding process was performed using the double pass technique by applying the electron beam on the top and bottom sides of the weld, as shown in Figure 5.10. The beam current was decreased to 70 mA and the rest of the welding parameters are listed in Table 3.11. Relatively best weld toughness was achieved where the sample did not break even after preparation for microscopic examination i.e. the samples passed the machining successfully. Using of relatively low heat input (70 mA weld current) with fast welding speed (20 and 25 mm/sec) helped in keeping of the AISI 316L and Ti6Al4V without being fully mixed and with aid of the preheating the residual stresses were also highly minimized.
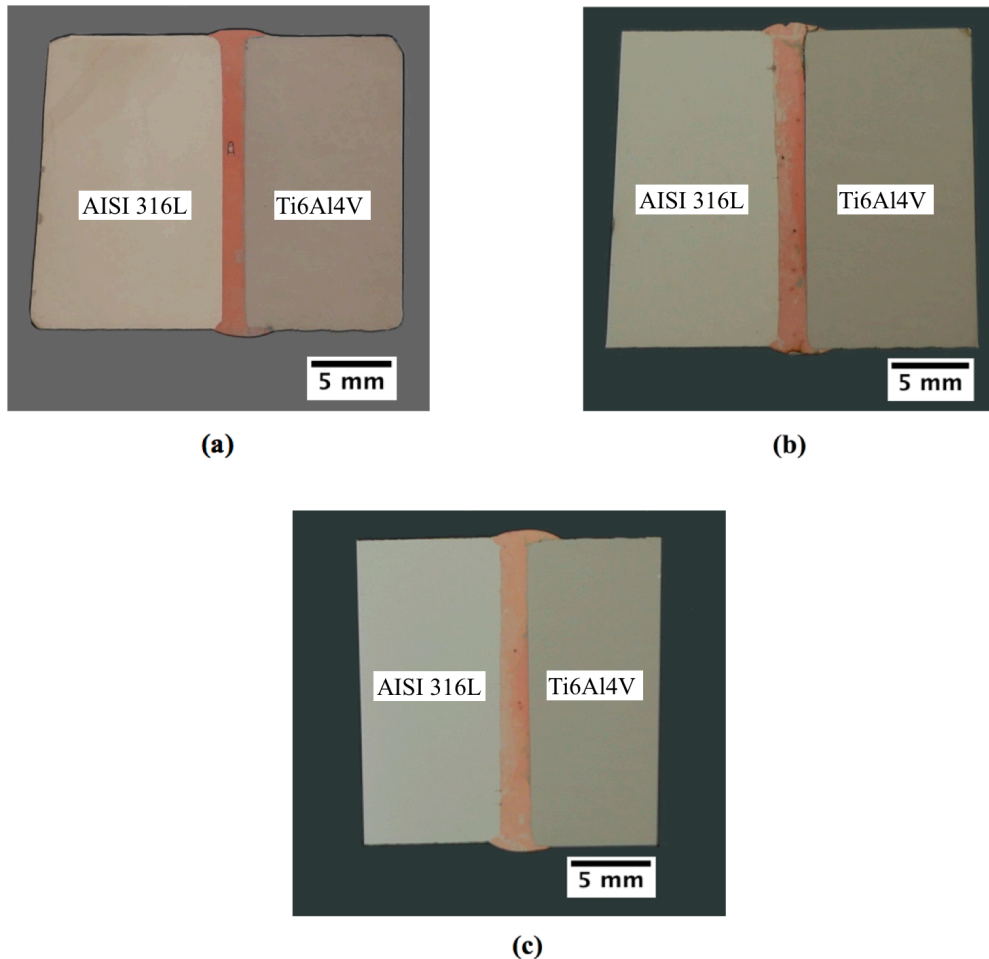
Figure 5.10 Cross section of Ti6Al4V-AISI 316L double pass welded preheated samples (a) weld 21 (b) weld 22 (c) weld 23. All welding parameters are listed in table 3.11.

5.7 Microstructure characterisation

Only the preheated weld samples could be prepared for microstructure examination as all the weld trails that were performed without preheating broke after removing the fixtures. However, single-pass preheated weld samples, Figure 5.8, had lack of penetration and high residual stresses developed in the root of the weld, which led to the presence of completely un-melted zone with clear distortion. Therefore, only double pass welds, Figure 5.10, were subjected to the microstructure examination since they were relatively successful in terms of weld penetration and free of crack in the as welded condition.

The weld microstructure was studied and analysed by SEM and EDS. The assumptions of the microstructure content were confirmed by XRD analysis. The weld microstructure was divided into three regions: stainless steel side, weld centre and titanium side, as shown in Figure 5.11, to simplify the understanding of the microstructure in various weld regions.

Each microstructure that has a distinguishable gray shade colour was identified by a letter, as can be seen in Figure 5.12. The identified microstructures were analysed by spot EDS to further investigate and determine the chemical composition. Major elements of each microstructure are listed in Table 5.1. With the aid of Ti-Fe, Ti-Cu binary system diagrams, Figure 2.52 and and 5.13 respectively, and Ti–Fe–Cu ternary phase diagram, Figure 5.14, the content of each microstructure can be predicted as concluded in Table 5.2. XRD analysis was used to confirm the existence of the alloying elements.

At the AISI 316L-Cu interface layer, there are two distinguishable microstructures. A steel-rich microstructure with intermediate gray colour (A) separated by thin layer of copper-rich with light gray colour microstructure (B), as shown in Figure 5.12 (a). (A) is an austenitic stainless steel and (B) contains copper and iron solid solutions.

The centre of the weld consisted of a light gray microstructure (C), which is a solid solution of copper and iron and dark gray steel-rich microstructure (D). (D) appears as irregular droplets distributed randomly throughout the copper solid solution, as can be seen in Figure 5.12 (b).

In the weld zone next to the titanium alloy, a large number of constituents and phases with different morphologies were observed. These are due to the high chemical activity of the titanium alloy. This area can be divided into three layers, marked as layer I, II, III. Each layer was featured with distinctive morphology and bordered with dashed line, as shown in Figure 5.12 (c, d and e).

Layer I contained three different microstructures; (E, F and G). Light gray (E) was surrounded by (F), which exists in a form of cells and thin interlayers. Microstructure (G) was located inside the cells of F, as shown in Figure 5.12 (c). Microstructure (E) consisted

of a solid solution of copper with $TiCu_3$. (F) and (G) were Ti_2Cu_3 and $FeTi+\tau$ intermetallics, respectively.

Layer II, Figure 5.12 (d) consisted of microstructures (H, I, J and K). The white microstructure (H) and light gray (I) both characterised by copper solid solution with $TiCu_3$ and located between blocks of Ti_2Cu_3 and $TiCu_3$ intermetallics (J microstructure). Dark gray (K) was found in a little amount inside (J) and contained $FeTi+\tau_2$ intermetallic.

Three types of microstructure were also detected in layer III, Figure 5.12 (e). A gray blocky (M), which consisted of $FeTi+\tau_2+\tau_5$ mixture, surrounded by interlayers light gray (L), which is $TiCu_2$ with $TiCu$ intermetallics. Microstructure (N) with dark gray colour located as a thin layer along the Ti-Cu interface and contained αTi solid solution strengthened by Ti_2Cu intermetallics.

It can be concluded that the microstructure of the weld near titanium alloy consisted of three main constituents: copper solid solution, titanium solid solution and intermetallic compounds of Cu-Ti and Fe-Cu-Ti. All the predicted constituents and phases of the microstructures are listed in Table 5.2. It can be seen that in layer III, the copper solid solution is no longer exist, this can consequently reduce the ductility of the weld in this area. Hence, the fracture is more likely to occur in layer III, as shown Figure 5.15.

The XRD pattern for the fracture surface at the copper-titanium side confirms the possibility of presence brittle Ti-Cu and Ti-Fe intermetallic phases, as shown in Figures 5.16 and 5.17. However, the presence of copper solid solution between the blocky intermetallic phases and the formation of Fe-Cu-Ti and Cu-Ti, which have lower brittleness than Fe-Ti intermetallic compound, relatively enhances the plasticity of the weld and increase the chance of obtaining weld that is free of crack. The XRD was also performed for weld cross-section at the stainless steel/copper interface, as shown in Figure 5.18. The results show peaks of FCC phase structure that correspond with XRD patterns of austenitic iron and copper solid solution, which confirm the existence of the two constituents in this region.
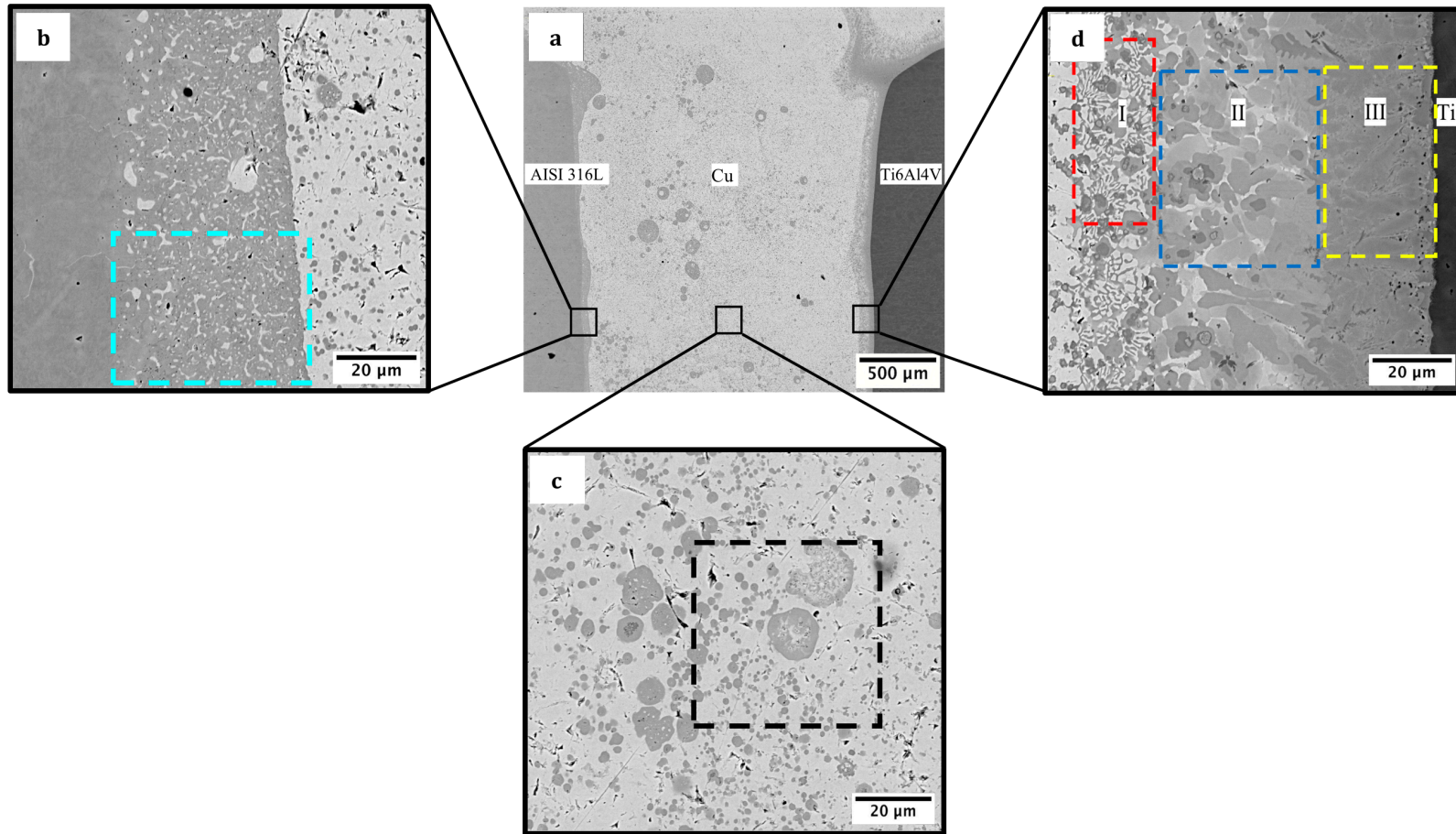
Figure 5.11 Microstructures of the AISI 316L-Cu-AISI 316L-Cu-Ti6Al4V weld (a) part of the AISI 316L-Cu-AISI 316L-Cu-Ti6Al4V weld microstructure (b) microstructure at higher magnification of the weld at the stainless steel side (c) microstructure at higher magnification for the region at centre of the weld (d) microstructure at higher magnification of weld at the titanium side. The dashed line areas represent the locations selected to be shown in further higher magnification.
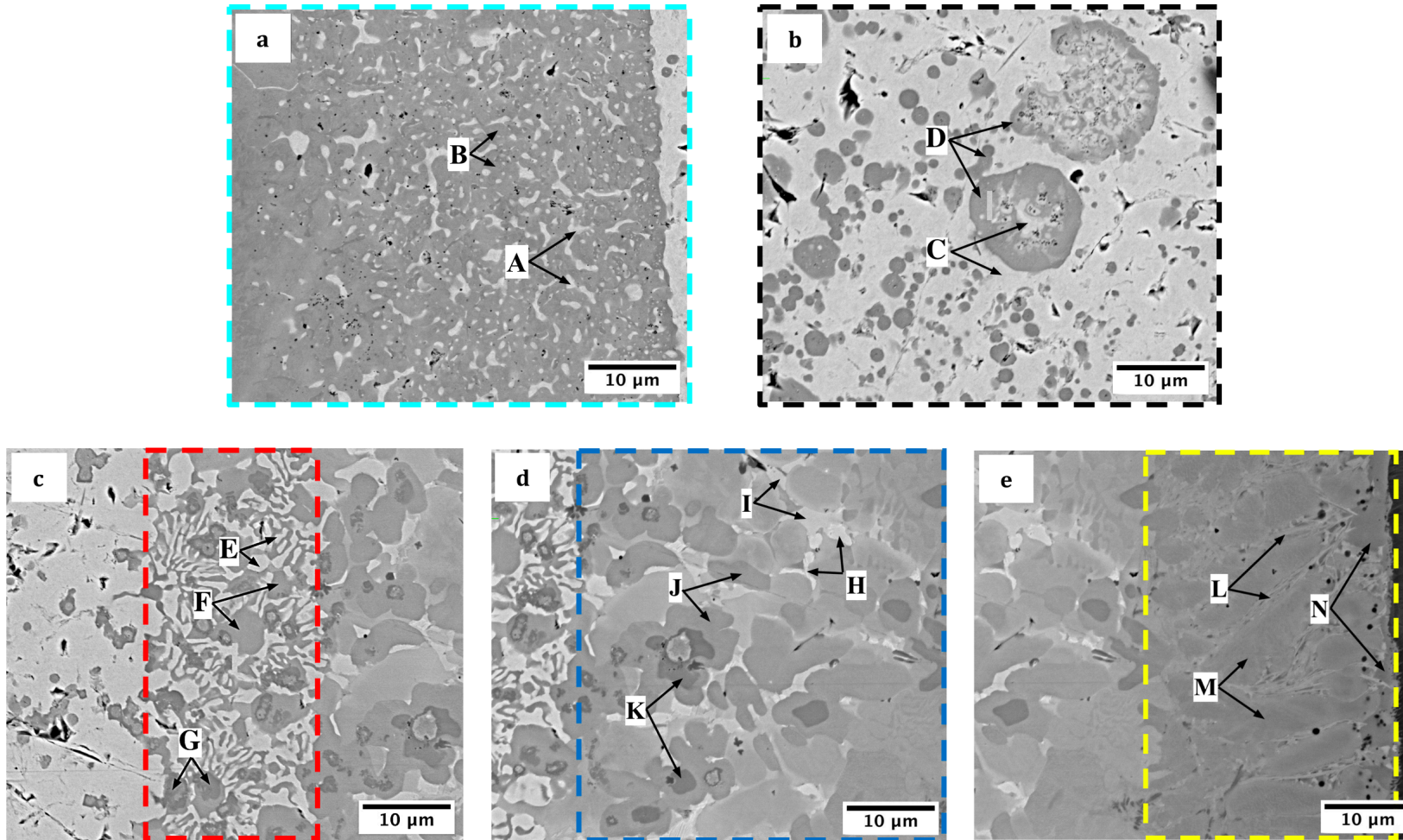
Figure 5.12 Microstructure of different regions in the AISI 316L-Cu-AISI 316L-Cu-Ti6Al4V weld at higher magnification (a) at the stainless steel side (b) at centre of the weld (c) Layer I at the titanium side (d) Layer II at the titanium side (e) Layer III at the titanium side.
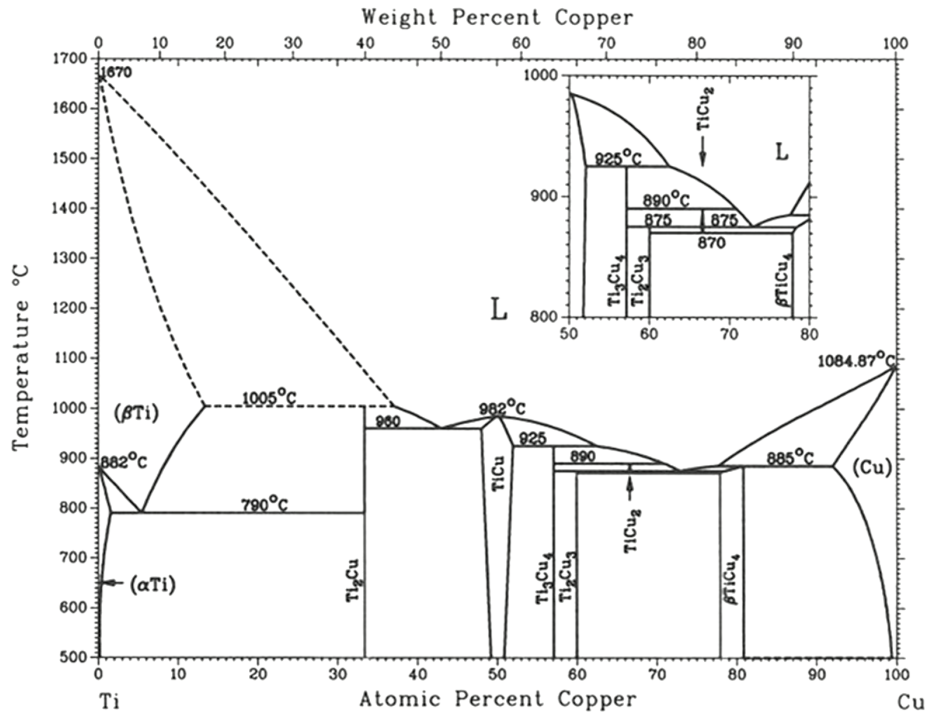
Figure 5.13 Ti-Cu binary phase diagram [148].
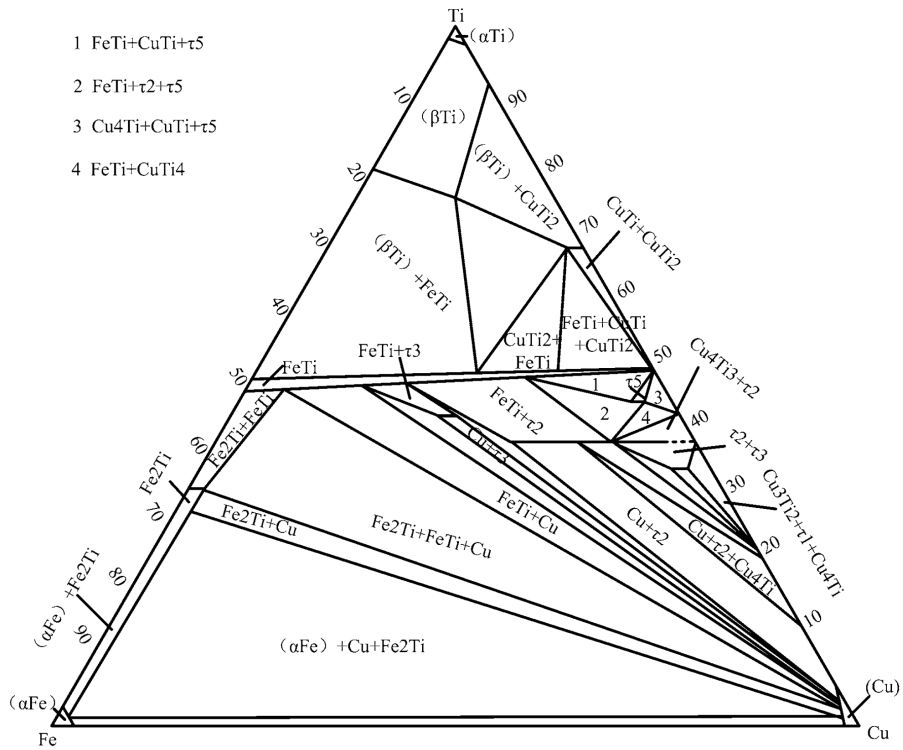
Figure 5.14 Ti-Fe-Cu ternary phase diagram [191].

143

Table 5.1 Major elements content of various microstructures in Ti-Cu-St weld (wt%)

Phase	Al	Ti	V	Cr	Fe	Ni	Cu
A	0.22±0.13	0.03	0.01	2.67±1.33	10.25±3.89	2.49±0.16	84.25±4.9
B	0.12±0.03	0.1±0.13	0.01	15.66±0.74	65.24±0.64	8.51±0.83	10.22±0.68
C	0.16±0.08	0.33±0.10	0.05±0.02	1.79±1.05	7.52±3.46	1.65±0.19	88.51±4.76
D	0.07±0.03	1.53±0.52	0.21±0.06	15.37±1.3	61.43±7.04	4.78±0.42	16.62±9.26
E	1.54± 0.17	6.93±0.39	0. 17	0.25±0.19	0.95±0.67	0.27±0.04	89.89±1.46
F	3.5±0.14	21.76±0.04	0.16±0.06	0.27±0.02	1.09±0.08	1.19±0.1	72.21±0.05
G	0.58±0.06	28.93±0.49	3.54±0.95	12.05±3.25	31.29±6.68	1.63±0.11	22.42±11.42
H	0.9±0.53	10.10±8.14	0.23±0.31	0.12±0.03	0.61±0.01	0.22±0.03	87.8±8.71
I	4.14±0.24	22.45±0.01	0.22±0.02	0.1±0.01	0.98±0.12	1.12±0.06	70.99±0.13
J	0.74±0.02	32.89±0.34	1.46±0.16	2.12±0.05	8.55±0.4	1.33±0.16	52.9±0.66
K	1.14±0.07	40.17±0.23	1.84±0.16	2.08±0.39	19.6±1.26	2.4±0.02	32.77±2
L	4.18±1.32	46.09±3.14	2.59±0.48	0.39±0.12	1.6±0.76	1.02±0.13	44.12±1.27
M	3.37±0.3	47.47±1.23	3.22±0.16	1.42±0.04	10.76±0.16	1.48±0.03	32.82±1.8
N	3.87±0.77	56.04±2.19	2.91±1.71	0.02±0.12	0.53±0.04	0.58±0.06	36.05±5.89

Table 5.2 Potential constituents and phases of the microstructures in Cu-Ti weld side

Layer	Microstructure	Possible constituent and phase type
I	E	$\alpha Cu + \beta TiCu_4$
I	F	$\beta TiCu_{4+} Ti_2Cu_3$
I	G	$Fe_2Ti + FeTi + Cu$
II	H	$\alpha Cu + \beta TiCu_4$
II	I	$\beta TiCu_{4+} Ti_2Cu_3$
II	J	$Cu + \tau_{2+} Cu_4Ti$
II	K	$Ti_2Cu + TiCu$
III	L	$Ti_2Cu + TiCu$
III	M	$\tau_2 + \tau_5 + FeTi$
III	N	$Ti_2Cu + TiCu$
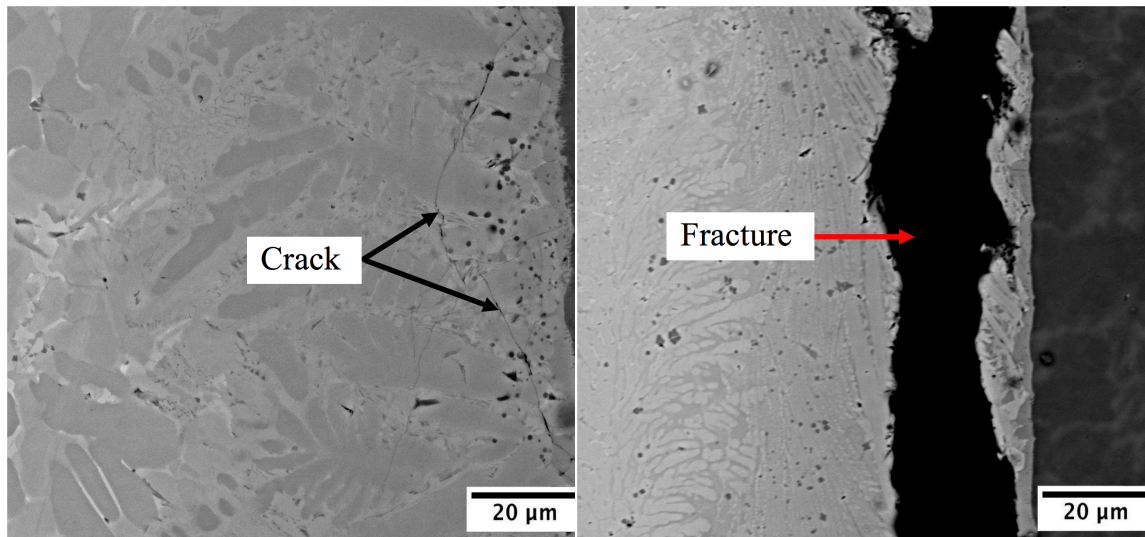
(a)   (b)

Figure 5.15 Weld microstructure at the Ti-Cu interface (layer III) (a) crack location (b) fracture location.
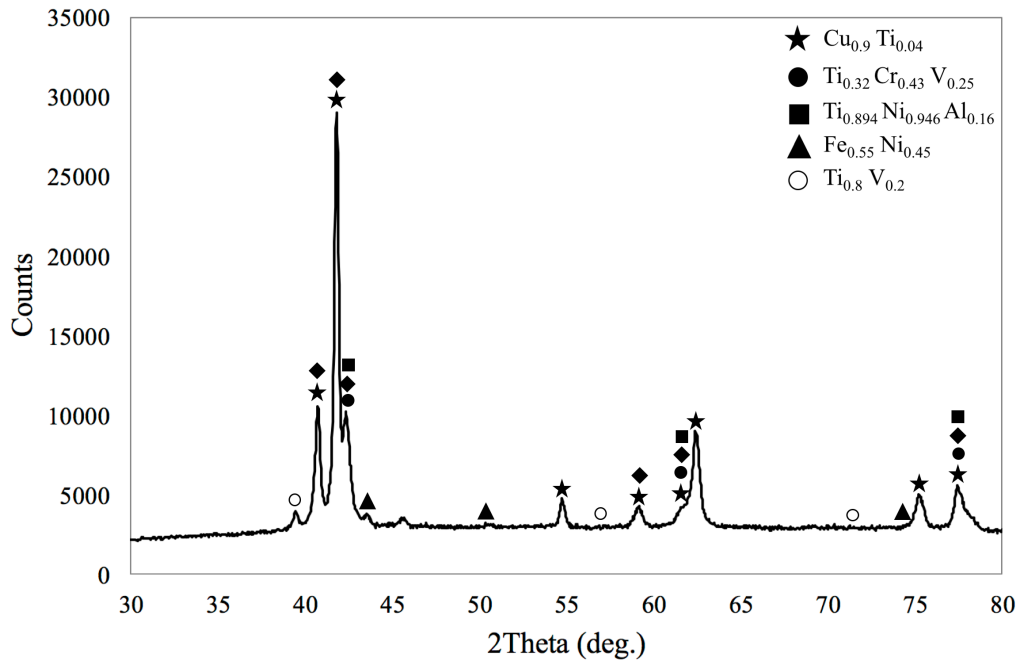
Figure 5.16 XRD pattern for the weld fracture surface at the titanium/copper interface at the copper surface side
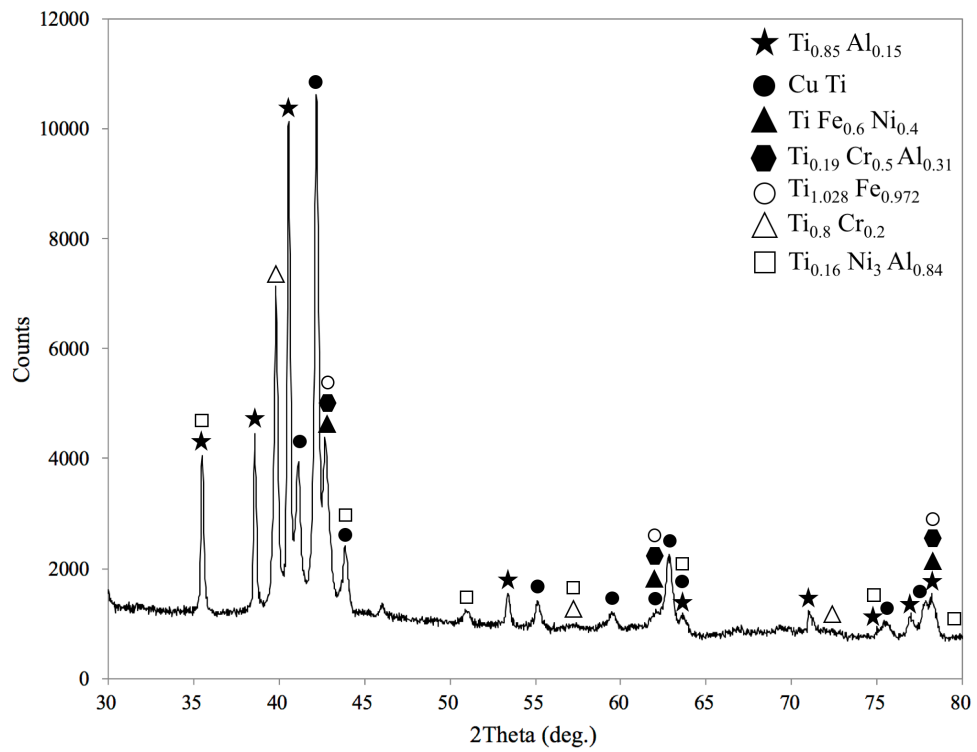
Figure 5.17 XRD pattern for the weld fracture surface at the titanium/copper interface at the titanium surface side.

146
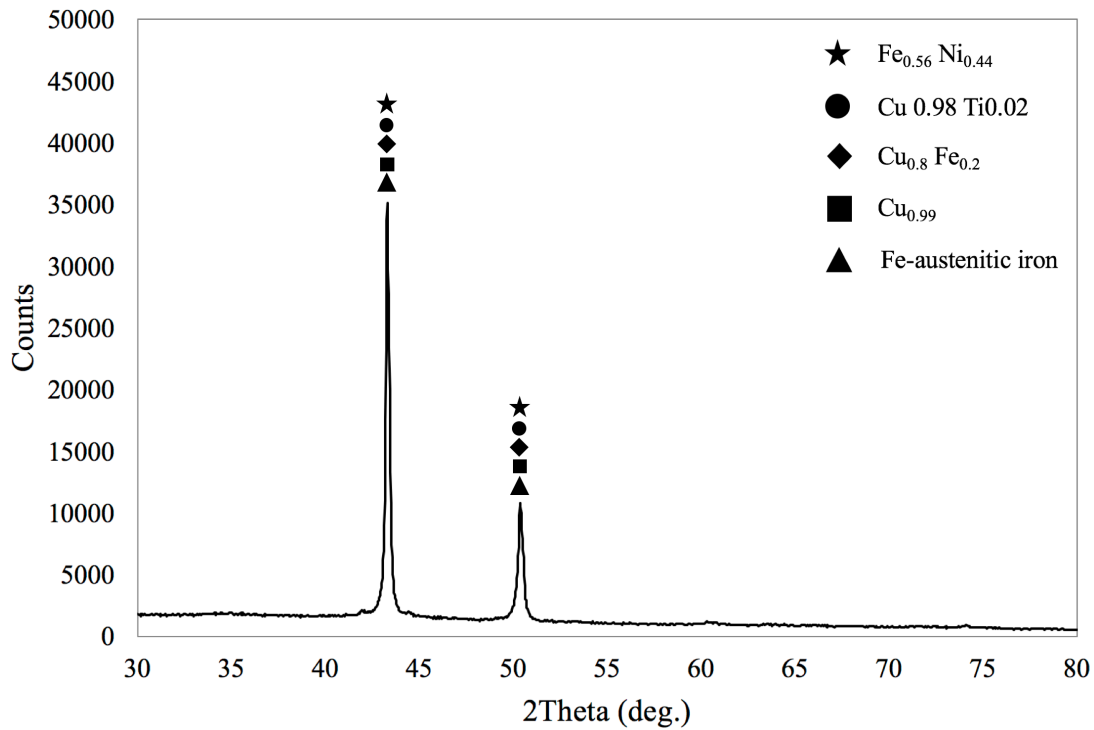
Figure 5.18 XRD pattern for the weld cross-section at the stainless steel/copper interface.

5.8 Microhardness evaluation

Vickers microhardness was used to measure across the weld to evaluate the ductility of the different interfaces. Figure 5.19 illustrates microhardness map for a part of the AISI 316L-Cu-Ti6Al4V weld cross section. The hardness at stainless steel side is about 250 HV and decreased toward the weld centre. At the stainless steel copper interaction area, the hardness decreased to about 200 HV and this possibly due to the effect of the copper solid solution. At the weld centre, the hardness reduced to 150 HV with some variation in hardness recorded in this area due to some stainless steel-rich zones that randomly distributed in the copper medium. Towards the titanium side, the hardness increased significantly. Highest hardness of 450 to 500 HV was observed in the region close to the titanium alloy. This could be attributed to the localisation of the brittle phases, e.g. Cu-Ti intermetallic, in this area. This suggests the low ductility in this region that make it more susceptible to cracking.
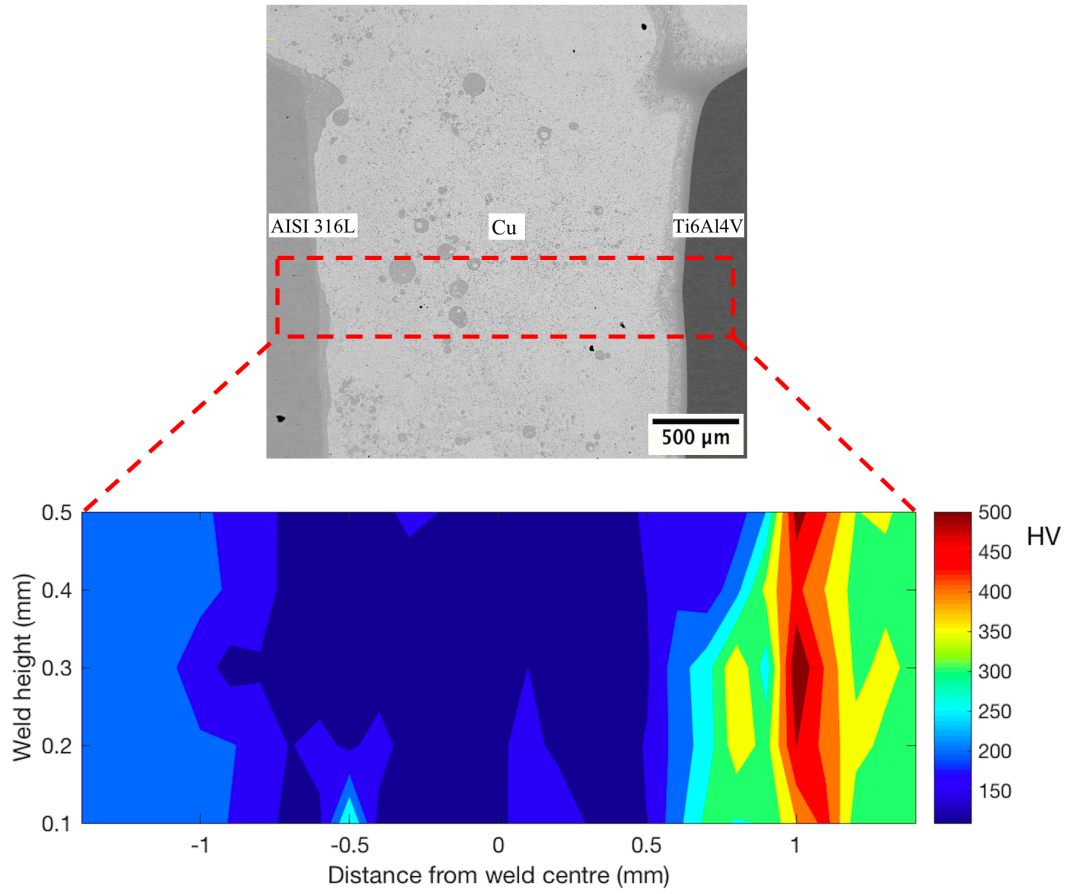
Figure 5.19 Microhardness map for a part of AISI 316L-Cu-Ti6Al4V weld

Chapter 6 Conclusions

6.1 Stainless steel-stainless steel welding

In this study, EBW parameters such as beam current, travel speed and focus offset were chosen to produce sound joints of 20 mm thick AISI 316L austenitic stainless steel. This was based on work conducted on data collected from several trials. Microscopy examinations allowed evaluation of the integrity of the structure. The Vickers microhardness and tensile strength test equipped with DIC were used to evaluate the mechanical properties of the welds. The main conclusions can be drawn as follows:

•   Weld number 2 of AISI 316L austenitic stainless steel to AISI 316L austenitic stainless steel with 110mA beam current and 9 mm/s travel speed displayed the optimum weld profile, penetration and was free of weld defects according to the BS EN ISO 13919-1:1997.

•   The FZ structure consisted of columnar and equiaxed dendritic ferrite and primary austenite, depending on the growth rate and thermal gradient across the weld. The dendrite spacing decreased towards the centre and the bottom of the weld. A clear boundary was found in the middle of the FZ ("parting" region), which is the weakest part of the weld.

•   The HAZ and BM have similar microstructures, which consisted of equiaxed austenite grains. However, there was a grain growth in the HAZ near to the fusion boundary and the average grain size in the HAZ was twice the grain size in the BM.

•   The results showed that the HAZ and BM have higher hardness than the FZ.

•   The optimum electron beam welding parameters used in W1 produced more symmetrical weld shape and more uniform distribution of the hardness than the relatively insufficient or excessive welding power used in W1 and W3 respectively.

•   The tensile strength test samples ruptured at the centre of the FZ, usually in the parting region.

•   The weld zone contained grains that have weak orientation and showed high Schmid factor intensity with interception between some strong grains and soft grains at the parting region which considered the main reason for the fracture in this area.

•   The bottom part of the weld had higher yield and ultimate tensile strength than the top and middle parts due to the effect of the high cooling rate and fine microstructure at

the root of the weld. Generally, the weld area showed high plastic deformation, which increased at the middle and bottom of the weld.

6.2 Stainless steel-titanium dissimilar welding

- Autogenous electron beam welding of AISI 316L stainless steel to Ti6Al4V was not possible due to the formation of Ti-Fe intermetallic compounds that resulted in a joint with very low ductility.

- The insertion of the copper interlayer was an option to enhance the weld ductility and minimise the mixing between the stainless steel and titanium. However, using of copper sheet with 1.5 mm thickness was the better choice than 0.5 and 1 mm thickness due to the relatively high heat input required for welding such high base metals thickness.

- In order to minimize the effect of the residual stresses and reduce the welding process heat input, a preheating technique was performed by heating the sample to approximately 450°C prior to the weld.

- Preheating the sample and applying lower heat input were combined with using a double pass welding technique to obtain a successful joint that is free of cracks.

- The formation of the intermetallic phases was not prevented but replaced with Cu-Ti intermetallic, which has greater ductility than Fe-Ti intermetallic and significantly improved the joint plasticity.

- All intermetallics are mainly located at the Cu/Ti interface, which makes his zone more sensitive to cracking.

Chapter 7 Recommendations for future work

Further investigations can be done based on the current studies. These could be relating to the welding procedure or to the characterisation methods in both similar and dissimilar welding and can be outlined as following:

7.1 Stainless steel-stainless steel welding possible further work

• Study the impact of welding speed and beam oscillation on the weld microstructure and mechanical properties.

• Apply a post weld heat treatment and study its impact on the weld microstructure and mechanical properties.

• Carry out EBSD test for different areas through weld thickness and study the effect of grains orientation on the joint strength.

• Analyse the residual stresses in the weld and study their influence on the mechanical properties of the joint.

• Use three dimensional finite element simulation of high density heat source for EBW technique using finite element code SYSWELD for predicting the temperature profile on AISI 316 stainless steel sheets that enables estimation of weld pool geometry, transient temperature, residual stresses and distortion.

• The results of the simulation can be compared with those from the experimental data for EBW joints.

7.2 Stainless steel-titanium dissimilar welding possible further work

• Study the effect of welding parameters such as beam current, welding speed and beam offset on the weld microstructure and joint strength.

• Study the variation in the microstructure through the weld thickness.

• Evaluate the joint strength through tensile test.

• Try more types of inter layer such as silver.

- Try welding the AISI 316L stainless steel to more weldable titanium alloy such as CP titanium to improve the possibility of dissimilar joining between the two metals.

References

[1]   Z. Sun and R. Karppi, "The application of electron beam welding for the joining of dissimilar metals: an overview," *Journal of Materials Processing Technology,* vol. 59, pp. 257-267, 1996.

[2]   B. Shanmugarajan and G. Padmanabham, "Fusion welding studies using laser on Ti–SS dissimilar combination," *Optics and Lasers in Engineering,* vol. 50, pp. 1621-1627, 2012.

[3]   K. Fan, G. Wang, F. Xuan, and S. Tu, "Local failure behavior of a dissimilar metal interface region with mechanical heterogeneity," *Engineering Failure Analysis,* vol. 59, pp. 419-433, 2016.

[4]   X. Zhang, E. Ashida, S. Tarasawa, Y. Anma, M. Okada, S. Katayama*, et al.*, "Welding of thick stainless steel plates up to 50 mm with high brightness lasers," *Journal of Laser Applications,* vol. 23, p. 022002, 2011.

[5]   R. K. Buddu, N. Chauhan, P. Raole, and H. Natu, "Studies on mechanical properties, microstructure and fracture morphology details of laser beam welded thick SS304L plates for fusion reactor applications," *Fusion Engineering and Design,* vol. 95, pp. 34-43, 2015.

[6]   T. Wang, B. Zhang, J. Feng, and Q. Tang, "Effect of a copper filler metal on the microstructure and mechanical properties of electron beam welded titanium–stainless steel joint," *Materials Characterization,* vol. 73, pp. 104-113, 2012.

[7]   Y. Gao, T. Tsumura, and K. Nakata, "Dissimilar welding of titanium alloys to steels," *Trans. JWRI,* vol. 41, pp. 7-12, 2012.

[8]   R. Rai, T. Palmer, J. Elmer, and T. Debroy, "Heat transfer and fluid flow during electron beam welding of 304L stainless steel alloy," *Weld. J,* vol. 88, pp. 54s-61s, 2009.

[9]   S. Böhm, "The electron beam as a welding tool: German study on the state of the art and future requirements," in *Proceedings-67th IIW International Conference, Seoul*, 2014.

[10]   S. Kou, *Welding metallurgy*, Second ed. Hoboken, New Jersey: John Wiley & Sons, 2003.

[11]   P. F. Mendez and T. W. Eagar, "New trends in welding in the aeronautic industry," presented at the 2nd Conference of New Manufacturing Trends, Bilboa, Spain, 2002.

[12]   I. Tomashchuk, P. Sallamand, N. Belyavina, and M. Pilloz, "Evolution of microstructures and mechanical properties during dissimilar electron beam welding of titanium alloy to stainless steel via copper interlayer," *Materials Science and Engineering: A,* vol. 585, pp. 114-122, 2013.

[13]   M. S. Węglowski, S. Błacha, and A. Phillips, "Electron beam welding–Techniques and trends–Review," *Vacuum,* vol. 130, pp. 72-92, 2016.

[14]   J. Norrish, *Advanced welding process-Technology and process control.* Cambridge, England: Wood head Publishing Limited, 2006.

[15]   H. Schultz, *Electron beam welding*. Cambridge: Abington publishing, 1993.

[16] G. Mladenov, K. Vutova, and S. Wojcicki, "Experimental investigation of the weld depth and thermal efficiency during electron beam welding," *Vacuum,* vol. 51, pp. 231-233, 1998.

[17] P. Fu, Z. Mao, C. Zuo, Y. Wang, and C. Wang, "Microstructures and fatigue properties of electron beam welds with beam oscillation for heavy section TC4-DT alloy," *Chinese Journal of Aeronautics,* vol. 27, pp. 1015-1021, 2014.

[18] N. Ahmed, *New developments in advanced welding.* Cambridge: Woodhead PublishingLimited, Abington publishing, 2005.

[19] P. Klemens, "Heat balance and flow conditions for electron beam and laser welding," *Journal of applied physics,* vol. 47, pp. 2165-2174, 2008.

[20] J. Huang, "The characterisation and modelling of porosity formation in electron beam welded titanium alloys," University of Birmingham, 2012.

[21] A. Handbook, "Volume 6: Welding, Brazing and Soldering," *ASM International,* vol. 2603, 1993.

[22] M. P. Groover, *Fundamentals of Modern Manufacturing.* New York: John Wiley & Sons, 2010.

[23] S. S. Gajapathi, S. K. Mitra, and P. F. Mendez, "Controlling heat transfer in micro electron beam welding using volumetric heating," *International Journal of Heat and Mass Transfer,* vol. 54, pp. 5545-5553, 2011.

[24] J. Robertw. Messler, *Pinciples of fusion welding*: WILEY-VCH Verlag GmbH & Co. KGaA, Weinheim, 2004.

[25] P. Petrov, C. Georgiev, and G. Petrov, "Experimental investigation of weld pool formation in electron beam welding," *Vacuum,* vol. 51, pp. 339-343, 1998.

[26] J. Lowry, J. Fink, and B. Schumacher, "A major advance in high-power electron-beam welding in air," *Journal of Applied Physics,* vol. 47, pp. 95-106, 1976.

[27] T. W. E. a. A. D. Mazzeo, *Welding Process Fundamentals* vol. Volume 6A: ASM International, 2011.

[28] C. Ho, "Fusion zone during focused electron-beam welding," *Journal of materials processing technology,* vol. 167, pp. 265-272, 2005.

[29] P. Wei and C. Ho, "Beam focusing characteristics effect on energy reflection and absorption in a drilling or welding cavity of paraboloid of revolution," *International journal of heat and mass transfer,* vol. 41, pp. 3299-3308, 1998.

[30] S. E. Oltean and M. Abrudean, "Advanced control of the electron beam welding," *Journal of Control Engineering and Applied Informatics,* vol. 10, pp. 40-48, 2008.

[31] B. Joseph, D. Katherasan, P. Sathiya, and C. S. Murthy, "Weld metal characterization of 316L (N) austenitic stainless steel by electron beam welding process," *International Journal of Engineering, Science and Technology,* vol. 4, pp. 169-176, 2012.

[32] I. Magnabosco, P. Ferro, F. Bonollo, and L. Arnberg, "An investigation of fusion zone microstructures in electron beam welding of copper–stainless steel," *Materials Science and Engineering: A,* vol. 424, pp. 163-173, 2006.

[33] D. R. A. a. P. P. Fulay, *Essentials of Materials Science and Engineering*, Second ed. USA: Cengage Learning, 2010.

[34] B. Leffler, "Stainless steels and their properties," *AvestaPolarit AB,* 1996.

[35] G. Krauss, *Steels: processing, structure, and performance*: Asm International, 2015.

[36] A. Elmesalamy, "Narrow Gap Laser Welding of 316L Stainless Steel for Potential Application in the Manufacture of Thick Section Nuclear Components," 2013.

[37] W. D. Callister and D. G. Rethwisch, *Materials science and engineering: an introduction* vol. 7: Wiley New York, 2007.

[38] J. Sundgren, P. Bodö, and I. Lundström, "Auger electron spectroscopic studies of the interface between human tissue and implants of titanium and stainless steel," *Journal of colloid and interface science,* vol. 110, pp. 9-20, 1986.

[39] J. Elmer, S. Allen, and T. Eagar, "Microstructural development during solidification of stainless steel alloys," *Metallurgical transactions A,* vol. 20, pp. 2117-2131, 1989.

[40] J. C. L. a. D. J. Kotecki, *Welding Metallurgy and Weldability of Stainless Steels*. USA: John Wiley & Sons Inc, 2005.

[41] F. Borgioli, E. Galvanetto, and T. Bacci, "Low temperature nitriding of AISI 300 and 200 series austenitic stainless steels," *Vacuum,* vol. 127, pp. 51-60, 2016.

[42] I. Souza Filho, M. Sandim, R. Cohen, L. Nagamine, J. Hoffmann, R. Bolmaro*, et al.*, "Effects of strain-induced martensite and its reversion on the magnetic properties of AISI 201 austenitic stainless steel," *Journal of Magnetism and Magnetic Materials,* 2016.

[43] H. Pommier, E. P. Busso, T. F. Morgeneyer, and A. Pineau, "Intergranular damage during stress relaxation in AISI 316L-type austenitic stainless steels: Effect of carbon, nitrogen and phosphorus contents," *Acta Materialia,* vol. 103, pp. 893-908, 2016.

[44] N. Parvathavarthini, R. Dayal, H. Khatak, V. Shankar, and V. Shanmugam, "Sensitization behaviour of modified 316N and 316L stainless steel weld metals after complex annealing and stress relieving cycles," *Journal of nuclear materials,* vol. 355, pp. 68-82, 2006.

[45] J.-H. Kim, S.-K. Kim, C.-S. Lee, M.-H. Kim, and J.-M. Lee, "A constitutive equation for predicting the material nonlinear behavior of AISI 316L, 321, and 347 stainless steel under low-temperature conditions," *International Journal of Mechanical Sciences,* vol. 87, pp. 218-225, 2014.

[46] M. Shimada, H. Kokawa, Z. Wang, Y. Sato, and I. Karibe, "Optimization of grain boundary character distribution for intergranular corrosion resistant 304 stainless steel by twin-induced grain boundary engineering," *Acta Materialia,* vol. 50, pp. 2331-2341, 2002.

[47] Z. Yanushkevich, A. Mogucheva, M. Tikhonova, A. Belyakov, and R. Kaibyshev, "Structural strengthening of an austenitic stainless steel subjected to warm-to-hot working," *Materials characterization,* vol. 62, pp. 432-437, 2011.

[48] I. Shakhova, A. Belyakov, Z. Yanushkevich, K. Tsuzaki, and R. Kaibyshev, "On Strengthening of Austenitic Stainless Steel by Large Strain Cold Working," *ISIJ International,* 2016.

[49] M. Tikhonova, R. Kaibyshev, X. Fang, W. Wang, and A. Belyakov, "Grain boundary assembles developed in an austenitic stainless steel during large strain warm working," *Materials Characterization,* vol. 70, pp. 14-20, 2012.

[50] Y. Idell, G. Facco, A. Kulovits, M. Shankar, and J. Wiezorek, "Strengthening of austenitic stainless steel by formation of nanocrystalline γ-phase through severe

plastic deformation during two-dimensional linear plane-strain machining," *Scripta materialia,* vol. 68, pp. 667-670, 2013.

[51] M. Somani, P. Juntunen, L. Karjalainen, R. Misra, and A. Kyröläinen, "Enhanced mechanical properties through reversion in metastable austenitic stainless steels," *Metallurgical and Materials Transactions A,* vol. 40, pp. 729-744, 2009.

[52] P. Ferrandini, C. Rios, A. Dutra, M. Jaime, P. Mei, and R. Caram, "Solute segregation and microstructure of directionally solidified austenitic stainless steel," *Materials Science and Engineering: A,* vol. 435, pp. 139-144, 2006.

[53] J. R. Davis, *Stainless Steels*. USA: ASM International, 1999.

[54] K. Rajasekhar, C. Harendranath, R. Raman, and S. Kulkarni, "Microstructural evolution during solidification of austenitic stainless steel weld metals: a color metallographic and electron microprobe analysis study," *Materials characterization,* vol. 38, pp. 53-65, 1997.

[55] K. Li, D. Li, D. Liu, G. Pei, and L. Sun, "Microstructure evolution and mechanical properties of multiple-layer laser cladding coating of 308L stainless steel," *Applied Surface Science,* vol. 340, pp. 143-150, 2015.

[56] T. Sourmail, "Precipitation in creep resistant austenitic stainless steels," *Materials science and technology,* vol. 17, pp. 1-14, 2001.

[57] T. Lienert, T. Siewert, S. Babu, and V. Acoff, "Fundamentals of Weld Solidification," 2011.

[58] H. Inoue and T. Koseki, "Clarification of solidification behaviors in austenitic stainless steels based on welding process," *Nippon Steel Technical Report,* vol. 95, pp. 62-70, 2007.

[59] D. R. Askeland, P. Fulay, and W. Wright, "The science and engineering of materials 6th edition," *Thomson learning Inc,* pp. 232-250, 2010.

[60] O. Hunziker, D. Dye, and R. Reed, "On the formation of a centreline grain boundary during fusion welding," *Acta materialia,* vol. 48, pp. 4191-4201, 2000.

[61] D. Dye, O. Hunziker, and R. Reed, "Numerical analysis of the weldability of superalloys," *Acta Materialia,* vol. 49, pp. 683-697, 2001.

[62] L. Cui, X. Li, D. He, L. Chen, and S. Gong, "Effect of Nd: YAG laser welding on microstructure and hardness of an Al–Li based alloy," *Materials Characterization,* vol. 71, pp. 95-102, 2012.

[63] W. Kurz, C. Bezencon, and M. Gäumann, "Columnar to equiaxed transition in solidification processing," *Science and technology of advanced materials,* vol. 2, pp. 185-191, 2001.

[64] F. Wang, S. Williams, P. Colegrove, and A. A. Antonysamy, "Microstructure and mechanical properties of wire and arc additive manufactured Ti-6Al-4V," *Metallurgical and Materials Transactions A,* vol. 44, pp. 968-977, 2013.

[65] M. KATO, F. MATSUDA, and T. SENDA, "Solidification mode in aluminum weld metal," *Transactions of the Japan Welding Society,* vol. 3, pp. 69-76, 1972.

[66] I. Hemmati, V. Ocelík, and J. T. M. De Hosson, "Microstructural characterization of AISI 431 martensitic stainless steel laser-deposited coatings," *Journal of materials science,* vol. 46, pp. 3405-3414, 2011.

[67] M. F. Dodge, "The effect of heat treatment on the embrittlement of dissimilar welded joints," Department of Engineering, 2014.

[68] S. Tjong, S. Zhu, N. Ho, and J. Ku, "Microstructural characteristics and creep rupture behavior of electron beam and laser welded AISI 316L stainless steel," *Journal of nuclear materials,* vol. 227, pp. 24-31, 1995.

[69] A. Norman, V. Drazhner, and P. Prangnell, "Effect of welding parameters on the solidification microstructure of autogenous TIG welds in an Al–Cu–Mg–Mn alloy," *Materials Science and Engineering: A,* vol. 259, pp. 53-64, 1999.

[70] J. Pavlović-Krstić, R. Bähr, G. Krstić, and S. Putić, "The effect of mould temperature and cooling conditions on the size of secondary dendrite arm spacing in Al-7Si-3Cu alloy," *Metalurgija,* vol. 15, pp. 106-113, 2009.

[71] C. Rui, Y.-f. SHI, Q.-y. XU, and B.-c. LIU, "Effect of cooling rate on solidification parameters and microstructure of Al-7Si-0.3 Mg-0.15 Fe alloy," *Transactions of Nonferrous Metals Society of China,* vol. 24, pp. 1645-1652, 2014.

[72] S. David and J. Vitek, "Correlation between solidification parameters and weld microstructures," *International Materials Reviews,* 2013.

[73] Z. Xue, S. Hu, D. Zuo, and J. Shen, "Correlation between process parameters and primary dendrite arm spacing in laser welding of Cu and Al," *Transactions of Tianjin University,* vol. 20, pp. 315-321, 2014.

[74] J. Yan, M. Gao, and X. Zeng, "Study on microstructure and mechanical properties of 304 stainless steel joints by TIG, laser and laser-TIG hybrid welding," *Optics and Lasers in Engineering,* vol. 48, pp. 512-517, 2010.

[75] S. David and J. Vitek, "Correlation between solidification parameters and weld microstructures," *International Materials Reviews,* vol. 34, pp. 213-245, 1989.

[76] J. Ma, Y. Yang, W. Tong, Y. Fang, Y. Yu, and Z. Hu, "Microstructural evolution in AISI 304 stainless steel during directional solidification and subsequent solid-state transformation," *Materials Science and Engineering: A,* vol. 444, pp. 64-68, 2007.

[77] J. Brooks and A. Thompson, "Microstructural development and solidification cracking susceptibility of austenitic stainless steel welds," *International Materials Reviews,* vol. 36, pp. 16-44, 1991.

[78] S. Katayama, T. Fujimoto, and A. Matsunawa, "Correlation among Solidification Process, Microstructure, Microsegregation and Solidification Cracking Susceptibility in Stainless Steel Weld Metals (Materials, Metallurgy & Weldability)," *Transactions of JWRI,* vol. 14, pp. 123-138, 1985.

[79] V. Shankar, T. Gill, S. Mannan, and S. Sundaresan, "Solidification cracking in austenitic stainless steel welds," *Sadhana,* vol. 28, pp. 359-382, 2003.

[80] H. Kokawa, M. Shimada, and Y. S. Sato, "Grain-boundary structure and precipitation in sensitized austenitic stainless steel," *Jom,* vol. 52, pp. 34-37, 2000.

[81] M. Terada, M. Saiki, I. Costa, and A. F. Padilha, "Microstructure and intergranular corrosion of the austenitic stainless steel 1.4970," *Journal of nuclear materials,* vol. 358, pp. 40-46, 2006.

[82] L. Li and R. Messler, "Segregation of phosphorus and sulfur in heat-affected zone hot cracking of type 308 stainless steel," *Rivista Italiana della Saldatura(Italy),* vol. 54, pp. 511-518, 2002.

[83] A. K. Jha and S. Arumugham, "Metallographic analysis of embedded crack in electron beam welded austenitic stainless steel chemical storage tank," *Engineering Failure Analysis,* vol. 8, pp. 157-166, 2001.

[84]   J. Lippold and W. Savage, "Solidification of austenitic stainless steel weldments: Part III--the effect of solidification behavior on hot cracking susceptibility," *WELDING J.,* vol. 61, p. 388, 1982.

[85]   H. Kumar, A. Somireddy, and K. Gururaj, "A review on critical aspects of 316ln austenitic stainless steel weldability," *International Journal of Materials Science and Applications,* vol. 1, pp. 1-7, 2012.

[86]   J. Yu, M. Rombouts, and G. Maes, "Cracking behavior and mechanical properties of austenitic stainless steel parts produced by laser metal deposition," *Materials & Design,* vol. 45, pp. 228-235, 2013.

[87]   C. Lundin, C. Chou, and C. Sullivan, "Hot cracking resistance of austenitic stainless steel weld metals," *Weld. J,* vol. 59, pp. 226s-232s, 1980.

[88]   C. Long and W. DeLong, "Ferrite content of austenitic stainless steel weld metal," *Welding journal,* vol. 52, p. 281, 1973.

[89]   L. Beres, "Proposed modification to Schaeffler diagram for chrome equivalents and carbon for more accurate prediction of martensite content," *Welding Journal,* vol. 77, pp. 273-276, 1998.

[90]   J. Feldstein and F. Lake, "A new constitution diagram for predicting ferrite content of stainless steel weld metals," *Materials and Design(UK),* vol. 14, pp. 345-348, 1993.

[91]   D. Lee, J. Byun, J. Sung, and H. Lee, "The dependence of crack properties on the Cr/Ni equivalent ratio in AISI 304L austenitic stainless steel weld metals," *Materials Science and Engineering: A,* vol. 513, pp. 154-159, 2009.

[92]   P. Korinko and S. Malene, "Considerations for the weldability of types 304L and 316L stainless steel," *Practical failure analysis,* vol. 1, pp. 61-68, 2001.

[93]   T. Ogawa and E. Tsunetomi, "Hot Cracking Susceptibility of Austenitic Stainless Steels," *WELDING J.,* vol. 61, p. 82, 1982.

[94]   L. Li and R. W. Messler, "Effects of Phosphorus and Sulfur on Susceptibility to Weld Hot Cracking in Austenitic Stainless Steels," *Welding Research Council Bulletin,* 2003.

[95]   J. Lippold, "Solidification behavior and cracking susceptibility of pulsed-laser welds in austenitic stainless steels," *Welding Journal Including Welding Research Supplement,* vol. 73, p. 129s, 1994.

[96]   S. Wessman, "Evaluation of the WRC 1992 diagram using computational thermodynamics," *Welding in the World,* vol. 57, pp. 305-313, 2013.

[97]   D. Kotecki, "A Martensite Boundary on the WRC-1992 Diagram—Part 2: The Effect of Manganese," *Welding journal,* vol. 79, pp. s346-s354, 2000.

[98]   D. Kotecki and T. Siewert, "WRC-1992 constitution diagram for stainless steel weld metals: a modification of the WRC-1988 diagram," *Welding Journal,* vol. 71, pp. 171-178, 1992.

[99]   F. Hull, "Delta Ferrite and Martnesite formation in stainless steels," *Welding journal,* vol. 52, p. 193, 1973.

[100]   W. Kurz and D. J. Fisher, "Dendrite Growth at the Limit of Stability - Tip Radius and Spacing," *Acta Metallurgica,* vol. 29, pp. 11-20, 1981.

[101]   J. Brooks, M. Baskes, and F. Greulich, "Solidification modeling and solid-state transformations in high-energy density stainless steel welds," *Metallurgical Transactions A,* vol. 22, pp. 915-926, 1991.

[102] S. Fukumoto and W. Kurz, "The δ to γ transition in Fe-Cr-Ni alloys during laser treatment," *ISIJ international,* vol. 37, pp. 677-684, 1997.

[103] J. Elmer, S. Allen, and T. Eagar, "The influence of cooling rate on the ferrite content of stainless steel alloys," in *Proceedings of the 2nd International Conference on Trends in Welding Research*, 1989, pp. 14-18.

[104] R. Kaul, P. Ganesh, P. Tripathi, R. Nandedkar, and A. Nath, "Comparison of laser and gas tungsten arc weldments of stabilized 17 wt% Cr ferritic stainless steel," *Materials and Manufacturing Processes,* vol. 18, pp. 563-580, 2003.

[105] A. Lakshminarayanan and V. Balasubramanian, "Comparison of electron beam and friction stir weldments of modified 12 wt% ferritic stainless steel," *Materials and Manufacturing Processes,* vol. 26, pp. 868-877, 2011.

[106] J. Rodelas, J. Lippold, J. Rule, and J. Livingston, "Friction stir processing as a base metal preparation technique for modification of fusion weld microstructures," *Friction Stir Welding and Processing VI,* pp. 323-331, 2011.

[107] M. Gustafsson, M. Thuvander, E.-L. Bergqvist, E. Keehan, and L. Karlsson, "Effect of welding procedure on texture and strength of nickel based weld metal," *Science and Technology of Welding and Joining,* vol. 12, pp. 549-555, 2007.

[108] M. Wu, R. Xin, Y. Wang, Y. Zhou, K. Wang, and Q. Liu, "Microstructure, texture and mechanical properties of commercial high-purity thick titanium plates jointed by electron beam welding," *Materials Science and Engineering: A,* vol. 677, pp. 50-57, 2016.

[109] T. Saukkonen, M. Aalto, I. Virkkunen, U. Ehrnstén, and H. Hänninen, "Plastic strain and residual stress distributions in an AISI 304 stainless steel BWR pipe weld," in *15th International Conference on Environmental Degradation of Materials in Nuclear Power Systems-Water Reactors. New Jersey, Canada*, 2012.

[110] W. Lin, J. Lippold, and W. Baeslack III, "An evaluation of heat-affected zone liquation cracking susceptibility, Part I: Development of a method for quantification," *WELDING JOURNAL-NEW YORK-,* vol. 72, pp. 135-s, 1993.

[111] J. Lippold, W. Baeslack, and I. Varol, "Heat-affected zone liquation cracking in austenitic and duplex stainless steels," *Welding Journal(USA),* vol. 71, p. 1, 1988.

[112] M. Thomas, "On the characterisation of subsurface deformation microstructures in aerostructural titanium alloys," 2012.

[113] C. Leyens and M. Peters, *Titanium and titanium alloys*: Wiley Online Library, 2003.

[114] G. Lütjering and J. C. Williams, *Titanium*: Springer, 2007.

[115] L. A. Marshall, "The influence of aluminium additions on titanium during machining through the application of a novel orthogonal cutting test method," University of Sheffield, 2014.

[116] P. Crawforth, "Towards a Micromechanistic Understanding of Imparted Subsurface Deformation During Machining of Titanium Alloys," University of Sheffield, 2014.

[117] I. Weiss and S. Semiatin, "Thermomechanical processing of alpha titanium alloys—an overview," *Materials Science and Engineering: A,* vol. 263, pp. 243-256, 1999.

[118] H. Flower, "Microstructural development in relation to hot working of titanium alloys," *Materials Science and Technology,* vol. 6, pp. 1082-1092, 1990.

[119] V. A. Joshi, *Titanium alloys: an atlas of structures and fracture features*: Crc Press, 2006.

[120] X. Jiang, "Microstructure and crystallographic texture evolution in stationary shoulder friction Stir welded Ti-6Al-4V," University of Sheffield, 2012.

[121] W. Kearns, "Welding Handbook–Metals and their Weldability, Vol," ed: Miami, FL: American Welding Society, 1981.

[122] J. Barreda, F. Santamarıa, X. Azpiroz, A. Irisarri, and J. Varona, "Electron beam welded high thickness Ti6Al4V plates using filler metal of similar and different composition to the base plate," *Vacuum,* vol. 62, pp. 143-150, 2001.

[123] C. Zheng, F. Wang, X. Cheng, K. Fu, J. Liu, Y. Wang, *et al.*, "Effect of microstructures on ballistic impact property of Ti–6Al–4V targets," *Materials Science and Engineering: A,* vol. 608, pp. 53-62, 2014.

[124] W. Sha and S. Malinov, *Titanium alloys: modelling of microstructure, properties and applications*: Elsevier, 2009.

[125] M. J. Donachie, *Titanium: a technical guide*: ASM international, 2000.

[126] W. Lu, Y. Shi, Y. Lei, and X. Li, "Effect of electron beam welding on the microstructures and mechanical properties of thick TC4-DT alloy," *Materials & Design,* vol. 34, pp. 509-515, 2012.

[127] P. Wanjara, M. Jahazi, H. Monajati, and S. Yue, "Influence of thermomechanical processing on microstructural evolution in near-α alloy IMI834," *Materials Science and Engineering: A,* vol. 416, pp. 300-311, 2006.

[128] G. Lütjering and J. C. Williams, *Titanium* vol. 2: Springer, 2003.

[129] A. Mateo, "On the feasibility of BLISK produced by linear friction welding," *Revista de Metalurgia,* vol. 50, pp. 1-11, 2014.

[130] G. M. Reddy and K. S. Rao, "Microstructure and mechanical properties of similar and dissimilar stainless steel electron beam and friction welds," *The International Journal of Advanced Manufacturing Technology,* vol. 45, pp. 875-888, 2009.

[131] M. Sireesha, V. Shankar, S. K. Albert, and S. Sundaresan, "Microstructural features of dissimilar welds between 316LN austenitic stainless steel and alloy 800," *Materials Science and Engineering: A,* vol. 292, pp. 74-82, 2000.

[132] A. Celik and A. Alsaran, "Mechanical and structural properties of similar and dissimilar steel joints," *Materials Characterization,* vol. 43, pp. 311-318, 1999.

[133] M. Marya and S. Liu, "Search for filler metal for welding of ferrous alloys to titanium," *Science and Technology of Welding & Joining,* 2013.

[134] A. Irisarri, J. Barreda, and X. Azpiroz, "Influence of the filler metal on the properties of Ti-6Al-4V electron beam weldments. Part I: Welding procedures and microstructural characterization," *Vacuum,* vol. 84, pp. 393-399, 2009.

[135] P. V. Ramana, G. M. Reddy, T. Mohandas, and A. Gupta, "Microstructure and residual stress distribution of similar and dissimilar electron beam welds–maraging steel to medium alloy medium carbon steel," *Materials & Design,* vol. 31, pp. 749-760, 2010.

[136] S. A. Mousavi and P. F. Sartangi, "Effect of post-weld heat treatment on the interface microstructure of explosively welded titanium–stainless steel composite," *Materials Science and Engineering: A,* vol. 494, pp. 329-336, 2008.

[137] S. Chen, M. Zhang, J. Huang, C. Cui, H. Zhang, and X. Zhao, "Microstructures and mechanical property of laser butt welding of titanium alloy to stainless steel," *Materials & Design,* vol. 53, pp. 504-511, 2014.

[138] H.-C. Chen, G. Bi, B. Y. Lee, and C. K. Cheng, "Laser welding of CP Ti to stainless steel with different temporal pulse shapes," *Journal of Materials Processing Technology,* vol. 231, pp. 58-65, 2016.

[139] E. K. Molchanova, "Phase diagrams of titanium alloys," 1965.

[140] M. Fazel-Najafabadi, S. Kashani-Bozorg, and A. Zarei-Hanzaki, "Joining of CP-Ti to 304 stainless steel using friction stir welding technique," *Materials & Design,* vol. 31, pp. 4800-4807, 2010.

[141] K. Ishida, Y. Gao, K. Nagatsuka, M. Takahashi, and K. Nakata, "Microstructures and mechanical properties of friction stir welded lap joints of commercially pure titanium and 304 stainless steel," *Journal of alloys and compounds,* vol. 630, pp. 172-177, 2015.

[142] N. Orhan, T. Khan, and M. Eroğlu, "Diffusion bonding of a microduplex stainless steel to Ti–6Al–4V," *Scripta Materialia,* vol. 45, pp. 441-446, 2001.

[143] M. Ghosh and S. Chatterjee, "Characterization of transition joints of commercially pure titanium to 304 stainless steel," *Materials Characterization,* vol. 48, pp. 393-399, 2002.

[144] M. Ghosh and S. Chatterjee, "Diffusion bonded transition joints of titanium to stainless steel with improved properties," *Materials Science and Engineering: A,* vol. 358, pp. 152-158, 2003.

[145] N. Kahraman, B. Gülenç, and F. Findik, "Joining of titanium/stainless steel by explosive welding and effect on interface," *Journal of Materials Processing Technology,* vol. 169, pp. 127-133, 2005.

[146] S. A. Mousavi and P. F. Sartangi, "Experimental investigation of explosive welding of cp-titanium/AISI 304 stainless steel," *Materials & Design,* vol. 30, pp. 459-468, 2009.

[147] C. Xia and Z. Jin, "On the evolution of microstructure and diffusion paths in the titanium-steel explosion weld interface during heat treatment," *Journal of the Less Common Metals,* vol. 162, pp. 315-322, 1990.

[148] W. Ting, B.-G. Zhang, G.-Q. Chen, J.-C. Feng, and T. Qi, "Electron beam welding of Ti-15-3 titanium alloy to 304 stainless steel with copper interlayer sheet," *Transactions of Nonferrous Metals Society of China,* vol. 20, pp. 1829-1834, 2010.

[149] C. Muralimohan, M. Ashfaq, R. Ashiri, V. Muthupandi, and K. Sivaprasad, "Analysis and Characterization of the Role of Ni Interlayer in the Friction Welding of Titanium and 304 Austenitic Stainless Steel," *Metallurgical and Materials Transactions A,* vol. 47, pp. 347-359, 2016.

[150] R. Kumar and M. Balasubramanian, "Experimental investigation of Ti–6Al–4V titanium alloy and 304L stainless steel friction welded with copper interlayer," *Defence Technology,* vol. 11, pp. 65-75, 2015.

[151] W. Ting, B.-g. Zhang, and J.-c. Feng, "Influences of different filler metals on electron beam welding of titanium alloy to stainless steel," *Transactions of Nonferrous Metals Society of China,* vol. 24, pp. 108-114, 2014.

[152] I. Tomashchuk, P. Sallamand, H. Andrzejewski, and D. Grevey, "The formation of intermetallics in dissimilar Ti6Al4V/copper/AISI 316 L electron beam and Nd: YAG laser joints," *Intermetallics,* vol. 19, pp. 1466-1473, 2011.

[153] A. H. Volume, "2: Properties and Selection: Nonferrous Alloys and Special-Purpose Materials," *ASM international,* pp. 889-896, 1990.

[154] A. A240/A240M-08, "Standard Specification for Chromium and Chromium-Nickel Stainless Steel Plate, Sheet, and Strip for Pressure Vessels and for General Applications," 2015.

[155] B. ASTM, "265-99—Standard Specification for Titanium and Titanium Alloy Strip, Sheet, and Plate," *West Conshohocken, Pennsylvania: American Society for Testing and Materials,* 1999.

[156] M. Shabani and A. Mazahery, "Prediction of mechanical properties of cast A356 alloy as a function of microstructure and cooling rate," *Arch Metall Mater,* vol. 56, pp. 671-675, 2011.

[157] G. Tagore and G. R. Janardhana, "Evolution of Artificial Neural Network (ANN) Model for Predicting Secondary Dendrite Arm Spacing in Aluminium Alloy Casting," 2010.

[158] G. Vander Voort, "Introduction to quantitative metallography," *Tech-Notes: Using Microstructural Analysis to Solve Practical Problems,* vol. 1, pp. 1-6, 1997.

[159] A. Standard, "E8M-04," *Standard test methods for tension testing of metallic materials. West Conshohocken (PA): ASTM International,* 2004.

[160] H. Lemmen, R. Alderliesten, R. Benedictus, J. Hofstede, and R. Rodi, "The power of Digital Image Correlation for detailed elastic-plastic strain measurements," in *WSEAS international conference on engineering mechanics, structures, engineering geology. Crate Island, Greece,* 2008.

[161] C. Leitão, I. Galvão, R. Leal, and D. Rodrigues, "Determination of local constitutive properties of aluminium friction stir welds using digital image correlation," *Materials & Design,* vol. 33, pp. 69-74, 2012.

[162] M. Sutton, W. Wolters, W. Peters, W. Ranson, and S. McNeill, "Determination of displacements using an improved digital correlation method," *Image and vision computing,* vol. 1, pp. 133-139, 1983.

[163] D. Olson, "Prediction of austenitic weld metal microstructure and properties," *Welding journal,* vol. 64, pp. 281s-295s, 1985.

[164] T. Lienert and J. Lippold, "Improved weldability diagram for pulsed laser welded austenitic stainless steels," *Science and Technology of Welding and Joining,* vol. 8, pp. 1-9, 2003.

[165] E. ISO, "13919-1: Welding: Electrons and Laser Beam Welded Joints," *Guidance On Quality Levels For Imperfections. Part,* vol. 1.

[166] A.-M. El-Batahgy, "Effect of laser welding parameters on fusion zone shape and solidification structure of austenitic stainless steels," *Materials Letters,* vol. 32, pp. 155-163, 1997.

[167] A. Zambon, P. Ferro, and F. Bonollo, "Microstructural, compositional and residual stress evaluation of CO_2 laser welded superaustenitic AISI 904L stainless steel," *Materials Science and Engineering: A,* vol. 424, pp. 117-127, 2006.

[168] K. Poorhaydari, B. Patchett, and D. Ivey, "Estimation of cooling rate in the welding of plates with intermediate thickness," *Welding journal,* vol. 84, pp. 149s-155s, 2005.

[169] V. A. Ventrella, J. R. Berretta, and W. De Rossi, "Pulsed Nd: YAG laser seam welding of AISI 316L stainless steel thin foils," *Journal of Materials Processing Technology,* vol. 210, pp. 1838-1843, 2010.

[170] C. C. Silva, H. C. de Miranda, H. B. de Sant'Ana, and J. P. Farias, "Microstructure, hardness and petroleum corrosion evaluation of 316L/AWS E309MoL-16 weld metal," *Materials Characterization,* vol. 60, pp. 346-352, 2009.

[171] S. David, "Ferrite morphology and variations in ferrite content in austenitic stainless steel welds," Oak Ridge National Lab., TN1981.

[172] J. Fu, Y. Yang, J. Guo, J. Ma, and W. Tong, "Microstructure evolution in AISI 304 stainless steel during near rapid directional solidification," *Materials Science and Technology,* vol. 25, pp. 1013-1016, 2009.

[173] M. Paulus, H. Schroeder, and J. Deutz, "The interaction of fatigue and creep in wledments of AISI 316L austenitic steel after helium implantation," *Journal of nuclear materials,* vol. 191, pp. 798-802, 1992.

[174] Y. Dai and H. Schroeder, "Helium effects on the post-implantation creep properties and the microstructure of AISI 316L welds and parent material," *Journal of nuclear materials,* vol. 191, pp. 754-758, 1992.

[175] Y. Dai and H. Schroeder, "Creep properties and microstructures of helium implanted AISI 316L electron-beam weld and parent material," *Fusion engineering and design,* vol. 30, pp. 261-273, 1995.

[176] M. Zhang, G. Chen, Y. Zhou, and S. Liao, "Optimization of deep penetration laser welding of thick stainless steel with a 10kW fiber laser," *Materials & Design,* vol. 53, pp. 568-576, 2014.

[177] L. Holappa and A. Helle, "Inclusion control in high-performance steels," *Journal of materials processing technology,* vol. 53, pp. 177-186, 1995.

[178] D. E. Williams, M. R. Kilburn, J. Cliff, and G. I. Waterhouse, "Composition changes around sulphide inclusions in stainless steels, and implications for the initiation of pitting corrosion," *Corrosion science,* vol. 52, pp. 3702-3716, 2010.

[179] H. Yin and S. Felicelli, "Dendrite growth simulation during solidification in the LENS process," *Acta Materialia,* vol. 58, pp. 1455-1465, 2010.

[180] I. Gilath, J. Signamarcheix, and P. Bensussan, "A comparison of methods for estimating the weld-metal cooling rate in laser welds," *Journal of materials science,* vol. 29, pp. 3358-3362, 1994.

[181] C.-C. Hsieh, X. Guo, C.-M. Chang, and W. Wu, "Dendrite evolution of delta (δ) ferrite and precipitation behavior of sigma (σ) phase during multipass dissimilar stainless steels welding," *Metals and Materials International,* vol. 16, pp. 349-356, 2010.

[182] B. Zheng, Y. Zhou, J. Smugeresky, J. Schoenung, and E. Lavernia, "Thermal behavior and microstructure evolution during laser deposition with laser-engineered net shaping: part II. Experimental investigation and discussion," *Metallurgical and Materials Transactions A,* vol. 39, pp. 2237-2245, 2008.

[183] H. Schroeder and W. Liu, "Dependence of the tensile properties of 316 L parent material and welds on implanted hydrogen and/or helium," *Journal of nuclear materials,* vol. 191, pp. 776-780, 1992.

[184] S. Kumar and A. Shahi, "Effect of heat input on the microstructure and mechanical properties of gas tungsten arc welded AISI 304 stainless steel joints," *Materials & Design,* vol. 32, pp. 3617-3623, 2011.

[185] S. Chowdhury, D. Chen, S. Bhole, E. Powidajko, D. Weckman, and Y. Zhou, "Fiber laser welded AZ31 magnesium alloy: the effect of welding speed on microstructure and mechanical properties," *Metallurgical and Materials Transactions A,* vol. 43, pp. 2133-2147, 2012.

[186] W. R. Osorio, P. R. Goulart, A. Garcia, G. A. Santos, and C. M. Neto, "Effect of dendritic arm spacing on mechanical properties and corrosion resistance of Al 9 Wt Pct Si and Zn 27 Wt Pct Al alloys," *Metallurgical and Materials Transactions A,* vol. 37, pp. 2525-2538, 2006.

[187] F. Grosselle, G. Timelli, F. Bonollo, and R. Molina, "Correlation between microstructure and mechanical properties of Al-Si diecast engine blocks," *Metallurgical Science and Tecnology,* vol. 27, 2013.

[188] Q.-Z. Dong, Y.-S. Choi, J.-H. Hong, and H.-Y. Hwang, "Prediction of mechanical properties of Al alloys with change of cooling rate," *China Foundry,* vol. 9, pp. 381-386, 2012.

[189] R. Abbaschian and R. E. Reed-Hill, *Physical metallurgy principles*: Cengage Learning, 2008.

[190] Y. Zhang, D. Sun, X. Gu, and Y. Liu, "Nd/YAG pulsed laser welding of TC4 titanium alloy to 301L stainless steel via pure copper interlayer," *The International Journal of Advanced Manufacturing Technology,* pp. 1-9, 2016.

[191] T. Wang, B. Zhang, H. Wang, and J. Feng, "Microstructures and Mechanical Properties of Electron Beam-Welded Titanium-Steel Joints with Vanadium, Nickel, Copper and Silver Filler Metals," *Journal of materials engineering and performance,* vol. 23, pp. 1498-1504, 2014.

Appendices

Appendix- Publications

Journal Papers

- Alali, M., I. Todd, and B. P. Wynne. "Through-thickness microstructure and mechanical properties of electron beam welded 20mm thick AISI 316L austenitic stainless steel." *Materials & Design,* vol. 130, pp. 488-500, 2017.